

Analogue Studies for *In Situ* Surface Planetary Exploration

Thesis submitted for the degree of
Doctor of Philosophy
at the University of Leicester

By

Derek Pullan
Space Projects and Instrumentation Group
Department of Physics and Astronomy
University of Leicester

18th July 2008

Analogue Studies for *In Situ* Surface Planetary Exploration

Derek Pullan

Abstract

Analogue studies importantly underpin planetary missions and can provide essential continuity between payload development and actual mission operations. This thesis focuses on three topics related to analogue studies, namely planetary analogue materials, analogue experiments and the application of scientific autonomy for robotic missions. The common theme of the work relates to field geology on Mars and the search for life (astrobiology).

Examples of astrobiology-related missions to Mars are described to illustrate what has been undertaken so far and what strategies are planned for the future, including where and how one might look for signs of past and present life. A range of *in situ* techniques essential for planetary field geology are reviewed including imaging (multi-scale), analytical measurements (spectroscopy) and geotechnics (physical interaction with surface materials).

A comprehensive specimen archive and associated experiment database called GSPARC (Geological Specimen Archive) is described. Samples from the archive were used in the experimental part of this thesis.

Two mission-like studies were undertaken based on the ability of a combination of imaging and spectroscopic techniques (X-ray, Mössbauer and Raman) to unambiguously identify morphological biosignatures and to assess the biogenic potential of sedimentary structures in ancient rocks. The techniques employed confirmed their effectiveness for *in situ* astrobiology when used collectively.

Empowering planetary robots with scientific autonomy has the potential to increase science return and extend ground coverage. To address these desires, a novel approach to autonomous science operations is defined and the results from robotic trials using an early implementation of the concept showed that basic geological parameters can be recognised, appropriately scored and used to influence operations.

The need for further work within each of the topics is argued and recommendations are made to ensure the continuation of an integrated programme of analogue studies. Spin-off potential to other areas of science is highlighted.

Declaration

I hereby declare that no part of this thesis has been previously submitted to this or any other university as part of the requirement for a higher degree. The work described herein was conducted solely by the undersigned except for those colleagues and other workers acknowledged in the text.

Derek Pullan

18th July 2008

Dedication

For Theresa and Matthew

Acknowledgements

Embarking on a PhD under normal circumstances is a huge undertaking. Embarking on a PhD through part-time study whilst holding down a demanding job is possibly tantamount to madness! Needless to say I took the mad option and this is the result. The journey was not made in isolation however and I am much indebted to a number of individuals who deserve recognition for their guidance and support throughout the endeavour.

Firstly, I would like to thank my supervisors George Fraser (Physics and Astronomy) and Tim Brewer (Geology) for their unfailing guidance and constant belief in me. Both were never too busy to discuss my progress or explain the complicated stuff. Sadly Tim passed away in 2007 and his loss is still keenly felt by colleagues and friends.

Although we did not get the chance to do some science on Mars, Beagle 2 was an amazing experience and I thank Mark Sims personally for the skilled and professional way he led the project from the outset. My appreciation also extends to John Holt for all the mechanical and electrical bits-and-bobs he managed to cobble together for me over the years.

I am indebted to several members of the Geology Department at Leicester, in particular to Nick Marsh for his infectious enthusiasm for all things geochemical and willingness to devote his time to me when folk were queuing out the door. Many thanks to Jan Zalasiewicz and Andy Saunders for reviewing the contents of this work and providing extremely useful feedback, and of course to Mike Lovell and Dick Aldridge for the use of their departmental facilities, especially sample preparation, XRF and XRD during their respective terms as Head of Department.

Special thanks go to Frances Westall for introducing me to the Early Archaean and sharing in my long-held belief that good geology, good food, good wine and good company are a perfect combination. Frances was instrumental in helping to establish and promote PAFS-net and for that I am eternally grateful.

To the members of PAFS-net that contributed to this work I thank Howell Edwards (University of Bradford) and Susana Jorge Villar (University of Burgos) for the Raman data, Christian

Schröder (NASA JSC) and Göstar Klingelhöfer (University of Mainz) for the Mössbauer data, and Gordon Cressey (Natural History Museum, London) for the *in situ* XRD data. In addition I express my thanks to Beda Hofmann (Natural History Museum, Bern), Charles Cockell (Open University), John Parnell (University of Aberdeen), Dave Barnes (Aberystwyth University), Lucia Marinangeli (University of Pescara) and of course to the rest of the PAFS-net membership.

Others who deserve my thanks include Kevin Yates (National Space Centre), Phil Potts (Open University), Andrew Griffiths (MSSL), Andy Shaw (SciSys Ltd) and Benjamin Lüthi (University of Bern).

Finally, I would like to thank my wife Theresa and son Matthew for tolerating my long periods of solitary confinement in the study. At times it must have seemed to them that the whole thing would never end.

Publications

Some of the results presented in this thesis have been incorporated into the following peer reviewed papers. Other contributions (not peer reviewed) are listed in the Bibliography.

Edwards, H.G.M., Jorge Villar, S.E., **Pullan, D.**, Hargreaves, M.D., Hofmann, B.A., and Westall, F. (2007) Morphological biosignatures from relict fossilised sedimentary geological specimens: a Raman spectroscopic study, *J. Raman Spectrosc.* 38, 1352-1361, doi: 10.1002/jrs.1775

Pullan, D., Westall, F., Hofmann, B.A., Parnell, J., Cockell, C.S., Edwards, H.G.M, Jorge Villar, S.E., Schröder, C., Cressey, G., Marinangeli, L., Richter, L., and Klingelhöfer, G. (2008) Identification of Morphological Biosignatures in Martian Analogue Field Specimens using *In Situ* Planetary Instrumentation, *Astrobiology* 8, 119-156.

Shaw, A., Woods, M., Honary, E., Rendell, P., **Pullan, D.**, Barnes, D. Pugh, S., and Long, D. (2007) CREST Robotic Scientist, *Proc. Towards Autonomous Robotic Systems (TAROS)*, 3rd - 5th September 2007, University of Aberystwyth.

Woods, M., Shaw, A., Barnes, D., Price, D., Long, D., and **Pullan, D.** (2009) Autonomous Science for an ExoMars Rover like Mission, *Journal of Field Robotics* 26, Issue 4, 358-390, doi: 10.1002/rob.20289.

Table of Contents

Abstract.....	ii
Declaration.....	iii
Dedication	iv
Acknowledgements.....	v
Publications.....	vii
Chapter 1 Introduction.....	1
Chapter 2 The Search for Life on Mars.....	3
2.1 Mars Exploration and the Search for Life	3
2.1.1 Astrobiology Missions	3
2.1.1.1 Viking.....	6
2.1.1.2 Beagle 2	8
2.1.1.3 ExoMars	11
2.2 Habitats for Life on Mars (Past and Present)	13
2.2.1 Aqueous Environments	14
2.2.2 Hydrothermal Environments.....	15
2.2.3 Endolithic Environments.....	16
2.3 Field Techniques for <i>In Situ</i> Astrobiology	17
2.3.1 Imaging	20
2.3.1.1 Remote and Near-Field Imaging	20
2.3.1.2 Close-Up Imaging (Macroscopy)	23
2.3.1.3 <i>In situ</i> Microscopy	25
2.3.2 Analytical	26
2.3.2.1 X-Ray Spectroscopy	28
2.3.2.2 Raman Spectroscopy	30
2.3.2.3 Mössbauer Spectroscopy	32
2.3.3 Geotechnics	32
2.3.3.1 Grinding.....	33
2.3.3.2 Sampling.....	36
2.3.3.3 Splitting	38
2.4 Summary	39

Chapter 3 The Planetary Analogue Archive and Database	40
3.1 Introduction	40
3.1.1 The Planetary Context.....	42
3.1.2 Analogue Research, Networks and Archives.....	44
3.2 The GSPARC Specimen Archive and Experiment Database.....	48
3.2.1 Organising Principles.....	49
3.2.2 Database Design.....	50
3.2.2.1 Standalone Version.....	50
3.2.2.2 On-line Version	56
3.2.3 Research and Mission Support.....	59
3.2.3.1 Collaborations and Studies	59
3.2.3.2 The Planetary Analogue Field Studies Network (PAFS-net)	61
3.2.4 Education and Public Outreach.....	62
3.2.4.1 SpaceROX.....	63
3.3 Summary	65
Chapter 4 Study Samples for <i>In Situ</i> Astrobiology	67
4.1 Introduction	67
4.2 Experimental Study 1: Morphological Biosignatures	70
4.3 Experimental Study 2: Ancient Sedimentary Structures.....	72
4.4 Samples for Related Experiments	73
4.4.1 Geotechnics.....	74
4.4.2 Fluorescence Imaging	75
4.4.3 Colour Stereo Macroscopic Imaging	75
4.5 Summary	76
Chapter 5 Payload Experiments: Astrobiology Studies	78
5.1 Introduction	78
5.2 Morphological Biosignatures: Microbial filaments	79
5.2.1 Freshwater limestone, Hainsfarth, Ries Crater, Germany (140).....	79
5.2.1.1 Physical Properties	79
5.2.1.2 Chemistry and Mineralogy	83
5.2.1.3 Geobiological Evaluation	88
5.2.2 Opaline Sinter, Yellowstone Park, Wyoming, USA (169)	88
5.2.2.1 Physical Properties	88
5.2.2.2 Chemistry and Mineralogy	92
5.2.2.3 Geobiological Evaluation	95

5.2.3 Chalcedony, Cady Mountains, California, USA (45)	95
5.2.3.1 Physical Properties	95
5.2.3.2 Chemistry and Mineralogy	98
5.2.3.3 Geobiological Evaluation	101
5.2.4 Goethite, Cerro de Pasco, Peru (179).....	102
5.2.4.1 Physical Properties	102
5.2.4.2 Chemistry and Mineralogy	104
5.2.4.3 Geobiological Evaluation	107
5.3 Morphological Biosignatures: Endoliths	107
5.3.1 Orthoquartzite, McMurdo, Victoria Land, Antarctica (114).....	108
5.3.1.1 Physical Properties	108
5.3.1.2 Chemistry and Mineralogy	112
5.3.1.3 Geobiological Evaluation	117
5.3.2 Marble, McMurdo, Victoria Land, Antarctica (194)	117
5.3.2.1 Physical Properties	117
5.3.2.2 Chemistry and Mineralogy	121
5.3.2.3 Geobiological Evaluation	125
5.3.3 Gypsum, Houghton Crater, Devon Island, Canada (44)	125
5.3.3.1 Physical Properties	125
5.3.3.2 Chemistry and Mineralogy	128
5.3.3.3 Geobiological Evaluation	132
5.4 Ancient Sedimentary Structures	132
5.4.1 Banded Chert, Kitty’s Gap, Pilbara, Australia (190)	132
5.4.1.1 Physical Properties	133
5.4.1.2 Chemistry and Mineralogy	135
5.4.1.3 Geobiological Evaluation	138
5.4.2 Stromatolitic Chert, North Pole Dome, Pilbara, Australia (159)	139
5.4.2.1 Physical Properties	139
5.4.2.2 Chemistry and Mineralogy	139
5.4.2.3 Geobiological Evaluation	143
5.4.3 Banded Iron Formation (BIF), Barberton, South Africa (163)	145
5.4.3.1 Physical Properties	145
5.4.3.2 Chemistry and Mineralogy	146
5.4.3.3 Geobiological Evaluation	149
5.5 Summary	150
Chapter 6 Field Applications and Scientific Autonomy	151

6.1 Introduction	151
6.2 A Methodology for Autonomous Science.....	154
6.2.1 Fundamental Attributes.....	155
6.2.1.1 Structure	156
6.2.1.2 Texture.....	157
6.2.1.3 Composition	160
6.2.2 Target Scoring.....	162
6.2.3 Contextual Model.....	164
6.2.4 Fuzzy Logic.....	165
6.2.5 Example Scenarios	166
6.3 Feature Detection	168
6.3.1 Image Processing	168
6.3.1.1 Segmentation	168
6.3.1.2 Morphological Smoothing.....	170
6.3.1.3 Edge Detection	170
6.4 The Autonomous Robot Scientist (ARS)	172
6.4.1 The Planetary Analogue Terrain (PAT) Laboratory	175
6.4.2 Science Targets	176
6.4.3 Rover Trials.....	178
6.5 Summary	180
Chapter 7 Conclusions and Further Work.....	181
7.1 Introduction	181
7.2 The Planetary Analogue Archive	182
7.2.1 Future Work	182
7.3 Astrobiology Studies.....	183
7.3.1 Future Work	188
7.4 Scientific Autonomy	190
7.4.1 Future Work	190
7.5 The Analogue Study Programme	191
7.6 Applications in Forensic Science	192
7.7 Summary	192
Appendix A Geological Specimen Archive (GSPARC) Specification	194
A.1 Basic Sample Identification.....	194
A.2 Sample Formats.....	196

A.3 Sample Identifier Extensions.....	200
A.4 Sample Documentation	203
Appendix B Sample Descriptions	207
B.1 Freshwater limestone, Hainsfarth, Ries Crater, Germany (140).....	207
B.2 Opaline Sinter, Yellowstone Park, Wyoming, USA (169).....	210
B.3 Chalcedony, Cady Mountains, California, USA (45).....	212
B.4 Goethite, Cerro de Pasco, Peru (179)	214
B.5 Orthoquartzite, McMurdo, Victoria Land, Antarctica (114)	216
B.6 Marble, McMurdo, Victoria Land, Antarctica (194).....	220
B.7 Gypsum (var. selenite), Haughton Crater, Devon Island, Canada (44).....	221
B.8 Banded Chert, Kitty’s Gap, Pilbara, Australia (190).....	223
B.9 Stromatolitic Chert, North Pole Dome, Pilbara, Australia (159).....	227
B.10 Banded Iron Formation (BIF), Barberton, South Africa (163).....	228
Appendix C Experimental Setup and Instrumentation.....	231
C.1 Introduction	231
C.2 Imaging.....	233
C.2.1 Proximal and macroscopic imaging	233
C.2.2 Microscopic imaging.....	239
C.3 Analytical	240
C.3.1 X-Ray Fluorescence (XRF).....	240
C.3.2 Raman Spectroscopy	244
C.3.3 Mössbauer spectroscopy.....	246
C.3.4 X-Ray Diffraction (XRD)	248
C.4 Geotechnics	251
Glossary of Terms and Acronyms	253
Bibliography	264

Table of Figures

Figure 2.1 The Viking mission to Mars	7
Figure 2.2 The Beagle 2 lander	9
Figure 2.3 The Beagle 2 Flight Model PAW	10
Figure 2.4 Artist's impression of the ExoMars rover.....	12
Figure 2.5 Evidence for ancient aqueous and hydrothermal deposits on Mars.....	15
Figure 2.6 Cape St. Vincent, Victoria Crater, Mars, observed by the Opportunity rover.....	21
Figure 2.7 Near-field and close-up imaging of Serpent Trench, Gusev Crater, Mars.....	25
Figure 2.8 <i>In situ</i> X-ray spectrometers for MER and Beagle 2.....	29
Figure 2.9 <i>In situ</i> geotechnics with the MER RAT.....	35
Figure 3.1 Apollo 17 landing site in Taurus Littrow valley, Serenitatis Basin	44
Figure 3.2 Analogue field measurements.....	46
Figure 3.3 Access development environment for the GSPARC database.....	52
Figure 3.4 Relationships between key parameters in the GSPARC database	53
Figure 3.5 Example design forms for <i>DATfamily</i> and <i>DATitem</i>	54
Figure 3.6 The standalone version of GSPARC.....	55
Figure 3.7 Working prototype of the on-line GSPARC search page	57
Figure 3.8 Flow diagram of the GSPARC concept.....	58
Figure 5.1 Proximal and macroscopic imaging of samples 140HS332 and 140HS420.....	81
Figure 5.2 Microscopic imaging of sample 140HS332.....	82
Figure 5.3 <i>In situ</i> Raman analysis of sample 140HS420	85
Figure 5.4 <i>In situ</i> Mössbauer analysis of sample 140HS333	86
Figure 5.5 <i>In situ</i> XRD analysis of selected targets on specimen 140HS332X	87
Figure 5.6 Proximal imaging of sample 169HS330.....	90
Figure 5.7 Macroscopic and microscopic imaging of sample 169HS330.....	91
Figure 5.8 <i>In situ</i> Mössbauer analysis of sample 169HS330	94
Figure 5.9 Bulk XRD analysis of homogenised powder derived from sample 169HS331.....	94
Figure 5.10 Proximal and macroscopic imaging of sample 45HS265	97
Figure 5.11 Microscopic imaging of sample 45HS265.....	97
Figure 5.12 <i>In situ</i> Mössbauer analysis of sample 45HS325	100
Figure 5.13 Bulk XRD analysis of homogenised powder derived from sample 45HS325.....	101
Figure 5.14 Proximal and microscopic imaging of sample 179HS367.....	103

Figure 5.15 Stereo macroscopic imaging of sample 179HS367	104
Figure 5.16 <i>In situ</i> Mössbauer analysis of sample 179HS588	105
Figure 5.17 Bulk XRD analysis of homogenised powder derived from sample 179HS367.....	107
Figure 5.18 Proximal and macroscopic imaging of samples 114HS353 and 114HS587.....	110
Figure 5.19 Macroscopic imaging of sample 114HS587	111
Figure 5.20 Microscopic imaging of sample 114HS353.....	112
Figure 5.21 <i>In situ</i> Raman analysis of samples 114HS353, 114HS354 and 114HS380	115
Figure 5.22 <i>In situ</i> Mössbauer analysis of sample 114HS353	116
Figure 5.23 Bulk XRD analysis of homogenised powder derived from 114	116
Figure 5.24 Proximal, macroscopic and microscopic imaging of sample 194HS435.....	119
Figure 5.25 Macroscopic imaging of sample 194HS435	120
Figure 5.26 Macroscopic and microscopic imaging of sample 194HS435.....	120
Figure 5.27 <i>In situ</i> Raman analysis (785 nm laser) of sample 194HS435	123
Figure 5.28 <i>In situ</i> Raman analysis (514 nm laser) of sample 194HS435	124
Figure 5.29 Bulk XRD analysis of homogenised powder derived from sample 194HS435.....	124
Figure 5.30 Proximal, macroscopic and microscopic imaging of sample 44HS419.....	127
Figure 5.31 <i>In situ</i> Raman analysis of a sample similar to 44HS340.....	130
Figure 5.32 <i>In situ</i> Raman profile of a sample similar to 44HS340.....	131
Figure 5.33 Bulk XRD analysis of homogenised powder derived from sample 44HS340.....	131
Figure 5.34 Proximal and macroscopic colour imaging of sample 190HS390	134
Figure 5.35 Microscopic imaging of sample 190HS390.....	135
Figure 5.36 <i>In situ</i> XRD analysis of samples 190HS390 and 159HS304	138
Figure 5.37 Proximal and macroscopic imaging of sample 159HS304	141
Figure 5.38 Proximal and macroscopic imaging of sample 163HS586	146
Figure 5.39 <i>In situ</i> Mössbauer analysis of sample 163HS586	147
Figure 5.40 Bulk XRD analysis of sample 163HS303.....	149
Figure 6.1 Proposed scenario for the evaluation of opportunistic science	167
Figure 6.2 An example of image segmentation.....	169
Figure 6.3 Edge detection techniques applied to robotic field geology	171
Figure 6.4 Selection of test images from the image library	174
Figure 6.5 Evaluation of the Science Assessment and Response Agent (SARA).....	175
Figure 6.6 Half-scale rover equipped with camera systems.....	176
Figure 6.7 Three-dimensional science targets.....	177
Figure 6.8 Demonstration of opportunistic science with the Autonomous Robot Scientist.....	179

Figure A.1 Microbial algal stromatolite structures (209FE569)	198
Figure A.2 Hand specimen of sandstone (75HS136)	198
Figure A.3 Rock slab of garnetiferous anorthosite (42RS71-1SA50).....	199
Figure A.4 Martian soil simulant JSC Mars-1	199
Figure B.1 Simplified context map of the Ries and Steinheim impact sites	207
Figure B.2 Freshwater limestone in outcrop (140FE570).....	209
Figure B.3 Study specimens 140HS332 (A) and 140HS333 (B).....	209
Figure B.4 Geology of Hillside Springs, Yellowstone National Park.....	211
Figure B.5 Study specimens 169HS330 (A) and 169HS331 (B).....	211
Figure B.6 Satellite image of the Sleeping Beauty Ridge region.....	213
Figure B.7 Well preserved vein of chalcedony	213
Figure B.8 Geological map of the Cerro de Pasco district.....	215
Figure B.9 Outer surface of study specimen 179HS367	215
Figure B.10 Landsat 7 image of the McMurdo Dry Valleys.....	217
Figure B.11 Exfoliating orthoquartzite at Battleship Promontory	218
Figure B.12 Study specimen of marble (194HS435)	221
Figure B.13 Geological sketch map of the Haughton impact crater	222
Figure B.14 Study specimen 44HS340 (A) of microbe-bearing gypsum	222
Figure B.15 Geological sketch map of the Pilbara craton.....	225
Figure B.16 Geological sketch map of the Kitty’s Gap locality	226
Figure B.17 Stratigraphic sequence visible in the topography at Kitty’s Gap	226
Figure B.18 Geological map of a section of the North Pole Dome region	228
Figure B.19 Study specimen 159HS304 of Strelley Pool Chert	228
Figure B.20 Geological map of the Barberton Greenstone Belt	230
Figure B.21 Specimen of BIF (163HS303).....	230
Figure C.1 Experimental set up for proximal, macroscopic, and microscopic imaging	234
Figure C.2 Demonstration of macroscopic and microscopic fluorescence imaging.....	236
Figure C.3 Spectral characteristics of the light sources	237
Figure C.4 Cropping procedure for all Beagle 2 stereo camera (B2SCSS) images	238
Figure C.5 TN Technologies Spectrace 9000 portable X-Ray spectrometer	242
Figure C.6 Beagle 2 Qualification Model (QM) Mössbauer sensor head.....	247
Figure C.7 Laboratory X-Ray Diffractometer (NHMXRD\$)	249
Figure C.8 <i>In situ</i> coring and rock splitting of sample 146HS274.....	252

Chapter 1

Introduction

Of particular relevance to the exploration of the surface of Mars is the detection of life in whatever form it might take. Astrobiology payloads for future missions will include miniaturised analytical laboratories to specifically look for chemical signatures of life within rocks and soils but such measurements will be performed following sample acquisition. What to sample and where to sample relies on the collective interpretation of a variety of *in situ* data in the form of imaging, *in situ* analytical measurements (i.e., spectroscopy), and geotechnics (i.e., physical interaction with the surface). In addition to providing the essential context for post-sampling analysis, *in situ* data also have the ability to identify geological features exhibiting morphological, chemical and mineralogical signatures associated with biological activity. Given an appropriate suite of *in situ* techniques, surface elements (i.e., rovers) would be well equipped for planetary geological fieldwork.

Compared with terrestrial field campaigns, missions to the surface of Mars are rare (one per decade) and are currently limited to exploring small areas over a relatively long time. For example the NASA Mars Exploration Rovers have travelled a total of only 21 km in 5 Earth years. In contrast Apollo 17 astronauts traversed a total of 35 km (within an area of 80 km²) in three EVAs totalling about 22 hours. By empowering planetary robots with on-board scientific decision making capability (scientific autonomy), the prospect of increased science return and ground coverage could be realised. It is therefore essential to invest in these missions by conducting a dedicated programme of analogue studies, both laboratory and field based, where scientific autonomy can be incorporated into the programme and proven at an early stage.

This thesis focuses on three themes related to analogue studies, namely planetary analogue materials, analogue experiments and the application of scientific autonomy. The common theme of the work relates to robotic planetary field geology and the search for life (astrobiology). An outline of the thesis is given below.

Chapter 2 presents a summary of Mars surface exploration and the search for life. Three examples of astrobiology missions are described to illustrate what has been undertaken so far and what strategies are planned for the future. The second part of the Chapter discusses where one

might look for signs of past and present life on Mars. This is followed with a review of *in situ* techniques of relevance to astrobiology and robotic field geology that have either already been proven or are proposed for future missions.

Chapter 3 discusses the role of planetary analogues and describes a comprehensive specimen archive and associated database called GSPARC (Geological Specimen Archive), established for use in research, education and public outreach. Study specimens are referred to throughout the thesis by the GSPARC coding system specified in Appendix A. Also introduced in this Chapter is the Planetary Analogue Field Studies Network (PAFS-net).

Chapter 4 introduces the study samples used in the experimental part of this thesis. The specimens were selected from GSPARC on the basis of astrobiological significance and appropriate scale of features observable in the context of robotic or human *in situ* field exploration at Mars. A full geological description of these samples is given in Appendix B.

Chapter 5 presents the results of field-like experiments performed on the aforementioned study samples using the *in situ* techniques described in Appendix C. Two astrobiology-related studies were undertaken based on the ability of these collective techniques to unambiguously identify morphological biosignatures such as fossils and biologically mediated structures, and to assess the biogenic potential of visible sedimentary structures in ancient rocks.

Chapter 6 describes some fundamental aspects of terrestrial geological field practice and discusses how they could be implemented into a robotic mission to a planetary surface. A novel approach to autonomous science operations is defined and the requirements for field evaluation specified. The Chapter also presents some results from rover trials using an early implementation of the concept.

Chapter 7 summarises the conclusions drawn from the topics covered in this thesis. The need for further work within each topic is argued and recommendations are made to ensure the continuation of an integrated programme of analogue studies. Spin-off potential to other areas of science is also highlighted.

Chapter 2

The Search for Life on Mars

This Chapter presents a brief synopsis of Mars exploration with an emphasis on surface missions and the search for life. Three examples of astrobiology missions are described to illustrate what has been undertaken so far and what strategies are planned for the future. The second part of the Chapter discusses where one might look for signatures of past and present life on Mars. This is followed with a review of *in situ* techniques of relevance to astrobiology and robotic field geology that have either already been proven or are proposed for future missions.

2.1 Mars Exploration and the Search for Life

Following many years of speculative telescopic observations, Mars exploration using space probes commenced in the early 1960s. Although the majority of missions since that time have not been successful (Table 2.1), a few notable exceptions have contributed to the wealth of data we now have on the planet (for a summary of Martian geology see Barlow, 2008, and references therein).

At the time of writing, only six surface elements (four missions) have conducted field-like investigations at the surface of Mars: the Viking Landers (1976 to 1982), Mars Pathfinder (1997), the Mars Exploration Rovers (2004 to present) and Phoenix (May to November 2008). The emphasis of future programmes is being placed on geological exploration and the search for traces of habitable environments (past and present), as well as traces of life (past and present) that will culminate in sample return and perhaps human missions. Whatever the exploration scenario, *in situ* investigations will play a crucial role throughout the entire Mars programme.

2.1.1 Astrobiology Missions

From the inventory of missions to the surface of Mars shown in Table 2.1, Viking (in Godwin, 2000), Beagle 2 (Pullan *et al.*, 2004), and ExoMars (Vago *et al.*, 2003) can be considered to be true astrobiology missions since the primary scientific objective is the search for extant and extinct life. Mars Pathfinder (MPF) was essentially a technology demonstrator (Golombek, 1997)

and a precursor to the Mars Exploration Rovers (MER) Spirit and Opportunity, which are designed to look for signs of past aqueous activity (Squyres *et al.*, 2003). Phoenix (Shotwell, 2005) and Mars Science Laboratory (MSL) (Crisp *et al.*, 2008) are concerned with assessing the potential habitability for past and present life at the surface or near-surface. Mars Sample Return (MSR) (MEPAG ND-SAG, 2008) and the Astrobiology Field Laboratory (AFL) (Steele *et al.*, 2006) may be modelled on the MSL design but details (including payload) are currently speculative. Other astrobiology missions currently at an early proposal stage include the Mars Origins Mission (MOM) (Westall and Klingelhöfer, 2007; Klingelhofer *et al.*, 2008). MOM would be designed specifically to search Noachian terrains for traces of the transition from a pre-biotic world to the very early evolution of life (if it ever existed). All these missions will be heavily influenced by astrobiology in terms of payload, landing site and sampling strategies.

Table 2.1 Chronology of Mars exploration from 1960 to 1973 ¹

Mission	Country	Year	F	O	L	R	Outcome
Marsnik 1	USSR	1960	●				Failed to reach Earth orbit
Marsnik 2	USSR	1960	●				Failed to reach Earth orbit
Sputnik 22	USSR	1962	●				Achieved Earth orbit only
Mars 1	USSR	1962	●				Lost at 160 million km
Sputnik 24	USSR	1962	●				Achieved Earth orbit only
Mariner 3	USA	1964	●				Shroud failed
Mariner 4	USA	1964	●				Flyby 1965; 21 images
Zond 2	USSR	1964	●				Failed to return planetary data
Mariner 6	USA	1969	●				Flyby 1969; 75 images
Mariner 7	USA	1969	●				Flyby 1969; 126 images
Mariner 8	USA	1971	●				Failed during launch
Kosmos 419	USSR	1971			●		Achieved Earth orbit only
Mars 2	USSR	1971		●	●		Arrived 1971; no useful data
Mars 3	USSR	1971		●	●		Arrived 1971; first image from Mars surface, no useful data
Mariner 9	USA	1971		●			Orbited 1971-1972; 7329 images
Mars 4	USSR	1973		●			Flew past Mars 1974
Mars 5	USSR	1973		●			Arrived 1974; some data
Mars 6	USSR	1973		●	●		Arrived 1974; some data
Mars 7	USSR	1973		●	●		Arrived 1974; some data

¹ Successful missions are highlighted. Mission type key: F = Flyby, O = Orbiter, L = Lander, R = Rover.

Table 2.1 (cont.) Chronology of Mars exploration from 1975 to 2008¹

Mission	Country	Year	F	O	L	R	Outcome
Viking 1	USA	1975	●	●			VO1(1976-1980); VL1(1976-1982) in Chryse Planitia
Viking 2	USA	1975	●	●			VO2(1976-1987); VL2(1976-1980) in Utopia Planitia
Phobos 1	USSR	1988	●	●			Lost 1988 en-route
Phobos 2	USSR	1988	●	●			Lost 1989 near Phobos
Mars Observer	USA	1992	●				Lost just before arrival 1993
Mars Global Surveyor	USA	1996	●				Arrived 1997; lost contact during third extension to mission in November 2006. Major contributions include global mapping of surface, high resolution topography and thermal emission maps.
Mars 96	Russia	1996	●	●			Failed during launch
Mars Pathfinder	USA	1996			●	●	Landed July 4 th 1997 in Ares Vallis (19.28°N,33.22°W); Sojourner operated for 11 weeks
Nozomi (Planet-B)	Japan	1998	●				Performed two lunar swing-bys in 1998 and two Earth swing-bys in 2002 and 2003 before an electrical failure terminated the mission in December 2003.
Mars Climate Orbiter	USA	1998	●				Failed during orbit insertion due to navigational error
Mars Polar Lander Deep Space 2	USA	1999	●	●			Failed during landing; no signals returned from lander or penetrators
Mars Odyssey	USA	2001	●				Arrived October 2001; global mapping and relay for surface elements; hydrogen detected close to surface; mission extended to September 2008.
Mars Express	Europe	2003	●				Arrived December 2003; high resolution stereo imaging, thematic mapping (OMEGA) and radar; currently active in second extended mission phase.
Beagle 2	Europe	2003			●		Probe failed during entry, descent or landing
MER Spirit	USA	2003				●	Landed January 4 th 2004 in Gusev Crater (14.57° S, 175.49° E); currently active
MER Opportunity	USA	2003				●	Landed January 25 th 2004 in Meridiani Planum (1.94°S, 354.47°E); currently active
Mars Reconnaissance Orbiter	USA	2005	●				Arrived March 2006; high resolution images (HiRise) and climate analysis; currently active
Phoenix	USA	2007			●		Landed May 25 th 2008 in Vastitas Borealis; evidence of sub-surface ice; end of mission November 2 nd 2008.

¹ Successful missions are highlighted. Mission type key: F = Flyby, O = Orbiter, L = Lander, R = Rover.

The astrobiological aspects of Viking, Beagle 2 and ExoMars are discussed in the following sections. Some of the techniques used by these and other missions are also discussed in Section 2.3 from the perspective of a) scientific capability in terms of robotic field geology, and b) relevance to *in situ* astrobiology.

2.1.1.1 Viking

The Viking mission consisted of two landers and two orbiters (Godwin, 2000). The original mission was designed to last for 90 days but following the continued performance of both landers and orbiters, the mission ran for 6.4 years (3.4 Martian years). In this time a wealth of data was accumulated (Kieffer *et al.*, 1992) which formed the basis of Mars studies for the next 20 years.

The Viking Landers (VL1 and VL2) (Figure 2.1) were equipped with instruments designed to image the site and study the biology, chemical composition (organic and inorganic), and physical properties of the Martian surface (Viking Science Team, 1977). VL1 touched down on the 20th July 1976 in a Hesperian flood plain in western Chryse Planitia (22.697° N, 48.222° W). VL2 landed on the 3rd September 1976 in a Hesperian region¹, approximately 200 km west of crater Mie, in Utopia Planitia (48.269° N, 225.990° W). The landings provided early clues as to the nature of the surface material. Three hydrazine rockets were used for assisted terminal descent and although the engines had nozzles to disperse the exhaust and minimise the effects on the surface, in some places the uppermost layer of dust was blasted away. Images of these areas revealed an underlying polygonal texture reminiscent of terrestrial “duricrust” (Kieffer *et al.*, 1992).

VL1 and VL2 were each equipped with four biological experiments (Klein, 1978), three of which were designed to amplify and detect metabolic activity in samples of Martian soil collected from the surface. Only one of the biology experiments produced a positive result: the Labelled Release (LR) experiment.

¹ Hesperian Knobby member (Hvk) of the Vastitas Borealis Formation (Greeley and Guest, 1987)

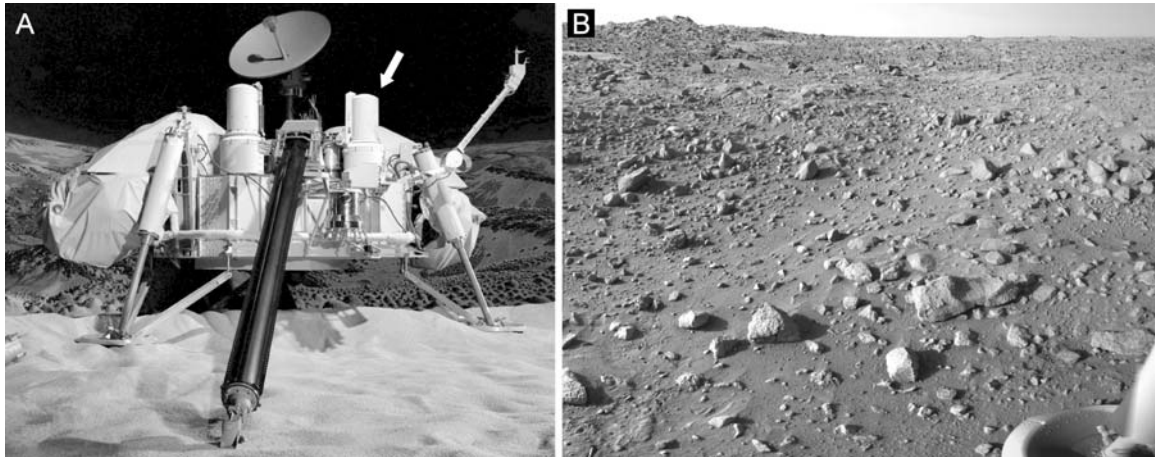


Figure 2.1 The Viking mission to Mars. Each lander (A) (ID PIA09703) was equipped with two facsimile cameras (one of which is arrowed) for panoramic imaging of the landing sites. VL1 landed in Chryse Planitia (B) (ID PIA03164) and VL2 in Utopia Planitia. Although VL1 and VL2 were 6500 km apart both terrains were geologically similar. Courtesy NASA/JPL.

The LR experiment was based on the assumption that any indigenous organisms present within samples collected from the surface, and in contact with a CO₂ atmosphere, were capable of metabolising simple carbon compounds. The process involved a dilute aqueous solution of radioactively labelled carbon (¹⁴C) compounds that were injected onto small quantities (0.5 cm³) of soil that had been previously collected from the surface and incubated (at 8 °C to 17 °C) for several days. Throughout the experiment, a solid-state beta detector was used to monitor for evidence of the biological release of radioactive gases from the ¹⁴C-labelled compounds. Gas was indeed steadily released immediately after the first aqueous solution was injected, indicating active biology, but not following subsequent injections.

All the other biological experiments produced negative results (*op. cit.*). The Gas Chromatograph Mass Spectrometer (GCMS) measurements indicated no significant amount of organic carbon in the Martian soil. The concentrations that were observed were attributable to contamination of the spacecraft acquired during assembly on Earth. The Gas Exchange (GEX) experiment did not detect the presence of metabolising organisms (via released gases such as methane) when Martian soil was incubated, injected with nutrients and water, and subjected to first helium and then to the Martian atmosphere. Oxygen was however detected (see below). The Pyrolytic Release (PR) experiment did not detect any products of photosynthetic fixation of CO₂ commonly attributable to cyanobacteria on Earth. For this a ¹⁴C labelled CO₂/CO gas mix was used. No radioactivity was detected from soil samples following incubation and subsequent pyrolysis (i.e., subjecting

samples to high temperatures to break down any organic compounds).

Laboratory studies performed on Earth to replicate the Viking experiments showed that highly reactive oxidants (i.e., H₂O₂), or “superoxides” (i.e., O₂⁻), if present in the Martian soil would have reacted with any injected aqueous solutions thus accounting for the GEX results (Klein, 1978; Yen *et al.*, 2000). In light of the incomplete results from the LR experiment and the lack of supporting evidence for active biology from the GCMS, GEX and PR, the Viking results remain enigmatic (Mancinelli, 1998).

2.1.1.2 Beagle 2

Europe’s first planetary mission incorporated an orbiter (Mars Express) and a lander (Beagle 2). Mars Express was launched in June 2003 and arrived at Mars in December of the same year. The mission consists of a suite of experiments designed to investigate the surface, subsurface and atmosphere of Mars (Wilson, 2004). The Beagle 2 probe carrying the lander was released from Mars Express on the 19th December 2003 in preparation for coast, entry, descent, and eventual landing on the surface on the 25th December 2003. Unfortunately, the probe failed at some point during this phase (Sims, 2004).

The lander (Figure 2.2) was equipped with a highly-integrated scientific payload designed to conduct *in situ* geological and astrobiology-related experiments at a landing site located within Isidis Planitia (Bridges *et al.*, 2002). The site provided an opportunity to investigate a relatively recent (Amazonian) terrain comprised of sedimentary materials derived from older Noachian units to the south. Beagle 2 might have sampled materials not previously encountered by other missions.

The Beagle 2 payload (Pullan *et al.*, 2004) was divided into three elements: the Gas Analysis Package (GAP), an on-board chemical laboratory for isotopic analysis of soil, rock, and atmospheric samples, the PAW (Figure 2.3), an integrated package of *in situ* instruments and tools, and the Environmental Sensor Suite (ESS), an array of sensors for measuring UV flux, dust, air temperature, pressure, and wind speed/direction (see also Towner *et al.*, 2004). An Anthropomorphic Robotic Manipulator (ARM) was used to position the PAW for measurements and interaction with the surface. The PAW instruments relevant to this work are discussed in Section 2.3.

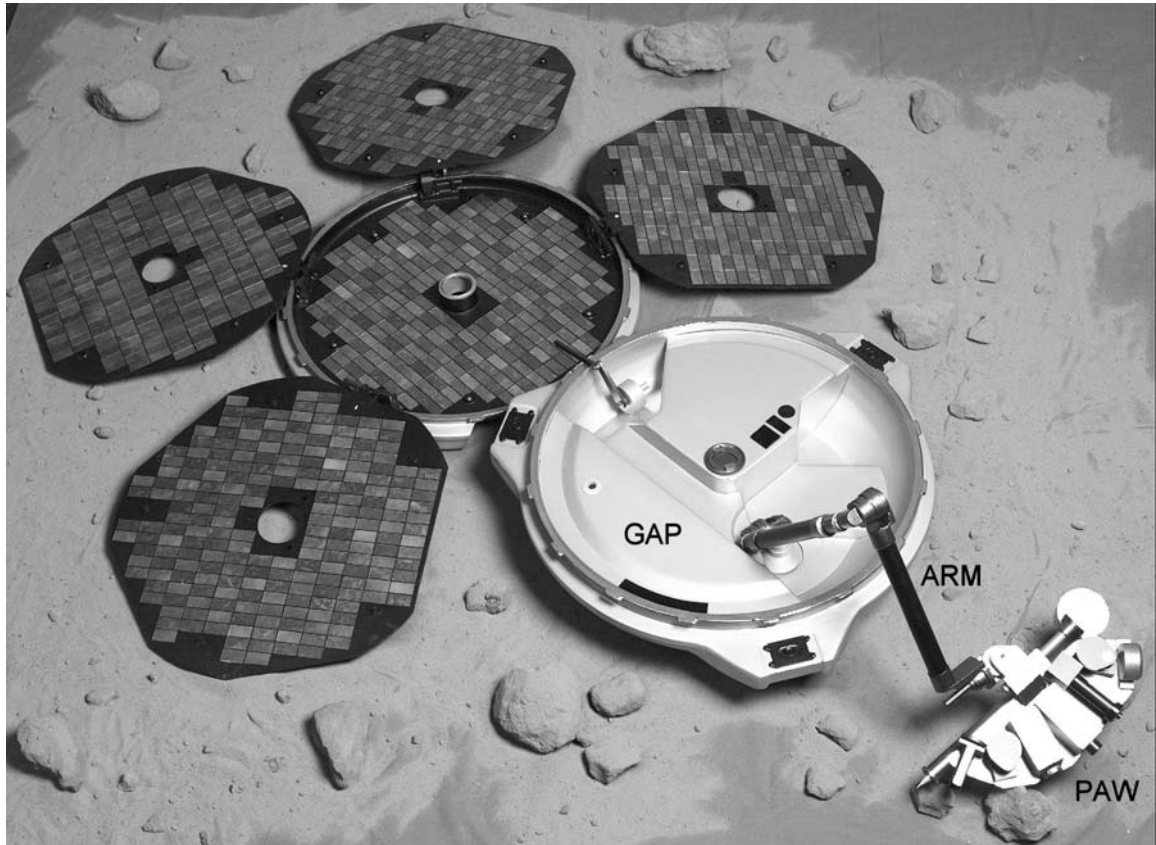


Figure 2.2 The Beagle 2 lander. Once deployed at the surface (as shown), the ARM would position the PAW (see Figure 2.3) to conduct panoramic, macroscopic and microscopic imaging, *in situ* compositional analysis, and sample acquisition for the Gas Analysis Package (GAP) experiment. Diameter of the lander base is 66 cm. Courtesy Beagle 2.

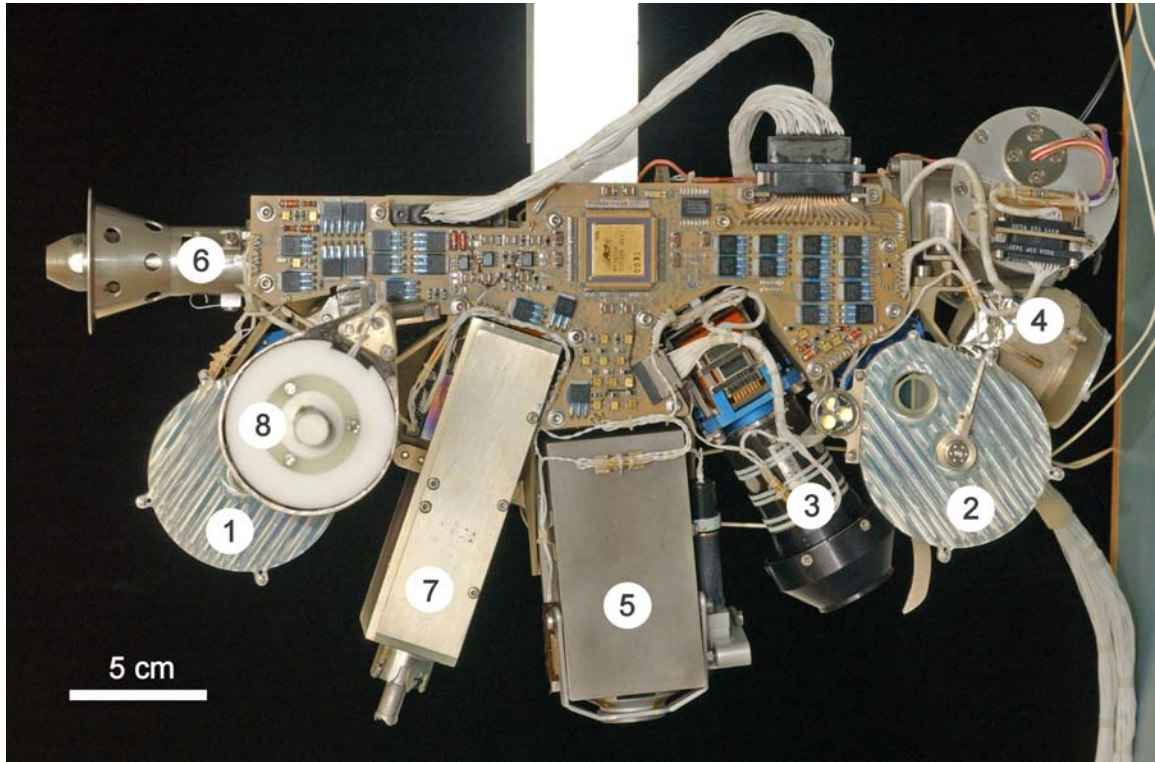


Figure 2.3 The Beagle 2 Flight Model PAW fully assembled and ready for sterilisation by hydrogen peroxide gas plasma (HPGP). The XRS detector head (see Figure 2.8B) was not fitted since it is self-sterilising due to the presence of the ^{55}Fe and ^{109}Cd sources. Similarly the sampling tip from PLUTO was removed for sterilisation with isopropanol alcohol (IPA). These components were fitted during the assembly of the lander. Key: 1 and 2 = Stereo Camera System (SCS), 3 = Microscope, 4 = X-Ray Spectrometer (XRS), 5 = Mössbauer spectrometer, 6 = Planetary Underground Tool (PLUTO), 7 = Rock Corer Grinder (RCG), 8 = Wide Angle Mirror (WAM).

The primary scientific objective of the Beagle 2 mission was to establish whether there was convincing evidence for past life on Mars, or to assess if the conditions were ever suitable. Of the six important indicators of biology recommended by an exobiology study commissioned by ESA in 1997 (Wilson, 1999), five would have been investigated by Beagle 2. These were the presence of water, associated inorganic minerals such as carbonate, carbonaceous debris, organic matter of complex structure, and evidence for isotopic fractionation (i.e., between organics and carbonate). The sixth indicator, chirality, was omitted from the Beagle 2 investigation on the grounds that the additional analytical processing steps needed for such measurements would have over-complicated the instrumentation.

The GAP was capable of performing quantitative isotopic measurements of H₂, N₂, O₂ and CO₂ extracted from samples of soil or rock acquired by the PAW (see Section 2.3.3.2). Analysis of the Martian atmosphere was also possible via a special inlet port. The experiment could also process and identify some noble gases (Ne, Ar and Xe) as well as anticipated trace constituents such as CH₄.

The search for organics used the process of stepped combustion, a technique that distinguishes carbon species by the temperature at which they burn or degrade in oxygen. Unlike pyrolysis (as used on Viking), combustion converts all carbon present into CO₂ so a complete isotopic composition can be determined by mass spectroscopy. Thus the GAP instrument was equipped with a 6 cm-radius magnetic sector mass spectrometer. A carousel of 12 ovens (for carrying out the stepped combustion process) allowed for a limited number of samples (probably 6) to be analysed during the mission. The target sample size was between 50 mg and 100 mg. With such quantities of material the detection limit for carbon was expected to be ~0.02 ppm. Choosing appropriate soil/rock samples for the GAP would have relied on the collective analysis of *in situ* data acquired with the PAW instruments.

The ability to measure methane at the surface of Mars was unique to Beagle 2 and important for exobiology. On Earth, a great variety of primitive organisms produce methane as a by-product of metabolism. The gas is chemically short-lived (< 300 years on Mars) since it is destroyed by photolytic oxidation. Methane in the Martian atmosphere (at levels of ~10 ppb) was detected by Mars Express in 2004 confirming previous Earth-based observations (Formisano *et al.*, 2004). Speculation continues as to whether this is due to recent volcanism (< 300 years) or extant biology. It is feasible to assume that if the Beagle 2 probe had not failed, the lander may have resolved this question since any extant methane-producing microbes on Mars, if they existed, would have been indirectly detectable by GAP.

2.1.1.3 ExoMars

ExoMars is a European Space Agency (ESA) mission to the surface of Mars due for launch in 2016 and arrival at Mars in 2017. The landing site has yet to be determined but engineering constraints restrict the location to be between 45° N and 15° S. The principal scientific objective of ExoMars is the search for extinct or extant life but, unlike Beagle 2, the mission will have high surface mobility provided by a rover (Figure 2.4) with a range of several kilometres. The

scientific payload, called Pasteur (Baglioni, 2003; ExoMars Project Team, 2007b), will be accommodated on the rover and perform a variety of functions ranging from *in situ* analysis to sub-surface sampling to biology-related experiments. The Pasteur instruments relevant to this work are discussed in Section 2.3.

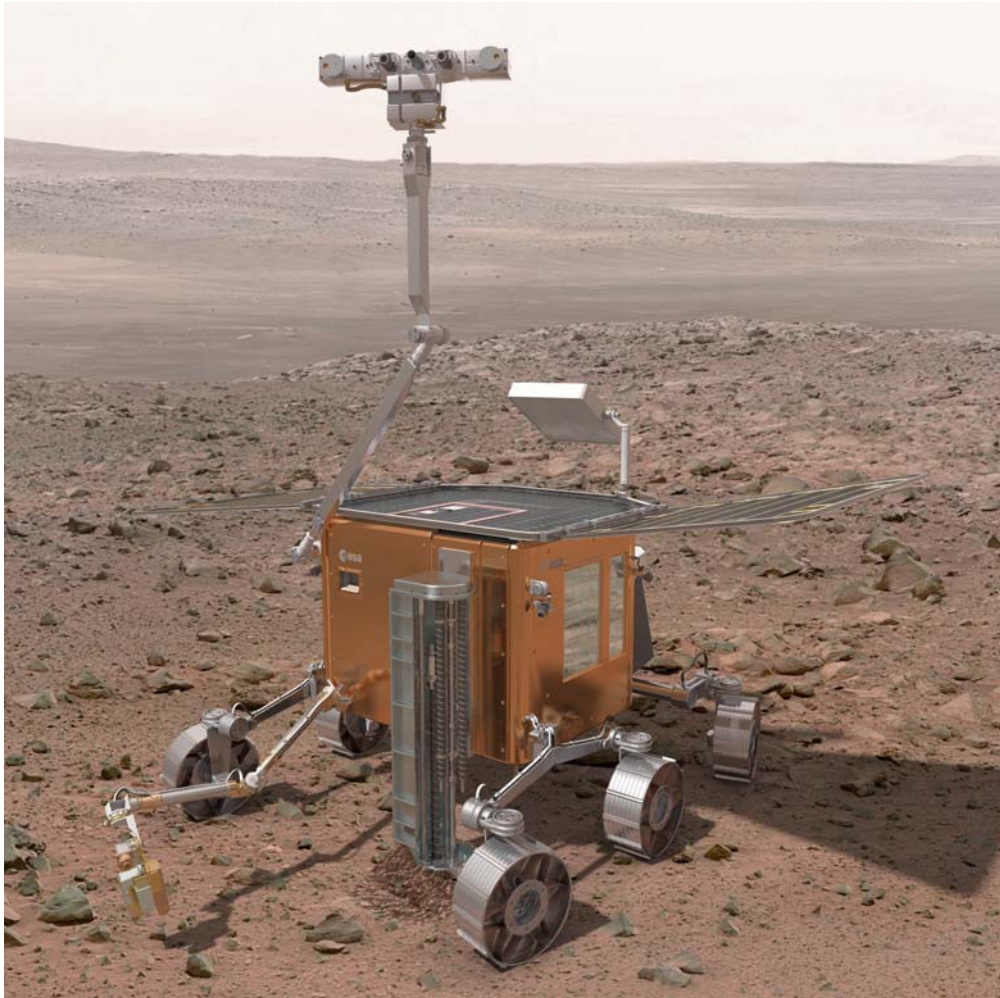


Figure 2.4 Artist's impression of the ExoMars rover. After deployment, the mast supporting the PanCam system (top) remains in the position shown, approximately 2 m above the Martian surface. PanCam itself can pan 360° and tilt $\pm 90^\circ$. Note the robotic arm with *in situ* instrument package (bottom left) and subsurface drilling system (lower centre). Courtesy ESA.

In addition to the astrobiology investigations, the rover will also characterise the aqueous/geochemical properties of the sub-surface and study the surface environment, to understand the hazards applicable to future human missions. The lander will include a geophysics and environmental package (Lognonné *et al.*, 2006) to study the UV and ionising radiation flux,

the composition of the atmosphere, meteorology, and the planetary interior (seismology).

Rover science operations will be based on the concept of the “experimental cycle” similar to that proposed for Beagle 2 (Pullan *et al.*, 2004). For ExoMars, a complete experimental cycle will consist of the following steps (see Glossary for explanation of acronyms):-

- Remote and proximal (near-field) survey: PanCam, MIMA, GPR (optional)
- Macroscopic (close-up) survey: CLUPI, Mössbauer spectrometer, Raman-LIBS
- Sample acquisition: Drill/corer (rock or soil)
- Microscopic survey: MicrOmega, Raman-LIBS
- Sample preparation: Rock grinder (prepare bulk powder for laboratory analysis)
- Laboratory analysis: XRD, Urey, MOMA, LMC

The nominal duration of the mission will be 180 sols (Martian days) in which ten experimental cycles (anticipated duration about 12 to 18 sols) and two vertical surveys (duration unknown) will be performed (ExoMars Project Team, 2007a). If the mission is extended then ten further experimental cycles are planned. The vertical surveys will comprise nominally five samples obtained at 50 cm increments to 2 m at the same location to observe the vertical distribution of soil chemistry, oxidants, water, and if present, organics.

2.2 Habitats for Life on Mars (Past and Present)

The present-day surface of Mars is extremely hostile to extant life. This is primarily due to a high UV radiation flux, low temperatures, and the absence of water.

Unlike present-day Earth which has a persistent, almost-global, protective ozone layer (O₃), the UV spectrum reaching the surface of Mars today is dominated by biologically damaging shorter wavelengths such as UVC (200 nm to 280 nm) and UVB (280 nm to 315 nm). Other wavelengths are either absorbed by CO₂ and a weak (seasonal) ozone column, or scattered by atmospheric dust. The UV environment of early Mars (4.5 Ga to 4.2 Ga) may have been much the same as today (Cockell, 2000) or slightly less extreme as a result of a thicker CO₂ atmosphere.

Early Mars was undoubtedly wetter than today and must have been warm enough to sustain

liquid water at the surface for a period of time (e.g., Kargel, 2004). In fact Mars and the early Earth (4 Ga to 3.3 Ga) may have shared similar environmental conditions, if not globally, then probably locally. Commonalities included extensive volcanism and impact cratering, the presence of large bodies of water with pH ranging from alkaline to slightly acidic, similar surface temperatures (at least locally), and comparable levels of atmospheric O₂. One major difference persists however: the current role of plate tectonics on Earth and the absence of it then and now on Mars.

Three types of environment potentially suited to life on Mars at some point in the planet's history (and possibly the present) are discussed below: aqueous, hydrothermal and endolithic (i.e., within rocks). These categories are relevant to the work presented in later chapters of this thesis. Given what is known about ancient and extant systems on Earth, it is likely that such environments were not mutually exclusive (Westall, 2005b).

2.2.1 Aqueous Environments

The abundance of water-related features currently observed from orbit such as valley networks and channels is testimony to a “warm and wet” past (Kargel, 2004). In reality the term “cold and wet” may be more appropriate to describe periglacial conditions where freeze/thaw mechanisms prevailed (Cabrol and Grin, 2005). Some studies question the term “wet” altogether by contesting the aqueous origin of some (Musselwhite *et al.*, 2001) or all (Hofmann, 2000) flow features observed on Mars, citing CO₂ as the primary fluid mechanism for their formation. These hypotheses, however, fail to explain a number of factors including how such a huge source of CO₂ could be accumulated and sustained, the observed global distribution of H₂O ice and hydrated minerals (Feldman *et al.*, 2002; Poulet *et al.*, 2005), and how minerals such as hematite, unambiguously identified at the surface of Mars (Klingelhöfer *et al.*, 2004), formed without the intervention of water.

Notwithstanding the on-going debate, free-standing bodies of water during the Noachian are still postulated by the majority of researchers. The most extensive of these include the concept of a single northern ocean or giant lake network (Carr and Head, 2003). Such large bodies of water would not only have provided a variety of potential habitats in which life could have developed and thrived in the northern hemisphere, but may have been responsible for vapour cloud formation, precipitation and subsequent hydrological cycles in the Southern Highlands. Indeed,

other (smaller) bodies of water may have resulted in the southern hemisphere via this mechanism thus producing other potential life habitats.

Examples of fluvio-lacustrine geomorphological features are particularly well portrayed near Holden Crater (Figure 2.5A). Evidence for diverse aqueous mineral deposits such as layered phyllosilicates, layered hematite/sulphates, hydrated silica deposits, gypsiferous ergs, and chloride salts have recently been reported by Murchie *et al.* (2008). Depending on the size of these aqueous environments, life habitats on early Mars may have ranged from benthonic to littoral to subaerial (Westall, 2005b).

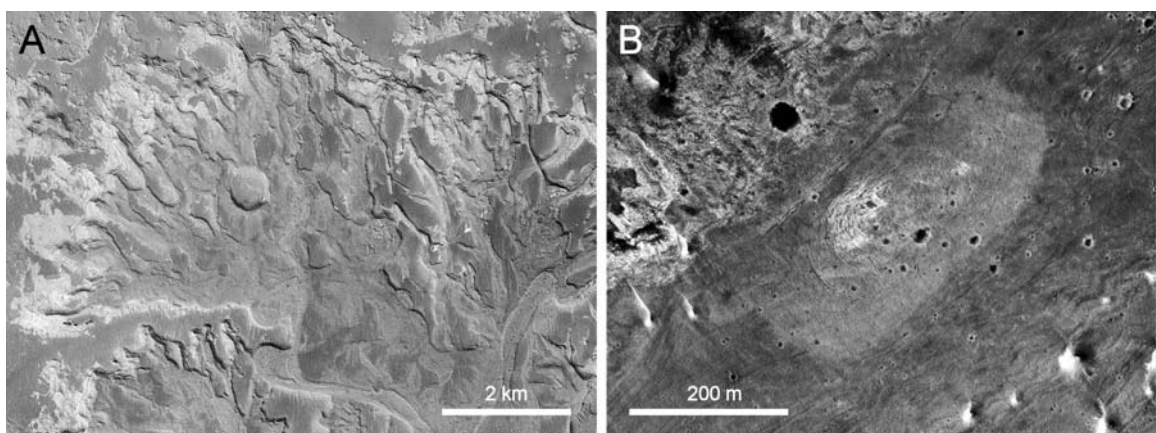


Figure 2.5 Evidence for ancient aqueous and hydrothermal deposits on Mars. Eroded distributary fan (A) ~60 km NE of Holden Crater (~24° S, ~327° E), Mars (ID PIA04869). Geological features associated with flowing water include river meanders and cut-off meanders. A hydrothermal spring-like mound (B) in Vernal Crater (~6° N, ~355° E), SW Arabia Terra, Mars (ID PSP_002812_1855). These light-toned, low-relief features closely resemble terrestrial spring mounds found at Dalhousie, Australia (Figure 4 in Allen and Oehler, 2008). Courtesy NASA/JPL/Malin Space Science Systems (A) and NASA/JPL/University of Arizona (B).

2.2.2 Hydrothermal Environments

Evidence for volcanic activity and liquid water at the surface of Mars during the early history of the planet would suggest that hydrothermal systems also existed. Exogenic processes (cosmic impacts) would also have added to the overall thermal budget. Although volcanism on early Mars was less extensive than on the early Earth, the geochemical energy available for life to develop was sufficient (Jakosky and Shock, 1998). Hydrothermal environments may have served as

protected habitats during the hostile conditions of early Mars history. Indeed, it is conceivable that chemosynthetic life may have adapted to the subsurface during the first 500 Ma, and provided with the right conditions i.e., water, heat and nutrient supply (from volcanic rocks), may continue to persist to the present day. This is entirely plausible since active volcanism is reported to have occurred within the last few Ma (Neukham *et al.*, 2004) confirming the continued presence of active heat sources. Magmatic interactions with the cryosphere at depth may result in hydrothermal activity that could possibly extend close to the surface (Clifford, 1987) thus providing an opportunity to access potential biological environments using robotic drilling systems.

On the early Earth, hydrothermal processes were influential in preserving organisms within the fossil record. Hydrothermal fluids are characteristically rich in dissolved minerals such as silica, calcium carbonate and iron oxide. Silicification in particular has been found to be a favourable mechanism for preserving Early Archaean (4 Ga to 3.2 Ga) biosignatures (Toporski *et al.*, 2002; Orberger *et al.*, 2006; Westall *et al.*, 2006b). Other research suggests it may also be effective in the preservation of iron microbes (Schieber *et al.*, 2008). Recent identification of amorphous silica at the surface of Mars (Squyres *et al.*, 2008) may be an indicator of hydrothermal/fumarolic activity (Yen *et al.*, 2008). Ancient silicified or mineral encrusted rocks exposed at the surface may therefore be desirable targets to look for signatures of life since recent material may be too friable or difficult to reach.

A preliminary list of potential hydrothermal sites on Mars has been compiled by Schulze-Makuch *et al.* (2007). These regional- to local-scale targets are based on a number of selection criteria including geomorphological evidence for liquid water, stratigraphic evidence for volcanic constructs/lava flows, impact cratering in ice-rich regions, hydrated mineral signatures, and similarities to terrestrial hydrothermal systems. More recently, light-toned, low-relief features seen in HiRise images of Arabia Terra have been interpreted as potential ancient hydrothermal spring deposits (Allen and Oehler, 2008, and Figure 2.5B).

2.2.3 Endolithic Environments

Rock-dwelling microbial communities are important eco-systems in high-latitude regions of the Earth today. Studies have shown that endolithic microbes inhabit a variety of rock types including sandstone (Friedmann, 1982), gypsum (Parnell *et al.*, 2004), basalt (Jorge Villar *et al.*,

2006), and shocked gneiss (Cockell *et al.*, 2002a).

Under evaporating conditions on early Mars (i.e., littoral environments) anaerobic photosynthesis may have played a part in addition to chemosynthesis (Westall, 2005b; Westall *et al.*, 2006a). The high UV flux at the surface of Mars may have encouraged photosynthetic organisms to colonise the interior of rocks (endolithic behaviour), and adopt additional radiation protection strategies such as the secretion of radiation-tolerant pigments (Wynn-Williams *et al.*, 2002). Under the right circumstances, endolithic organisms may be extant on Mars today albeit probably confined to niche environments (Cockell *et al.*, 2002b).

Endolithic colonies are relatively subtle bio-features so examples on Mars would be difficult to find. However, extant examples on Earth have been shown to be responsible for bioweathering resulting from chemical reactions between oxalic acid and the host rock (especially aluminosilicates and silicates) (Blackhurst *et al.*, 2005). Examples of bioweathering caused by microbial activity in colonised rocks include exfoliation (Büdel *et al.*, 2004) and iron staining (due to remobilisation of iron compounds). These potentially macroscopic features may indicate the presence of extant endolithic microbial communities, or extinct biosignatures in the form of fossilised pigments (Hiscox, 2001).

2.3 Field Techniques for *In Situ* Astrobiology

Robotic spacecraft deployed at a planet's surface and equipped with imaging, analytical and geotechnical (i.e., sampling) capabilities have demonstrated the effectiveness of remote *in situ* geological site investigation (Squyres and Knoll, 2005, and references therein). With increasing demand for extra mobility and autonomy (Gilmore *et al.*, 2000; Schenker *et al.*, 2003), a wide variety of spatial and spectral capabilities of imaging instruments will likely be required to span the entire scale range for future missions. In addition, fundamental analytical measurements remain crucial for establishing reliable ground truth and essential geological context (Clark *et al.*, 2005). Similarly, versatile and effective sample preparation and acquisition methods are important, especially for missions with life detection or sample return objectives, or both (Richter *et al.*, 2002; Gorevan *et al.*, 2003a). Suitably equipped payloads could, therefore, play a significant role in the access to, and identification of, direct or indirect visual indicators of life, if such features exist at the planetary surface or in the sub-surface.

Searching for visual signs of extinct or extant life at or below the surface of a planet such as Mars is particularly challenging given the constraints imposed by engineering, environment and operations. Nevertheless, strategies adopted by robots on Mars should follow the standard rules of geological field practice including the identification and assessment of fundamental attributes (structure, texture and composition) and establishing local (and regional) context. To achieve this, planetary rovers should/will always be equipped with essential "field" equipment such as multi-scale/multi-spectral cameras, geotechnical devices and *in situ* analysers (chemistry/mineralogy). The capability of such a payload will be crucial in identifying key indicators (or clues) of life, if they exist and are detectable by the instrumentation, and justifying sampling and detailed analysis using the on-board laboratory.

Essential geological fieldwork involves three types of activity, irrespective of whether it is performed by humans or robots: visual observation, analytical measurement, and physical interaction. In practice, these are achieved by employing appropriate imaging, analytical and geotechnical techniques. The following sections discuss each of these categories and describe a variety of *in situ* (i.e., pre-sampling) techniques that have either already been used on Mars or will be part of future mission payloads.

Table 2.2: Mars surface payloads: *In situ* imaging¹

Instrument	Mode	Type²	Characteristics
Lander cameras (<i>VL</i>)	Panoramic	Fixed	PSA (12 diodes); facsimile camera; six diodes with filters covering the range 400 to 1000 nm
Rover cameras (<i>MFP</i>)	Macro	Fixed	CCD (768 x 484); 2 x mono (stereo), 1 x colour (RGB pixel masked); extreme WA; fixed positions on rover
IMP (<i>MFP</i>)	Panoramic (stereo)	Fixed	CCD (256 x 248 per “eye”); mono; 14.4° x 14° FOV; stereo baseline 150 mm; focus 0.5 m to ∞ (optimised at 1.3 m); scale 0.98 mrad pix ⁻¹ ; filter wheels (see Table 2.3)
SCS (<i>Beagle 2</i>)	Panoramic (stereo) + Macro	Deploy	CCD (1064 x 1064); mono; 48° FOV; stereo baseline 209 mm; focus 0.6 m to 1.2m or 1.2m to ∞; scale 0.75 mrad pix ⁻¹ ; CUL mode 51 mm ∅ FOV (60 μm pix ⁻¹) at 80 mm; filter wheels (see Table 2.3)
Microscope (<i>Beagle 2</i>)	Microscopic	Deploy	CCD (1064 x 1064); mono; illumination LEDs (R,G,B,UV); 4 mm square FOV (4 μm pix ⁻¹) at 12 mm; focusing mechanism; fine z-stacking/depth map on-board; see Section C.2.2 for more details
PanCam (<i>MER</i>)	Panoramic (stereo)	Fixed	CCD (1024 x 1024); mono; 16° x 16° FOV; stereo baseline 300 mm; focus 1.5 m to ∞ (optimised at 3 m); scale 0.273 mrad pix ⁻¹ ; filter wheels (see Table 2.3)
MI (<i>MER</i>)	Macro	Deploy	CCD (1024 x 1024); mono; Kapton polyimide dust cover (orange); 31 mm square FOV (30 μm pix ⁻¹) at 66 mm; focusing with IDD; z-stacking/depth map on Earth
RAC (<i>Phoenix</i>)	Macro	Deploy	CCD (512 x 256); mono; 54° x 27° FOV at ∞ focus; illumination incandescent lamps (R,G,B); resolution 23 μm pix ⁻¹ at minimum focus 11 mm
PanCam (<i>ExoMars</i>)	Panoramic (stereo) + Zoom	Fixed	WAC: CCD (1024 x 1024); mono; 65° FOV; stereo baseline 500 mm; focus 1 m to ∞; filter wheels (see Table 2.3); HRC: CMOS (1024 x 1024); colour; 8.8° FOV; scale 50 μrad pix ⁻¹ ; 1.5 mm pix ⁻¹ at nominal 10 m
CLUPI (<i>ExoMars</i>)	Macro	Deploy	APS (2048 x 2048); RGB filter; illumination LEDs (TBD); 38 mm x 27 mm FOV (15 μm pix ⁻¹) at 100 mm
MastCam (<i>MSL</i>)	Panoramic (stereo) + Zoom	Fixed	CCD (1200 x 1200 single-frame, 1280 x 720 video); RGB filter; wide to zoom; stereo baseline ~200 mm; resolution 10 cm pix ⁻¹ (at 1 km); filter wheel (see Table 2.3)
MAHLI (<i>MSL</i>)	Macro + Microscopic	Deploy	CCD (1600 x 1200); RGB filter; illumination LEDs (W,UV); resolution 75 μm pix ⁻¹ (at 180 mm) to 12.5 μm pix ⁻¹ (at 30 mm); focusing mechanism; fine z-stacking/depth map on-board
RMI (<i>MSL</i>)	Remote	Fixed	CCD (1024 x 1024); telescope optics; resolution 80 μradians; min focus 2 m; see ChemCam (Table 2.4)

¹ See Glossary for explanation of acronyms.² Key: Fixed (i.e., mast or chassis mounted), Deploy (i.e., positioned with robotic arm).

2.3.1 Imaging

The first useful images from the surface were obtained in 1976 by Viking (see VL pages in the Mars section of <http://photojournal.jpl.nasa.gov/>). These were restricted to panoramic and near-field views seen from the perspective of the lander. Such imaging is essential for geological context (Figure 2.6) and has featured in all missions since Viking, both for static landers (MPF, Beagle 2, and Phoenix) and rovers (MER, ExoMars, and MSL) (Table 2.2). Missions also now incorporate close-up imaging (MPF, Beagle 2, MER, and Phoenix) as an essential geological field technique (i.e., equivalent to a geologist's hand lens), especially in support of *in situ* analysis (see Section 2.3.2). Field microscopy is more challenging than macroscopy. However, Beagle 2 was notable in that it was the first planetary mission to be equipped with a true *in situ* microscope.

2.3.1.1 Remote and Near-Field Imaging

Complete panoramic mosaics of both Viking landing sites (Section 2.1.1.1) were acquired using two facsimile cameras mounted 1 m apart on the deck of each lander (Figure 2.1A). Images were constructed from individual line scans acquired by mechanically rotating the camera aperture and incrementally tilting a mirror to direct light onto a Photosensor Array (PSA) of twelve diodes (Mutch *et al.*, 1972). Six diodes were fitted with band pass filters between 400 nm and 1100 nm for colour imaging and NIR spectroscopy. Colour images acquired with the Viking cameras suffered from calibration uncertainties, in particular the relative brightness of the red and blue channels. This resulted in initial composite images having an unrepresentative blue or red sky, and orange soil.

The Imager for Mars Pathfinder (IMP) (Smith *et al.*, 1997) consisted of a dual aperture, single CCD camera system (Table 2.2) mounted to a mast which, once deployed, was extended to a height equating to 1.5 m above the Martian surface. Each aperture was fitted with a filter wheel consisting mostly of filters optimised for geology (Table 2.3). Images acquired with IMP were used to assist in navigating the Sojourner rover to interesting geological targets for close-up investigation and *in situ* analysis. The Surface Stereo Imager (SSI) on Phoenix is an upgraded version of IMP with high resolution detectors (Table 2.2) and separate optical channels. The extendable mast positions the cameras 2 m above the Martian surface.

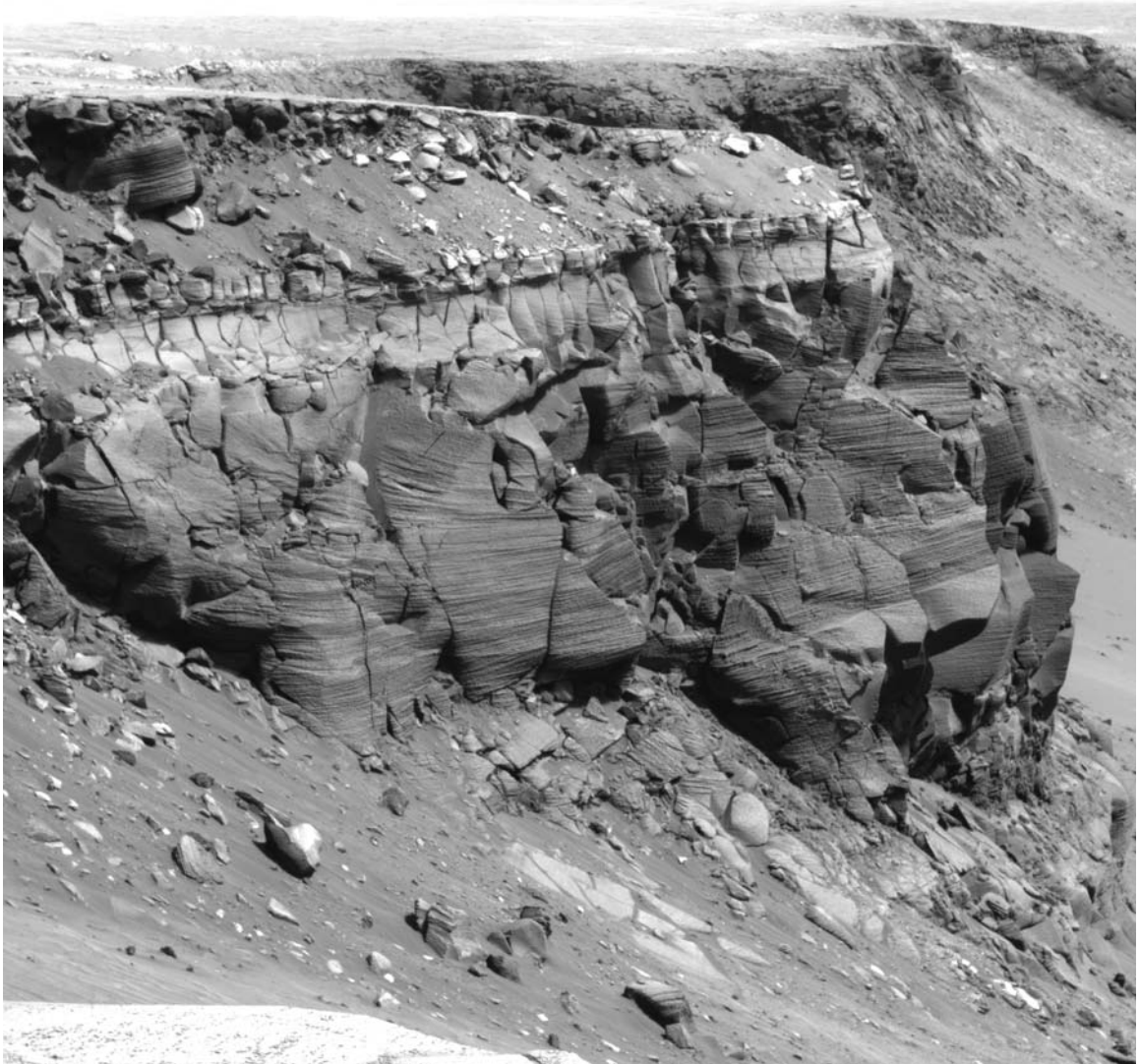


Figure 2.6 Cape St. Vincent, Victoria Crater, Mars, observed by the Opportunity rover on Sol 1167. The promontory is located on the northern rim of Victoria Crater and is approximately 12 m high. The view is to the east. Fine examples of metre scale cross bedding are visible in the lower units of the outcrop. The “super-resolution” image (ID PIA10210) is a composite of sixteen different Pancam images acquired using the 480 nm filter. Courtesy NASA/JPL.

Table 2.3 Mars surface payloads: *In situ* imaging (spectral characteristics)¹

λ_{ideal}	MFP ²	Beagle 2 ³	MER ⁴	Future Missions ⁵
	Pos: λ_{ideal} (bandpass)	Pos: λ_{ideal} (bandpass)	Pos: λ_{ideal} (bandpass)	(details TBD)
435			L7: 432 (32)	MSL
435			R1: 436 (37)	
440	L0: 443.3 (26.2)	L2: 438.8 (21.6)		ExoMars
440	R0: 443.3 (26.2)	R9: 440.3 (22.2)		
460				ExoMars
480	R10: 479.9 (27.0)	L1: 481.0 (28.0)	L6: 482 (30)	MSL, ExoMars
530	R9: 530.8 (29.6)	L3: 532.0 (32.0)		ExoMars
530		R10: 532.0 (32.0)		ExoMars
535			L5: 535 (20)	MSL
540				ExoMars
600	R8: 599.5 (21.0)	R2: 601.5 (21.0)	L4: 601 (17)	MSL, ExoMars
660				ExoMars
670	L5: 671.4 (19.7)	L7: 669.0 (17.2)		ExoMars
670	R5: 671.2 (19.5)	L8: 671.0 (17.2)		
670		R7: 668.0 (17.2)		
670		R8: 668.0 (17.2)		
675			L3: 673 (16)	MSL
720		R1: 720.0 (560.0)*		
750	R6: 752.0 (18.9)	L4: 750.0 (18.0)	L2: 753 (20)	MSL, ExoMars
750			R2: 754 (20)	
800	L6: 801.6 (21.0)	R3: 799.0 (20.0)	R3: 803 (20)	MSL, ExoMars
860	L7: 858.4 (34.4)	L5: 857.0 (34.0)		ExoMars
865			R4: 864 (17)	MSL
880				MSL
900	L8: 897.9 (40.8)	R4: 906.0 (42.0)		ExoMars
905			R5: 904 (26)	MSL
930	L9: 931.1 (27.0)	L6: 930.0 (32.0)		ExoMars
935			R6: 934 (25)	MSL
965	R11: 966.8 (29.6)	R5: 960.5 (29.0)		ExoMars
965	L11: 968.0 (31.4)			
1000	L10: 1002.9 (29.1)	R6: 1003.0 (28.0)		ExoMars
1010			R7: 1009 (38)	MSL
420-680				MSL

¹ All values in nm. Left and right filter positions shown for each camera system. Excludes filters for atmospheric science.² Imager for Pathfinder (IMP) (Smith *et al.*, 1997)³ Stereo Camera System (SCS) (Griffiths *et al.*, 2005). Curved filters shown in bold.⁴ Mars Exploration Rover Pancam (Bell III *et al.*, 2003)⁵ Mars Science Laboratory (MSL) MastCam (Malin *et al.*, 2005), ExoMars PanCam (Coates *et al.*, 2006)

* Close up lens (see Section C.2.1)

The Stereo Camera System (SCS) on Beagle 2 (Griffiths *et al.*, 2005) was part of the PAW (Figure 2.3 and Table 2.2) and designed to acquire panoramic images when the ARM was extended vertically (~1.5 m above the surface). Near-field imaging was achieved by articulating and panning the ARM so that the accessible area around the lander (“the working zone”) could be surveyed at distances between 0.6 m and 1.2 m prior to sampling. The SCS used a spectrally similar set of filters to those of IMP (Table 2.3). Further details on the SCS are given in Section C.2.1.

The Pancam on MER (Bell III *et al.*, 2003; Table 2.2 and Figure 2.9A) is a multi-spectral, stereoscopic CCD imaging system mounted on a mast 1.5 m above the Martian surface. The mast is capable of rotating and tilting Pancam by 360° and ± 90° respectively. Each camera has 8 selectable filters most of which are assigned for geology (Table 2.3). Pancam has an effective spatial resolution of ~1 mm pixel⁻¹ at a distance of 3 m (Figure 2.7A).

Future missions will exploit existing heritage and, where appropriate, incorporate new technologies. The PanCam on ExoMars (Coates *et al.*, 2006) will consist of a pair of wide-angle CCD cameras for stereoscopy, and a high resolution zoom colour APS camera. The stereo cameras will be based on the Beagle 2 system and use a similar filter set (Table 2.3). The MastCam on MSL (Malin *et al.*, 2005) will improve on the MER specification by having optical zoom and high-definition video capability. Spatial resolutions of 150 µm pixel⁻¹ will be possible for near-field objects. MSL will have a similar filter wheel design to MER (Table 2.3). Also on MSL will be the Remote Micro-Imager (RMI) (Table 2.2) associated with the ChemCam instrument (Maurice *et al.*, 2005) which uses a Laser-Induced Breakdown Spectrometer (LIBS) for active elemental analysis of targets between 2 m and 13 m from the rover. The RMI will establish spatial context with the analytical data from ChemCam (Table 2.4).

2.3.1.2 Close-Up Imaging (Macroscopy)

The first close-up images of the surface of Mars were acquired during the MPF mission in 1997. Sojourner was equipped with three cameras, a pair of monochrome cameras mounted on the front of the rover (for navigation and obstacle avoidance), and one colour camera mounted on the rear (Table 2.2). Unfortunately the images obtained with these cameras were poor (see examples PIA00671 and PIA00672 in the Mars section of <http://photojournal.jpl.nasa.gov/>).

Beagle 2 was capable of macroscopic imaging using one of the stereo cameras. The filter wheel associated with the left-hand camera (Figure 2.3) incorporated a filter called the Close Up Lens (CUL) which reduced the focusing distance to ~80 mm (Table 2.3). At this standoff distance objects 50 mm across fill the FOV at a spatial resolution of $60 \mu\text{m pixel}^{-1}$. The camera would have been positioned with the ARM without making contact with the target. Only greyscale images could be acquired in close-up mode. Further details on the use of the stereo camera in macroscopic mode are given in Section C.2.1.

The Microscopic Imager (MI) on MER is a fixed-focus CCD camera (Table 2.2) located on the end of the Instrument Deployment Device (IDD) (Herkenhoff *et al.*, 2003 and Figure 2.9B). At the required standoff distance of 69 mm, objects 31 mm across fill the FOV at a spatial resolution of $30 \mu\text{m pixel}^{-1}$ (hence the classification as a macroscopic imager in the context of this work). The Depth of Field (DOF) is ± 3 mm so “high relief” targets (i.e., $\gg 6$ mm) require several images to be combined to produce an in-focus image. The IDD provides the coarse focusing by moving the MI away from the target at ~2 mm increments. Image reconstruction is performed on Earth. Crude colour information is possible by combining images acquired with and without the 400-700 nm spectral band pass window in position over the aperture (see images PIA05679 and PIA05208 in the Mars section of <http://photojournal.jpl.nasa.gov/>). Alternatively, colour can be derived from Pancam images of the same target (Figure 2.7B).

Other macroscopic imagers currently in use on Mars or being developed for future missions include the Robotic Arm Camera (RAC) on Phoenix (Keller *et al.*, 2001), the Close Up Imager (CLUPI) on ExoMars (Josset *et al.*, 2006) and the Mars Hand Lens Imager (MAHLI) on MSL (Edgett *et al.*, 2005). The specifications for these instruments are shown in Table 2.2.

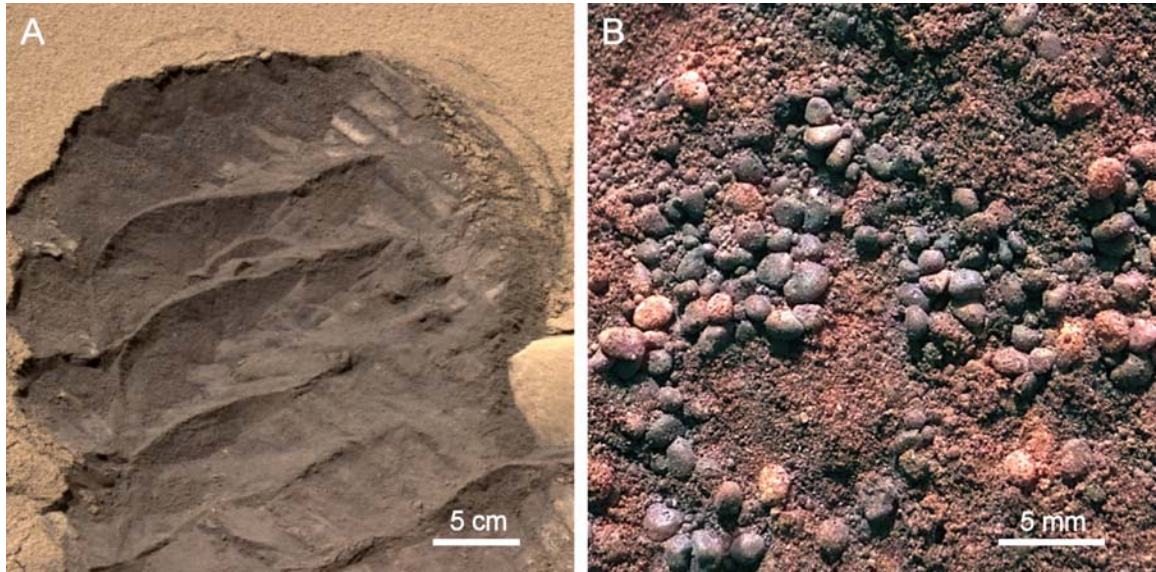


Figure 2.7 Near-field and close-up imaging of Serpent Trench, Gusev Crater, Mars. The Pancam image (ID PIA05592) (A) is a mosaic of colour images acquired using the 750 nm, 530 nm and 430 nm filters (Table 2.3). The excavated drift deposit (trench) is ~30 cm across and ~45 cm long and was created using the rover wheels. A close-up view obtained with the Microscopic Imager (ID PIA05597) (B) used colour information from Pancam to colourise the image. The “pea-shaped” grains (~1 to 2 mm sized) are native to the surface (crust) of the drift and lost their dust coatings as a result of digging the trench (note the variation in colour). The grain size of the drift material itself is more akin to silt (~60 μm). Courtesy NASA/JPL/Cornell/USGS.

2.3.1.3 *In situ* Microscopy

The Beagle 2 microscope (Thomas *et al.*, 2004) was designed for imaging small (4 mm x 4 mm) regions of interest observed in close-up images acquired with the SCS (see above). The spatial resolution of the instrument was 4 $\mu\text{m pixel}^{-1}$. A nominal working distance of 12 mm between the front of the microscope and the target was achieved with the ARM and a standoff “thumb” attached to the PAW (Figure 2.3). Physical contact with the sample was necessary and this needed to be maintained stable for the duration of the image acquisition phase (which could take several minutes). The extremely small Depth of Field (DOF) of the instrument (40 μm) required many images to be combined to produce an in-focus image. Focusing was achieved by moving the microscope with respect to the target using a precision stepper motor on the PAW, and illumination was provided by an annular array of individually switched LEDs (white, red, green, blue, and UV). The UV LEDs were included to detect the presence of mineral or biological

fluorescence. The Beagle 2 microscope was capable of imaging a variety of surface types ranging from smooth cores to complex open fabric materials; thus the instrument was entirely suited for both geological and astrobiological applications. Further details on the Beagle 2 microscope are given in Section C.2.2.

The Phoenix lander is equipped with an optical microscope which is designed to image soil particles between $\sim 10 \mu\text{m}$ and $\sim 1 \text{ mm}$ in diameter (see Phoenix pages at <http://www.mps.mpg.de/>), and an Atomic Force Microscope (AFM) for imaging particles down to $\sim 10 \text{ nm}$ (Gautsch, 2002). However, these activities are performed post-sampling. It is interesting to note that the Phoenix and Beagle 2 microscopes both have spatial resolutions of $4 \mu\text{m pixel}^{-1}$ and use similar illumination methods. Given the geomorphology of the Phoenix landing site (i.e., flat polar plain with no rocks or outcrops) there was no requirement for *in situ* microscopy on this mission.

Like their predecessor Sojourner, the Spirit and Opportunity rovers do not have the capability for *in situ* microscopy. This will also be the case for ExoMars. However, the Pasteur payload will include a combined VIS-IR microscope/NIR spectrometer called MicrOmega as part of the on-board analytical laboratory (Bibring *et al.*, 2006 and Table 2.6).

In addition to being a macroscopic imager, the MAHLI instrument on MSL is also capable of *in situ* microscopy since the instrument can be positioned close enough to targets to achieve spatial resolutions of $12 \mu\text{m pixel}^{-1}$. Given its focusing capability, MAHLI should be as useful for geological and astrobiology-related studies as the Beagle 2 microscope would have been.

2.3.2 Analytical

Three analytical techniques are considered important for robotic field geology and the *in situ* analysis of rocks and soils: X-ray fluorescence spectroscopy to determine elemental composition (see Section C.3.1), Raman spectroscopy to determine mineralogy and identify organic compounds (see Section C.3.2), and Mössbauer spectroscopy to determine iron mineralogy and oxidation state (see Section C.3.3). Raman spectroscopy has yet to be demonstrated on Mars but both X-ray and Mössbauer spectroscopy have established mission heritage.

Table 2.4: Mars surface payloads: *In situ* analysis¹

Instrument ²	Type	Characteristics
APXS (<i>MFP</i>)	Contact	Si-PiN diode (7 mm ² , 8 μm Be window); nine ²⁴⁴ Cm sources (total 1.7 GBq) and alpha detectors; energy resolution ~260 eV (6.4 keV); elements (C, N, O, Na, Mg, Al, Si, K, Ca, Fe, P, S, Cl, Ti, Cr, Mn); sampling area 50 mm Ø
XRS (<i>Beagle 2</i>)	Contact	Si-PiN diode (7 mm ² , 7.5 μm Be window); two ⁵⁵ Fe sources (total 60 MBq) and two ¹⁰⁹ Cd sources (total 5 MBq); 5.9 keV, 6.49 keV, 22.16 keV, 24.94 keV X-rays; energy resolution ~340 eV (5.9 keV); elements (Mg, Al, Si, K, Ca, Ti, Fe, Rb, Sr, Y, Zr); sampling area 22 mm Ø; see Figure 2.8B
Mössbauer (<i>Beagle 2</i>)	Contact	MIMOS II; four Si-PiN diodes; ⁵⁷ Co/Rh sources (both 148 MBq landed); 6.4 keV (X-rays), 14.41 keV (X-rays and γ-rays) and 122 keV (X-rays); sampling area 15 mm Ø; shutter mechanism with Fe foil calibration target; see Figure 2.3
APXS (<i>MER</i>)	Contact	Silicon drift X-ray detector (10 mm ² , 5 μm Be window); six ²⁴⁴ Cm sources (total 1.1 GBq) and alpha detectors; energy resolution ~160 eV (5.9 keV); elements (C, N, O, Na, Mg, Al, Si, K, Ca, Fe, P, S, Cl, Ti, Cr, Mn); sampling area 25 mm Ø; see Figure 2.8A
Mössbauer (<i>MER</i>)	Contact	MIMOS II; same as Beagle 2 instrument apart from a) no shutter mechanism, b) less strategic shielding, and c) stronger primary ⁵⁷ Co/Rh source (12.2 GBq)
Raman-LIBS (<i>ExoMars</i>)	~10 cm	Raman laser (532 nm CW); LIBS laser (1064 nm pulsed); external head with fibre optic feed to single spectrometer (240-840 nm); spectral resolution < 8 cm ⁻¹ (Raman) and < 0.2 cm ⁻¹ (LIBS); all details TBC; see also Table 2.6
Mössbauer (<i>ExoMars</i>)	Contact	MIMOS IIa; silicon drift detectors for enhanced energy resolution (<150 eV TBC), tenfold better SNR and shorter integration times; XRF for elemental composition (range of elements equivalent or better than for the Beagle 2 XRS)
MA_MISS (<i>ExoMars</i>)	~cm?	Down-hole IR spectrometer; spectral range 800-2800 nm; imaging slit tens to hundreds μm wide; “image” compiled from contiguous slit images; see Table 2.5
APXS (<i>MSL</i>)	Contact	Enhanced version of MER APXS (shorter data acquisition times)
Mössbauer (<i>MSL</i>)	Contact	Probably similar to ExoMars instrument
ChemCam (<i>MSL</i>)	~10 m	Nd ³⁺ :YAG pulsed laser (commandable 5 to 30 mJ); pulse < 8 ns; range 2 m to 13 m; three spectrographs for UV (225-320 nm), blue (381-471 nm) and red (497-928 nm); see RMI in Table 2.2

¹ Remote sensing spectrometers such as Mini-TES (MER) and MIMA (ExoMars) not included² See Glossary for explanation of acronyms.

Other analytical techniques that have been demonstrated on Mars or slated for future missions are listed in Table 2.4. Although relevant to overall mission objectives, and in some cases to astrobiology, these techniques are performed post-sampling so are beyond the immediate scope of this work.

2.3.2.1 X-Ray Spectroscopy

The first *in situ* measurements of the elemental composition of Martian rocks were made with the Alpha Proton X-ray Spectrometer (APXS) on the MFP Sojourner rover (Rieder *et al.*, 1997 and Table 2.4)². The instrument was sensitive to most major elements that commonly occur in rocks such as Na, Mg, Al, Si, K, Ca, Fe, P, S, Cl, Ti, Cr and Mn, in addition to lighter elements such as C and O. A deployment mechanism fitted to the rear of the rover enabled the APXS head to be positioned at a variety of elevations and (rotational) orientations. The assembly had sufficient compliance (~20°) to facilitate contact with irregular measurement surfaces such as rocks. The MFP APXS attempted to measure carbon abundance, and hence recognise carbonates, but none were found. Unfortunately, the effects of atmospheric CO₂ intervened between the uneven rock surfaces and the detector resulting in a major background signal. In total, 27 measurements were made with the MFP APXS including 11 “atmospheric” readings when the APXS failed to make contact with a sampling surface. Of the 16 remaining measurements where contact was achieved with geological materials, only 11 (5 rocks and 6 soils) were considered to be of sufficient quality to be converted to oxide abundance.

The Beagle 2 X-ray Spectrometer (XRS) was loosely based on the MFP APXS experiment but favouring the excitation method used by the Viking spectrometers (see Table 2.4). The XRS head assembly (Figure 2.8B) was mounted on the PAW (Figure 2.3) and positioned with the ARM (Figure 2.2 and Figure 3.2C). The head contained the radioactive sources, the X-ray detector element, and first stage pre-amplification. The main electronics unit was located within the lander compartment. The contact ring on the front of the XRS head established a standoff distance of 11.5 mm between target and detector. The diameter of the sampling area was 22 mm. The instrument was sensitive to a number of major elements that occur in rocks such as Mg, Al, Si, K, Ca, Ti, and Fe, plus the trace elements Rb, Sr, Y, and Zr (Talboys, 2006). Detection of lighter

² The elemental composition of Martian soil was first determined by “laboratory” X-ray Fluorescence Spectroscopy (XRFS) in 1976 by Viking (Clark *et al.*, 1977).

elements was unnecessary given the capabilities of the GAP (Section 2.1.1.2).

The APXS for MER (Rieder *et al.*, 2003 and Figure 2.8A) is similar to the instrument used on MFP (Table 2.4) but technological advances in X-ray detector spectral resolution (160 eV versus 260 eV for MFP) and sensitivity rendered the proton mode of the MFP APXS unnecessary. Therefore the Alpha “Particle” X-ray Spectrometer for MER benefited from improved reliability and performance. The MER instrument was also modified to reduce the effects of CO₂-induced background that compromised the Pathfinder APXS measurements. The diameter of the sampling area is 25 mm (Jolliff *et al.*, 2005), comparable to that of the XRS even though the Beagle 2 instrument was much smaller (Figure 2.8B). The MER APXS has been used to determine the major and trace geochemistry of a variety of rock and soil types within Gusev Crater (Gellert *et al.* 2004) and Meridiani Planum (Rieder *et al.*, 2004).

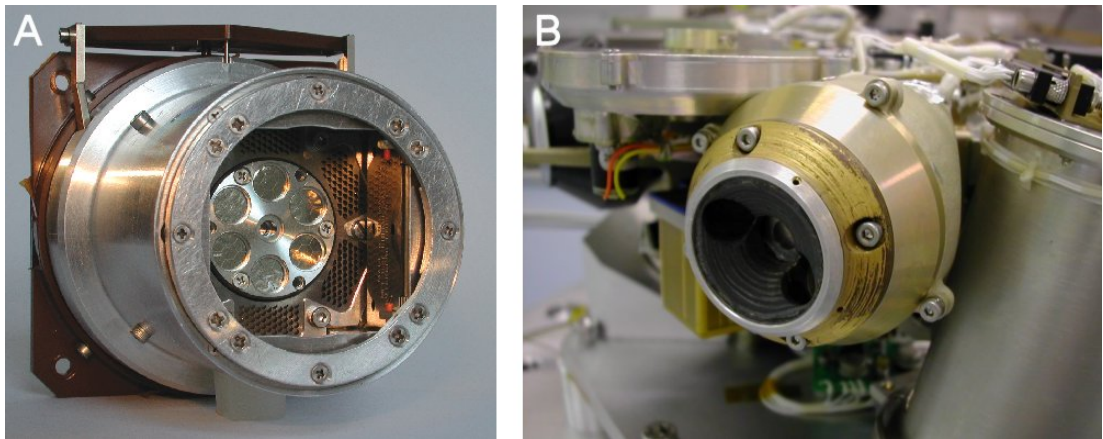


Figure 2.8 *In situ* X-ray spectrometers for MER and Beagle 2. The flight model Alpha Particle X-ray Spectrometer (APXS) as used on MER Spirit and MER Opportunity (A). The instrument head (as shown) measures 84 mm by 52 mm and weighs 250 g. The XRS for Beagle 2 (B) is smaller (47 mm x 47 mm) and weighs significantly less at 58 g. Details of both instruments are given in Table 2.4. Courtesy NASA/JPL/Max-Planck-Institute for Chemistry (A) and the University of Leicester (B).

MSL will include an enhanced version of the MER APXS (see APXS page at <http://mars.jpl.nasa.gov/msl/>). ExoMars will not be equipped with an XRS, opting instead for post-sampling analysis of prepared powders by X-ray Diffraction (XRD) and X-ray Fluorescence (XRF) using the Mars-XRD instrument (Marinangeli *et al.*, 2007 and Table 2.6). However, the Mössbauer for ExoMars (MIMOS IIa) will be able to determine elemental composition *in situ* (Table 2.4). Post-sampling XRF/XRD will also feature on MSL in the form of CheMin

(<http://chemin.lanl.gov/> and Table 2.6).

2.3.2.2 Raman Spectroscopy

The Pasteur payload on ExoMars will include a Raman-LIBS instrument to determine the elemental chemistry and mineralogy of Martian rocks and soils, and importantly for astrobiology identify any organic compounds that may be present (Rull and Martinez-Frias, 2006). By incorporating two separate optical heads connected to a single spectrometer with a spectral range of 240 to 840 nm, the instrument will be capable of performing both *in situ* and laboratory measurements on samples (Table 2.4 and Table 2.6 respectively). One head will be mounted on the robotic arm and the other mounted within the analytical laboratory in association with MicroOmega (Bibring *et al.*, 2006), for combined analysis of acquired drill cores prior to crushing. Each head will be equipped with a continuous wave laser for Raman (532 nm TBC) and a pulsed laser for LIBS (1064 nm TBC). The resolution of the spectrometer is expected to be better than 8 cm^{-1} for Raman and better than 0.2 nm for LIBS. Although remote Raman-LIBS systems (~10 m) are being considered for the future, the range of the ExoMars instrument for *in situ* measurements will be limited to ~10 cm (i.e., CLUPI working distance).

In addition to being able to identify organic functional groups, Raman is particularly sensitive to minerals formed under aqueous conditions such as sulphates, oxides and hydroxides. LIBS on the other hand allows for precise identification of chemical elements. By targeting the Raman and LIBS measurements on the same spot, important spatial context will be possible with the instrument. This applies to both *in situ* and post-sampling measurements. LIBS will also have the ability to remotely ablate thin coatings on rocks and thus potentially provide access to fresh material.

Table 2.6: Mars surface payloads: Laboratory analysis¹

Instrument	Function	References
XRFS (VL)	Elemental analysis of soil by XRF; ⁵⁵ Fe and ¹⁰⁹ Cd excitation; four proportional counter detectors; elemental range Mg to U	Clark <i>et al.</i> , 1977
GCMS (VL)	Separation and identification of organic species using gas chromatography and mass spectrometry	Viking Science Team, 1977
Biology (VL)	Detection of metabolic by-products from soil samples; see Section 2.1.1.1.	Klein, 1978 Viking Science Team, 1977
GAP (Beagle 2)	Detection of organic matter and light element composition; stepped combustion and pyrolysis; separation and identification of species using mass spectrometer; see Section 2.1.1.2.	Pullan <i>et al.</i> , 2005
LMC (ExoMars)	Detection of specific molecules by exploiting highly specific binding properties of protein based receptors; uses fluorescent dye labelling and CCD imaging of assays; currently an optional instrument	Sims <i>et al.</i> , 2005
MicrOmega (ExoMars)	Structural and compositional analysis of rock cores; VIS-IR polarising microscope (4 µm pix ⁻¹) and NIR multi-spectral imaging spectrometer (850-2600 nm); ~4 nm spectral resolution	Bibring <i>et al.</i> , 2006
Raman-LIBS (ExoMars)	Mineralogical and molecular analysis of core samples; internal head connects to the same spectrometer described in Table 2.4	ExoMars Project Team, 2007b Rull and Martinez-Frias, 2006
Mars-XRD (ExoMars)	Mineralogical (XRD) and elemental (XRF) analysis of prepared bulk powder; ⁵⁵ Fe X-ray source; detector array of four X-ray CCDs arranged on a 12 cm radius curved ceramic substrate	Marinangeli <i>et al.</i> , 2007
Urey (ExoMars)	Identification of organic compounds using sub-critical water extraction to leach organics from rock/soil; MOD detects amino group compounds and PAHs by laser induced fluorescence; another part of the system determines chirality. MOI determines the oxidation state of samples.	ExoMars Project Team, 2007b
MOMA (ExoMars)	Detection of volatile and non-volatile molecules present in the atmosphere or sedimentary rocks/soils at ppb to ppt levels; uses pyrolysis and GCMS to separate and identify species	ExoMars Project Team, 2007b
CheMin (MSL)	Mineralogical (XRD) and elemental (XRF) analysis of prepared bulk powder or crushate; piezoelectric actuator to vibrate powder; Co source; X-ray CCD	http://chemin.lanl.gov/
SAM (MSL)	Light element composition of rocks, soils and atmosphere using GCMS; tunable laser spectrometer for precise isotope ratios and abundances in targeted species (H ₂ O, CH ₄ , CO, CO ₂ , H ₂ O ₂ , N ₂ O)	http://ael.gsfc.nasa.gov/marsSAM.html

¹ See Glossary for explanation of acronyms.

2.3.2.3 Mössbauer Spectroscopy

The MIMOS Mössbauer spectrometers for the Mars Exploration Rovers and Beagle 2 (Klingelhöfer *et al.*, 2003) and slated for ExoMars and MSL are miniaturised instruments designed for identifying Fe-mineral speciation (olivine, pyroxene, ilmenite), oxidation state (Fe^{2+} , Fe^{3+} , Fe^0), and coordination state (octahedral Fe^{3+} , tetrahedral Fe^{2+}) at the planetary surface.

With the exception of additional radiation shielding, source intensities, and the inclusion of a shutter mechanism, the Mössbauer spectrometer for Beagle 2 was identical to the instruments used on MER (Figure 2.3 and Table 2.4). The instrument uses a backscatter geometry and requires contact with the surface to be measured. This is achieved using a robotic arm such as the IDD on MER or the ARM on Beagle 2. Once in position the diameter of the measurement area is ~ 1.5 cm. The sampling depth of the illuminating 14.4 keV ^{57}Co gamma radiation for coherent rock and air-fall dust is ~ 0.2 mm and ~ 3 mm respectively.

Mössbauer results from the MERs Spirit and Opportunity have confirmed the presence of several Fe-bearing minerals on Mars including goethite, hematite, jarosite, olivine, and pyroxene (Klingelhöfer *et al.*, 2004; Morris *et al.*, 2006). Mössbauer spectroscopy has also been cited as a useful tool for *in situ* astrobiology (Wilson, 1999; Schröder *et al.*, 2005). Terrestrial studies using the technique have identified microbe-induced changes in Fe oxidation state within hydrothermal vent systems.

2.3.3 Geotechnics

As discussed earlier, effective sample preparation and acquisition are important aspects of planetary field work. To date *in situ* geotechnics on Mars has been limited to either grinding rocks (MER) or collecting soil samples (Viking Landers and Phoenix). Beagle 2 was uniquely equipped with a suite of preparation and acquisition tools but these were never demonstrated on the surface of Mars following failure of the probe during landing. Future missions intend to incorporate grinders, plus subsurface drilling/coring systems. All these geotechnical assets provide essential benefits to the scientific payload and objectives of each mission. Geotechnical devices that have been utilised at the surface of Mars, or are being proposed for future missions are listed in Table 2.5.

In some cases however, the techniques employed may be detrimental to some types of *in situ* investigation. It is rare for terrestrial field geologists to resort to grinding or drilling into rocks without having previously used a hammer to expose fresh material and potentially informative visual characteristics.

2.3.3.1 Grinding

In 2003, three spacecraft were *en route* to Mars with payloads equipped with tools designed for preparing the surface of rocks in support of *in situ* scientific investigations; MER Spirit, MER Opportunity and Beagle 2. The Rock Abrasion Tool (RAT) on Spirit and Opportunity (Figure 2.9), and the Rock Corer Grinder (RCG) on Beagle 2 (Figure 2.3), were all originally designed to remove superficial material on rocks including dust and weathering/alteration rinds to reveal underlying fresh material, and in doing so prepare a flat surface on which to conduct close-up imaging and spectroscopic measurements. Both RATs sent to Mars were true grinders but the Beagle 2 RCG lost much, if not all, of its ability to grind during the final stages of manufacturing when the mechanism designed to translate the coring bit about a fixed radius circle (Figure 11 in Pullan *et al.*, 2004) was removed due to mass constraints and contamination concerns. Thus the RCG as delivered to Mars was in fact just a coring device.

Although not a complete replacement of a “geologist’s hammer” as falsely claimed by the media and others (for example Gorevan *et al.*, 2003b), the RAT is nevertheless an important geotechnical tool for field geology. The cutting mechanism (Figure 2.9C) is more akin to a paddle wheel than a simple grinding wheel although the latter term is still used to describe the operation. The cutting wheel consists of a rotating bar (23.37 mm long) with diamond impregnated phenolic resin cutting edges at each end. This high speed (3000 rpm) rotating mechanism is itself rotated slowly (0-2 rpm) about the central axis of the RAT and thus in one complete revolution abrades a 45 mm diameter surface (Figure 1 in Bartlett *et al.*, 2005). After each revolution the grinding wheel part of the RAT is advanced by predetermined increments (i.e., 0.05 mm rev^{-1} for basalt), whilst the IDD maintains a preload force of between 10 and 100 N to ensure complete stability between the rover and Mars. The grinding process repeats until the desired depth has been achieved. This is determined by software and active feedback, and is typically 5 mm, but in certain circumstances can reach 15 mm. For hard rocks grinding operations can last up to 4 hours.

Table 2.5: Mars surface payloads: *In situ* geotechnics

Instrument ¹	Type	Characteristics
Surface sampler (<i>VL</i>)	Soil sampler	Scoop on extendable boom arm; max depth achieved 20 cm; sample size 6 cm ³ for biology experiments; see Figure 2.1A.
PLUTO (<i>Beagle 2</i>)	Soil sampler + Hammer	Tethered inertial penetrator; 890 g (340 g Mole); 17 W; max depth 2 m; sample size 20-27 mm ³ ; see Figure 2.3 and Figure C.8C
RCG (<i>Beagle 2</i>)	Rock corer	Rotary/percussive corer; 348 g; 6 W; max penetration depth 6 mm; sample size 4 mm x 2.5 mm \emptyset ; see Figure 2.3, Figure 3.2BC, and Figure C.8AB
RAT (<i>MER</i>)	Rock grinder + Brush	Rotary grinder and fines remover; 687 g; ~10 W; preparation surface 45 mm \emptyset ; grinding depth 5 mm; see Figure 2.9 and Section 2.3.3.
Surface sampler (<i>Phoenix</i>)	Soil and ice sampler	Scoop with serrated blades and ripper tines; scoop sample size ~250 cm ³ ; max depth possible 1 m
Drill (<i>ExoMars</i>)	Rock and soil sampler	Rotary/percussive drill/coring tool (700 mm long) plus 3 extension rods (500 mm each); max depth 2 m; sample size 3 cm x 1 cm \emptyset (TBD); equipped with position/temperature sensors, and optical head and lamp for an IR spectrometer (MA_MISS)
RAT (<i>MSL</i>)	Rock grinder + Brush	Probably similar to MER RAT
Surface sampler (<i>MSL</i>)	Rock and soil sampler	Scoop for caching rock samples up to 1.5 cm in size for MSR
Drill/mini-corer (<i>MSL</i>)	Rock and soil sampler	Currently TBD; sample size ~5 g; max penetration depth 10 cm
ChemCam (<i>MSL</i>)	Micro ablation	1067 nm laser delivers ≥ 1 GW cm ² at ≤ 1 mm target spot to remove dust at ~ 1 mm pulse ⁻¹ and weathering rind at ≤ 0.3 μ m pulse ⁻¹

¹ See Glossary for explanation of acronyms.

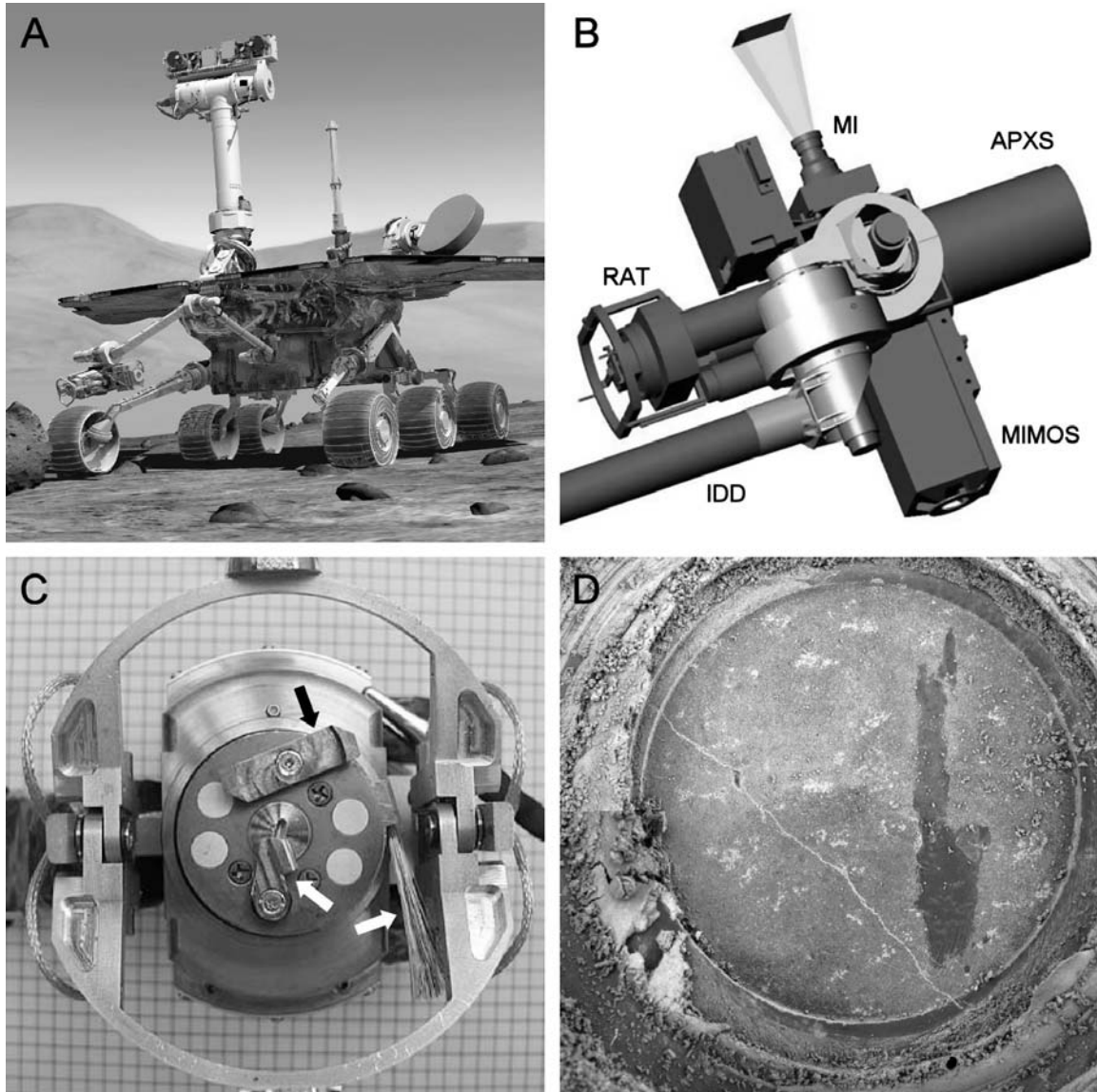


Figure 2.9 *In situ* geotechnics with the MER RAT. Virtual rendition of the MER showing the RAT being deployed during *in situ* operations (A). Position of the RAT with respect to other instruments on the IDD (B). The front of the RAT (C) consists of a grinding wheel (black arrow) and a pair of brushes (white arrows). Note the second brush has been removed from this model. Example of a ~3.5 hour grinding operation on rock Mazatzal (target “New York”) imaged with the MI (ID PIA05661) (D). Diameter of the flat region is ~45 mm. Courtesy NASA/JPL (AB), Honeybee Robotics (C) and NASA/JPL/Cornell/USGS (D).

The RAT is also equipped with two stainless steel brushes, one to remove cuttings during the high speed grinding process and displace them to the perimeter of the 45 mm surface being abraded, and another to push these fines out further to ensure newly cut materials can be

displaced and not obstruct the area being ground. The result is a clean prepared surface suitable for close-up imaging and *in situ* spectroscopic analysis (Figure 2.9D). In some situations the cuttings may be of interest and since they are retained about the periphery, they are also available for examination. Removal of adhered material from the head is crucial to avoid degrading the performance of the grinding operation and the risk of cross-contamination between measurements. Head cleaning is achieved by operating the RAT against a third brush located on the IDD.

The first attempt at grinding a rock on Mars was performed by the Spirit rover on Sol 34 (February 6th 2004) in the plains region of Gusev Crater. The chosen target was a rock called Adirondack which offered a relatively dust free and flat sided face on which to deploy the RAT. Subsequent *in situ* analysis confirmed Adirondack to be unaltered olivine basalt. The RAT performed extremely well on this target, grinding to a depth of ~3 mm, especially since basalt was considered to be the hardest material the RAT was designed for (Gorevan *et al.*, 2003b).

Two weeks later, during operations at Meridiani Planum (Sol 30, February 23rd 2004), the RAT on the Opportunity rover was used for the first time on a target called “McKittrick MiddleRAT”, part of a section of El Capitan, a small sedimentary outcrop in Eagle Crater. A depth of 4 mm was achieved. In comparison to Adirondack, the outcrop material was extremely soft, almost akin to Plaster of Paris (Dr. Steve Gorevan, Honeybee Robotics, personal communication, 2004), and the spherical concretions i.e., “blueberries” contained within it, relatively hard.

The RAT on the Spirit rover performed a total of 15 grinding operations, on mostly hard volcanic rocks, before the teeth were considered too worn for continued usage in this mode. Damage to the robotic arm would likely result due to excessive vibration during grinding. However, the device can still remove dust using the brush. The RAT on Opportunity has exceeded Spirit’s operational count and continues to be used to grind the softer sulphate deposits of Meridiani Planum. Following these successes, future missions such as MSL will also be equipped with a RAT, and a similar device is currently being considered for ExoMars (EADS Astrium and University of Leicester collaboration).

2.3.3.2 Sampling

Static landers such as Viking, Beagle 2, and Phoenix rely on robotic arms to collect

unconsolidated samples from the top few centimetres of the surface within a limited arc close to the spacecraft. Beagle 2 had the added advantage of being able to acquire material from the subsurface to a depth of ~2 m using PLUTO (Richter *et al.*, 2002) but the quantity was small (between ~5 mm³ and 200 mm³ as dictated by the GAP experiment). Whether or not sampling is a requirement, robotic arms have now become a feature of planetary rovers and a versatile means of positioning contact instruments and sample preparation tools such as the RAT (i.e., on MER Spirit and Opportunity).

Acquisition of rock cores will be a feature of future missions. Beagle 2 may have been capable of extracting small cores (up to 4 mm long and 2.5 mm diameter) from some types of rocks within reach of the RCG (see Chapter 5). A more traditional (albeit miniaturised) drilling/coring system is proposed for ExoMars which is designed to reach depths of up to 2 m and deliver cores up to 30 mm long and 10 mm diameter (see drill page at <http://www.esa.int/SPECIALS/ExoMars/>). Ultrasonic techniques (Bar-Cohen *et al.*, 2005) may be used as a novel means of acquiring cores in the future. MSL will also include a drill/corer in addition to a simple soil scoop capable of collecting loose material with a fragment size less than ~1.5 cm.

Drilling and coring on Mars is technologically complex and made more challenging in the case of ExoMars given the astrobiological focus of the mission. The NASA Mars Astrobiology Research and Technology Experiment (MARTE) is therefore undertaking a programme of field trials in which lessons can be learned using Earth analogues to understand the practicalities of autonomous drilling (Cannon *et al.*, 2007).

For extreme core drilling applications (i.e., at the planetary surface) it is crucial to know whether the structural, compositional and biological attributes observed in a core are geologically representative or have been altered by the coring process in some way. Such contamination issues apply to various forms of coring processes including rotary, percussive and ultrasonic. Structural contamination of soft or semi-lithified sediments, where inter-grain motion is possible, may range from slightly disturbed to completely disturbed (destroyed). The resulting effect on the core, and drill hole if this could be examined *post facto*, could range from minor edge effects to extreme bowing to massive flow-in. Structural deformation may also redistribute or compromise any extant or extinct biosignatures especially if they are associated with bedding or lamination features.

Sudden changes in lithology including void spaces may also introduce catastrophic contamination. Polymict materials comprised of various mineral species or rock clasts with different physical properties may also introduce preferential core loss. The bulk composition of the acquired core may not be representative of the rock from which it was cored.

2.3.3.3 Splitting

There are no plans to equip planetary vehicles with geological hammers even though it was suggested over a decade ago that intact rocks were preferable to cores, powders or cuttings for future sample return missions (Cheng and Farmer, 1997). The RAT described in Section 2.3.3.1 is clearly a grinder and not a “geological hammer”. However, there are circumstances when splitting rocks is a more appropriate way of accessing potential targets of interest without destroying them in the process. It is true that in many cases grinding can be preferable to splitting, especially when dealing with igneous rocks or well-cemented sediments. However, certain geological materials also exhibit characteristic fabrics and structural features that if abraded would most likely be destroyed and, crucially for astrobiology, such features may be the very targets that contain the macroscopic life signatures or paleo-environmental indicators being sought. These aspects will become apparent in later chapters.

Admittedly, splitting rocks is inherently more challenging than grinding, not least because of the increased dexterity required for positioning the tool and manipulating samples once they have been removed. There are also operational risks associated with flying debris. Splitting would not replace drilling or grinding, but rather add an essential element to the geotechnical tool-kit.

During the development of PLUTO for Beagle 2 (Richter *et al.*, 2002) it was evident that the mechanism used for soil penetration could provide sufficient energy to fracture harder materials such as rock (Dr. Lutz Richter, DLR, personal communication). Tests at DLR in Cologne and at the University of Leicester verified this capability (see Chapter 5) and it was proposed to incorporate rock splitting operations in the latter stages of the mission when all primary objectives had been fulfilled and tool tip wear was less of a concern. Unfortunately, failure of the Beagle 2 probe prevented such a unique opportunity to try out a real geological hammer on Mars.

2.4 Summary

The three examples of astrobiology missions discussed in this Chapter provide insights into the evolving strategies and technologies needed for searching for past and present life on Mars. The Viking Landers were limited in terms of *in situ* science and mobility but demonstrated the importance of effective sampling and on-board laboratory analysis. Beagle 2 was well equipped for both *in situ* field geology and sample analysis (especially in respect to isotopic chemistry), but lacked mobility. Assuming the Pasteur payload is not de-scoped, ExoMars should be well equipped for *in situ* field geology, sample analysis (especially in respect to life detection instruments), and will be highly mobile.

Environments potentially suited to life on Mars in the past (and possibly the present) include aqueous, hydrothermal and endolithic (i.e., within rocks). Volcanism and water were significant on Early Mars and, in combination, may have provided a range of suitable habitats for life to develop. Ancient lake deposits or extinct hydrothermal systems may be the best candidates to search for fossilised evidence of life. Extant life, if it exists at all, is likely to be below the surface. Increasingly extreme conditions at the surface towards the end of the Noachian would likely have persuaded microbes to adopt radiation protection strategies and endolithic behaviour. Targets of interest may be sites associated with active hydrothermal springs if such features can be found and accessed.

Essential geological fieldwork requires visual observation, analytical measurement and physical interaction. This also holds true for robots deployed at the planetary surface to search for signs of past or present life. An effective array of *in situ* techniques is crucial for optimised target selection and to establish essential geological context prior to sampling. Technology has now reached a stage in which surface elements can be feasibly equipped with the essential equipment needed to carry out *in situ* geological fieldwork on Mars. Some techniques described in this Chapter already have technological heritage (i.e., the field microscope on Beagle 2), and some have been demonstrated at the surface (i.e., the Mössbauer spectrometer on MER), whilst others are being designed for future missions (i.e., the Raman-LIBS for ExoMars).

Chapter 3

The Planetary Analogue Archive and Database

This Chapter discusses the role of planetary analogues in space exploration and describes a comprehensive specimen archive and associated database called GSPARC (Geological Specimen Archive), established by the author for use in planetary research, education and public outreach. The physical specimen archive was initiated in 2002, and has continued to expand over the course of this project. A standalone database application, complete with search engine, was developed between 2003 and 2005 to manage the growing archive, and to organise the results of experiments performed on the samples with a variety of instruments. Plans for the interactive on-line version of the database are described.

Also introduced in this Chapter is the Planetary Analogue Field Studies Network (PAFS-net) which was established by the author in 2004 following experience acquired during the Beagle 2 project. The astrobiology-related experiments described in Chapter 5 (Pullan *et al.*, 2008), and the robotic activities described in Chapter 6 (Shaw *et al.*, 2007), are examples of the type of integrated studies performed by the network. PAFS-net currently has a membership of more than 40 scientists and engineers from 10 countries, and is a recognised entity within the planetary science community (Pullan, 2007).

3.1 Introduction

The availability of planetary material for study in the laboratory is extremely limited. Excluding the Earth, we currently only have examples from two major bodies in our Solar System, namely the Moon and Mars. Approximately 382 kg of lunar material (mostly rocks) were hand collected and returned from the Moon during the latter phase of the Apollo programme (1969-1972) and only 300 gm of soil in total were returned by three Russian robotic probes between 1970 and 1976. In addition the current inventory of lunar meteorites totals about 7 kg. To date no samples have yet been returned from Mars but our current stock of SNCs (class of meteorites originating from Mars) amounts to approximately 85 kg.

Primitive bodies (asteroids) are represented by an impressive ~500 tonnes of meteorites³. A total of 4660 samples (494,625 kg) were collected between 1740 and 1990 and further meteorites of all types (including planetary) continue to be found in Antarctica and other parts of the world. Irons (asteroid cores) dominate this inventory (> 90%) as expected due to their resilience and ease of identification. Near-surface material accounts for only a tiny percentage of the remainder. Samples from comets are non-existent. However, the NASA Stardust mission to Wild-2 (<http://stardust.jpl.nasa.gov/>) successfully collected particles from the comet's tail in 2005 and slightly less than an expected 1 mg of material was returned to Earth in early 2006.

Until dedicated robotic sampling missions can be realised, the quantity and variety of returned planetary material will remain static for the time being (as above for the Moon and zero for all other planets). The number of lunar and martian meteorites is increasing, albeit gradually, with new finds.

However, these samples of planetary material are not pristine, having undergone ejection from the parent body, interplanetary transit, atmospheric entry, impact and subsequent terrestrial weathering. They also lack context since one can only speculate their actual place of origin on the parent planet. Although we can extrapolate much from these samples, the collection does not represent the range of available rock types and geological processes that are thought to exist on these planets and thus gaps in our knowledge remain.

A complete mimic of a planetary material is unlikely if not impossible. Therefore the term “planetary analogue” describes a terrestrial rock, soil sample (natural or synthetic) or field locality in terms of its partial characteristics that are synonymous with what is known, what is believed to exist, or what has potential to exist on other planets. The term may have a different meaning depending on the field of study, the purpose of the experiment being conducted, or even the mindset of the individual.

For example, instruments that analyse the mineralogy or elemental composition of rocks require materials with appropriate composition, grain size, texture and weathered state. On the other hand tools developed for soil sampling are concerned primarily with the mechanical properties of

³ This excludes the contribution from micrometeorites (< 2 mm) which totals ~40,000 tonnes per annum (50% of which reaches the Earth's surface) (Love and Brownlee, 1993).

homogenized or heterogeneous materials of various “grades” (particle size distribution, clastic content, cohesiveness, etc.). Field analogues by their nature are more complex and often involve field associations and interrelationships. In astrobiology (the study of the origin of life and life beyond the Earth), it is important to consider terrestrial examples of extreme bio-habitats associated with impact craters, cold/dry high latitude deserts or ancient rocks that have preserved features from an era when planets experienced similar conditions (Earth and Mars in particular). Samples from these localities provide important alternatives (analogues) on which to exercise the ability of space instruments to collectively identify and corroborate signatures of life. This is specifically addressed in Chapter 4 and Appendix B.

For the foreseeable future, robotic missions conducting *in situ* measurements on a planetary body will be our only source of “ground truth” data. It is important therefore to ensure that the instrumentation delivered to the surface of a planet is fully capable of observing, analysing or interacting with a broad range of materials exhibiting an equally broad range of variables in order to maximise effectiveness and success.

Close or part analogues of planetary material are available here on Earth thanks to the geological diversity of our own planet. Several localities around the world are commonly considered planetary analogue sites, being either ancient examples of geological/biological processes preserved in the rock record or modern extreme environments where such processes are currently at play. By bringing field samples to instruments in the laboratory, or taking instruments into the field, planetary analogues play an important role in the development and operation of mission payloads, and planetary science in general.

3.1.1 The Planetary Context

Many assumptions and preconditions have to be made in order to place studies utilising analogue materials into the planetary context. This is crucial in order to validate the experimental results and enable researchers to formulate meaningful interpretations. Robotic fieldwork on Mars is difficult, restricted and generally data-poor compared with terrestrial fieldwork conducted by humans. Therefore, all experiments must be carefully controlled and constrained. All non-analogous features and aspects of the study materials (i.e., complex metazoan fossils, etc.) should be either avoided or ignored. Fortunately the small measurement footprints of most planetary instruments cater for this.

Consideration must also be given to instruments and tools that are influenced by environmental parameters such as temperature, pressure, gravity, atmospheric composition, etc. If any of these effects are significant to the operation or performance then some experiments need to be conducted using environmental chambers or other simulators. Conducting experiments under these conditions becomes restrictive when natural field specimens are involved. If the environmental effects are minor, or can be factored out, then it is preferable to perform all measurements in the open lab where versatility allows for more realistic experiments to be done. In some cases it is more desirable or meaningful to employ terrestrial variants of the instrumentation or commercial systems. It is normal practice to cross-calibrate flight instruments with development models and terrestrial versions in order to provide laboratory support during active missions. In the absence of flight-type instruments or development prototypes, commercial instruments play a vital role in both the laboratory and the field.

Other considerations are the practicalities of measurement. On Earth, field geologists benefit from greater mobility, accessibility and dexterity compared with robotic spacecraft such as rovers. Humans can cover greater distances and constantly evaluate the terrain presented to them. Apollo 17 astronauts traversed a total of 35 km (within an area of 80 km²) in three EVAs totalling about 22 hours (Figure 3.1A). In comparison, the MERs could probably cover less than 100 metres during the equivalent period without performing any measurements.

In geotechnics (the study of the physical properties of rocks and soils), the mechanical characteristics of materials are of primary importance so a range of rocks exhibiting variation in hardness and grain size would be appropriate even if the rock type is not petrologically analogous (i.e. granite, a material not currently thought to be encountered beyond Earth). Soils can be prepared to emulate planetary upper regolith fines (Figure A.4). These are particularly useful for soil sampling experiments and dust coating studies.

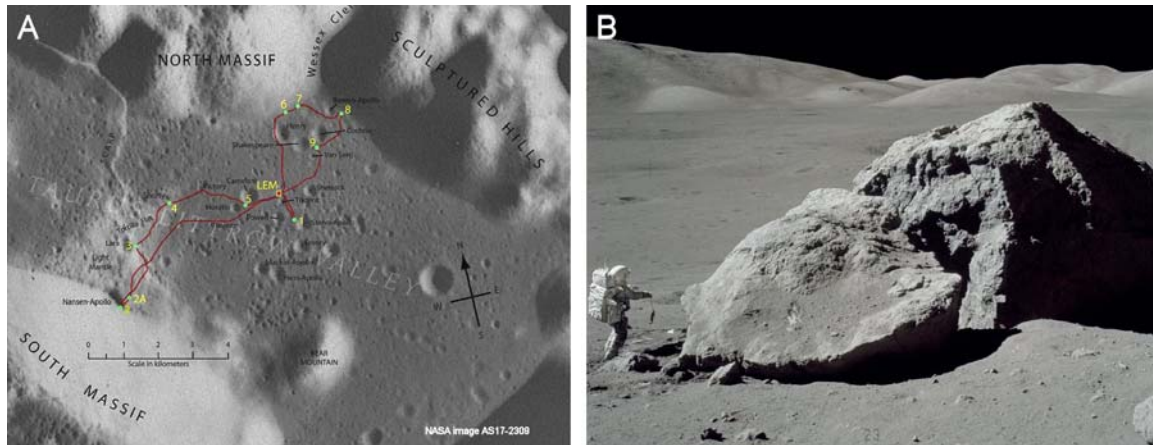


Figure 3.1 Apollo 17 landing site in Taurus Littrow valley, Serenitatis Basin (A). The three EVA traverses are shown emanating from the Lunar Excursion Module (LEM). Astronauts Schmidt and Cernan travelled a total of 35 km visiting 9 sites of interest including Tracey’s Rock (B) at station 6. Courtesy NASA AS17-2309 (A) and NASA AS17-140-21496 (B).

Other analogues are selected on the basis of discoveries made *in situ* or from orbit by robotic probes. For example, instrumentation on the MER Opportunity rover detected what is interpreted to be the mineral jarosite (hydrated iron sulphate), relatively rare on Earth but found as a weathering product of sulphides in arid regions (Martinez-Frías *et al.*, 2004). The same rover also observed the aptly named “blueberries”, iron oxide spherules indicative of aqueous deposition. Similar concretions can be found at various localities on Earth (Chan *et al.*, 2004).

3.1.2 Analogue Research, Networks and Archives

Since the 1960s, when Apollo astronauts received basic training in field geology in the Arizona desert, Hawai’i, Iceland and Germany (see Ries Crater Section B.1), there has been an increase in the number of locations on Earth recognised as planetary analogue sites (American Astronomical Society, 2001; Farr *et al.*, 2002; Chapman, 2007). Analogous criteria vary greatly from site to site, and range from large scale geomorphological features (*op. cit.*) to microscopic extremophile habitats (Blackhurst *et al.*, 2005). Table 3.1 lists some of the more important field sites with relevance to Mars and the search for life, and summarises the qualities of each site.

Table 3.1: Important planetary analogue sites pertaining to Mars and the search for life

Analogue Site	Characteristics and Activities	Section
Svalbard <i>Norwegian Arctic</i>	Extant rock-dwelling extremophiles (Jorge Villar <i>et al.</i> , 2006). Carbonate spherules similar to those in Mars meteorite ALH84001 (Steele <i>et al.</i> , 2007). JPL robotic trials (Huntsberger <i>et al.</i> , 2007). Arctic Mars Analogue Svalbard Expedition (AMASE) (http://amase.ciw.edu/).	
Devon Island <i>Canadian Arctic</i>	Haughton impact crater (Sherlock <i>et al.</i> , 2005). Extant rock-dwelling extremophiles (Parnell <i>et al.</i> , 2004). Human and robotic mission simulations (http://www.marssociety.org/). Canadian Analogue Research Network (http://www.space.gc.ca/).	B.7
Dry Valleys <i>Antarctica</i>	Extant rock-dwelling extremophiles (Friedmann <i>et al.</i> , 1988; Siebert <i>et al.</i> , 1996).	B.5 B.6
Rio Tinto <i>Spain</i>	Subsurface chemolithotrophic organisms (Fernández-Remolar, 2006) and acid sulphate deposits (Martinez-Frías <i>et al.</i> , 2004). Robotic astrobiology (McGuire <i>et al.</i> , 2004). Mars Analog Rio Tinto Experiment (MARTE) (http://www.nasa.gov/centers/ames/missions). Centro de Astrobiología (CAB) (http://www.cab.inta.es).	
Pilbara <i>Western Australia</i>	Early Archaen (~3.5 Ga) micro-environments potentially comparable to Noachian Mars (Westall, 2005b). Well preserved sedimentary structures and sub-microscopic biosignatures (Allwood <i>et al.</i> , 2006).	B.8 B.9
Atacama <i>Chile</i>	Mars-like soil and extant extremophiles (Navarro-González <i>et al.</i> , 2003). Robotic astrobiology (Zoë) and Life in the Atacama project (http://www.frc.ri.cmu.edu/atacama/).	
Barberton <i>South Africa</i>	Early Archaen (~3.5 Ga) micro-environments potentially comparable to Noachian Mars (Westall, 2005b). Well preserved sedimentary structures and sub-microscopic biosignatures (Westall and Walsh, 2006).	B.10

No one analogue site (or region) can claim to be ideal for all analogue research. Some sites listed in Table 3.1 have nationally-imposed access and sampling restrictions, and fieldwork is often logistically difficult, costly, or both. Access to such sites is therefore intermittent and available only to a select few.

Notwithstanding the importance of analogue sites and the need to deploy planetary instruments in the field at some point (usually late in the development programme), in reality, much can be achieved using well-contextualised field specimens in the lab (Figure 3.2AB). Samples collected during an expedition to an interesting locality at an analogue site can form the basis of a set of targets to be scrutinised in the lab by a representative payload of instruments. As mentioned

previously, detailed scientific measurements conducted at the planetary surface, by both humans and robots, involve relatively small targets similar in size to field specimens. One possible lab-based study, for example, may be to determine stratigraphy from a limited number of measurements on samples collected at known positions from a succession. This is entirely valid as long as measurements are suitably constrained and geological context is maintained (i.e., with the aid of outcrop images, remote sensing data and other information acquired in the field). Alternatively, samples collected from a variety of completely different analogue sites can be studied on the basis of a common theme such as extant and fossilised biosignatures or relict sedimentary structures. This latter case is well illustrated in Chapter 4 and Chapter 5.

From an engineering perspective, representative measurements of geological analogues can also be made using robots in the lab and “planetary yard” in preparation for analogue site operations (Figure 3.2CDE). Incorporating relevant science into the robotics programme early on inevitably provides a better understanding of the practicalities of robotic field geology. Scientifically, this may lead to more effective measurement strategies, and potentially greater science return.



Figure 3.2 Analogue field measurements performed in the lab with standalone instruments (A), tools (B), and robotic payloads (C). Mission-like complexity is further introduced during controlled trials in planetary yards (D), and ultimately, in the field (E). Courtesy NASA JPL (E).

At the time of writing, a number of databases are available in support of planetary surface analogue research, although these are usually specialised, covering dedicated topics ranging from Mössbauer spectroscopy (<http://www.mtholyoke.edu/courses/mdyar/marsmins/>), to rock/mineral

reflectance spectra (<http://speclib.jpl.nasa.gov/> and <http://pubs.usgs.gov/of/2003/ofr-03-395/ofr-03-395.html>), to human missions to Mars (Jarntimarra Database JNT-DB) (<http://www.marssociety.org.au/>). Importantly for this work, none of them are associated with a physical sample archive that can be used in coordinated *in situ* experiments involving a range of mission representative techniques. Physical collections of planetary analogue specimens do exist but these are held by research groups, university departments, museums and other institutes, and are often specific to the needs of the individual researchers. The NASA Johnson Space Centre Astromaterials Research and Exploration Science (ARES) Directorate (<http://ares.jsc.nasa.gov/>) is primarily concerned with extraterrestrial samples.

To the author's knowledge no centrally coordinated archive of planetary analogue samples exists with sufficient scope to serve the broad diversity of collective *in situ* measurement and observation required by scientists interested in planetary fieldwork. To date, only instrument-focused collaborations between hardware teams and institutes with collections (i.e., universities, museums etc.) have been undertaken as either extensions to calibration programmes, or as tests in support of active mission operations (i.e., MER).

As for the user community, there is no single group, or network, that encompasses all aspects of planetary field work in a coordinated way for the benefit of the wider community. Well-respected groups do exist but these are often heavily embedded into their own specific analogue sites, disciplines and research programmes. Examples include the Arctic Mars Analogue Svalbard Expedition (AMASE) (<http://amase.ciw.edu/>), the Centro de Astrobiologia (CAB) (<http://www.cab.inta.es>), and the Canadian Analogue Research Network (CARN) (<http://www.space.gc.ca/>).

To broaden the reach of analogue research and support future planetary missions more effectively than is currently the case, the following is urgently required:-

- An accessible archive of fully characterised planetary analogue samples (and field sites)
- An accessible database of experiments performed on samples from the physical archive
- A coordinated user network of specialists interested in all aspects of planetary fieldwork
- A programme of relevant lab-based and field-based studies

An integrated solution to address all these points is presented in the following section and

subsequent chapters of this thesis.

3.2 The GSPARC Specimen Archive and Experiment Database

The need for a centrally-coordinated archive of planetary analogue specimens to serve the operational requirements of the Beagle 2 scientific payload (Pullan *et al.*, 2003) was evaluated by the author in late 2001. Prior to delivery to the spacecraft, the flight instruments from the Beagle 2 PAW underwent formal calibration using simple materials (i.e., test targets, homogenised powders, slabs, etc.). The flight spare instruments were also calibrated (with some exceptions), and the tools benefited from tests using a variety of soil types and house bricks! No formal plans were made for the flight spare hardware to undergo more representative testing on a range of natural geological samples prior to actual operations on Mars. Some hardware teams took the initiative of testing their instruments on real rocks, but these were unilateral activities.

To address this issue, the author (then Instrument Manager and Science Operations Planning Manager for Beagle 2), proposed a six-month programme of coordinated laboratory experiments using the flight-spare instruments from the PAW, and appropriately selected planetary analogue field specimens. The programme was to be carried out during the mission cruise phase between June and December 2003, with the prime objective of providing the Beagle 2 science team with “hands-on” experience using the deployable suite of instruments and tools of the PAW prior to actual surface operations at Mars. For technical and programmatic reasons, however, the flight spare instruments (for standalone laboratory measurements) and the lander ground test model (for instrument placement and sampling scenarios) were only made available for a small fraction of this period.

An initial collection of geological specimens was accumulated in 2002 in readiness for the proposed laboratory programme. Samples of various colours, textures, fabrics, compositions, physical states and sizes were sourced from within the UK and overseas. Some specimens were analogous to Mars and some were generic. A cataloguing scheme was developed to describe each specimen and its relationship with others in the collection. Experiments were similarly indexed. These organising principles subsequently formed the basis of a sample repository and database called GSPARC which is introduced in the next section.

Following the failure of the Beagle 2 mission in December 2003, the flight-spare instruments and

tools were subsequently dedicated to a laboratory characterisation programme at the University of Leicester in support of future missions such as ExoMars (to be launched in 2016). Some of the results presented in Chapter 5 were obtained as part of this programme.

3.2.1 Organising Principles

A common approach to the organisation of the GSPARC physical archive and the experiment database was envisaged since both are inherently linked. Physical samples effectively serve the experiments performed on them, and consequently the instruments and techniques employed, so it was logical to assume that specimens should provide the kernel for a knowledge base of this kind. Furthermore, instruments evolve, and new versions would be expected to benefit from the same samples used in previous experiments. Specimens also provide a link to larger geological features such as exposures and formations, and the wider geological context in general. This is important for maintaining continuity with large scale activities such as orbital remote sensing, field mapping and local site surveys. At the other end of the scale, specimens act as reference material for analytical measurement and microscopic sampling. Physical specimens therefore provide a comprehensive means of linking a broad programme of related planetary analogue studies.

The GSPARC physical archive is divided into collections which in turn are populated with samples. Physical samples exist as either individuals or groups of individuals. All samples are assigned attributes which can be used to uniquely identify them, and associate with other samples and data. Within the database, identifiers define the structural components required for effective search and retrieval. External to the database, identifiers can be usefully employed in association with descriptive text, annotated images and diagrams, data folders and file names. Examples of each appear throughout this thesis.

Table 3.2 lists the basic sample identifiers used by GSPARC. A complete specification of the organising structure, identifiers and parameters is given in Appendix A. This provides all the essential information for two tables of data that serve the physical archive, *DATfamily* and *DATitem*. These tables form the backbone of the GSPARC database described in the next section.

Table 3.2 Some basic GSPARC sample identifiers ¹

Identifier	Meaning	Reference
<sample>	Basic identifier (made up of <family>, <format> and <item>)	A.1
<family>	A number unique to a group of samples (can occur many times)	A.1
<format>	The form the sample is in (i.e., hand specimen, rock slab, etc)	A.1
<item>	A number unique to the sample itself (can occur once only)	A.1
<target>	Area on the sample of interest (i.e. fresh surface)	A.3
<experiment>	Experiment performed on the sample	A.3
<descriptor>	What the sample is (i.e., basalt)	A.4
<site>	Coordinates and elevation of the sampled locality (if known)	A.4
<mineralogy>	Mineralogical classification (string of mineral codes)	A.4

¹ See Appendix A for complete list and associations

3.2.2 Database Design

The organising principles established for the GSPARC physical archive described in Section 3.2.1 provide a framework on which to design a database. The most logical design requires two elements: a database application, and an external, indexed directory structure containing coded folders and data files. The database application stores all the relevant parameters (Appendix A), and assigns the appropriate relationships between them. Key parameters within the database act as pointers to external data, which are coded in compliance with organising principles outlined in Section 3.2.1. This is important since many data products generated during experiments may use a customised format as a consequence of unique data acquisition software (i.e. Beagle 2 microscope). Data that can be incorporated within the database itself, such as reference elemental composition, are stored in specially designed tables (i.e., *DATanalysis_major* and *DATanalysis_trace*).

3.2.2.1 Standalone Version

The software products chosen in 2003 for the development of the standalone version of the GSPARC database were Microsoft Visual Basic 6 (VB6) and Microsoft Access 97 (later Access

2000). This decision was partly based on years of software experience already established by the author using these products, and partly on the migration potential of the Access database to the eventual web version. Access itself was considered inadequate for hosting both the database and the user interface, so was assigned to the database only. The Graphical User Interface (GUI) and the search engine routines were developed in VB6. Communication between the GUI and the database was established using Search and Query Language (SQL) (Date, 1997), administered in code.

An overview of the GSPARC database architecture is presented in Figure 3.3. Tables designed for data are assigned the prefix *DAT*, and tables containing reference information are assigned the prefix *LUT* (Look Up Table). The relationships between tables are shown in Figure 3.4. By way of example, the design forms for *DATfamily* and *DATitem* are shown in Figure 3.5.

The visual interface for the standalone version was developed as an SDI (Single Document Interface) application (Figure 3.6). The main window is based on the search form. At the top right of the form are text and combo controls to specify the main sample parameters such as <family>, <format>, <item>, <descriptor> etc. These controls are always visible. Additional search criteria are revealed, via a tab control, according to theme (i.e., composition). Results of searches are displayed as a list of samples satisfying the search (bottom left of form), and details, including an image, of the currently selected sample from this list (top left of form). Alternative images, data plots and maps, associated with the current sample are also displayable in the main image portion of the browse tab control (centre right of form). This facility can also be used to display other visual data selected from the directory list control (not shown). Double clicking on either image area of the form opens a separate, sizeable, window for more detailed viewing.

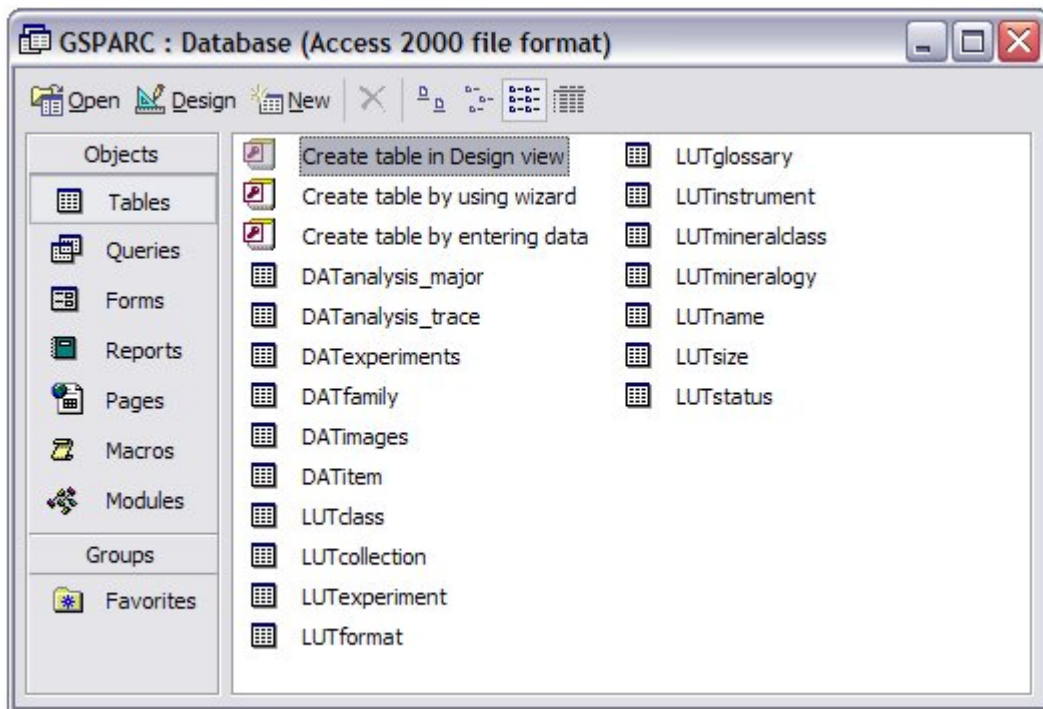


Figure 3.3 Access development environment for the GSPARC database showing the complete list of tables. Tables designed for data are prefixed DAT, and tables containing reference information are prefixed LUT (Look Up Table). Design forms for DATfamily and DATitem are shown in Figure 3.5.

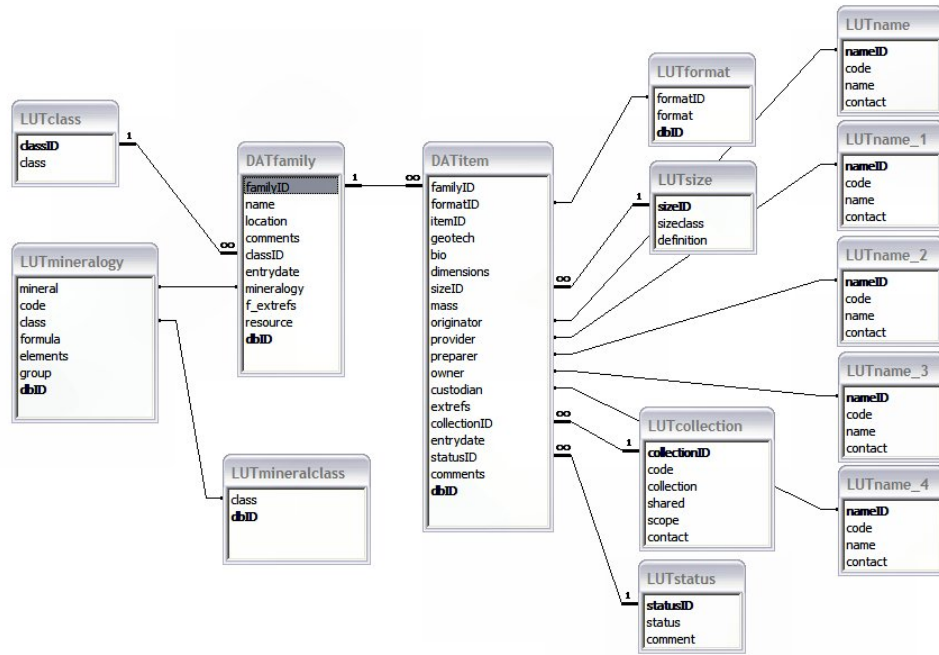


Figure 3.4 Relationships between key parameters in the GSPARC database. Note particularly the One-to-Many relationship between *DATfamily* and *DATitem* (see Appendix A).

DATfamily : Table

Field Name	Data Type	Description
familyID	Number	Unique specimen number (prefixes all derived samples) Must be first!!
name	Text	Sample name or descriptor
location	Text	Source location
comments	Text	General comments, references etc
classID	Number	Type of sample (rock, mineral, soil etc)
entrydate	Date/Time	Date entered into system (the software interprets the default date 01/01/00 as a wishlist sample)
mineralogy	Text	Parsable string of minerals
f_extrefs	Text	External references (non-parsable) - families only
resource	Text	Approximate residual quantity (volume and/or mass) available for formatting
dbID	AutoNumber	

Field Properties

General | Lookup

Field Size	Long Integer
Format	0000
Decimal Places	Auto
Input Mask	
Caption	
Default Value	0
Validation Rule	
Validation Text	
Required	Yes
Indexed	Yes (No Duplicates)

A field name can be up to 64 characters long, including spaces. Press F1 for help on field names.

DATitem : Table

Field Name	Data Type	Description
familyID	Number	Must be first!!!!
formatID	Text	Two character code for sample format (HS=hand specimen etc)
itemID	Number	Unique specimen number (used in association with sample number masID)
geotech	Yes/No	Y = Geotechnical (destructive); N = Analytical (non destructive)
bio	Yes/No	Y = Has biological features and/or significance
dimensions	Text	Dimensions in mm unless otherwise stated (diameter, thickness, XYZ if irregular)
sizeID	Number	Size class (i.e. MINATURE, CABINET etc)
mass	Text	Mass in grams unless otherwise stated
originator	Number	Who provided the original sample/specimen
provider	Number	Who provided it to collection
preparer	Number	Who prepared it
owner	Number	Who owns it
custodian	Number	Who is the custodian
extrefs	Text	Parsable string of external references (items only)
collectionID	Number	
entrydate	Date/Time	Date when entered into collection
statusID	Number	Status (see LUTstatus)
comments	Text	Relevant comments (blemishes, broken etc)
dbID	AutoNumber	

Field Properties

General | Lookup

Field Size	2
Format	
Input Mask	
Caption	
Default Value	"XX"
Validation Rule	
Validation Text	
Required	Yes
Allow Zero Length	No
Indexed	Yes (Duplicates OK)
Unicode Compression	No
IME Mode	No Control
IME Sentence Mode	None

A field name can be up to 64 characters long, including spaces. Press F1 for help on field names.

Figure 3.5 Example design forms for *DATfamily* and *DATitem*.

The details of the sample currently loaded in the viewing portion of the form are also used to parse folder names in the external part of the GSPARC database (i.e., the data directory). This can be used to list all experiments that are relevant to this sample. Alternatively, the default “filter” can be modified to narrow the search further, or completely changed to look for other samples, families, formats, instruments and so on.

Data stored in tables *DATanalysis_major* and *DATanalysis_trace* can be used to refine searches based on geochemistry (Figure 3.6). Specific elements and compounds can be selected from a periodic table together with an appropriate range of values in weight % oxide (for major elements) and parts per million (from trace elements). Similarly, mineralogical data stored in the parameter <mineralogy>, can be selected on the basis of mineral species listed in table *LUTmineralogy*.

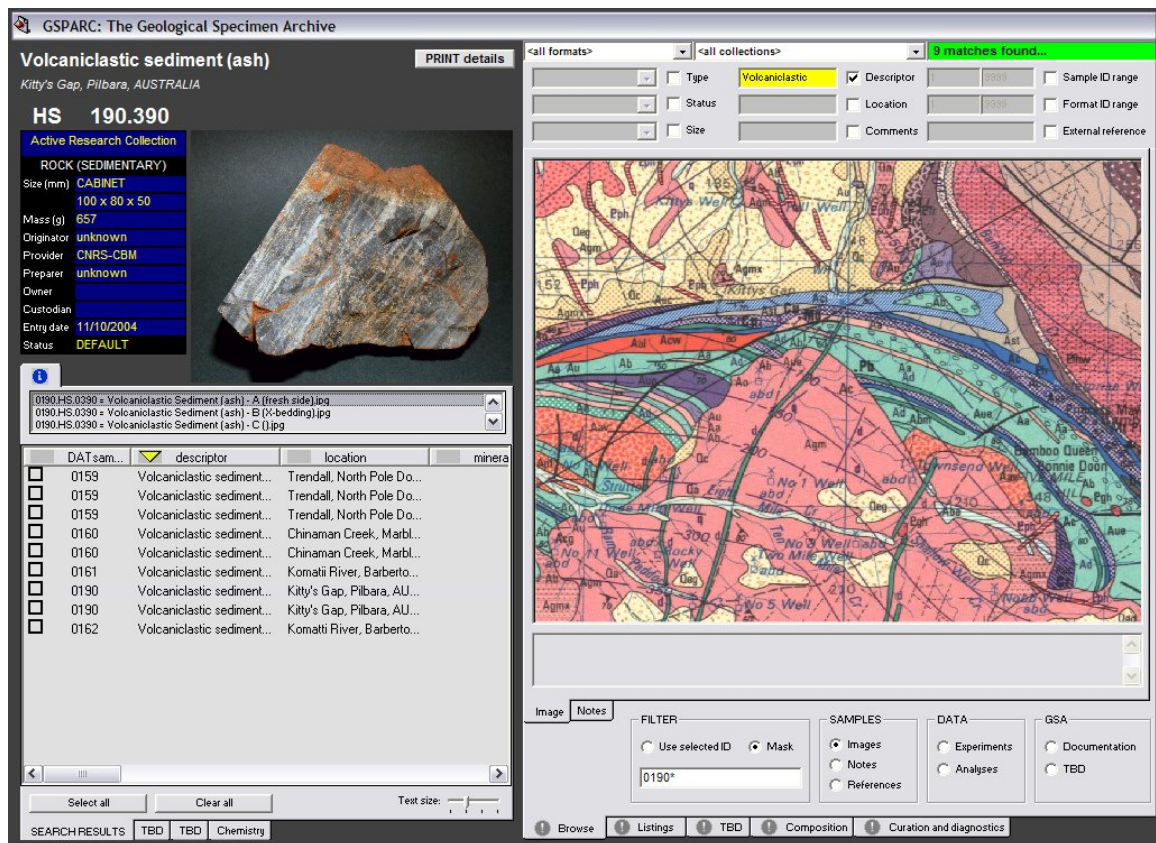


Figure 3.6 The standalone version of GSPARC showing the search controls (top centre and right) and details of the currently selected sample (top left and centre). Active search parameters are automatically highlighted in yellow. Map insert courtesy GSWA.

All search criteria selected via the GUI are interpreted by the software, and compiled into a valid SQL string prior to issuing the search. To help the user keep track of what is being searched for all active controls (i.e. those involved in the search) are highlighted. Once issued, the final SQL string is displayed in the diagnostics section of the tab control.

Finally, a log of all the samples selected and viewed since the application was executed is displayed at the bottom of the form (Figure 3.6). Selecting any record from this list reloads the sample details.

3.2.2.2 On-line Version

Although the standalone version demonstrates the usefulness and versatility of the GSPARC database, it is restricted to a single user. This is acceptable for managing the experiment database and physical archive, but the next step is to establish the application online for access by the planetary community. A web version is currently being developed in ASP.NET (Figure 3.7). This application utilises the database already designed and populated for use with the standalone version.

The concept of the on-line version of GSPARC, and the relationships between the data archive, physical archive, and user community, are shown in Figure 3.8. Three levels of data access are applied, two of which require password protection. Level 1 provides full search access to the database, and is only available to the planetary research community who are members of the Planetary Analogue Field Studies Network (PAFS-net) (see Section 3.2.3.2). Level 1 passwords are allocated on an annual basis to the current PAFS-net membership. Level 2 provides access to material derived from research data, and suitably compiled for the benefit of educators, schools and *bona fide* knowledge sites. In some cases, there may be an association between the education sector and the physical archive (i.e., SpaceROX, see Section 3.2.4.1). Level 2 passwords are also allocated annually. Level 3 provides open access to selected information of interest to the general public including local and national involvements in planetary analogue research and space missions.

- Home
- The Archive
- GSPARC guide
- PAFS-net
- SpaceROX
- External links

Sub sections:

Select a section.. ▾

Version 0.0 Only fundamental attributes are selectable at this time.

Physical Sample and Experimental Data Archive: Search Facility

FamilyID ItemID *fast track to a specific family or individual*

Description LIKE Location LIKE

Collection ▾

Sample Format ▾ Sample class ▾

Size class ▾

External references LIKE

Order results by ▾

All categories

Fossil

Impactite

Metal/Ore

Meteorite

Mineral

Mineral precipitate

Rock (IG Plutonic)

Rock (IG Volcanic)

Rock (Metamorphic)

Rock (Sedimentary)

Soil (Consolidated)

Soil (Loose)

Synthetic/simulant

Figure 3.7 Working prototype of the on-line GSPARC search page (<http://www.gsparc.com/search.asp>). The page is written in ASP.NET and functions in a similar way to the standalone version shown in Figure 3.6. Search criteria are defined via drop-down combo controls (i.e., Sample class Rock (IG volcanic)) and partial string controls (i.e., location LIKE hawaii). For the on-line version, the database (Access 2000) and SQL processing routines are located server-side.

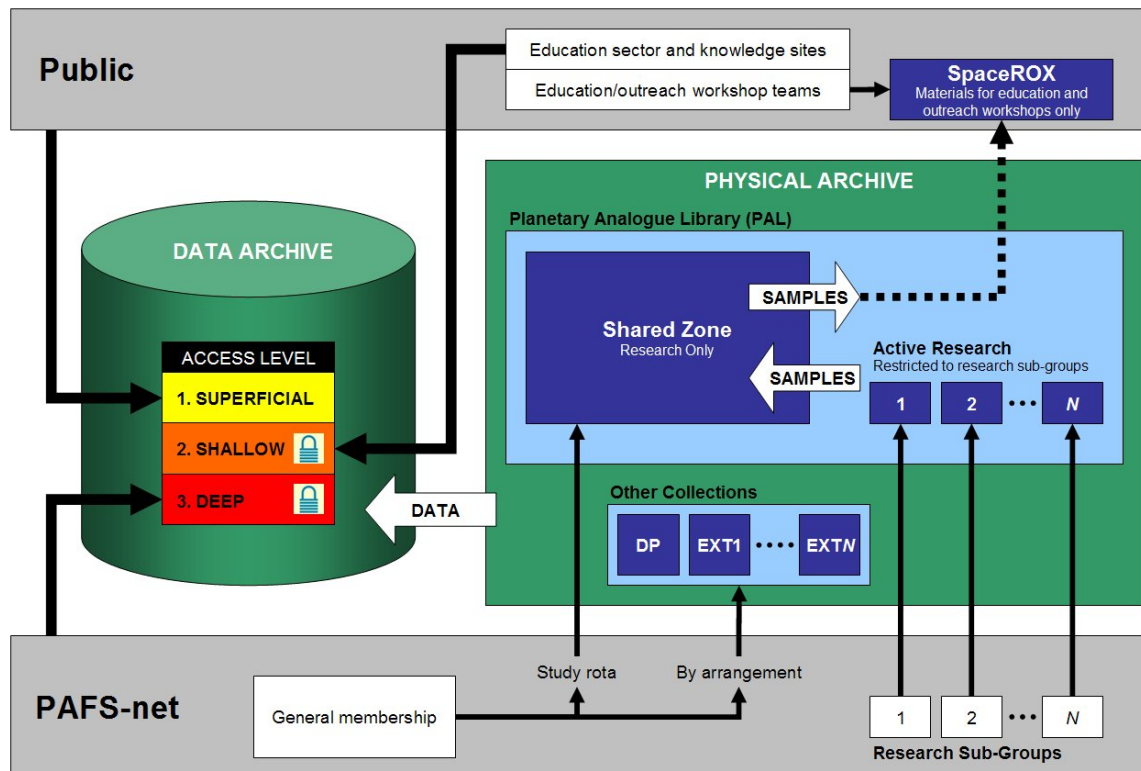


Figure 3.8 Flow diagram of the GSPARC concept showing the relationships between the physical archive, the experiment database and the user community. Full access to the data archive and selected samples is only available to members of the Planetary Analogue Field Studies Network (PAFS-net) described in Section 3.2.3.2. Other user categories have restricted data access and no access to research samples.

A few important points need to be stressed with regard to the on-line facility. Firstly, all experimental results made available for download are already in the public domain (i.e., via published papers, conference proceedings, reports etc.). Actual papers are cited only, and not made available digitally unless permission has been previously granted by the journal concerned. Secondly, educational materials for download have been approved by the appropriate authorities (education sector), and are compliant with national curricula. Thirdly, the server-side database is read-only and maintained off-line by the curator of the physical archive. Finally, certain research activities involving proprietary samples, or new technologies, may not become visible to other level 1 users until the work has been published. This is to ensure confidentiality within the research groups involved (Figure 3.8).

3.2.3 Research and Mission Support

Although spawned from the requirements of a specific mission, to a specific planet, i.e., Beagle 2 to Mars, the GSPARC physical archive and experiment database clearly have potential to serve all planetary surface missions where geological field work is to be undertaken, whether this involves humans, robots or both. GSPARC is sample-focused so mission-like experiments on suitably characterised planetary analogues, or generic standards, can be performed well in advance of missions, initially using close approximations of payload instruments (i.e., emulators), and eventually using the flight qualified space instruments themselves. This process not only maintains synergy between scientific “end users” and payload developers from initial design through to actual operations, it also can provide insight into what can, and cannot, be achieved by future missions.

3.2.3.1 Collaborations and Studies

In addition to the studies described in Chapter 5 and Chapter 6, GSPARC has contributed to a number of additional research activities since 2003. Table 3.3 summarises some of these.

Other collaborations and studies currently in the proposal stage are described in Chapter 7.

Table 3.3: GSPARC support in other research activities (since 2002)

Samples ¹	Activity ²
Total 3 samples (42, 52, 61) <i>(see Figure A.3)</i>	Elemental mapping using imaging X-Ray Fluorescence spectroscopy and Micro Channel Plate (MCP) optics. (Price <i>et al.</i> , 2004). Collaboration with MCP group at University of Leicester (UK).
Total 10 samples (1, 2, 24, 29, 54, 55, 56, 57, 58, 195)	Measurement of fluorescent radiation from planetary analogue rock samples using monochromatized synchrotron radiation in support of X-ray emission studies from planetary surfaces, especially Mercury (Owens <i>et al.</i> , 2008). Collaboration with ESA/ESTEC Sci-A (Netherlands).
Total 19 samples (156, 157, 158, 164, 165, 166, 167)	Bleached and unbleached quartz arenites, and hematite concretions including “Moqui Marbles”. Imaging and Mössbauer spectroscopy measurements. Work in progress. Collaboration with University of Utah (USA) and University of Mainz (Germany).
Total 54 samples (24, 41, 65, 81, 140, 144, 148, 149, 199, 200, 201, 202, 203, 204, 205, 206, 207, 208)	Prepare, analyse and characterise a collection of analogue specimens for planetary instrumentation support activities at ESA/ESTEC. Collaboration with ESA/ESTEC Sci-A (Netherlands) and University of Leicester Geology Department (UK).
Total 3 samples (81, 204, 207)	Soft X-ray multi-angular (surface roughness) experiments on Mercury analogues (Näränen <i>et al.</i> , 2008). Collaboration with BepiColombo Mercury Imaging X-ray Spectrometer (MIXS) team at University of Leicester (UK) and University of Helsinki (Finland).
Total ~10 samples <i>To be assigned</i>	Raman Spectroscopy in Astrobiology Field Workshop, NW Highlands of Scotland September 2006. Stromatolites (1.2 Ga), long-term alteration surfaces and hydrothermal activity. Field exposure characterisation and selective sampling. Principal collaboration with University of Aberdeen (UK) and University of Bradford (UK).
Total ~10 samples <i>To be assigned</i>	Coordinated site reconnaissance and sampling expedition to Krafla, Askja and Kverkfjöll, Iceland (2007). Sites specified by the author based on personal fieldwork carried out in 1988, 1989 and 1990. Collaboration with University College London (UK).
<i>Pending</i>	Prepare and characterise a collection of analogue minerals and rocks in support of Mars XRD instrument development. Collaboration with MarsXRD team at University of Leicester (UK).

¹ GSPARC <family> identifiers (see Appendix A)² Sci-A = Office for Science Payload and Advanced Concepts (ESA/ESTEC)

3.2.3.2 The Planetary Analogue Field Studies Network (PAFS-net)

The Planetary Analogue Field Studies Network (PAFS-net) (Pullan, 2006) is an international group of scientists and engineers with a common interest in the practical challenges of planetary exploration. The network was formally established by the author in 2004 and currently has a membership of over 40 specialists from 10 countries.

The need for such a network was realised by the author in the latter stages of the Beagle 2 project during preparations for surface operations (described in the introduction to Section 3.2). The limited experiments and sampling scenarios that were performed during late 2003 provided the science team, many of them terrestrial geologists, with valuable first-hand insight into the application of the payload, the difficulties of instrument placement and measurement, the interpretation of mission-like multi-thematic data sets, and, remote-robotic geological site investigation in general.

It was evident to the author and other members of the science team, that such last-minute and limited preparations were totally inadequate for a mission as complex and challenging as Beagle 2. The consensus was that future missions would be wise to consider an appropriately scoped and funded analogue study programme running from early payload development (to ensure engineering solutions were scientifically “fit for purpose”) through to planetary operations, thus ensuring “end users” (i.e. science teams) were well prepared for planetary fieldwork. One key aspect of the programme was the need for multi-disciplinary mission operations teams to share a mutual appreciation of both science and engineering. As a result of these experiences and concerns, the author approached a number of eminent colleagues from the planetary science and engineering communities, and established PAFS-net.

A range of disciplines is represented within PAFS-net including geology, microbiology, geophysics, rock/soil mechanics, instrumentation and robotics. The primary activity of the network is to undertake a programme of integrated thematic studies, relevant to the surface exploration of the planets, incorporating analogue materials and a range of *in situ* techniques. PAFS-net relies on the extensive library of well characterised, close and part analogue geological samples provided by the GSPARC physical archive (Section 3.2.1), accessible analogous field sites (Section 3.1.2), and an array of instruments from laboratory/field equipment to space hardware (Appendix C). Results from individual studies are subsequently stored in the GSPARC

database, which, together with the collective experience acquired by the PAFS-net membership, provides an invaluable resource for future planetary missions.

The range of *in situ* techniques used in PAFS-net studies is broad, and includes multi-scale imaging, spectroscopy and geotechnics (sample preparation and acquisition). Where possible, PAFS-net exploits space-qualified, or prototype, instruments with which to conduct experiments. In the absence of either, studies make use of available laboratory equipment (especially portable kit), and adopt an emulation strategy. Equipment assets are disseminated worldwide, usually at the home institutes of participating members. Study samples therefore migrate back and forth between labs and appropriate instruments are taken into the field during sampling and/or robotic trials. Crucially experiments are “multi-technique” and “sample-centred” (as would be the case at the planetary surface), and are conducted within the appropriate constraints of *in situ* operations.

Examples of PAFS-net studies are presented in Chapter 5 (*in situ* astrobiology, geotechnics and macroscopic imaging techniques) and Chapter 6 (autonomous science).

3.2.4 Education and Public Outreach

As described in Section 3.2.2.2, the on-line GSPARC database may be of use beyond the specialised planetary research community. In recent times, education and public outreach have become important components of international and national space agencies (<http://www.esa.int/>; <http://www.nasa.gov/>; <http://www.bnsc.gov.uk/>). These bodies excel at conveying the big picture and high profile missions, but do not provide a suitable interface between active planetary analogue research (often involving national expertise in space engineering, robotics and science), and the public (who may not be aware of any national involvement).

Educationally, planetary analogues can be classed as logical extensions to meteorite collections in that they can provide an invaluable “hands-on” link to images returned from the surface of planets. High-profile facilities such as UK National Space Centre in Leicester (<http://www.spacecentre.co.uk/>) provide an ideal stage for communicating research and mission involvement using planetary analogues to teachers, pupils and the interested public.

3.2.4.1 SpaceROX

During the course of this project the author was awarded a research council grant to establish a collection of planetary analogue materials (SpaceROX) suitable for supporting educational workshops and public events within the arena of the National Space Centre (NSC), Leicester. The specific remit was to:-

1. Specify, acquire and prepare the SpaceROX collection of specimens
2. Train NSC staff (Education and Communication Teams) in aspects of planetary geology
3. Provide scientific guidance for implementation of NSC workshops/presentations

Samples for the SpaceROX collection were selected on the basis of analogy, theme and suitability. In total 16 material types were prepared (Table 3.4), and allocated GSPARC identifiers (Appendix A) to link to sibling specimens in the research archive.

A number of criteria were considered during the sample selection process including:-

1. Usefulness to Key Stage core subjects (i.e. physics, biology, chemistry and technology)
2. Illustrating the differences and similarities between various planetary materials
3. Providing context for visual data returned from current missions (i.e. Mars rovers)
4. Unravelling the bigger picture from integrated scientific measurement
5. Highlighting UK analogue research activities to educators, students and the public
6. Illustrating the challenges of *in situ* exploration and stimulating problem-solving

The SpaceROX collection provides a framework in which to investigate interesting topics related to planetary exploration. How the collection is exploited by the NSC depends on what is currently topical (i.e., in the news), what events are being scheduled and the needs of the National Curriculum. Table 3.5 lists some of the suggested themes and questions that both the educational workshops and public gallery presentations could cover at different depths depending on the audience profile. Some of these themes have already been successfully incorporated into the communication and education programmes.

A key benefit of SpaceROX is the ability to enhance the basic learning process by associating real research (such as described in Chapter 5 and Chapter 6) being carried out on similar samples

from the same GSPARC <family>, especially within the UK planetary science community. Most of the samples in the SpaceROX collection benefit from experimental data supplied via PAFS-net (see Section 3.2.3.2).

Table 3.4 The SpaceROX sample collection

Description ¹	Characteristics	Source locality	Analogue
Anorthosite (208)	Felsic	Portsoy, Grampian, Scotland	Moon/Mercury?
Basalt (81)	Olivine-rich	Kilbourne Hole, NM, USA	Mars
Basalt (188)	Oxidised, vesicular	Kilauea, Hawai'i, USA	Mars
Basalt (221)	Fresh, black, pāhoehoe	Kilauea, Hawai'i, USA	Venus/Moon
Basalt (222)	Vesicular, grey	Unknown locality	Moon/Mars
Breccia (193)	Impact melt, polymict	Haughton Crater, Canada	Moon/Mercury/Mars
Flintag (189)	Geotechnical soil simulant	Industrial (pulverised flint)	Moon
Goethite (220)	Dust simulant	Denmark	Mars
Hematite (155)	Concretions (spherules)	Jura, Switzerland	Mars
Hematite (215)	Massive, weathered	Isola d'Elba, Italy	Mars
Jarosite (214)	Acid sulphate mineral	Barranco del Jaroso, Spain	Mars
Limestone (140)	Impact crater lake deposit	Ries Crater, Germany	Mars?
Palagonite (1)	Geochemical soil simulant	Pu'u Nene, Hawai'i, USA	Mars
Sandstone (146)	Microbial life (endoliths)	Brewer, MO, USA	Mars?
Stromatolite (50)	Stromatolite	Big Horn Mtns, WY, USA	Mars?
Sulphur (219)	Active volcanic crater lake	Poas volcano, Costa Rica	Io

¹ GSPARC <family> identifier (see Appendix A)

Table 3.5 Suggested topics to address in hands-on workshops

Theme	Question	SpaceROX samples ¹
Basic	Why are some basalts grey and others red?	188, 221, 222
Basic	Why are some basalts smooth and others rough and blocky?	81, 188, 221, 222
Basic	What can breccia tell us about the planet's interior?	193
Basic	What is the significance of hematite and jarosite?	155, 214, 215
Basic	What are the dark and light regions of the Moon?	208, 222
Basic	How old are planetary surfaces?	1, 208, 221, 222
Operations	What measurements can we do at the surface?	All
Operations	How do we decide which rock would be best to sample?	140, 146
Life	How can we identify life?	50, 140, 146
Life	What are the environmental limits for life?	50, 140, 146

¹ GSPARC <family> identifier (see Appendix A)

3.3 Summary

The importance of analogue studies in support of future planetary surface exploration has been discussed in this Chapter. A critical assessment of the current level of coordinated planetary analogue activities has led to the author establishing a unique analogue specimen archive and associated experiment database called GSPARC, and a user community with specific interests in the practicalities of planetary fieldwork called the Planetary Analogue Field Studies Network (PAFS-net).

The GSPARC physical archive of specimens was initiated in 2002 and many samples have already been used in several analogue studies including those specific to this work (Chapters 4 through 6). The organising principles used to specify the physical archive were subsequently employed to develop a relational database which incorporates the results of experiments performed on the samples with space instruments and emulators. The original database was designed as a standalone application but is currently being developed for the web.

PAFS-net was established in 2004 and currently has a membership of over 40 scientists and engineers from 10 countries. Specific disciplines, and experimental studies on GSPARC

specimens, range from microbiology to robotics. Results from the analogue study programme have been presented at a number of international conferences.

In addition to providing a coordinated service to the relevant sector of the planetary research community, GSPARC and PAFS-net have also established important outreach links with projects such as SpaceROX (hands-on science using analogues).

Chapter 4

Study Samples for *In Situ* Astrobiology

This Chapter introduces the study samples used in conjunction with the experimental studies presented in Chapter 5. The specimens were selected from GSPARC (Chapter 3) on the basis of astrobiological significance and appropriate scale of features observable in the context of robotic or human *in situ* field exploration on Mars. A full geological description of the samples is given in Appendix B.

Two related experimental studies were undertaken using these samples and a suite of *in situ* instruments representative of current and future payload technology (Appendix C). The first study focused on the ability of this payload to unambiguously identify morphological biosignatures (fossils, biologically mediated structures etc.). The second study focused on the ability of the payload to assess the biogenic potential of visible sedimentary structures in ancient rocks as palaeo-environmental indicators of conditions once favourable to life.

Additional samples were selected from GSPARC to support the biologically related studies. These included fluorescent minerals (for evaluation of imaging techniques), a range of generic rock types (for evaluation of sample preparation techniques) and a variety of coloured/varying relief samples (for evaluation of colour stereo imaging). All samples were sourced and fully characterised by the author. The latter involved a variety of laboratory techniques to establish and confirm whole rock geochemistry by wavelength dispersive X-ray fluorescence spectroscopy (WDXRF), mineralogy by X-ray powder diffractometry (XRD), and petrology (by thin section polarised microscopy).

4.1 Introduction

If life once existed on Mars, or indeed, if it still exists there, to what form it evolved and whether evidence (visual or otherwise) is preserved in the rock record remains unknown. What we might plausibly find in terms of morphological evidence can, at least initially, be guided by analogy to terrestrial systems (Friedmann *et al.*, 1988; Hofmann and Farmer, 2000; Cockell and Lee, 2002; Bishop *et al.*, 2004; Westall, 2005a) and what has been observed (or not as the case may be) so

far on Mars (Squyres and Knoll, 2005; Knoll *et al.*, 2005; Des Marais *et al.*, 2005)

The long term preservation of biosignatures, including those expressing macroscopic morphology, is an important consideration both in terms of where to look and what to look for. Rapid silicification of host rocks such as volcanoclastic deposits, carbonates, and sandstones provides an effective mechanism of preserving microfossils and relict sedimentary structures for billions of years (Toporski *et al.*, 2002; Westall *et al.*, 2006a, 2006b; Orberger *et al.*, 2006). Other materials such as Fe-Mg silicates, especially serpentinized olivines and pyroxenes (Oze and Sharma, 2005), volcanic glasses (Banerjee *et al.*, 2004) and possibly impact glasses (Lindgren, 2006) are also promising candidates.

Although the lithologies observed at Meridiani Planum exhibit cross-bedding and a sub-aqueous history (Squyres and Knoll, 2005) they are thought to offer little preservation potential for organics (Sumner, 2004). More suitable targets for *in situ* astrobiological investigations of organic biosignatures may be clay-rich deposits, cherts and carbonates. Phyllosilicates have been detected in several regions of Mars (Poulet *et al.*, 2005) and silica-rich deposits have been inferred from THEMIS data in Eos Chasma (Hamilton, 2006) and observed by Spirit in Gusev Crater (Sol 1187, NASA image PIA09491). Mg-bearing carbonates have recently been identified from orbit in Nili Fossae (Ehlmann *et al.*, 2008).

The post-depositional history of host rocks, such as diagenesis and metamorphism that may involve recrystallisation and deformation, will determine their long term preservation potential. This is particularly well demonstrated by deposits from the Early Archaean at selected sites on Earth where morphological traces of life have been obliterated in highly metamorphosed rocks, such as at Isua in Greenland, but are well preserved in the low grade metamorphosed sediments of the Pilbara in Australia (Allwood *et al.*, 2006) and Barberton in South Africa (Westall and Walsh, 2006).

A number of geological environments can be considered well suited for biosignature formation and preservation. Closed-system lacustrine basins provide favourable circumstances for aqueous deposition of fine-grained sediments (including volcanic ash) and evaporites. Lakes were probably common on Mars during the post-Noachian when valley networks outflowed into lowland regions (Clifford, 2001). However, the actual locations of such suitable palaeo-lacustrine shorelines remain controversial (Leverington and Ghent, 2004; Leverington, 2006). Impact

craters are known to provide potential for the development of unique ecosystems (Cockell and Lee, 2002). Subaerial, subaqueous and shallow subsurface spring systems (Farmer and Des Marais, 1999) together with deep chemolithic hydrothermal systems (Hofmann and Farmer, 2000) are also important.

Clearly, evidence needs to be accumulated using various methods in order to corroborate the involvement of biota in any potential candidate feature observed via imaging techniques (Boston *et al.*, 2001; Westall, 2005b). Multi-scale/multi-spectral imaging forms the basis for initial reconnaissance of candidate targets. In the case of hidden signatures (i.e. existing within the fabric of rocks), indirect evidence may be all that is at hand. Expending precious mission resources to split a rock open will be a challenging decision and may be based on subtle textural or spectral anomalies of external weathered surfaces, or both. Analytical instruments play a crucial role by measuring specific characteristics of the material under scrutiny. Such measurements establish context, minimise ambiguity, and provide direction for adopting best sampling strategies.

In addition to recognising signatures of extinct life, we must also be able to identify direct and indirect indicators of extant life. All surface and near-surface dwelling cyanobacteria respond to light and radiation by producing carotenoids (anti-oxidants), scytonemin (UV screening pigment) and chlorophyll-a (product of photosynthesis) (Wynn-Williams, 2002). Detection of these pigments (especially scytonemin which can only be formed by living organisms) *in situ* at a planetary surface, or in an uncontaminated laboratory sample, would be a primary indicator of life. Furthermore, naturally occurring fluorophores such as chlorophyll and phycobiliprotein in cyanobacteria and algae can be detected by fluorescent imaging (further discussed in Appendix C). Spatial association by other means (multi-spectral imaging) would help to corroborate such biosignatures. How rock-dwelling organisms alter the nature of their host environments is also of interest (Plate 2 in Edwards *et al.*, 2004) especially for identifying suitable targets for sampling.

The variety of potential scenarios described above, although not exhaustive, represents a sufficiently challenging yet relevant set of diverse variables with which to investigate the ability of *in situ* payloads to identify extant and extinct indicators of life under field-like conditions. Analogue samples related to these scenarios are described in the following sections.

4.2 Experimental Study 1: Morphological Biosignatures

Morphological biosignatures include *bona fide* fossils, extant microbial communities inhabiting the fabric of rocks, or microbially mediated sedimentary structures. Stromatolites for example, are generally considered to be microbially mediated sedimentary structures (Malcolm, 1978; Krumbein, 1983), but in the ancient rock record, the biogenic origin of some stromatolite-like structures is questioned (e.g. Lowe, 1980; Walter *et al.*, 1980; Hofmann *et al.*, 1999; Awramik and Grey, 2005), or disputed (Walter, 1983; Lowe, 1994; Grotzinger and Rothman, 1996; Grotzinger and Knoll, 1999).

Morphology alone however, does not always allow for the determination of biogenic origin (Cady *et al.*, 2003; Ruiz *et al.*, 2002; Westall, 2005b). Candidate features also require further *in situ* analysis to confirm their biogenicity. In the case of sample return missions, this would inevitably be extended to include exhaustive laboratory analysis back on Earth. Geological context is crucial in order to demonstrate the syngenicity and antiquity of biological remains, and geochemical evidence is important for biological processing (Rose *et al.*, 2006).

Conversely, the absence of organic matter in samples that express morphological features does not necessarily prohibit the identification of a biosignature if reasonable supporting evidence is available. For example, mineral-encrusted cyanobacterial filaments from Yellowstone hot springs demonstrate morphological characteristics that are clearly biogenic, yet the organic matter has been completely oxidised (Cady and Farmer, 1996). Similarly, indirect identifiers such as microbially mediated wrinkle structures (Parizot *et al.*, 2005) may also be relevant.

The specimens selected for this study exhibit morphological features related to extant or extinct biology. All were obtained from planetary (martian) analogue field sites on Earth, including modern high latitude extreme environments, and Tertiary (~10-39 Ma) crater lake or hydrothermal deposits. Samples broadly fall into two morphological categories: fossilised microbial filaments and endolithic microbial communities (Table 4.1).

Observable features range in size between sub-millimetre and a few centimetres. The preservation states on different surfaces of each specimen range from pristine (fresh) to degraded (weathered). All physical specimens are referred to by their simplified GSPARC database identifiers described in Appendix A.

Table 4.1: Samples for experimental study 1: Morphological Biosignatures

Samples	Origin and Characteristics	Section
Limestone (140) <i>Ries Crater, Germany</i>	Microbial filamentous morphology Macroscopic/microscopic morphological biosignatures Impact crater site Aqueous environment Formed on or just below solid surface	B.1
Opaline sinter (169) <i>Yellowstone Park, USA</i>	Microbial filamentous morphology Macroscopic/microscopic morphological biosignatures Hot spring environment Formed on or just below solid surface	B.2
Chalcedony (45) <i>Mojave Desert, USA</i>	Microbial filamentous morphology Macroscopic/microscopic morphological biosignatures Formed at depth (metres) below solid surface	B.3
Goethite (179) <i>Cerro de Pasco, Peru</i>	Microbial filamentous morphology Macroscopic/microscopic morphological biosignatures Oxidation zone of hydrothermal ore deposit Formed at depth (metres) below solid surface	B.4
Orthoquartzite (114) <i>Dry Valleys, Antarctica</i>	Recent or modern (currently active) extreme biohabitat Macroscopic/microscopic morphological biosignatures Cold-dry valley environment Formed on or just below solid surface	B.5
Marble (194) <i>Dry Valleys, Antarctica</i>	Recent or modern (currently active) extreme biohabitat Macroscopic/microscopic morphological biosignatures Cold-dry valley environment Formed on or just below solid surface	B.6
Selenite (44) <i>Haughton Crater, Canada</i>	Recent or modern (currently active) extreme biohabitat Macroscopic/microscopic morphological biosignatures Impact crater site Formed on or just below solid surface	B.7

Specimens that contain fossilised microbial filaments exhibit microscopic morphology (isolated individuals) or macroscopic morphology (communities/assemblages), or both. To provide chemo-mineralogical variation, three modes of preservation are represented: calcification (freshwater limestone), silicification (opaline sinter and chalcedony), and heavy metal precipitation (goethite).

Specimens that contained endolithic microbial colonies were obtained from the extreme environments of two high latitude sites on Earth: McMurdo dry valleys, Antarctica (Friedmann, 1982) and Haughton Crater, Devon Island, Canada (Cockell *et al.*, 2002a). Examples of both cryptoendoliths (microbes thriving within the intergranular fabric of rocks) and chasmoendoliths (microbes exploiting existing fractures and voids) were included. The specimens' host

mineralogies range from quartz (orthoquartzite) to dolomite (marble) to gypsum (var. selenite). Examples of endoliths in other rock types, including volcanics, are being sourced for future integrated studies (Cockell *et al.*, 2002a; Jorge Villar *et al.*, 2003; Jorge Villar *et al.*, 2006).

A complete description of all the samples used in this study is given in Appendix B.

4.3 Experimental Study 2: Ancient Sedimentary Structures

Cross-bedding and other ordered sedimentary structures may not have a direct biogenic origin but could indicate favourable palaeo-environmental conditions in which life could flourish. Importantly for *in situ* astrobiology, prokaryotic microfossils may be preserved within such rocks and revealed following sampling (Westall *et al.*, 2001; Westall *et al.*, 2006b).

The specimens selected for this study are from an early period in Solar System history (~3.5 Ga) when Earth and Mars were thought to have experienced similar localised conditions and therefore provided similar opportunities for the development of life (Westall *et al.*, 2005b). Only a few localities exist on Earth where rocks from this epoch (the Early Archaean) are suitably well preserved. These include the Barberton region of South Africa and the Pilbara of Western Australia (Table 4.2).

Although the selected samples are reported to contain the oldest known evidence of life on Earth (Allwood *et al.*, 2006; Westall and Southam, 2006; Westall and Walsh, 2006), direct observation of microfossils and related signatures is beyond the capability of the instrumentation suite used here (see Appendix C). The purpose of this study is to assess whether the morphological and contextual evidence at the proximal to microscopic scale is sufficiently strong in order to justify targeted sampling and laboratory-based *in situ* analysis.

As described for the morphological biosignature study, observable features range in size between sub-millimetre and a few centimetres. Similarly, all physical specimens are referred to by their simplified GSPARC database identifiers described in Appendix A.

Table 4.2: Samples for experimental study 2: Ancient Sedimentary Structures

Samples	Origin and Characteristics	Section
Chert (190) <i>Pilbara, Australia</i>	Relict sedimentary structures (laminated) Ancient (Early Archaean) environment Sub-microscopic morphological biosignatures ¹ Aqueous environment Formed on or just below solid surface	B.8
Chert (159) <i>Pilbara, Australia</i>	Relict sedimentary structures (stromatolite) Ancient (Early Archaean) environment Sub-microscopic morphological biosignatures ¹ Aqueous environment Formed on or just below solid surface	B.9
BIF (163) <i>Barberton, South Africa</i>	Relict sedimentary structures (banded) Ancient (Early Archaean) environment Sub-microscopic morphological biosignatures ¹ Aqueous environment Formed on or just below solid surface	B.10

¹ Not visible in the context of this study

The Early-Mid Archaean samples of ~3.45 Ga volcanoclastic sedimentary rocks from the Pilbara, Western Australia (Figure B.15), and a 3.2 Ga Banded Iron Formation (BIF) from the Barberton Greenstone Belt, South Africa (Figure B.20A), represent an era when the Earth and Mars possibly experienced similar conditions (Westall, 2005b and Section 2.2). These low grade metamorphosed rocks (prehnite-pumpellyite to lower greenschist), are highly silicified and exhibit well preserved sedimentary structures, such as laminations, cross-bedding, flaser-linsen bedding and load structures. They are reported to contain traces of microbial life and activity in the form of microfossils, stromatolites and chemical signatures (see review in Westall and Southam, 2006), although there is some debate concerning the biogenic interpretations of some of these signatures (*op. cit.*). Specimens were provided by Dr. Frances Westall (Centre de Biophysique Moléculaire, CNRS, Orléans, France).

A complete description of all the samples used in this study is given in Appendix B.

4.4 Samples for Related Experiments

As a precursor to, and in support of, the experiments described in Chapter 5, a number of techniques were evaluated and verified using additional specimens from GSPARC. Some samples were selected on the basis of their geotechnical properties and used to assess the

beneficial and detrimental effects of grinding, drilling and splitting rocks containing morphological features. Other samples, with fluorescence properties, were used to test the capability of the camera systems described in Appendix C for imaging under UV light. Finally, samples of different colour, surface lustre and relief were used to evaluate *in situ* colour stereo imaging with a single greyscale camera and appropriate illumination.

4.4.1 Geotechnics

The study samples described in this Chapter are typically hand specimen sized showing a variety of characteristics related to astrobiology. The quantity of material available is understandably limited since the samples originate from extreme remote locations, and were, and still are, expensive to obtain. The samples also exhibit unique features which need to be preserved for continued research. As such, only non-destructive measurements are allowed to be performed on the study samples.

However, sample preparation and acquisition activities such as grinding, drilling, coring and splitting play an important role in *in situ* exploration, and potentially provide a means of accessing otherwise hidden geological features, especially those displaying morphology. In order to place the work described in Chapter 5 into better context, a number of related geotechnical experiments were performed on a close “physical” analogue of one of the study sample materials plus a number of generic rock types ranging in physical properties.

An orthoquartzite from Brewer, Montana, USA (146) (Figure C.8) provided a close analogue for the samples of orthoquartzite (Beacon Sandstone) from Antarctica (114) (Figure B.11). Sufficient quantity of the Montana orthoquartzite was supplied to GSPARC in 2003 via Prof. Ray Arvidson of Washington University in St Louis, USA, as part of a collaboration established by the author between Beagle 2 and the Mars Exploration Rover Rock Abrasion Tool (RAT) team. Coincidentally, some of the Montana specimens contained cryptoendoliths, and thus provided an ideal example for use in this work of an astrobiological target that could be tested with planetary tools such as the Beagle 2 rock corer and sampling mole (PLUTO).

Additional materials used to support the geotechnical experiments included samples from a variety of locations in Missouri, USA: a friable shale from Leadwood/Gumbo (143), a massive limestone from St Louis (144), and a felsic conglomerate from north of Knob Lick (145).

4.4.2 Fluorescence Imaging

Some terrestrial geological materials exhibit fluorescence, either as a consequence of mineralogy (mineral fluorescence) or biology (bio-fluorescence) or both. It is feasible therefore that such a property may also be applicable to planetary materials. Certainly, planetary payloads should be capable of detecting fluorescence, especially as part of any close-up imaging survey, if only to corroborate the mineralogical data.

A number of common rock-forming minerals including calcite (CaCO_3) and gypsum ($\text{CaSO}_4 \cdot 2\text{H}_2\text{O}$) fluoresce when subjected to UV light. Similarly, some biological compounds contained in rock-dwelling cyanobacteria fluoresce when illuminated under a variety of wavelengths including UV. It is important, therefore, to exploit any potential fluorescent properties of geological targets, especially in the context of *in situ* astrobiology (Mormile and Storrie-Lombardi, 2005). The microscope for Beagle 2 (see Section C.2.2) was the first planetary camera to be equipped with UV LEDs for such a purpose. This work extends this capability to close-up imaging (macroscopy).

Fluorite (185HS379) from Nenthead, Yorkshire, UK, and amber (178HS369) from Plasselbschlund, Fribourg, Switzerland were used as examples of mineral fluorescence. Both were chosen for their intense visible fluorescence under UV light, in order to establish a suitable benchmark for the camera systems (Figure C.2).

4.4.3 Colour Stereo Macroscopic Imaging

Relatively small working distances required for *in situ* macroscopic imaging (a few centimetres) inevitably introduce illumination problems caused by self shadowing. In photography, the solution is to use a ring flash, or ring light, situated around the front of the lens. The Beagle 2 microscope, which required even smaller standoff distances for *in situ* microscopy (~1 cm), adopted such a solution using coloured LEDs. The Beagle 2 camera (see Section C.2.1), however, when used for macroscopic imaging, did not. The so-called “torches” on the Beagle 2 PAW consisted of a pair of 3 clustered super bright LEDs positioned near the aperture of each camera (Pullan *et al.*, 2003). The purpose was to partially illuminate the shadowed recess of the inlet of the Gas Analysis Package (GAP) for close-up imaging of samples prior to committing them for analysis. The torches were not designed for, or suitable for, *in situ* macroscopy.

All forms of close-up imaging would benefit from self-illumination, not only to avoid shadowing problems, but also to provide a controlled way of obtaining true colour images, since ambient lighting conditions at the planetary surface vary, and natural “daylight” is often difficult to characterise. The close-up cameras for both Beagle 2 and MER use monochromatic CCDs so colour information is not direct. Other benefits include controlled illumination geometry in order to either highlight sample relief or compensate for it. Macroscopic imaging can also benefit from small lateral displacements of the camera with respect to the sample (or *vice versa*) thus achieving the potential for stereo imaging. These criteria are particularly important for geological specimens or exposures containing morphological features such as stromatolites, microbial filaments or sedimentary structures.

A number of samples were selected from GSPARC on the basis of colour, surface relief (for stereo), and lustre (for reflectivity). These specimens, together with standard photographic calibration targets, were used to evaluate colour stereo macroscopic imaging using a modified version of the Beagle 2 camera (see Section C.2.1). Most of the specimens have already been described previously in this Chapter. The additional samples included a pisolithic iron ore (168HS349) from Feuerthalen, Switzerland, and a bleached (157HS316) and unbleached (158HS320) quartz arenite (Jurassic Navajo Sandstone) from Spencer Flat, Grand Staircase National Monument, Utah, USA.

4.5 Summary

The samples described in this Chapter are planetary analogues of relevance to Mars and the search for extant and extinct life. Although not exhaustive, they provide a means to support two relevant experimental studies related to *in situ* astrobiology: the identification of morphological biosignatures and the interpretation of relict sedimentary structures.

The study specimens originated from martian analogue field sites on Earth, including modern high latitude extreme environments, Tertiary (~10-39 Ma) crater lake or hydrothermal deposits, and well preserved Early Archaean (~3.45 Ga) deposits. Samples broadly fall into three morphological categories: fossilised microbial filaments, endolithic microbial communities and ancient sedimentary structures. Additional samples were selected from GSPARC and used to support other experiments related to both studies. These included geotechnical analogues to

evaluate the advantages and disadvantages of robotic sampling, fluorescent minerals to evaluate UV imaging techniques and generic specimens to evaluate 3D macroscopic imaging.

Such a collection of specimens presents an interesting array of different, yet relevant, challenges for the *in situ* instrumentation and methods used in both studies (Chapter 5). Moreover, these examples provide an opportunity to evaluate scientific strategies for justifying subsequent sampling (Chapter 5 and Chapter 6).

Chapter 5

Payload Experiments: Astrobiology Studies

“Nothing would be more tragic in the exploration of Mars than to encounter alien life or a biosignature and not recognise it”

Prof. Steven Benner, Department of Chemistry, University of Florida

New York Times, 7th July 2007

This Chapter presents the results of field-like experiments performed on the study samples introduced in Chapter 4 and described in Appendix B, using a representative payload of *in situ* techniques described in Appendix C. Two astrobiology-related studies were undertaken based on the ability of the payload to a) unambiguously identify morphological biosignatures such as fossils and biologically mediated structures, and b) assess the biogenic potential of visible sedimentary structures in ancient rocks. The experimental details for each technique are explained in Appendix C.

5.1 Introduction

The interpretations presented in this Chapter are based on experimental *in situ* data, and, therefore, do not represent a complete characterisation of each sample. The geobiological significance of each sample was therefore evaluated based on the *in situ* data available.

All proximal images are naturally of low resolution due to a combination of the small size of the samples and the spatial capabilities of the Beagle 2 SCS in proximal mode ($\sim 0.6 \text{ mm pix}^{-1}$ at 1 m). This, however, was not an issue for macroscopic and microscopic imaging where, in fact, specifications are very much state of the art ($60 \mu\text{m pix}^{-1}$ and $4 \mu\text{m pix}^{-1}$ respectively).

Where necessary, reference data were used to support or question the analytical results. Nevertheless, caution was duly applied when making comparisons between analytical data from bulk powders and analytical data from unprepared specimens belonging to the same <family>. All XRF data presented in this Chapter are semi-quantitative with errors in concentrations determined by counting statistics or the use of the Horwitz function (see Section C.3.1.1). Errors

are not stated in the text but are included in the data tables for each sample.

To emulate planetary surface operations, the measurement sequence adopted for all samples is proximal imaging, macroscopic imaging, microscopic imaging, XRF, Raman, Mössbauer, and XRD (post sampling).

5.2 Morphological Biosignatures: Microbial filaments

Samples that exhibit filamentous fabric (<family> = 140, 169, 45 and 179) generally presented high relief at macroscopic and microscopic scales. The open fabric exhibited by all these samples proved advantageous for 3D imaging with the use of stereo techniques (B2SCS\$CUL) and incremental focusing (B2MIC\$). Multi-spectral imaging was particularly useful, especially where mineralogical spectral signatures coincided with morphology (i.e. 140HS332). These signatures were also corroborated by selective *in situ* analysis by Raman and XRD.

5.2.1 Freshwater limestone, Hainsfarth, Ries Crater, Germany (140)

Section B.1 describes the geology of Ries Crater and the samples used for this study. Table 5.1 summarises the *in situ* imaging and analytical results for samples 140HS332, 140HS333, 140HS420, 140HS573 and 140HS584. Semi-quantitative geochemistry data are shown in Table 5.2.

5.2.1.1 Physical Properties

Observations of 140HS332 and 140HS420 at the proximal scale revealed a heterogeneous texture that consisted of a framework that showed preferred lineation, which, in some areas, appeared to be coated by a smooth surface film (Figure 5.1A). Imaging at this scale also differentiated external surfaces (sintered) from internal surfaces (lineated) on the basis of texture, overall reflectance, and coloration (due to iron staining).

Table 5.1: Summary of *in situ* results for Freshwater Limestone, Ries Crater, Germany (140)

<i>In Situ</i> Techniques ¹	Results	Reference
Proximal Imaging (B2SCS\$GEOL\$SOL)	Sintered and aligned textures	Section 5.2.1.1 Figure 5.1A
Macroscopic Imaging (B2SCS\$CUL\$RGB) (B2SCS\$CUL\$UV) (NUVIS\$MAC10\$SOL)	Evidence of open fabric Evidence of tubular morphology Mineralogical association with morphology Spectral signature of tubes and veneers	Section 5.2.1.1 Figure 5.1B Figure 5.1C Figure 5.1D
Microscopic Imaging (B2MIC\$\$RGB) (B2MIC\$\$UV)	3D morphology of tubes No mineral or organic fluorescence detected	Section 5.2.1.1 Figure 5.2
X-Ray Fluorescence (TN9K\$\$FCA) (AXIOS\$\$HS) (PW1K4\$)	Mg-carbonate with Sr enrichment Ca, Mg, Fe, Sr <i>Note: Fe associated with coatings on tubes</i>	Section 5.2.1.2 Table 5.2
Raman Spectroscopy (UBRAM\$\$514) (UBRAM\$\$785) (UBRAM\$\$1064)	Calcite (<i>fresh tubes, white masses</i>) Dolomite (<i>matrix, outer zones of fresh tubes, tube interiors</i>) Gypsum (<i>isolated spots within general fabric</i>) Unknown organic compound (<i>isolated black spots in matrix</i>)	Section 5.2.1.2 Figure 5.3
Mössbauer Spectroscopy (B2MBS\$)	Octahedral Fe ³⁺ (<i>tubes</i>) Octahedral Fe ³⁺ (<i>external sintered surface</i>) <i>Note: Effect more pronounced on fresh surfaces where tubes are presented in cross section.</i>	Section 5.2.1.2 Figure 5.4
X-Ray Diffraction (NHMXRD\$) (PW1010\$)	Calcite with dolomite (<i>fresh tubes</i>) Dolomite with minor calcite (<i>matrix/veneers</i>) Gypsum (<i>possibly as isolated crystals?</i>)	Section 5.2.1.2 Figure 5.5

¹ See Table C.1 for explanation of instrument mnemonics

Macroscopic imaging of the fibrous fabric revealed a delicately aligned, open texture, which consisted of intertwining rod- or tube-like constructs that were partially matted in appearance (Figure 5.1B).

Multi-spectral imaging also distinguished a spectral difference between these tubes and other surfaces (Figure 5.1D). Cross-sectional views suggested that they were indeed hollow tubes, and this was confirmed by the microscope images in which the rock fabric was viewed in both longitudinal (Figure 5.2A) and cross section (Figure 5.2C). Inner tube diameters are commonly ~40 µm. The tubes were defined by encrustations of a mineral with a regular thickness of about 40 µm. Specular reflections from fresh uncoated tubes suggest the presence of well-developed

crystals $<10\ \mu\text{m}$ in size. Precipitates of another mineral with a lower albedo and different reflectance occur around the high albedo-mineral encrusted tubes (Figure 5.2BD).

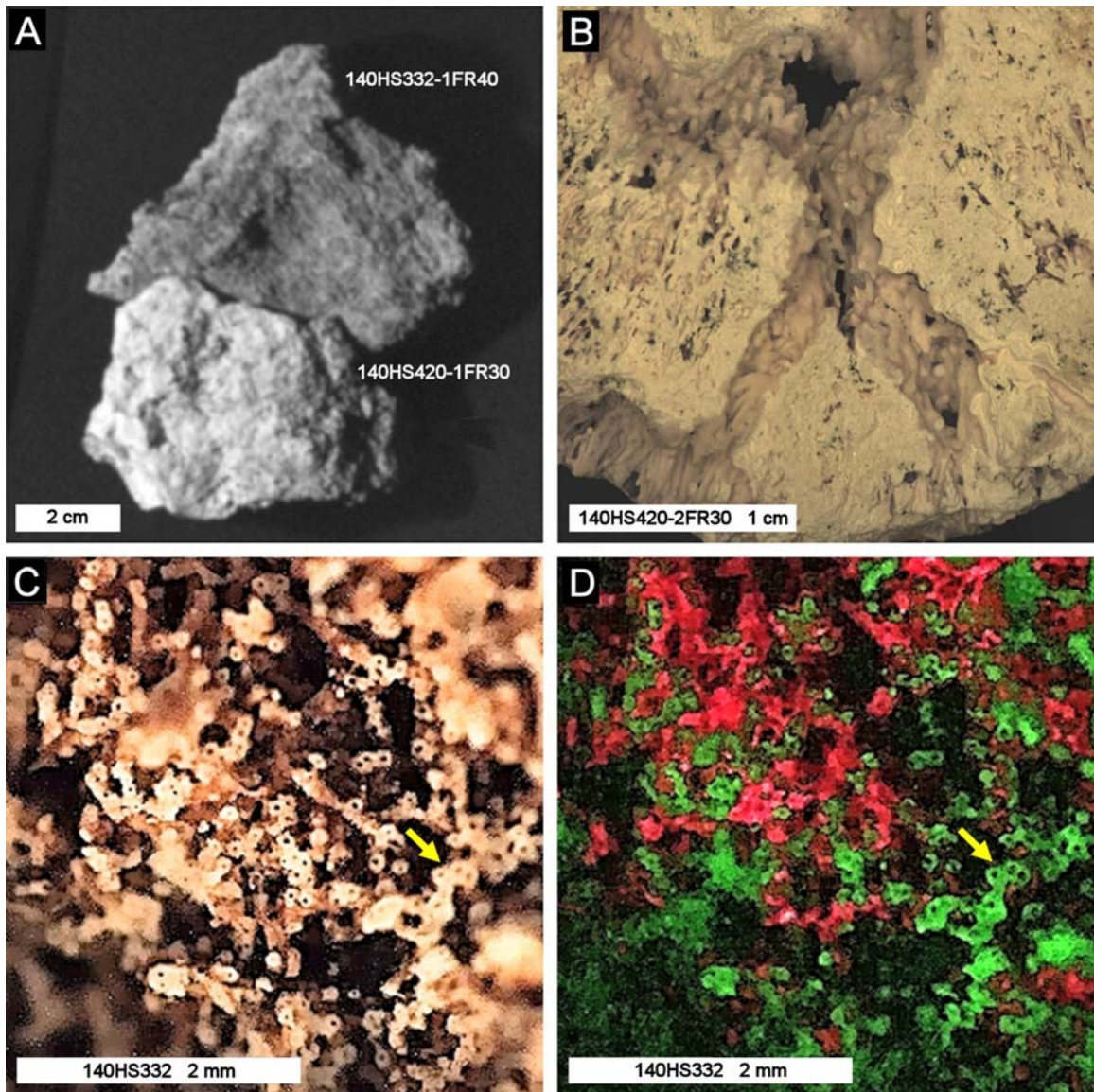


Figure 5.1 Proximal and macroscopic imaging of samples 140HS332 and 140HS420, (freshwater limestone). Images acquired at 60 cm reveal two surface textures, one light and smooth, and one dark and lineated (A). Colour images acquired at 8 cm show the texture to be associated with aligned tube-like features (B). Multi-spectral images (C and D) suggest that the tubes (arrows) are spectrally different to surface veneers. Instrumentation: B2SCS\$530\$SOL (A), B2SCS\$CUL\$RGB (B), and NUVIS\$MAC10\$SOL (C and D).

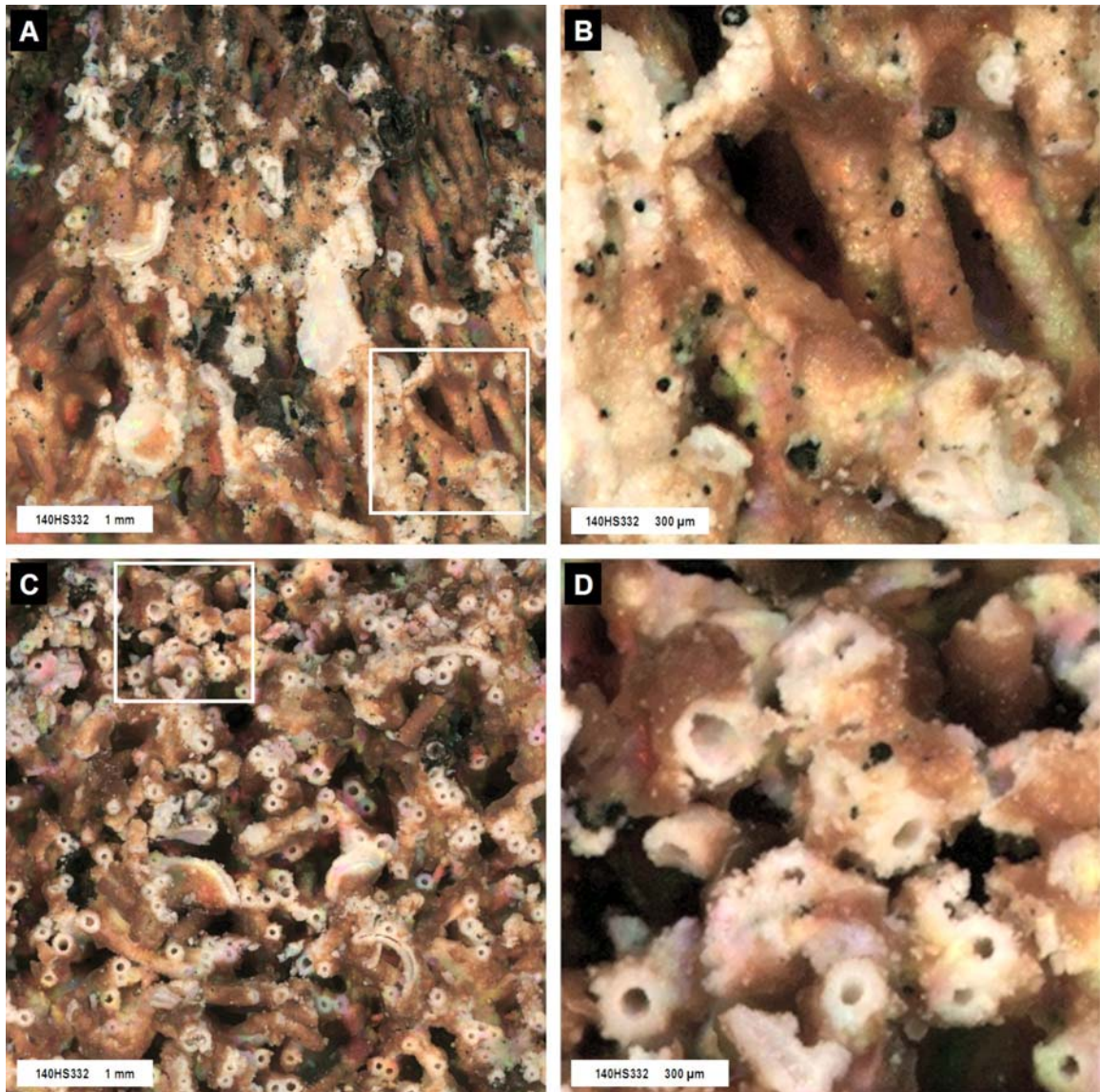


Figure 5.2 Microscopic imaging of sample 140HS332 (freshwater limestone). Individual tubes with consistent morphology and hollow cores are clearly visible in both longitudinal section (A) and cross section (C). Note the encrusted texture of the exterior of the tubes and isolated black spots (B) associated with an organic compound (see Section 5.2.1.2). The tubes were formed around threadlike cyanobacteria by calcification and later dolomitisation (D). See Section B.1 for more details. Instrumentation: B2MIC\$\$RGB.

Although these specimens exhibit an open fabric, sawing and grinding experiments on a specimen assigned for geotechnics (140HS493-1SA30) produced flat intact surfaces with tubes preserved within residual voids. These results suggest a relatively hard, intact material.

5.2.1.2 Chemistry and Mineralogy

In situ WDXRF analysis of 140HS573-1FR20 (tubes) and 140HS584-1FR25 (sinter) confirmed both surface types to be composed of Ca (31 and 36 wt % CaO respectively) and Mg (8 and 5 wt % MgO respectively). Surfaces predominantly made up of tubes were more oxidised (5 wt % Fe₂O₃) than sintered surfaces (2 wt % Fe₂O₃) and thus consistent with the visual evidence. Trace element concentrations in both these samples were higher than those recorded from 140PP431, in particular Sr which was close to 1.2% (tubes) compared with 2327 ppm (bulk). As mentioned in Section B.1, the bulk value falls within the range reported by Pache *et al.*, 2001 (2140 to 2940 ppm) and is thus comparable.

In situ EDXRF analysis of 140HS332-1FR40 (tubes) produced lower concentrations for Ca (25 wt % CaO) and Fe (2 wt % Fe₂O₃) whereas analysis of 140HS420-1FR30 (sinter) produced similar concentrations for Ca (37 wt % CaO) and lower Fe (0.6 wt % Fe₂O₃). Levels of Sr ranged from 1720 ppm (tubes) to 2236 (sinter).

In situ Raman spectroscopy was able to distinguish the fine-scale distribution of calcite (1086, 712, 281 and 156 cm⁻¹) within tube cores, and dolomite (1098, 725, 300 and 178 cm⁻¹) within the outer portions of the mineralised filaments (Figure 5.3A). Gypsum (1008, 669, 618, 492 and 413 cm⁻¹) was observed in one tube as isolated occurrences within the matrix (Figure 5.3B and Figure 11 in Pullan *et al.*, 2008), but did not appear in any other tubes examined. Some tubes were completely enveloped by dolomite and calcite was absent. Opaque black spots observed with the Beagle 2 microscope (Figure 5.2) were confirmed to be organic carbon but the spectral signature was broad, typical of degraded chemical species, so the compound could not be identified. However, the characteristic signatures of a carotenoid (near 1520 and 1155 cm⁻¹) were present (see Figure 7 in Edwards *et al.*, 2007). Importantly, there were no organic compounds associated with the tubes themselves, either as integrated remnants or as residues on the inner walls.

In situ Mössbauer data confirmed that the iron content of veneered surfaces was less than that observed on fresh surfaces, i.e., tubes in cross section (Figure 5.4). This coincided with the visual and *in situ* XRF data (Δ Fe ~3%).

Table 5.2 Semi-quantitative geochemical analysis of Ries Crater limestone (140)

<i>Instrument</i>	AXIOS\$	TN9K\$	AXIOS\$	TN9K\$	PW1K4\$
<i>Sample</i>	140HS573	140HS332	140HS584	140HS420	140PP431
<i>Target</i>	1FR20	1FR40	1FR25	1FR30	
	(tubes)	(tubes)	(sinter)	(sinter)	(bulk)
<u>Major elements</u>					
Na ₂ O	0.06 *	ND	0.1 *	ND	0.01 *
MgO	7.94 ± 0.97	ND	5.54 ± 1.15	ND	18.05 ± 0.18
Al ₂ O ₃	5.22 ± 0.78	ND	0.71 *	ND	0.09 ± 0.01
SiO ₂	12.84 ± 0.57	ND	1.56 ± 1.52	ND	0.64 ± 0.01
P ₂ O ₅	0.05 *	ND	0.02 *	ND	0.02 ± 0.01
SO ₃	0.52 *	ND	2.4 ± 0.84	ND	0.58 ± 0.01
Cl	0.04 *	ND	0.03 *	ND	0.06 ± 0.01
K ₂ O	0.33 *	0.5 ± 0.06	0.07 *		0.06 ± 0.01
CaO	31.24 ± 0.34	25.36 ± 1.86	36.18 ± 0.31	36.88 ± 2.58	32.33 ± 0.32
TiO ₂	0.39 *	0.12 ± 0.03	0.07 *		
V ₂ O ₅					
MnO	0.13 *	0.14 ± 0.03	0.17 *	0.12 ± 0.03	0.06 ± 0.01
Fe ₂ O ₃	4.86 ± 1.0	1.94 ± 0.21	2.06 ± 1.67	0.56 ± 0.06	0.15 ± 0.01
<u>Trace elements</u>					
Ni		194 ± 42		102 ± 24	
Cu					
Zn	110 *	74 ± 18	100 *	232 ± 48	5 ± 1
Ga					
As	350 *	72 ± 18	300 *	88 ± 21	15 ± 2
Rb	140 *	28 ± 9			3 ± 1
Sr	11770 ± 6508	1720 ± 270	8793 ± 7257	2236 ± 336	2327 ± 23
Y					
Zr					
Mo					
Ba	1380 *	156 ± 36		126 ± 30	107 ± 1
Pb					

¹ Concentrations normalised to 50% (carbonate)

² Major elements expressed in weight % oxide and trace elements in ppm

³ Errors (3σ SD) determined by counting statistics (AXIOS\$) or the Horwitz function (TN9K\$)

⁴ Bulk analysis precisions (PW1K4\$) ~1 % (> 10 ppm) and ~10-20% (< 10 ppm)

⁵ ND = Not Determined

⁶ See Table C.1 for explanation of instrument mnemonics

* Errors exceed concentration value (*in situ* analysis) or near LLD (bulk analysis)

In situ XRD was used to selectively analyse areas of a small thumbnail fragment derived from 140HS332 containing surfaces made up of tubes, veneers and a mixture of both (Figure 5.5). Dolomite was identified on each surface type. Calcite was only identified on surfaces containing tubes, and quartz was only identified on surfaces containing veneers. The conspicuous peak on the diffractogram associated with tubes, with a calculated d-spacing of 2.081 Å, is tentatively identified as gypsum (2.087 Å) rather than goethite (2.089 Å) or hematite (2.078 Å). This interpretation is based on a) the narrowness of the peak, b) the lack of any other Fe-oxide peaks from what are clearly oxidised surfaces, and c) highly specular, well-formed crystals observed within the beam footprint (Figure 5.5B). Bulk XRD analysis was also performed on homogenised powder and showed peaks for dolomite, calcite and quartz. No gypsum was identified.

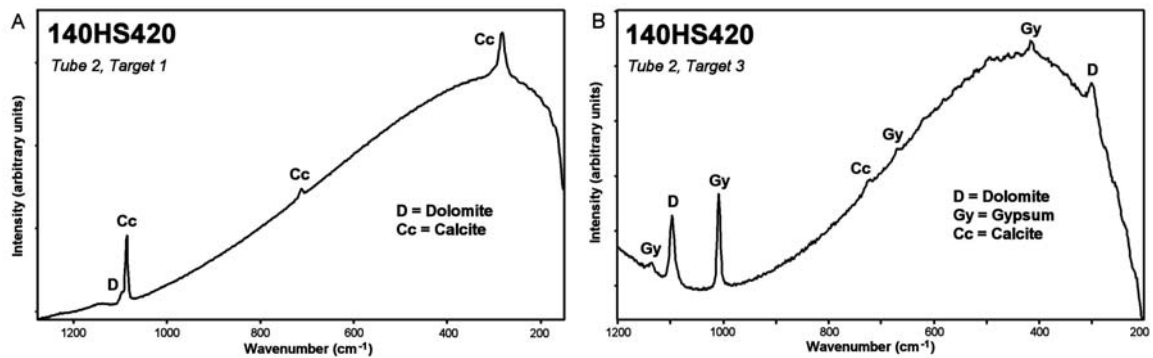


Figure 5.3 *In situ* Raman analysis of sample 140HS420 (freshwater limestone). Spectra were acquired from a single mineralised tube observed in cross-section using 785 nm laser excitation. The central portion of the tube (A) is mostly composed of calcite whereas the outer portion (B) is predominantly dolomite and gypsum. These results were not replicated for all tubes analysed (see text). For target locations see Figure 11 in Pullan *et al.*, 2008. Instrumentation: UBRAM\$785. Courtesy Prof. Howell Edwards, University of Bradford.

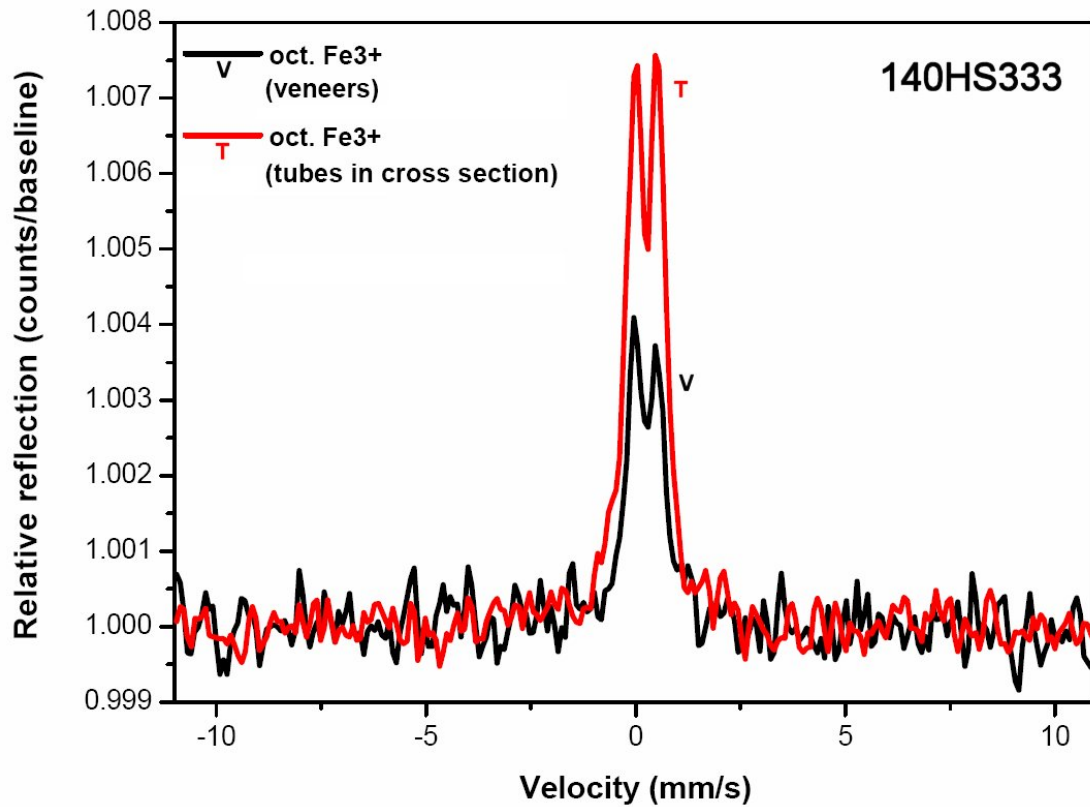


Figure 5.4 *In situ* Mössbauer analysis of sample 140HS333 (freshwater limestone). Surfaces made up of tubes show a higher (twofold) effect than surfaces comprised of veneers. This corresponds to the visual evidence (Figure 5.7B) and geochemical data. Instrumentation: B2MBS\$. Courtesy Dr. Christian Schröder, NASA JSC.

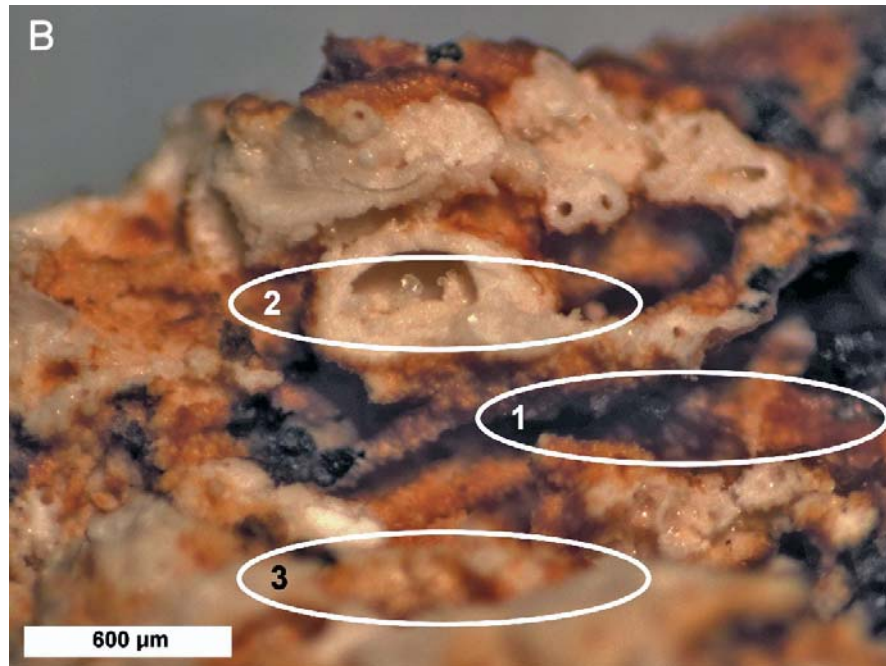
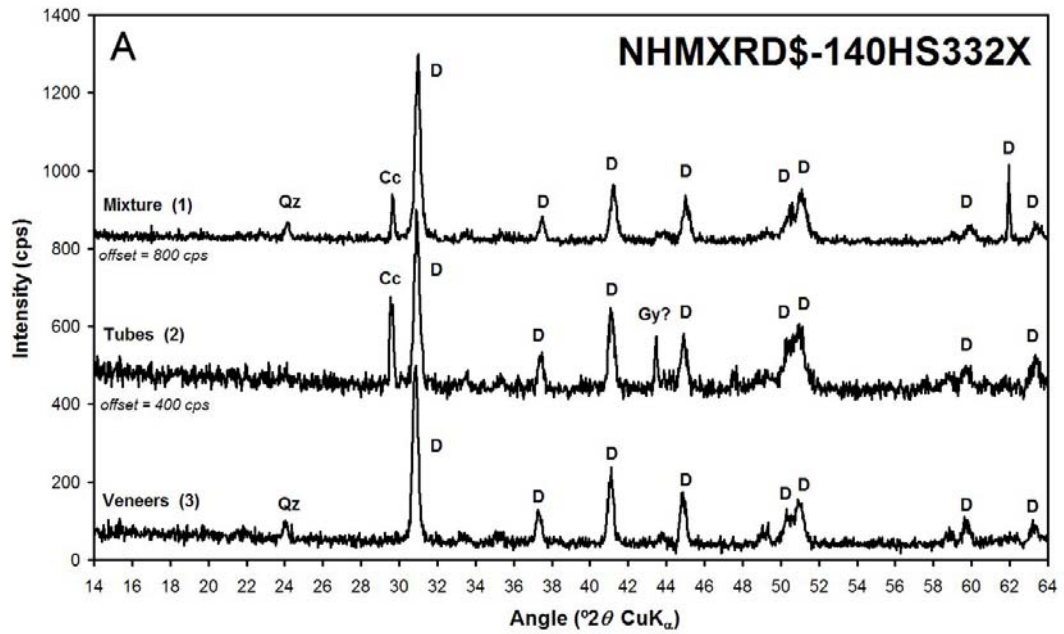


Figure 5.5 *In situ* XRD analysis of selected targets on specimen 140HS332X (freshwater limestone). Dolomite (D) is identified on all surfaces whereas calcite (Cc) is only associated with tubes. Quartz (Qz) is assumed to be of detrital origin. Gypsum (Gy) is tentatively identified in diffractogram 2 (tubes) partly due to the clear crystal observed in the target image (B). Instrumentation: NMHXRDS. Courtesy Dr. Gordon Cressey, Natural History Museum, London (B).

5.2.1.3 Geobiological Evaluation

These deposits formed in an impact crater lake, i.e., a habitable environment. The heterogeneous texture and fabric, along with the strongly aligned fibrous texture that is covered in places with a smooth film and the intertwined nature of the mineral-encrusted hollow tubes, point to a rock that could have biogenic potential. The calcite composition of the filaments and the dolomitic matrix/veneer are consistent with the environment of deposition and what is known about calcifying microbial filaments in such environments (Arp, 1995). Although no carbon was observed directly within the filaments, spots of organic carbon that have the characteristics of degraded carbon of biogenic origin are widely dispersed over the filaments. This carbon could, of course, have had an extraneous origin and may not necessarily be related to the potentially biogenic filaments. However, the morphological and mineralogical parameters of 140HS332 and related samples on their own suggest that there is a strong likelihood that the tubes actually represent mineralised microbial filament casings. It is concluded, that, on the basis of the observations and biogeochemical analyses, the evidence for a biogenic origin for this specimen is strong. In a Mars mission context sampling and further analysis would be justified.

5.2.2 Opaline Sinter, Yellowstone Park, Wyoming, USA (169)

Section B.2 describes the geology of Hillside Springs, Yellowstone Park and the samples used for this study. Table 5.3 presents a summary of the *in situ* imaging and analytical results for samples 169HS330 and 169HS331. Semi-quantitative geochemistry data are shown in Table 5.4.

5.2.2.1 Physical Properties

External surfaces of samples 169HS330 and 169HS331, parallel to the layering, appeared smooth, weathered, and discoloured (Figure 5.6). Macroscopic camera images showed a very heterogeneous structure consisting of parallel laminae and layers that have a predominantly vertical fibrous fabric (Figure 5.7). Oval to round void spaces are common. Stereo macroscopic imaging (Figure 5.7A) showed the fibrous structure more clearly, with the alternating fine parallel laminae interspaced by vertical columns between which void spaces occur. Individual fibrous threads, some tens to about 100 μm in diameter, stretch across the void space of the

cavities in a web-like fashion. Microscopic observation of the weathered external surface (Figure 5.7B) as well as the un-weathered fresh surface (Figure 5.7C), showed details of the threads that form a thick, but finely intertwined, matted or webbed network. The threads at this scale are of the order of 8 to 20 μm in diameter. 3D views derived from Beagle 2 microscope depth maps also helped to visualise the threads.

Table 5.3: Summary of *in situ* results for Opaline Sinter, Yellowstone Park, USA (169)

<i>In Situ</i> Techniques ¹	Results	Reference
Proximal Imaging (B2SCS\$GEOL\$SOL)	Evidence of layering	Section 5.2.2.1 Figure 5.6
Macroscopic Imaging (B2SCS\$CUL\$RGB)	Evidence of open fabric	Section 5.2.2.1 Figure 5.7A
Microscopic Imaging (B2MIC\$RGB)	3D morphology of clusters	Section 5.2.2.1 Figure 5.7B Figure 5.7C
X-Ray Fluorescence (TN9K\$FCA) (AXIOS\$HS)	Siliceous Si, Al, Fe, Ca, Ga, Zn, Zr, Rb (<i>fresh surface</i>) Si, Al, Fe, Ca, K, Cu, Zn, Ga, Rb, Sr, Y, Zr (<i>external surface</i>)	Section 5.2.2.2 Table 5.4
Raman Spectroscopy (UBRAM\$785) (UBRAM\$1064)	Quartz No organic signatures detected <i>Note: Incomplete survey performed</i>	
Mössbauer Spectroscopy (B2MBS\$)	Octahedral Fe ³⁺ (<i>fresh surface</i>) Octahedral Fe ³⁺ (<i>external surface</i>) <i>Note: Low signal (all surfaces). Slightly increased effect on external surfaces compared to fresh surfaces.</i>	Section 5.2.2.2 Figure 5.8
X-Ray Diffraction (PW1010\$)	Not analysed using NHMXRD\$ <i>Powder XRD analysis indicates amorphous silica.</i>	Section 5.2.2.2 Figure 5.9

¹ See Table C.1 for explanation of instrument mnemonics

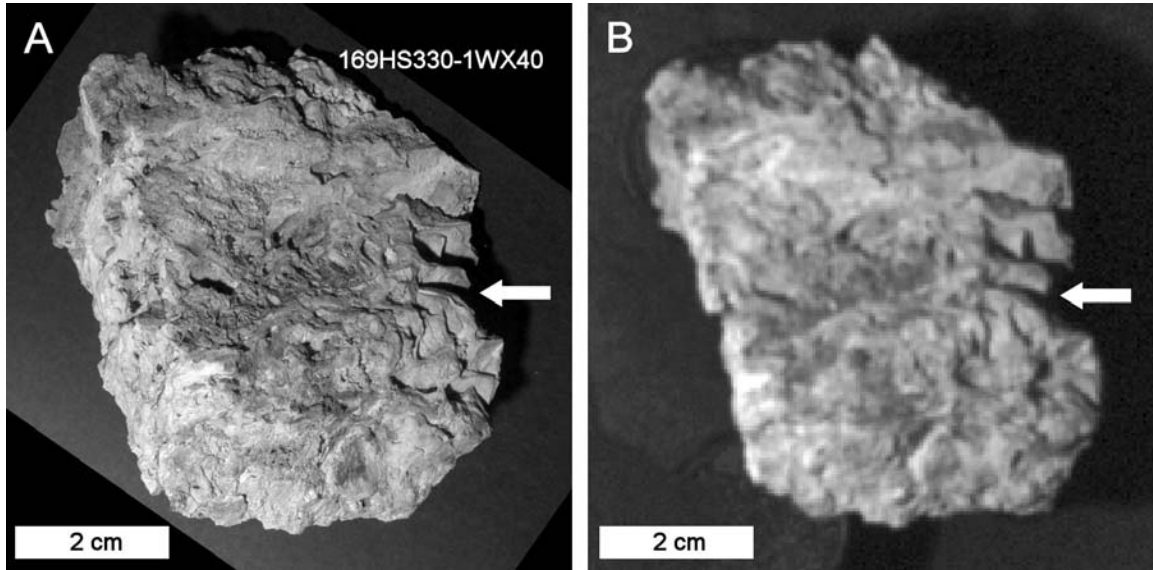


Figure 5.6 Proximal imaging of sample 169HS330 (opaline sinter). The external surface (1WX40) is generally smooth and discoloured (light brown in colour images) with evidence of layering as shown (A). The equivalent view obtained at 60 cm with the Beagle 2 camera, even with inferior resolution, still shows these characteristics (B). Instrumentation: Nikon D70 (A), B2SCS\$530\$SOL (B).

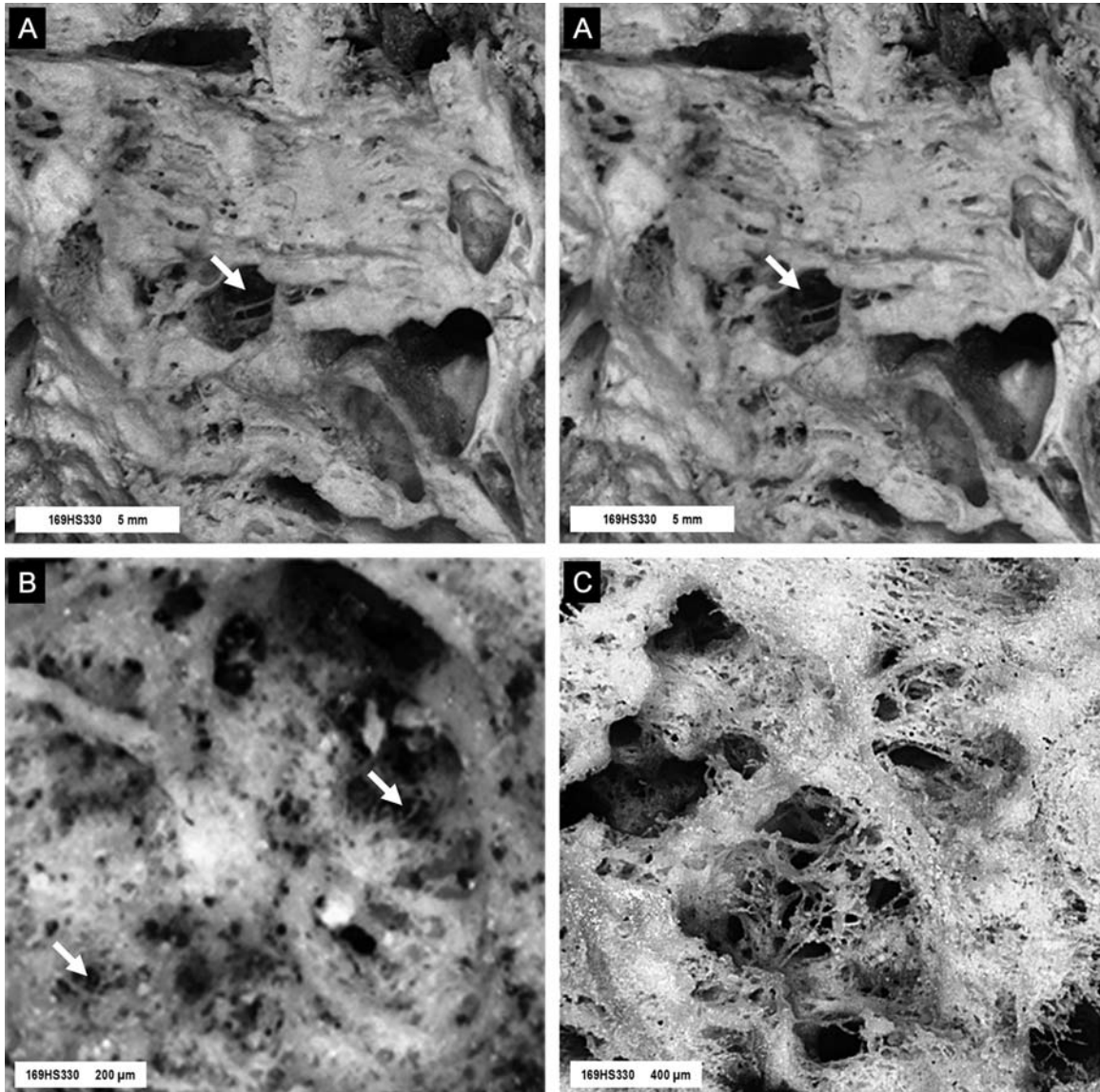


Figure 5.7 Macroscopic and microscopic imaging of sample 169HS330 (opaline sinter). Stereo imaging at 8 cm distance (1 cm baseline) reveals an extremely heterogeneous structure with fibrous fabric and evidence of thread-like features within voids (A). The stereo effect can be seen without the aid of a viewer. Microscopic imaging shows these features to be preserved on both weathered surfaces (B) and fresh surfaces (C). Instrumentation: B2SCS\$CUL\$W (A), B2MIC\$W (B and C).

5.2.2.2 Chemistry and Mineralogy

In situ WDXRF analysis of 169HS331-1FR30 confirmed a siliceous composition (97 wt % SiO₂) with minor Al (1.4 wt % Al₂O₃), Fe (0.8 wt % Fe₂O₃), K (0.2 wt % K₂O), Ca (0.3 wt % CaO), and trace elements Zn (96 ppm), Ga (97 ppm), Rb (73 ppm), and Zr (52 ppm). External surfaces (169HS331-2WX25) were slightly depleted in Si (91 wt % SiO₂), but more enriched in Al (3.7 wt % Al₂O₃), Fe (1.9 wt % Fe₂O₃), K (0.7 wt % K₂O), Ca (1.5 wt % CaO), and other major elements. Trace elements were also more abundant on external surfaces and included Cu (152 ppm), Zn (137 ppm), Ga (112 ppm), Rb (91 ppm), Sr (59 ppm), Y (39 ppm), and Zr (141 ppm).

In situ EDXRF analysis of 169HS330-1WX40 reported lower concentrations of K (0.2 wt % K₂O), Ca (0.4 wt % CaO), and Fe (0.2 wt % Fe₂O₃) compared with 169HS331-2WX25 analysed by *in situ* WDXRF, the values being closer to those reported for fresh material (169HS331-1FR30). This may suggest a heterogeneous distribution of chemistry within the external coatings, at least at the resolution of the measurement footprints (25 mm for the TN9K\$ and 26 mm for the AXIOS\$). Trace elements Cu, Zn, Rb, Sr and Zr were reported, but values were close to, or below the LLD (100, 63, 13, 14, 9 ppm respectively, see Table 1 in Potts *et al.*, 1995).

Only a preliminary Raman spectroscopic survey of 169HS331-1FR30 was undertaken which confirmed the presence of quartz as amorphous silica (Prof. Howell Edwards, University of Bradford, personal communication). No organic signatures could be identified in the spectra using 785 nm or 1064 nm laser excitation.

Mössbauer spectroscopy reported low bulk iron content (Figure 5.8) with the external surfaces exhibiting a slightly higher abundance than fresh surfaces.

Insufficient material was available for bulk WDXRF analysis but XRD confirmed the dominant mineral to be amorphous silica (Figure 5.9). The powders used for XRD analysis were derived from a mixture of fresh and weathered material.

Table 5.4 Semi-quantitative geochemical analysis of Opaline Sinter (169)

<i>Instrument</i>	AXIOS\$	AXIOS\$	TN9K\$
<i>Sample</i>	169HS331	169HS331	169HS330
<i>Target</i>	1FR30 (interior)	2WX25 (exterior)	1WX40 (exterior)
<u>Major elements</u>			
Na ₂ O	0.05 *	0.35 *	ND
MgO	0.11 *	0.32 *	ND
Al ₂ O ₃	1.42 *	3.7 ± 0.99	ND
SiO ₂	96.85 ± 0.23	90.73 ± 0.23	ND
P ₂ O ₅	0.05 *	0.1 *	ND
SO ₃	0.07 *	0.28 *	ND
Cl	0.02 *	0.1 *	ND
K ₂ O	0.17 *	0.69 *	0.19 ± 0.03
CaO	0.31 *	1.48 *	0.39 ± 0.06
TiO ₂	0.08 *	0.16 *	
V ₂ O ₅			
MnO	0.03 *	0.13 *	0.04 ± 0.01
Fe ₂ O ₃	0.81 *	1.86 ± 1.37	0.22 ± 0.03
<u>Trace elements</u>			
Ni			
Cu		152 *	
Zn	96 *	137 *	
Ga	97 *	112 *	
As			
Rb	73 *	91 *	
Sr		59 *	
Y		39 *	
Zr	52 *	141 *	10 ± 3
Mo			
Ba			
Pb			

¹ Concentrations normalised to 100%

² Major elements expressed in weight % oxide and trace elements in ppm

³ Errors (3σ SD) determined by counting statistics (AXIOS\$) or the Horwitz function (TN9K\$)

⁴ ND = Not Determined

⁵ See Table C.1 for explanation of instrument mnemonics

* Errors exceed concentration value (*in situ* analysis) or near LLD (bulk analysis)

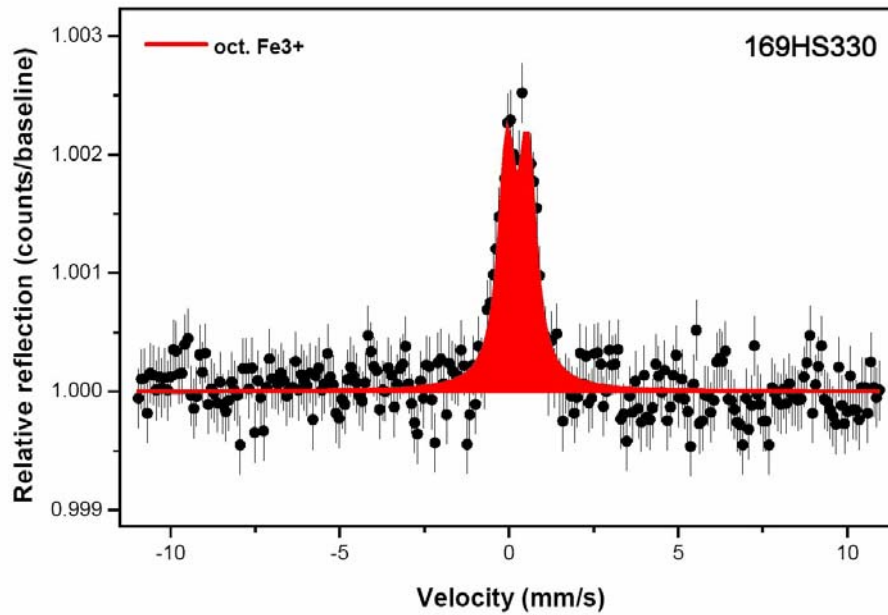


Figure 5.8 *In situ* Mössbauer analysis of sample 169HS330 (opaline sinter). Both external and fresh surfaces indicate a low octahedral Fe³⁺ content. Shaded area is a reference fit for octahedral Fe³⁺. External surfaces (shown) show a slightly more pronounced Mössbauer effect than internal surfaces. Instrumentation: B2MBSS. Courtesy Dr. Christian Schröder, NASA JSC.

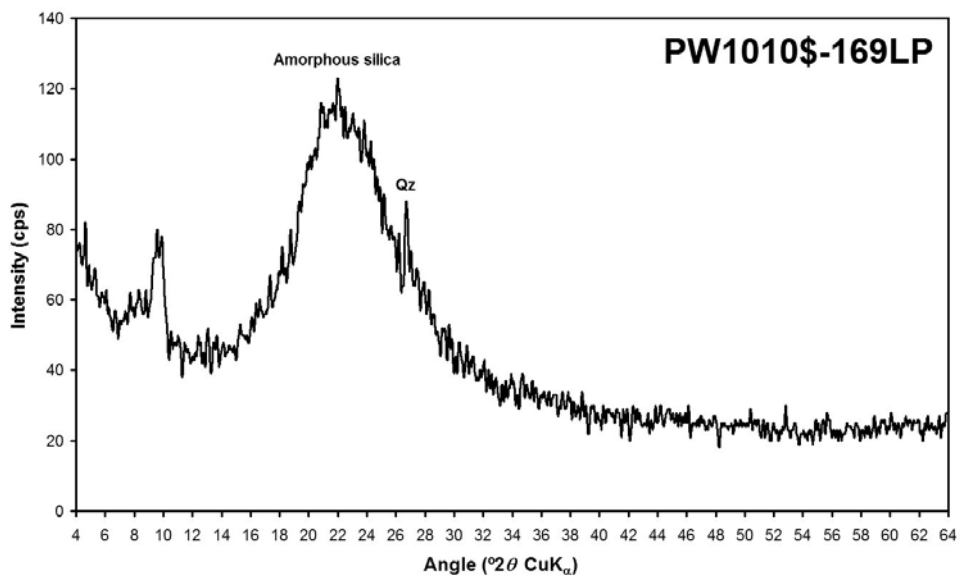


Figure 5.9 Bulk XRD analysis of homogenised powder derived from sample 169HS331 (opaline sinter). The broad signature indicates the silica to be generally amorphous although there is some crystalline quartz (Qz) present. Instrumentation: PW1010\$.

5.2.2.3 Geobiological Evaluation

As with the Ries Crater samples (i.e. 140HS332), the macroscopically visible heterogeneous structure of 169HS330, which consists of fibrous parallel laminae interspaced with vertical columns with visible webbed threads that span void spaces, is immediately suggestive of a biological structure related to microbial mat-forming behaviour. The composition is consistent with that of a microbialite formed in a siliceous hot spring environment. Indeed, the threads may represent bundles of several individual silica-encrusted filaments that range from 8 to 20 μm in diameter (Cady and Farmer, 1996). It should also be noted that Cady and Farmer (1996) observed that the organic component of such opaline microbial sinters from Yellowstone hot springs had been removed through oxidation. On the basis of the morphological and compositional information, it is possible to conclude that the probability of biogenicity is high. In a Mars mission context sampling and further analysis would be justified.

5.2.3 Chalcedony, Cady Mountains, California, USA (45)

Section B.3 describes the geology of the Sleeping Beauty Ridge region of Cady Mountains and the samples used for this study. Table 5.5 presents a summary of the *in situ* imaging and analytical results for samples 45HS265 and 45HS325. Semi-quantitative geochemistry data are shown in Table 5.6.

5.2.3.1 Physical Properties

Proximal imaging of samples 45HS265 and 45HS325 revealed a predominantly reddish brown surface that appeared to have a ribbed texture (Figure 5.10A). External surfaces were noticeably more yellow, which suggested that two iron phases were present. Macroscopic imaging showed the external and internal surfaces to be characterised by a heterogeneous texture that in some places appeared to be fibrous (Figures 5.10B). Inclusions of what appeared to be a clear mineral were also observed.

Table 5.5: Summary of *in situ* results for Chalcedony, Cady Mountains, USA (45)

<i>In Situ</i> Techniques¹	Results	Reference
Proximal Imaging (B2SCS\$GEOL\$SOL)	Red and brown coloration Ribbed texture	Section 5.2.3.1 Figure 5.10A
Macroscopic Imaging (B2SCS\$CUL\$RGB)	Visible filamentous structures Clear mineral inclusions	Section 5.2.3.1 Figure 5.10B
Microscopic Imaging (B2MIC\$RGB)	Morphology of Fe-encrusted filaments Highly reflective surfaces (clear mineral)	Section 5.2.3.1 Figure 5.11
X-Ray Fluorescence (TN9K\$FCA) (AXIOS\$HS) (PW1K4\$)	Silicate and iron oxide with trace element enrichment Si, Fe, Ca, Al, S, Mn, As, Ni, Zn, Pb, V, Sr, Mo	Section 5.2.3.2 Table 5.6
Raman Spectroscopy (UBRAM\$785) (UBRAM\$1064)	Quartz, hematite and goethite No organic signatures <i>Note: Incomplete survey performed</i>	Section 5.2.3.2
Mössbauer Spectroscopy (B2MBS\$)	Crystalline goethite and hematite (<i>external surface</i>) Hematite and crystalline goethite (<i>internal surface</i>) <i>Note: External goethite probably linked to yellow coloration (more pronounced on external surface) and hematite to red coloration (more pronounced on internal surface)</i>	Section 5.2.3.2 Figure 5.12
X-Ray Diffraction (PW1010\$)	Not analysed using NHMXRD\$ <i>Note: Powder XRD analysis indicates quartz with hematite.</i>	Section 5.2.3.2 Figure 5.13

¹ See Table C.1 for explanation of instrument mnemonics

In situ microscopy provided details of the fibrous areas showing that they were formed of parallel layers of mineral-encrusted tubes that ranged from ~20 µm to ~300 µm in diameter (Figure 5.11). Isolated thread-like features (~10 µm thick) occurred within void spaces. High reflectance on the surface of these samples was due to the abundance of the clear mineral previously observed in the macroscopic images (Figures 5.11B).

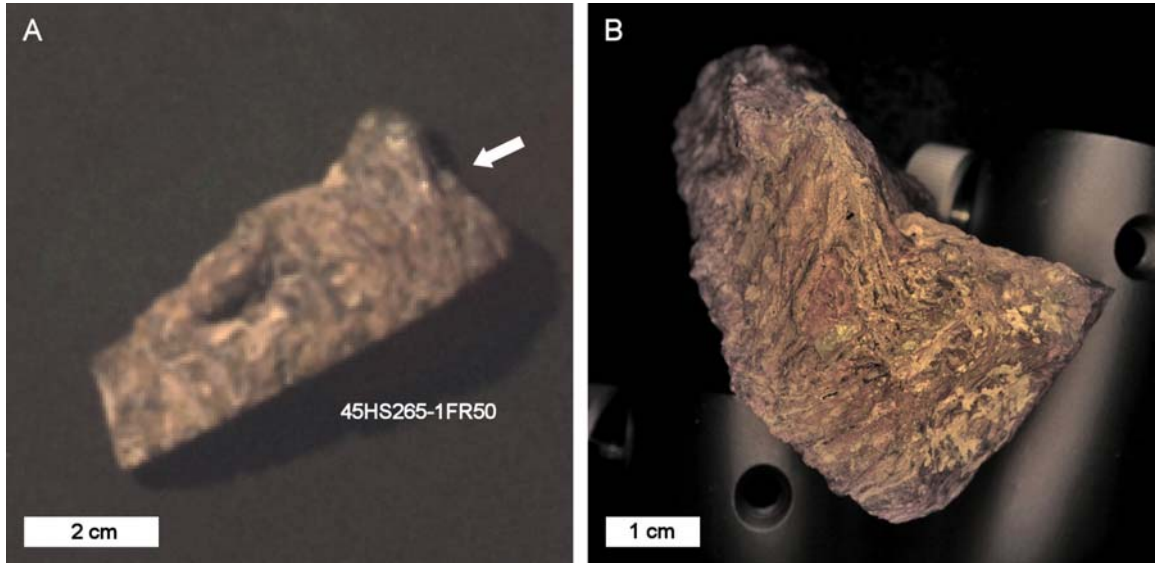


Figure 5.10 Proximal and macroscopic imaging of sample 45HS265 (chalcedony vein). Colour composite imaging at 60 cm reveals an aligned texture and a variety of shades of brown (A). Macroscopic imaging under controlled illumination at 8 cm shows a coarse filamentous fabric and clear mineral inclusions of quartz (B). The red and yellow areas correspond to hematite and goethite respectively. Instrumentation: B2SCS\$\$\$OL (A) and B2SCS\$CUL\$RGB (B).

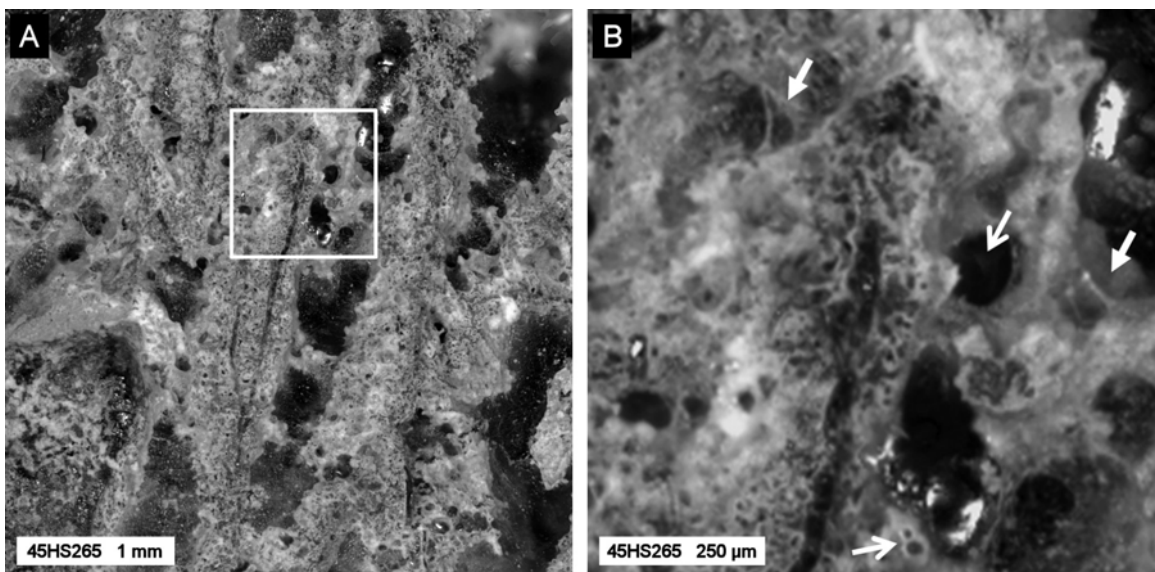


Figure 5.11 Microscopic imaging of sample 45HS265 (chalcedony vein). Close-up view of the coarse filamentous area shown in Figure 5.10B (A) and detail of boxed area (B). Note the preserved filament strands (block arrows) and tubular voids in cross section (skeletal arrows) (B). Instrumentation: B2MIC\$\$R.

5.2.3.2 Chemistry and Mineralogy

In situ WDXRF analysis of 45HS325-1SA20 revealed the principal elemental components to be Si (56 wt % SiO₂), Fe (40 wt % Fe₂O₃), and Ca (2 wt % CaO), with minor Al (0.34 wt % Al₂O₃), S (0.27 wt % SO₃), and Mn (0.15 wt % MnO). With the exception of Fe, which reported a lower value of 26 wt % Fe₂O₃, these values roughly corresponded to bulk major element abundances derived by WDXRF from 45PP428 (Table 5.6). Trace element concentrations determined by *in situ* WDXRF included V (370 ppm), Ni (1070 ppm), Zn (460 ppm), As (2680 ppm), Sr (160 ppm), Mo (160 ppm), and Pb (460 ppm). These were all higher than the values obtained from bulk analysis of 45PP428. In the case of Ni this was almost 40 times higher. Cu (21 ppm), Ga (8 ppm), Y (8 ppm) and Ba (151 ppm) were also detected in 45PP428 but were not reported by *in situ* WDXRF in 45HS325.

In situ EDXRF analysis of 45HS265-2SA50 showed that values determined for K and Mn, collectively agreed with both sets of WDXRF data, Ca (1 wt % CaO) was half, and Fe (21 wt % Fe₂O₃) was closer to that from bulk analysis (26 wt %). Trace element concentrations for Cu (129 ppm), Zn (186 ppm), As (443 ppm), Sr (45 ppm), Mo (40 ppm), Ba (43 ppm), and Pb (132 ppm) were generally lower than those determined by WDXRF. The absence of Ni in 45HS265-2SA50 may be associated with heterogeneous distribution, especially when one considers the difference between the results for 45HS325-1SA20 and 45PP428 (Table 5.6).

Table 5.6 Semi-quantitative geochemical analysis of Chalcedony (45)

<i>Instrument</i>	AXIOS\$	TN9K\$	PW1K4\$
<i>Sample</i>	45HS325	45HS265	45PP428
<i>Target</i>	1SA20	2SA50	
	(interior)	(interior)	(bulk)
<u>Major elements</u>			
Na ₂ O		ND	
MgO		ND	0.28 ± 0.01
Al ₂ O ₃	0.34 *	ND	0.44 ± 0.01
SiO ₂	56.27 ± 0.21	ND	63.33 ± 0.63
P ₂ O ₅	0.05 *	ND	0.02 ± 0.01
SO ₃	0.27 *	ND	0.11 ± 0.01
Cl	0.09 *	ND	0.04 ± 0.01
K ₂ O	0.05 *	0.06 ± 0.01	0.04 ± 0.01
CaO	2.07 ± 0.99	1.04 ± 0.12	1.9 ± 0.02
TiO ₂			
V ₂ O ₅	0.04 *		0.03 ± 0.01
MnO	0.15 *	0.12 ± 0.02	0.1 ± 0.01
Fe ₂ O ₃	40.11 ± 0.21	20.59 ± 1.56	26.24 ± 0.26
<u>Trace elements</u>			
Ni	1070 *		28 ± 1
Cu		129 ± 30	21 ± 1
Zn	460 *	186 ± 42	221 ± 2
Ga			8 ± 2
As	2680 *	443 ± 85	1362 ± 14
Rb			
Sr	160 *	45 ± 12	97 ± 1
Y			
Zr			
Mo	160 *	40 ± 12	76 ± 1
Ba		43 ± 12	151 ± 2
Pb	460 *	132 ± 30	274 ± 3

¹ Concentrations normalised to 100%

² Major elements expressed in weight % oxide and trace elements in ppm

³ Errors (3σ SD) determined by counting statistics (AXIOS\$) or the Horwitz function (TN9K\$)

⁴ Bulk analysis precisions (PW1K4\$) ~1 % (> 10 ppm) and ~10-20% (< 10 ppm)

⁵ ND = Not Determined

⁶ See Table C.1 for explanation of instrument mnemonics

* Errors exceed concentration value (*in situ* analysis) or near LLD (bulk analysis)

Only a limited *in situ* Raman spectroscopic survey of sample 45HS325 was performed but this was successful in identifying quartz, goethite and hematite (Prof. Howell Edwards, University of Bradford, personal communication). However, no organic compounds were identified on the surface examined.

Using surface colour as a guide for target selection, the *in situ* Mössbauer data confirmed the presence of hematite on fresh surfaces and goethite on external surfaces (Figure 5.12), thus tallying with the observed coloration.

Bulk analysis of homogenised powders by XRD confirmed the presence of hematite and quartz (Table 5.13) but no goethite was detected. This is probably due to the derived powder being preferentially, but unavoidably, sourced from fresh material.

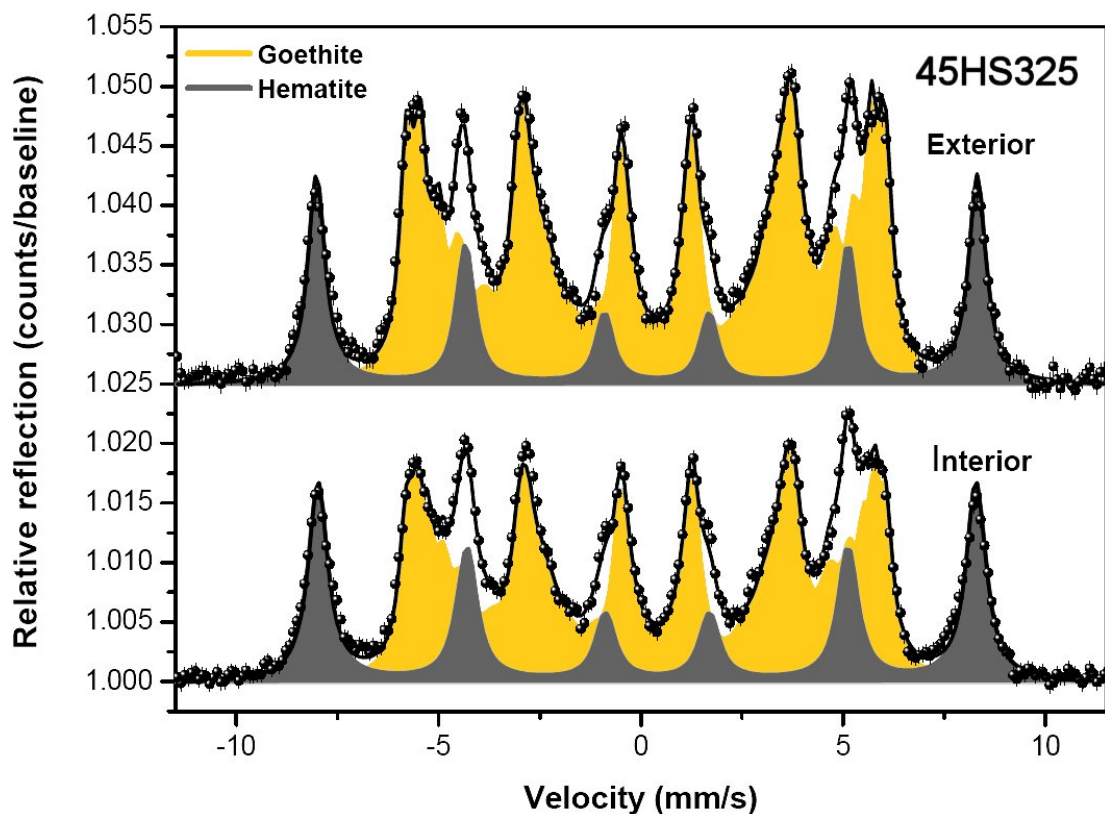


Figure 5.12 *In situ* Mössbauer analysis of sample 45HS325 (chalcedony vein). Two iron phases are present, hematite and goethite. Shaded areas are reference fits for each mineral. Goethite is more pronounced on external (more yellow) surfaces. Instrumentation: B2MBS\$. Courtesy Dr. Christian Schröder, NASA JSC.

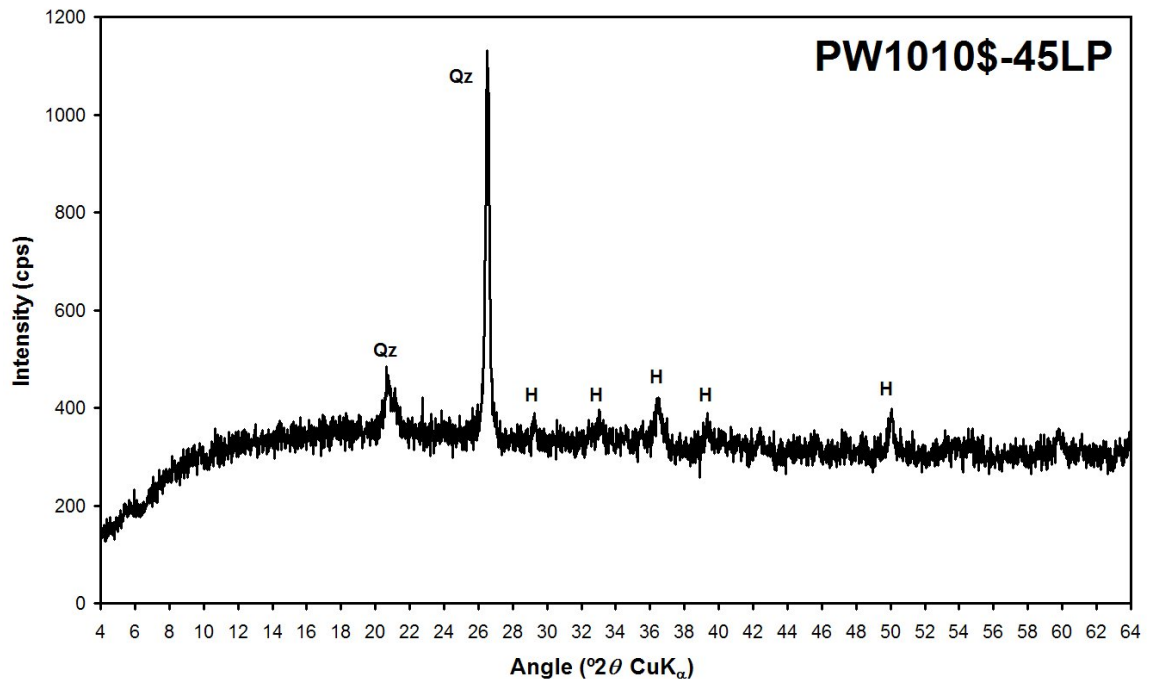


Figure 5.13 Bulk XRD analysis of homogenised powder derived from sample 45HS325 (chalcedony vein). Hematite (H) and quartz (Qz) were confirmed but no goethite was reported. This was probably due to the powder being unavoidably derived from internal (red) material. Instrumentation: PW1010\$.

5.2.3.3 Geobiological Evaluation

The heterogeneous fibrous texture of 45HS265 and 45HS325, plus matted, hollow tubes, are suggestive of a microbial origin, but more detailed microscopic examination of the matted fabric and mineral encrusted filaments, especially by Raman spectroscopy, would be useful for a more complete biogenic interpretation. On their own, the compositional data are suggestive of formation of a deposit in a hydrothermal, and thus habitable, environment. The evidence for biogenicity is moderately strong but more detailed morphological observations and organic carbon analyses would be useful. In a Mars mission context sampling may be justified but the decision would depend on the payload.

5.2.4 Goethite, Cerro de Pasco, Peru (179)

Section B.4 describes the geology of Cerro de Pasco region and the samples used for this study. Table 5.7 presents a summary of the *in situ* imaging and analytical results for samples 179HS367 and 179HS588. Semi-quantitative geochemistry data are shown in Table 5.8.

Table 5.7: Summary of *in situ* results for Goethite, Cerro de Pasco, Peru (179)

<i>In Situ</i> Techniques¹	Results	Reference
Proximal Imaging (B2SCS\$GEOL\$SOL)	Aligned texture	Section 5.2.4.1 Figure 5.14A
Macroscopic Imaging (B2SCS\$CUL\$RGB) (NUVIS\$MAC10\$SOL)	Evidence of open fabric Visible filaments	Section 5.2.4.1 Figure 5.15
Microscopic Imaging (B2MIC\$\$RGB)	Morphology of encrusted filaments	Section 5.2.4.1 Figure 5.14B
X-Ray Fluorescence (TN9K\$\$FCA) (AXIOS\$HS) (AXIOS\$PP)	Iron oxide with trace element enrichment Fe, Pb, Zn, Si, Al, Na, S, Ba, As, Cu, V, Zr <i>Note: Pb and Cu as external coating</i>	Section 5.2.4.2 Table 5.8
Raman Spectroscopy (UBRAM\$\$785) (UBRAM\$\$1064)	Broad spectral signature between 3500 and 500 cm ⁻¹ . Hematite unambiguously identified in region < 500 cm ⁻¹ . No organic signatures <i>Note: Lack of goethite bands may be due to nanophase state</i>	Section 5.2.4.2
Mössbauer Spectroscopy (B2MBSS)	Octahedral Fe ³⁺ attributed to goethite (<i>all surfaces</i>)	Section 5.2.4.2 Figure 5.16
X-Ray Diffraction (PW1010\$)	Not analysed using NHMXRDS <i>Note: Powder XRD analysis indicates goethite.</i>	Section 5.2.4.2 Figure 5.17

¹ See Table C.1 for explanation of instrument mnemonics

5.2.4.1 Physical Properties

The finely laminated, fibrous surface texture of 179HS367 is evident in proximal images (Figure 5.14A). Macroscopic stereo imaging of 179HS367-1FR40 confirmed an open, framework texture (Figure 5.15). Colour images revealed the lustrous nature of the outer surface suggesting a metallic composition.

Microscopic imaging showed the filaments in fine detail (Figure 5.14B). Although there is an overall parallel fabric, intertwining of the filaments is clearly apparent. Threads of various sizes (60 μm to 200 μm diameter) can be discerned, and unlike those in sample 140HS332 (Ries limestone) they are not hollow. Botryoids festoon the surface and some follow the filaments along their length. Others exhibit what appear to be regular septate divisions. Smaller filaments of about 50-60 μm in diameter are characterised by platy septal divisions of the order of about 25 μm , whereas larger filaments, about 100 μm in diameter, consist of regular chains of 100 μm spheres.

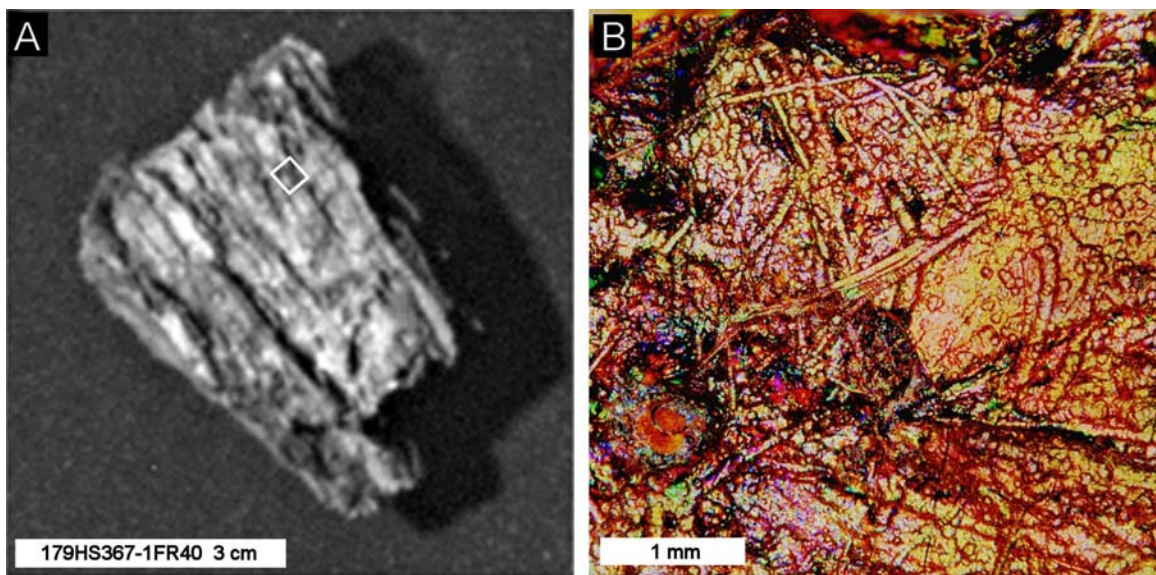


Figure 5.14 Proximal and microscopic imaging of sample 179HS367 (goethite). Imaging at 60 cm shows a well developed aligned texture (A). Microscopic imaging of the highlighted area (box) reveals a complex surface festooned with mineralised filaments (B). Instrumentation: B2SCS\$530\$SOL (A) and B2MIC\$\$RGB (B).

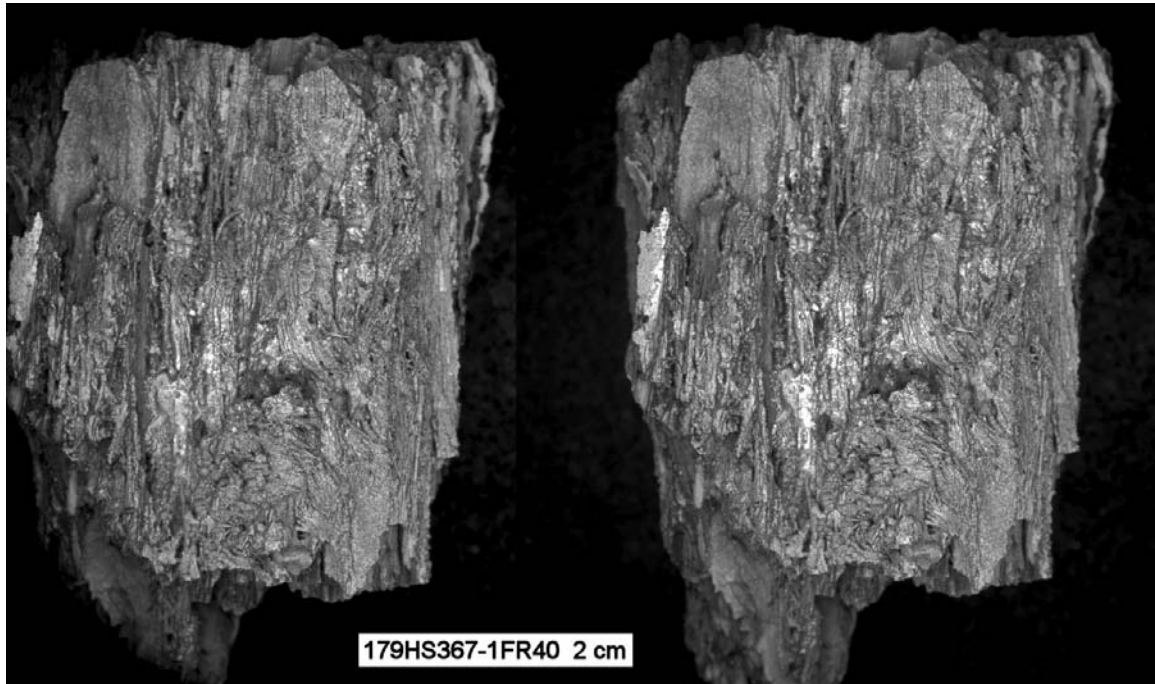


Figure 5.15 Stereo macroscopic imaging of sample 179HS367 (goethite) at 8 cm (1 cm baseline). The open fabric and aligned texture observed at proximal distance (Figure 5.14A) is seen in more detail. Assemblages of linear and chaotic mineralised filaments are also clearly visible. The stereo effect can be seen without the aid of a viewer. Instrumentation: B2SCS\$CUL\$R.

5.2.4.2 Chemistry and Mineralogy

Bulk WDXRF analysis of 179PP578 confirmed high concentrations of Fe (70 wt % Fe_2O_3), Cu (980 ppm), Zn (2.49 wt %), As (2390 ppm), Ba (3690 ppm), and Pb (4.5 wt %). The value for As is consistent with concentrations reported from this locality (Dr. Beda Hofmann, Natural History Museum, Bern, personal communication). Other significant elements present included Na (0.4 wt % Na_2O), Al (1 wt % Al_2O_3), Si (1.4 wt % SiO_2), S (0.4 wt % SO_3), and Zr (100 ppm).

In situ EDXRF analysis of 179HS367-1FR40 confirmed the presence of Fe (34 wt % Fe_2O_3), Cu (1000 ppm), As (1334 ppm), and Pb (4.9 wt %). Analysis of the more weathered surface (2WX40) confirmed similar levels of Fe (35 wt % Fe_2O_3), more Cu (1700 ppm), less As (656 ppm), and less Pb (4.4 wt %). No Zn and only small amounts of Zr (~16 ppm) were detected on both surfaces.

A comparison of the *in situ* (179HS367) and bulk (179PP578) data suggests that Pb and Cu (both

X-ray absorbers) occur as a dominant (but not complete) surface coating, masking elements such as Zn and Ba, and partially masking elements such as Fe and As that occur in significant amounts within the sample.

In situ Raman spectra acquired from sample 179HS588 using 785 nm excitation showed a relatively featureless broad signature between 3500 and 500 cm^{-1} . No goethite peaks could be identified but hematite was unambiguously present (405, 290 and 223 cm^{-1}) in some spectra. Interestingly, this did not tally with either the Mössbauer data (Figure 5.16) or the bulk powder XRD data (Figure 5.17), both of which only reported goethite. This is probably due to the combined effect of a larger measurement footprint of the Mössbauer spectrometer compared to the Raman spectrometer, plus the goethite being in a predominantly nanophase state. No organic signatures were identified using 1064 nm excitation.

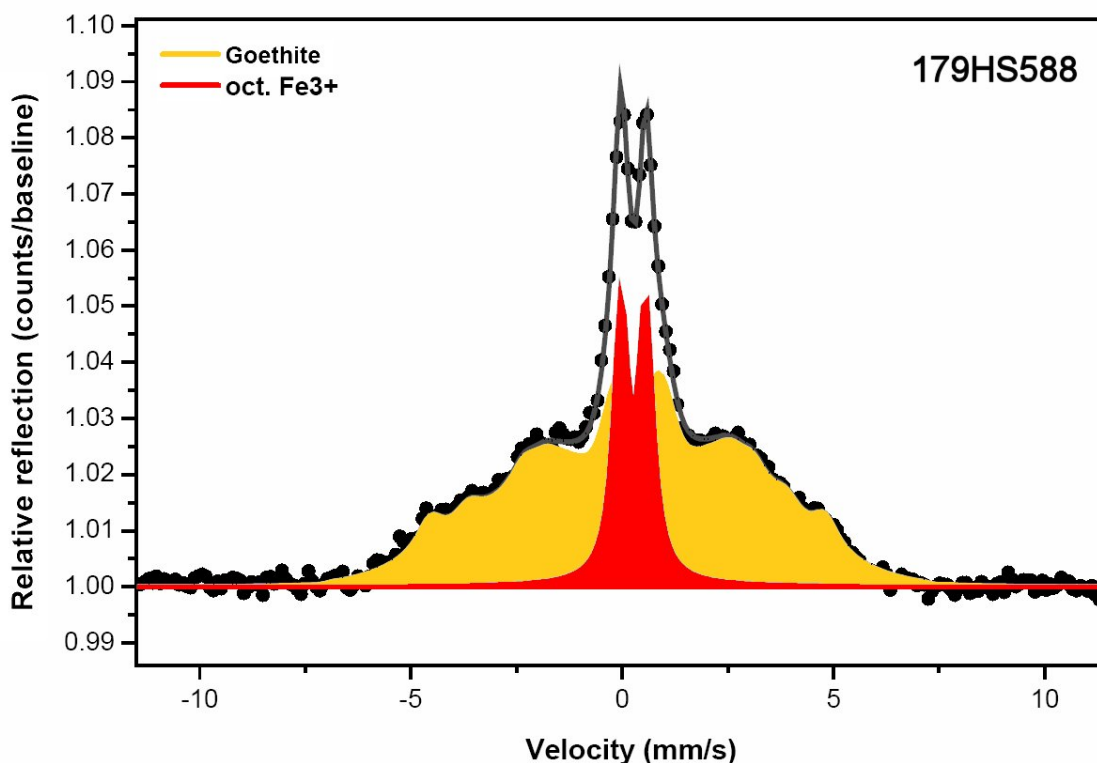


Figure 5.16 *In situ* Mössbauer analysis of sample 179HS588 (goethite). All surfaces confirmed the presence of goethite only. Shaded areas are reference fits for goethite and octahedral Fe^{3+} . Instrumentation: B2MBSS. Courtesy Dr. Christian Schröder, NASA JSC.

Table 5.8 Semi-quantitative geochemical analysis of Goethite (179)

<i>Instrument</i>	TN9K\$	TN9K\$	AXIOS\$
<i>Sample</i>	179HS367	179HS367	179PP578
<i>Target</i>	1FR40	2WX40	
	(exterior)	(interior)	(bulk)
<u>Major elements</u>			
Na ₂ O	ND	ND	0.41 ± 0.01
MgO	ND	ND	
Al ₂ O ₃	ND	ND	1.01 ± 0.01
SiO ₂	ND	ND	1.37 ± 0.01
P ₂ O ₅	ND	ND	0.04 ± 0.01
SO ₃	ND	ND	0.38 ± 0.01
Cl	ND	ND	
K ₂ O			
CaO	0.04 ± 0.01		0.04 ± 0.01
TiO ₂			
V ₂ O ₅			0.01 *
MnO	0.13 ± 0.03	0.09 ± 0.02	0.02 ± 0.01
Fe ₂ O ₃	34.15 ± 2.4	34.79 ± 2.46	69.72 ± 0.7
<u>Trace elements</u>			
Ni			
Cu	1000 ± 171	1700 ± 267	980 ± 10
Zn			24870 ± 249
Ga			
As	1334 ± 216	656 ± 120	2390 ± 24
Rb			
Sr			
Y			
Zr	16 ± 6	13 ± 3	100 ± 1
Mo			
Ba			3690 ± 37
Pb	49096 ± 4638	43840 ± 4212	44950 ± 450

¹ Concentrations normalised to 100%

² Major elements expressed in weight % oxide and trace elements in ppm

³ Errors (3σ SD) determined by the Horwitz function (TN9K\$)

⁴ Bulk analysis precisions (AXIOS\$) ~1 % (> 10 ppm) and ~10-20% (< 10 ppm)

⁵ ND = Not Determined

⁶ See Table C.1 for explanation of instrument mnemonics

* Errors exceed concentration value (*in situ* analysis) or near LLD (bulk analysis)

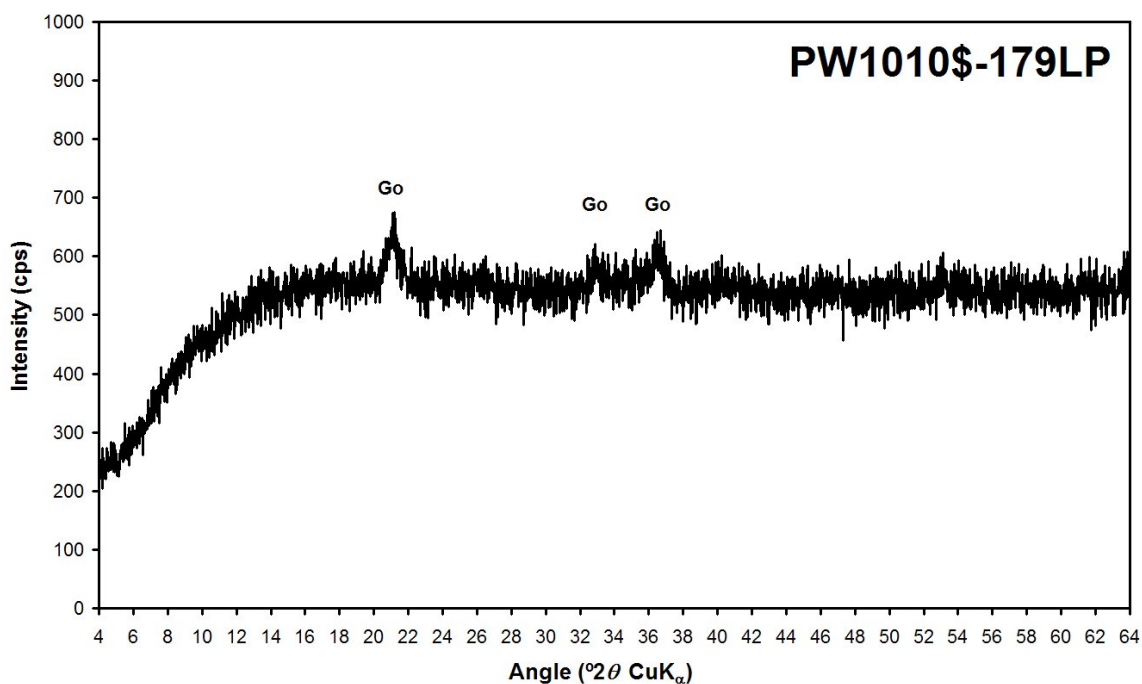


Figure 5.17 Bulk XRD analysis of homogenised powder derived from sample 179HS367 (goethite). All peaks are assignable to goethite (Go). Instrumentation: PW1010\$.

5.2.4.3 Geobiological Evaluation

High concentrations of trace elements such as Cu, As, Ba and very high (wt %) levels of Zn and Pb suggest a hydrothermal origin for this goethite specimen. Given these conditions, the orientated and interweaving filamentous texture of 179HS367 could be suggestive of a preserved biological fabric. The presence of what look like regular septate divisions along the lengths of some of the filaments (Figure 5.15B) also suggests a link to biology but more detailed microscopic analysis would be necessary to support such an interpretation. In conclusion, the possibility that these structures represent iron oxide mineralised microbial filaments (perhaps once chemosynthetic hydrothermal microbes) cannot be ruled out. In a Mars mission context this specimen would be a strong contender for sampling and further analysis (including microscopy).

5.3 Morphological Biosignatures: Endoliths

Endoliths are generally two-dimensional targets at the macroscopic and microscopic scale.

Samples that contain cryptoendoliths required splitting to expose a vertical sequence or lateral exposure to the lichen layer at the exfoliating interface (i.e. 114HS353). Chasmoendoliths on the other hand were exposed on surfaces following splitting along host fractures (i.e. 194HS435), or remained sandwiched between laminae when imaging could be performed through the host medium (i.e. 44HS419). Multi-spectral imaging at all three scales was particularly successful for one of the specimens (194HS435). UV imaging of this sample also revealed some organic compounds, which were identified by Raman spectroscopy to have detectable bio-fluorescent properties whilst others did not.

5.3.1 Orthoquartzite, McMurdo, Victoria Land, Antarctica (114)

Section B.5 describes the geology of McMurdo Dry Valleys region at Linnaeus Terrace and the samples used for this study. Table 5.9 presents a summary of the *in situ* imaging and analytical results for samples 114HS353, 114HS354 and 114HS380. Semi-quantitative geochemistry data are shown in Table 5.10.

5.3.1.1 Physical Properties

At proximal distance, 114HS353, 114HS354 and 114HS380 displayed a fine-grained homogenous texture with areas of coloration, which was especially evident on the pronounced exfoliation planes (Figure 5.18A). The external surface appeared case-hardened and distinctly orange-brown in colour, suggesting an iron coated surface that contrasted with the grey-white interior. A fresh vertical section revealed distinct layering that consisted of a brown outer crust beneath which was a black zone that paralleled the outer surface.

Macroscopic imaging showed the contact between the outer crust and the black zone to be sharp (Figure 5.18B), whereas the lower contact diffused into the rock. A whitish layer below the black zone was bordered by a parallel, diffuse red-brown zone. Multi-spectral imaging enhanced the layering pattern parallel to the outer surface of the rock and confirmed a spectral correspondence between the red-brown zone and the external surface (Figure 5.19). The finely reticulate texture of the red-brown zone seen in the spectral image suggests grains could be coated. Imaging under UV illumination did not reveal any signs of fluorescence.

Table 5.9: Summary of *in situ* results for Orthoquartzite, McMurdo, Antarctica (114)

<i>In Situ</i> Techniques ¹	Results	Reference
Proximal Imaging (B2SCS\$GEOL\$SOL)	Evidence of layering	Section 5.3.1.1 Figure 5.18A
Macroscopic Imaging (B2SCS\$CUL\$RGB) (B2SCS\$CUL\$UV) (NUVIS\$MAC10\$SOL)	Visible cryptoendoliths No fluorescence from either lichen or algal zone Spectral correspondence between exterior and Fe band	Section 5.3.1.1 Figure 5.18B Figure 5.19
Microscopic Imaging (B2MIC\$RGB) (B2MIC\$UV)	Grain coatings No fluorescence from lichen zone Fluorescence from algal zone	Section 5.3.1.1 Figure 5.20
X-Ray Fluorescence (TN9K\$FCA) (AXIOS\$HS) (PW1K4\$)	Quartz (<i>all surfaces</i>) Si, Al, Ca, Na, Mg, Fe, S, Ti, Zr (<i>fresh interior</i>) Si, Al, Fe, Na, S, Mg, K, Ca, Ti, Zr, Cu (<i>exterior</i>) <i>Note: SiO₂ (99 %) by WDXRF.</i>	Section 5.3.1.2 Table 5.10
Raman Spectroscopy (UBRAM\$785) (UBRAM\$1064)	Quartz (<i>all surfaces</i>) Goethite and hematite (<i>weathered exterior</i>) Hematite (<i>internal oxidised band</i>) Rutile (<i>fresh surface</i>) Chlorophyll, carotene, scytonemin, and Ca-oxalate monohydrate (<i>algal zone</i>) Chlorophyll, scytonemin, and Ca-oxalate monohydrate (<i>lichen zone</i>)	Section 5.3.1.2 Figure 5.21
Mössbauer Spectroscopy (B2MBS\$)	Red coloration of exterior and Fe-mobilised zone attributed to small amounts of octahedral Fe ³⁺ (probably as thin grain coatings). <i>Note: Low signal (all surfaces)</i>	Section 5.3.1.2 Figure 5.22
X-Ray Diffraction (NHMXRD\$) (PW1010\$)	Quartz with calcite (<i>all surfaces</i>) Amorphous substance (silica) (<i>matrix</i>) <i>Note: Powder XRD analysis indicates quartz only.</i>	Section 5.3.1.2 Figure 5.23

¹ See Table C.1 for explanation of instrument mnemonics

In situ microscopy revealed a variable grain size of between 0.2 mm and 0.5 mm diameter (Figure 5.20A). Under UV illumination, areas within the white zone exhibited fluorescence (Figure 5.20B) clearly associated with inter-granular dark spots and other regions observed in the macroscopic images. The black zone itself did not show any signs of fluorescence.

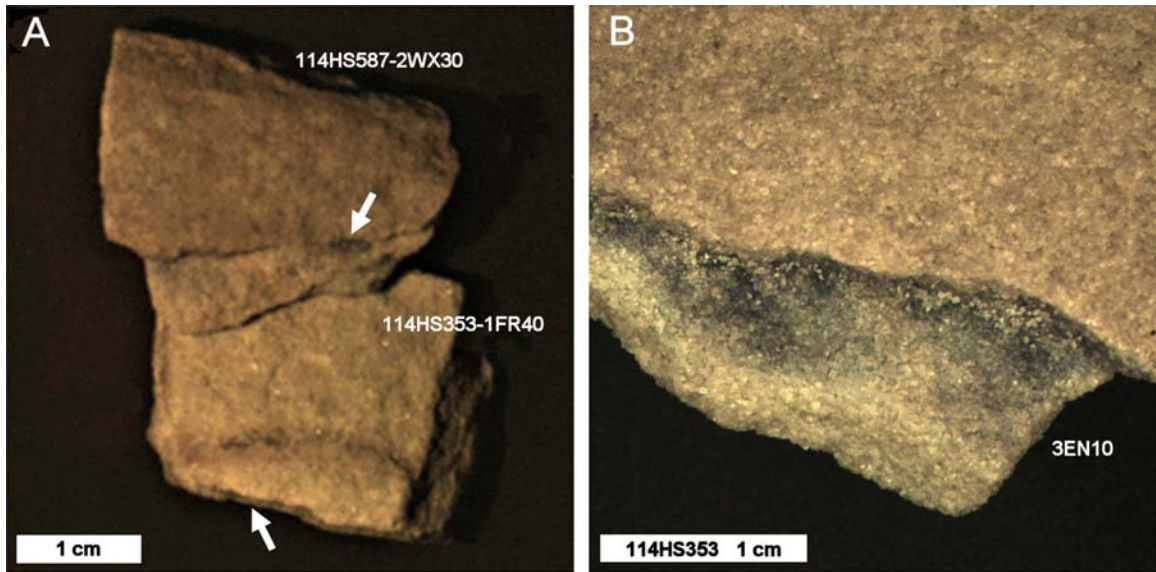


Figure 5.18 Proximal and macroscopic imaging of samples 114HS353 and 114HS587 (orthoquartzite). Colour composite imaging at 60 cm shows the case-hardened exterior (114HS587-2WX30) and iron mobilisation zone (114HS353-1FR40) to be distinctly red (A). The black lichen zone is also discernable (arrows). Macroscopic colour imaging at 8 cm shows the extent of the cryptoendolithic lichens more clearly on recently exfoliated surfaces (B). Instrumentation: B2SCS\$\$SOL (A) and B2SCS\$CUL\$RGB (B).

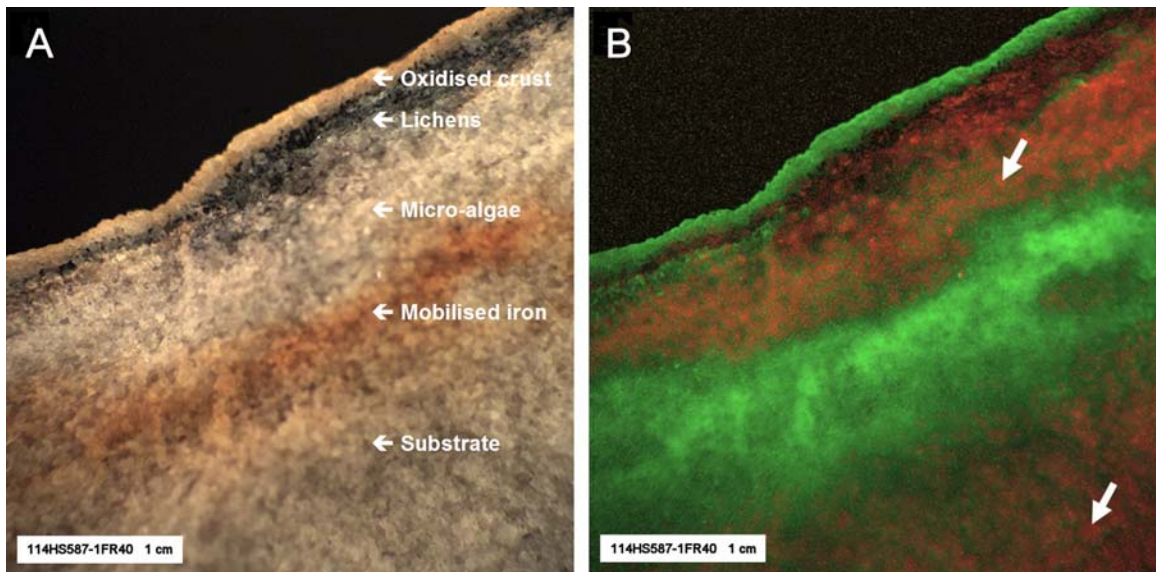


Figure 5.19 Macroscopic imaging of sample 114HS587 (orthoquartzite) with the Nuance multi-spectral system at 8 cm. A true colour image of surface 1FR40 (A) shows the sequence described in Section B.5. A spectrally classified image of the equivalent field of view (B) shows the external surface and internal iron mobilisation zone to be spectrally similar and distinguishable from the host quartz (red). Note the lichen layer appears opaque within this range (420 nm to 720 nm). Interstitial iron (as grain coatings) is inferred from the mottling within the fresh regions (arrows). Instrumentation: NUVISSMAC10SSOL.

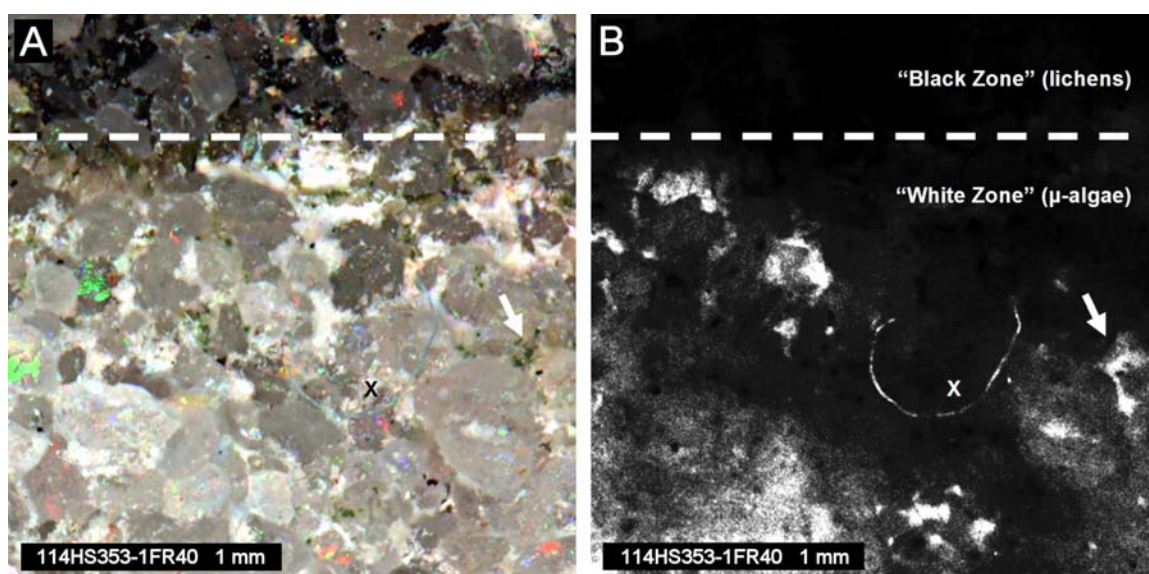


Figure 5.20 Microscopic imaging of sample 114HS353 (orthoquartzite). Colour composite imaging clearly shows the interstitial algae (arrow) within the white zone (A). Iron coatings indicated in Figure 5.19B are not discernable. UV fluorescence imaging of the same field of view (B) shows the lichen zone to be uniformly opaque and the algal zone to fluorescence in correspondence with both the visible areas (A) and elsewhere. Note the feature marked with an X is a synthetic fibre placed on the sample to assist processing of the UV image. Instrumentation: B2MIC\$\$RGB (A) and B2MIC\$\$UV (B).

5.3.1.2 Chemistry and Mineralogy

In situ WDXRF analysis of 114HS354-2FR20 showed a high Si content (94% SiO₂), and very little Fe (0.3% Fe₂O₃), plus Na (0.4 wt % Na₂O), Mg (0.2 wt % MgO), Al (3 wt % Al₂O₃), S (0.2 wt % SO₃), Ca (1.2 wt % CaO), Ti (0.2 wt % TiO₂), and Zr (141 ppm). Comparable analysis of the external surface 114HS354-1WX15 confirmed Si to be still dominant (92% SiO₂), and enrichment of some elements including Na (0.9 wt % Na₂O), Mg (0.7 wt % MgO), S (0.9 wt % SO₃), K (0.3 wt % K₂O), and Fe (1.7 % Fe₂O₃). Concentrations of Al, Ti and Zr remained relatively consistent, but Ca was depleted (0.2 wt % CaO). The presence of Cu (100 ppm) was also noted.

In situ EDXRF analysis of 114HS353-2WX40 (exterior surface) showed more Fe (0.2 wt % Fe₂O₃) to be present compared with 114HS353-1FR40 (<< 0.1 wt % Fe₂O₃), and Zr was detected

on both surfaces (44 and 37 ppm respectively). For those elements that could be measured, concentrations determined by *in situ* EDXRF were much lower than those determined by *in situ* WDXRF and similar to bulk analysis (114PP431).

In situ Raman spectroscopy was used to analyse internal and external surfaces using 785 nm laser excitation (Figure 5.21A). Quartz (465 cm^{-1}) was unambiguously identified on 114HS353-2WX40 and 114HS380-1WX30 but was also recognised in other spectra at 1230, 1161, 1081, 1066, 804, 696, 541, 396, 356 and 265 cm^{-1} . Rutile (608 and 443 cm^{-1}) was also identified in some spectra from 114HS354-2FR20, probably correlating with the Ti detected by *in situ* WDXRF. Goethite (299 and 246 cm^{-1}) and hematite (404 and 225 cm^{-1}) were both identified on 114HS354-1WX15. Analysis of 114HS354-4WX10 (the internal oxidised zone) showed strong Raman signatures for hematite (609 , 495 , 404 , 291 and 225 cm^{-1}) but no goethite was identified. Organic signatures were identified in spectra from 114HS354-3FR10 including chlorophyll (broad, intense feature centred at 1340 cm^{-1}), carotene (1517 and 1157 cm^{-1}), scytonemin (1630 cm^{-1}), and Ca-oxalate monohydrate (1494 , 1463 , 908 and 506 cm^{-1}). Similar results were obtained for 114HS380-2FR10 (Figure 5.21A) but carotene was not identified. No organic signatures were seen in spectra from external surfaces 114HS354-1WX15 or 114HS353-2WX40.

In situ Raman analysis of 114HS353-3EN10 (black layer at the base of the exfoliation surface shown in Figure 5.18B) was performed using 1064 nm excitation (Figure 5.21B). The spectral signature was similar to that previously reported in Jorge Villar *et al.*, 2003 (see Figure 1 therein). Analysis confirmed the dominance of quartz (1160 , 500 , 464 , 395 , 356 , 263 , 205 and 127 cm^{-1}) but also revealed chlorophyll (1318 cm^{-1}), carotene (1157 cm^{-1}), scytonemin (1587 cm^{-1}) and Ca-oxalate monohydrate (1620 and 1471 cm^{-1}).

In situ Mössbauer spectroscopy showed a low signal from oxidised surfaces (Figure 5.22). This together with the reticulate texture observed by macroscopic multi-spectral imaging suggested that Fe is present as very thin granular coatings.

Bulk XRD analysis revealed the dominant mineral to be quartz (Figure 5.23) but no indication of any Fe-oxide was evident, at least in the sample of homogenised powder used.

Table 5.10 Semi-quantitative geochemical analysis of Orthoquartzite (114)

<i>Instrument</i>	AXIOS\$	TN9K\$	AXIOS\$	TN9K\$	PW1K4\$
<i>Sample</i>	114HS354	114HS353	114HS354	114HS353	114PP430
<i>Target</i>	1WX15	2WX40	2FR20	1FR40	
	(exterior)	(exterior)	(interior)	(interior)	(bulk)
<u>Major elements</u>					
Na ₂ O	0.93 *	ND	0.36 *	ND	
MgO	0.66 *	ND	0.19 *	ND	0.15 ± 0.01
Al ₂ O ₃	2.9 ± 1.14	ND	2.97 ± 1.11	ND	0.57 ± 0.01
SiO ₂	91.98 ± 0.24	ND	94.42 ± 0.23	ND	99.06 ± 0.99
P ₂ O ₅	0.06 *	ND	0.02 *	ND	0.01 *
SO ₃	0.92 *	ND	0.15 *	ND	0.06 ± 0.01
Cl	0.12 *	ND	0.11 *	ND	0.01 *
K ₂ O	0.31 *	0.04 ± 0.01	0.06 *	0.06 ± 0.01	0.01 *
CaO	0.22 *	0.19 ± 0.03	1.21 *	0.09 ± 0.03	0.03 ± 0.01
TiO ₂	0.11 *	0.02 ± 0.01	0.18 *	0.03 ± 0.01	0.04 ± 0.01
V ₂ O ₅					
MnO					
Fe ₂ O ₃	1.75 ± 1.41	0.23 ± 0.03	0.32 *	0.02 ± 0.01	0.05 ± 0.01
<u>Trace elements</u>					
Ni					
Cu	100 *				
Zn					
Ga					3 ± 1
As					
Rb					
Sr					4 ± 1
Y					3 ± 1
Zr	185 *	37 ± 9	141 *	44 ± 12	87 ± 1
Mo					
Ba					23 ± 2
Pb					

¹ Concentrations normalised to 100%² Major elements expressed in weight % oxide and trace elements in ppm³ Errors (3σ SD) determined by counting statistics (AXIOS\$) or the Horwitz function (TN9K\$)⁴ Bulk analysis precisions (PW1K4\$) ~1 % (> 10 ppm) and 10-20% (< 10 ppm)⁵ ND = Not Determined⁶ See Table C.1 for explanation of instrument mnemonics* Errors exceed concentration value (*in situ* analysis) or near LLD (bulk analysis)

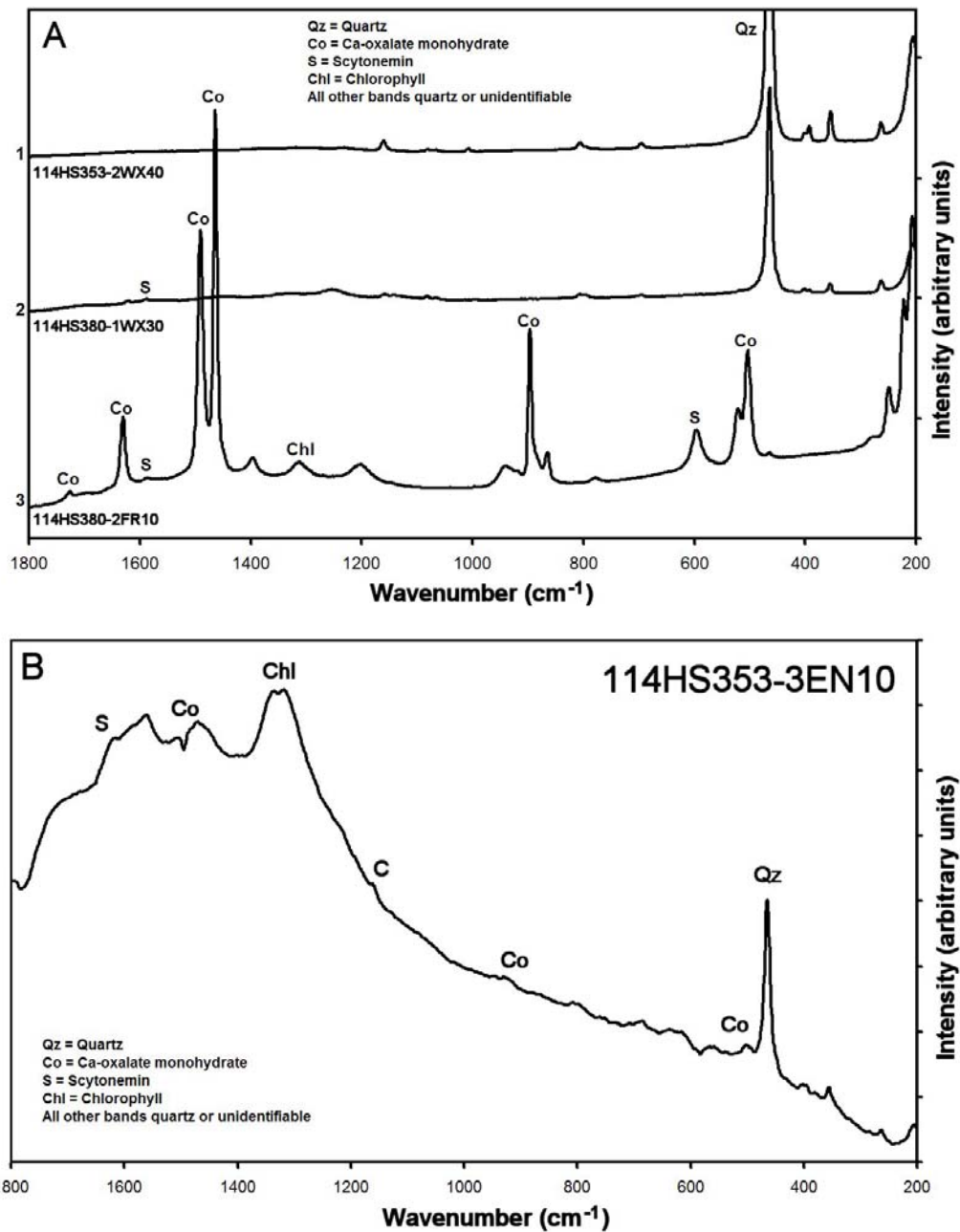


Figure 5.21 *In situ* Raman analysis of samples 114HS353, 114HS354 and 114HS380 (orthoquartzite). The case-hardened exterior is predominantly quartz with minor (disseminated) hematite and goethite (A). The white interior of the rock is also quartz but is colonised by cryptoendolithic microorganisms with characteristic Raman bands for chlorophyll, carotene, scytonemin and Ca-oxalate monohydrate. The black lichen layer between these zones reveals strong organic bands with 1064 nm excitation (B). Instrumentation: UBRAM\$785 (A) and UBRAM\$1064 (B). Courtesy Prof. Howell Edwards, University of Bradford.

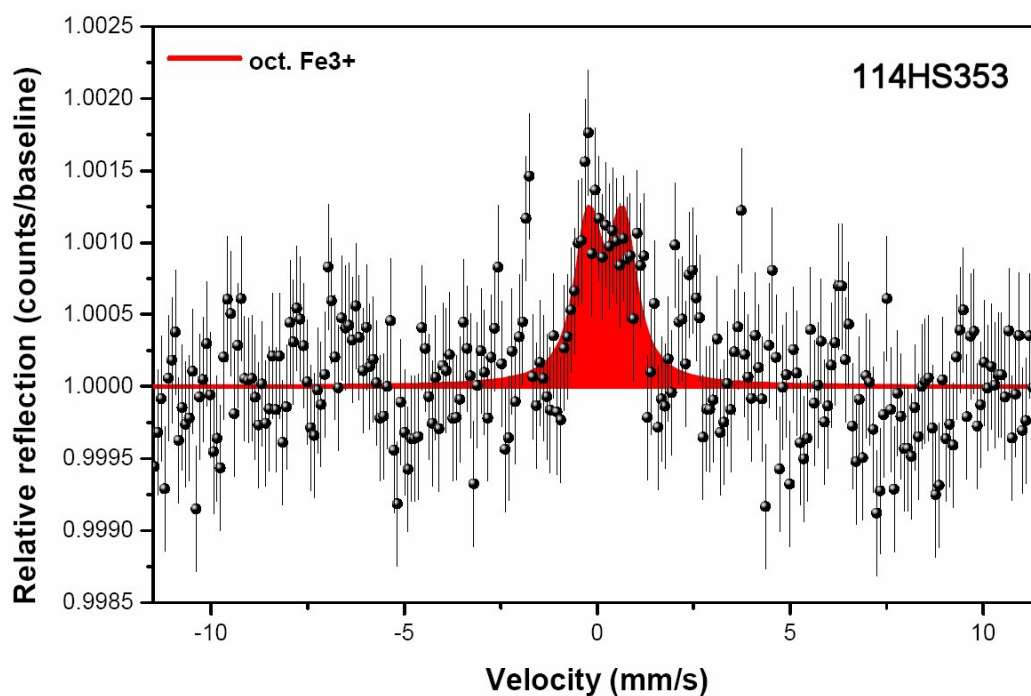


Figure 5.22 *In situ* Mössbauer analysis of sample 114HS353 (orthoquartzite). Although the external surface measured (2WX40) is clearly oxidised (XRF data and Figure 5.18B), the Mössbauer effect was weak. This suggests iron is present as thin grain coatings. Shaded area is a reference fit for octahedral Fe³⁺. Instrumentation: B2MBS\$. Courtesy Dr. Christian Schröder, NASA JSC.

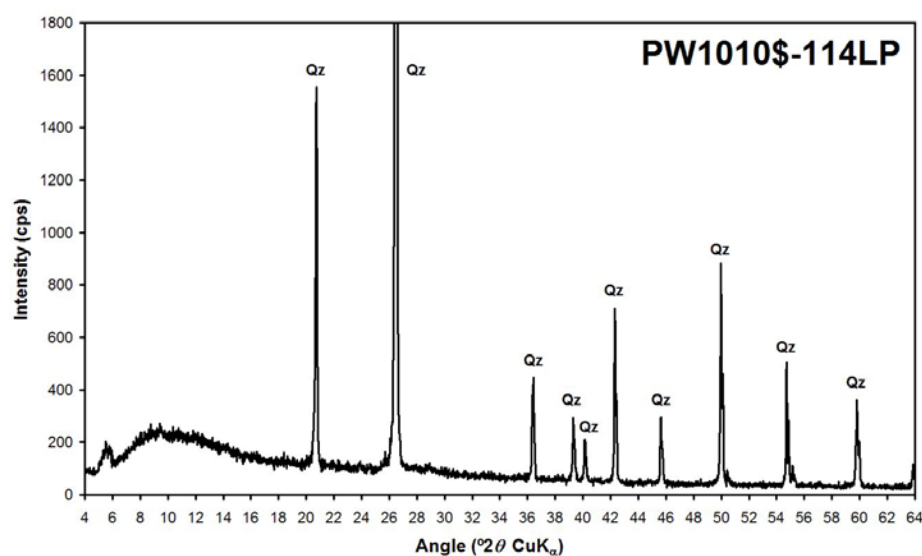


Figure 5.23 Bulk XRD analysis of homogenised powder derived from 114 (orthoquartzite). All peaks are assignable to quartz (Qz). No hematite was observed. Instrumentation: PW1010\$.

5.3.1.3 Geobiological Evaluation

The Raman organic signatures are indisputably the main indicators of biogenicity within these samples. Other data, however, provide critical information for evaluating the life habitat. The light-coloured, granular, slightly porous nature of this material indicates that it could be a suitable habitat for endolithic life forms. In addition, the case-hardened exterior provides a stabilising surface for the fresh interior and protection from the wind. These attributes, together with the observed grain size, are known to be favourable criteria for cryptoendolithic growth (see Section B.5). Furthermore, the combination of distinct colouring on the exfoliated surfaces, the distinct layers of different colours parallel to the outer surface, and bio-fluorescence (not mineral fluorescence) associated with specific coloured spots, is additional evidence for the presence of extant endolithic microorganisms. Multi-spectral imaging confirmed that mobilization of iron occurred and re-precipitation was in a manner consistent with the behaviour of endolithic microorganisms. In a Mars mission context the evidence for biogenicity in this sample is sufficiently strong to justify sampling and further analysis.

5.3.2 Marble, McMurdo, Victoria Land, Antarctica (194)

Section B.6 describes the geology of McMurdo Dry Valleys region at Andrews Ridge and the sample used for this study. Table 5.11 presents a summary of the *in situ* imaging and analytical results for sample 194HS435. Semi-quantitative geochemistry data are shown in Table 5.12.

5.3.2.1 Physical Properties

Proximal imaging of 194HS435 showed a coarse crystalline, granular texture with intergranular Fe-oxide staining on weathered surfaces, and areas of blue coloration (Figure 5.24A). Macroscopic colour images showed the blue regions in more detail and indicated other areas that were pink and black (Figure 5.24B). Spectral classification with the Nuance camera of these areas (Figure 5.25) indicated the possible presence of organic components (c-phycoyanin absorption peak at 618 nm) thus suggesting they are chasmoendolithic microbial colonies. Furthermore, the blue zones fluoresced when subjected to UV light (Figure 5.26A).

Table 5.11: Summary of *in situ* results for Marble, McMurdo, Antarctica (194)

<i>In Situ</i> Techniques ¹	Results	Reference
Proximal Imaging (B2SCS\$GEOL\$SOL)	Spectral anomalies	Section 5.3.2.1 Figure 5.24A
Macroscopic Imaging (B2SCS\$CUL\$RGB) (B2SCS\$CUL\$UV) (NUVIS\$MAC10\$SOL) (NUVIS\$MIC10\$SOL)	Bio-fluorescence Visible chasmoendoliths	Section 5.3.2.1 Figure 5.24B Figure 5.25 Figure 5.26A
Microscopic Imaging (B2MIC\$RGB) (B2MIC\$UV)	Globular texture of chasmoendoliths Distribution of bio-fluorescence	Section 5.3.2.1 Figure 5.24C Figure 5.24D Figure 5.26B
X-Ray Fluorescence (TN9K\$FCA) (AXIOS\$HS)	Mg-carbonate Ca, Mg, Si, Fe, Al, S, Ba, Sr (<i>fresh interior</i>) Ca, Mg, Si, Fe, Al, Mn, Ti, K, Sr, Zn (<i>exterior</i>) Ca, Mg, Si, Al, Fe, S, K, Na, Ti, Sr, Zn (<i>fracture</i>)	Section 5.3.2.1 Table 5.12
Raman Spectroscopy (UBRAM\$488) (UBRAM\$514) (UBRAM\$785) (UBRAM\$1064)	Dolomite with goethite (<i>pink zones</i>) Calcite (<i>black and pink zones</i>) Chlorophyll with a carotenoid (<i>pink and black zones</i>) Carotenes and c-phycoyanin (<i>blue-green zones</i>) Scytonemin (<i>black zones</i>) <i>Note: Quartz and olivine bands (probably detrital origin)</i>	Section 5.3.2.1 Figure 5.27 Figure 5.28
Mössbauer Spectroscopy	No analysed	
X-Ray Diffraction (PW1010\$)	Not analysed using NHMXRD\$ <i>Note: Powder XRD analysis indicates dolomite and calcite</i>	Section 5.3.2.1 Figure 5.29

¹ See Table C.1 for explanation of instrument mnemonics

In situ microscopy showed the chasmoendoliths to exhibit a globular texture (Figure 5.24CD). Under UV illumination these areas coincided with the visible areas of coloration (Figure 5.26B) but fluorescence also occurred within other areas, suggesting that the distribution of the biota is more pervasive than can be visually determined. Some parts of the visible colonies did not fluoresce, which leads one to assume these areas may be associated with UV protective pigments.

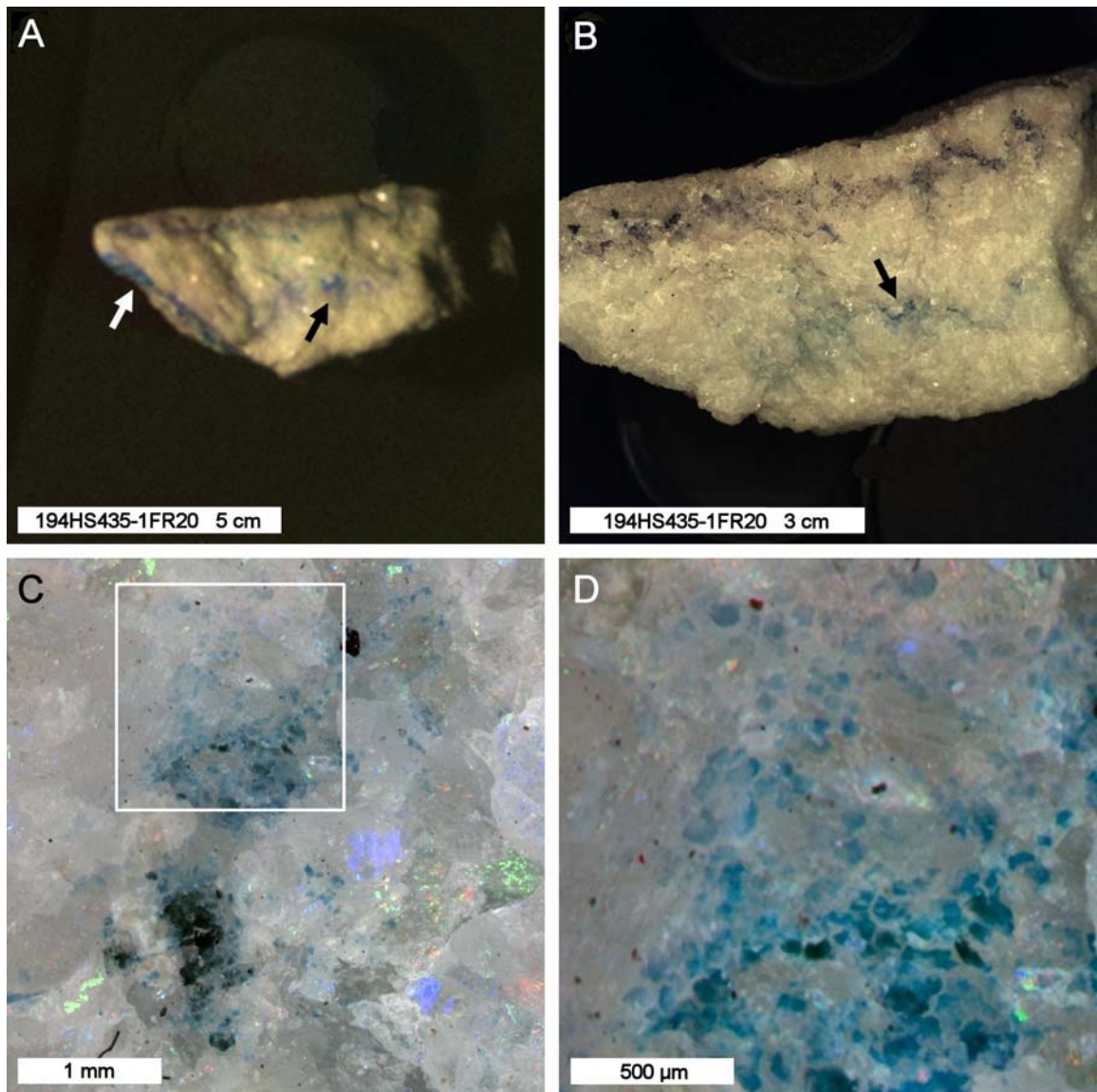


Figure 5.24 Proximal, macroscopic and microscopic imaging of sample 194HS435 (marble). Colour composite imaging at 60 cm reveals patches of blue-green on a variety of surfaces (A). Macroscopic imaging under controlled illumination at 8 cm reveals distinct areas of colour (chasmoendoliths) and a crystalline fabric (B). Microscopic imaging shows the chasmoendoliths to exhibit a globular morphology (C and D). Note the specular reflections from the crystalline surface (C) as a result of direct LED illumination. Instrumentation: B2SCS\$\$\$SOL (A), B2SCS\$CUL\$RGB (B) and B2MIC\$\$RGB (C and D).

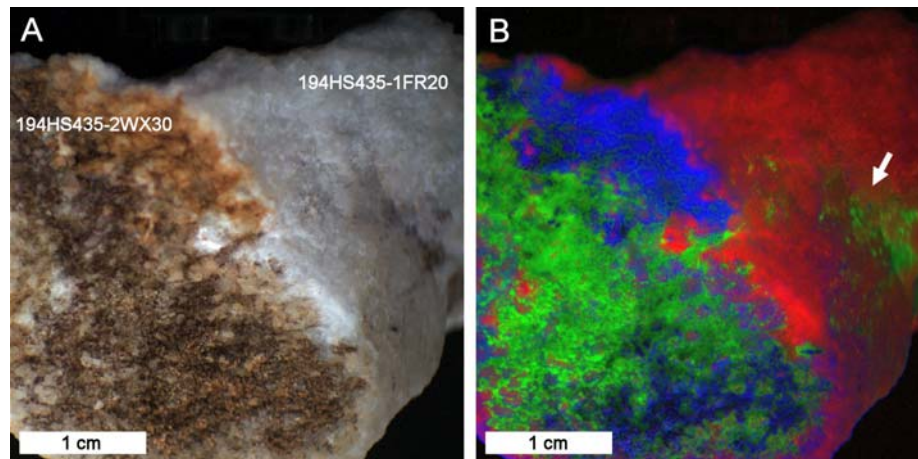


Figure 5.25 Macroscopic imaging of sample 194HS435 (marble) with the Nuance multi-spectral system at 8 cm. The true colour image (A) shows the extent of weathered (2WX30) and fresh (1FR20) surfaces. The spectrally classified image of the equivalent field of view (B) distinguishes three surface types, fresh dolomite (red), oxidised exterior (blue), and chasmoendolithic zones (green). The spectral characteristics of the endolithic zones are based on a strong absorption peak centred at 618 nm which may correspond to c-phycoyanin. See Figure 5.24CD and Figure 5.26B for detailed views of the area highlighted (arrow). Instrumentation: NUVISSMAC10SSOL.

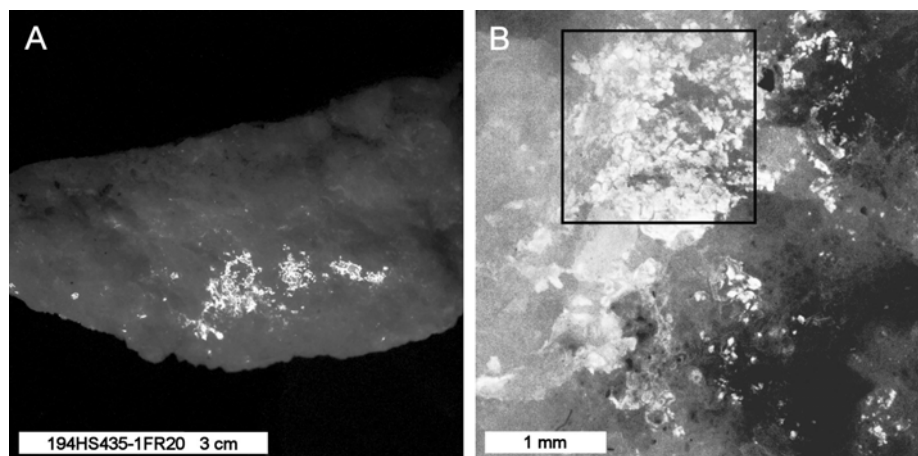


Figure 5.26 Macroscopic and microscopic imaging of sample 194HS435 (marble) under UV illumination. Imaging at 8 cm with off-axis UV illumination shows the chasmoendolithic regions observed in Figure 5.24B to fluoresce (A). Microscopic imaging using integral UV LEDs accentuates the detailed globular structure of the microbial communities (B). The highlighted area (box) is the same field of view as shown in Figure 5.24D. Instrumentation: B2SCS\$CUL\$365 (A) and B2MIC\$\$UV (B).

5.3.2.2 Chemistry and Mineralogy

In situ WDXRF analysis was performed on the three surface types visible on sample 194HS435 (Figure B.12). Fresh material (1FR20) was shown to consist of Mg (12 wt % MgO), Al (0.3 wt % Al₂O₃), Si (2.2 wt % SiO₂), S (0.2 wt % SO₃), Ca (34.5 wt % CaO), and Fe (0.4 wt % Fe₂O₃), with traces of Sr (228 ppm), and Ba (609 ppm). Both weathered surfaces (2WX30 and 3WX30) were slightly depleted in Mg and Ca, and enriched in all other major elements. Ba was not detected but Zn was present in both cases (145 ppm). The external surface (3WX30) was relatively more enriched in Si (5.5 wt % SiO₂), Mn (0.3 wt % MnO), and Fe (1.8 wt % Fe₂O₃) than the fracture surface (2WX30). Sr remained fairly consistent for all three surfaces, ranging from 219 ppm (3WX30) to 295 ppm (2WX30).

In situ EDXRF analysis of 194HS435-1FR20 revealed a partial composition consisting of K (0.2 wt % K₂O), Ca (30 wt % CaO), Fe (0.1 wt % Fe₂O₃), Zn (166 ppm), and Sr (60 ppm). Similar values were obtained from external surface 3WX30 although Ca was slightly lower (26 wt % CaO) and Fe slightly higher (0.6 wt % Fe₂O₃). Surface 2WX30 was not analysed by *in situ* EDXRF.

In situ Raman spectroscopic analysis of fresh surfaces (194HS435-1FR20) confirmed the sample to be composed of dolomite (1098, 724, 338, 300 and 174 cm⁻¹), with traces of goethite (688 and 388 cm⁻¹) associated with pink zones. Calcite was also present (1086, 713, 281 and 156 cm⁻¹) (Figure 5.27) and occurred as a white dust only within the black and pink zones of the sample. The identification of calcite is particularly interesting since the mineral was also clearly identified by XRD (Figure 5.29). Quartz (206 and 464 cm⁻¹) and olivine (956, 919, 881, 856 and 824 cm⁻¹) were also identified by Raman but were not corroborated by XRD. Given the composition of the host rock, these minerals are most likely to be of detrital origin, being exogenously emplaced by aeolian or fluvial processes into the fractures exploited by the chasmoendolithic cyanobacteria.

Table 5.12 Semi-quantitative geochemical analysis of Marble (194)

<i>Instrument</i>	AXIOS\$	TN9K\$	AXIOS\$	TN9K\$	AXIOS\$
<i>Sample</i>	194HS435	194HS435	194HS435	194HS435	194HS435
<i>Target</i>	3WX30	3WX30	1FR20	1FR20	2WX30
	(exterior)	(exterior)	(interior)	(interior)	(fracture)
<u>Major elements</u>					
Na ₂ O		ND	0.05 *	ND	0.13 *
MgO	11.09 ± 0.69	ND	12.06 ± 0.65	ND	10.61 ± 0.78
Al ₂ O ₃	1.47 ± 1.32	ND	0.3 *	ND	2.23 ± 1.17
SiO ₂	5.49 ± 0.74	ND	2.19 ± 1.14	ND	4.81 ± 0.87
P ₂ O ₅	0.03 *	ND	0.03 *	ND	0.08 *
SO ₃	0.05 *	ND	0.23 *	ND	0.44 *
Cl	0.02 *	ND	0.04 *	ND	0.07 *
K ₂ O	0.14 *	0.36 ± 0.06	0.04 *	0.16 ± 0.03	0.16 *
CaO	29.63 ± 0.3	25.7 ± 1.89	34.47 ± 0.27	29.8 ± 2.16	30.25 ± 0.32
TiO ₂	0.16 *	0.06 ± 0.01	0.04 *		0.11 *
V ₂ O ₅					
MnO	0.29 *	0.06 ± 0.01	0.06 *		0.09 *
Fe ₂ O ₃	1.77 ± 1.48	0.64 ± 0.09	0.43 *	0.1 ± 0.03	1.06 *
<u>Trace elements</u>					
Ni					
Cu					
Zn	145 *	184 ± 39		166 ± 36	145 *
Ga					
As					
Rb					
Sr	219 *	76 ± 18	228 *	60 ± 15	295 *
Y					
Zr					
Mo					
Ba			609 * (TBC)		
Pb	111 *				

¹ Concentrations normalised to 50% (carbonate)

² Major elements expressed in weight % oxide and trace elements in ppm

³ Errors (3σ SD) determined by counting statistics (AXIOS\$) or the Horwitz function (TN9K\$)

⁴ ND = Not Determined

⁵ See Table C.1 for explanation of instrument mnemonics

* Errors exceed concentration value (*in situ* analysis) or near LLD (bulk analysis)

Various organic components were also identified across 194HS435-1FR20. Chlorophyll (1327, 988 and 742 cm^{-1}) only occurs in the pink and black regions in association with a carotenoid (1512, 1155 and 1003 cm^{-1}). Two other carotenes were tentatively identified within the blue-green regions as beta-carotene (1515, 1154 and 1002 cm^{-1}) and zeaxanthin (1520, 1156 and 1005 cm^{-1}). It must be noted that specific identification of these carotenes is difficult due to the small wavenumber shift that differentiates them. Nevertheless, carotenes are unambiguously present. Also within the blue-green regions, numerous peaks could be attributed to the photosynthetic accessory pigment c-phycoyanin (1630, 1580, 1498, 1367, 1327, 1308, 1047, 739 and 661 cm^{-1}) (Figure 5.28). Together with chlorophyll, this is the most likely source of the bio-fluorescence observed with the Beagle 2 cameras (Figure 5.26). The UV protective pigment scytonemin (1603 to 272 cm^{-1}) is unambiguously identified within the black region (i.e., closest zone to the exterior of the rock). Finally, some of the other less well-defined (broader) peaks within the Raman spectra were possibly an additional organic compound which could not be identified without further measurements and detailed analysis.

In situ Mössbauer spectroscopy was not performed on sample 194HS435 due to unavailability of the instrument.

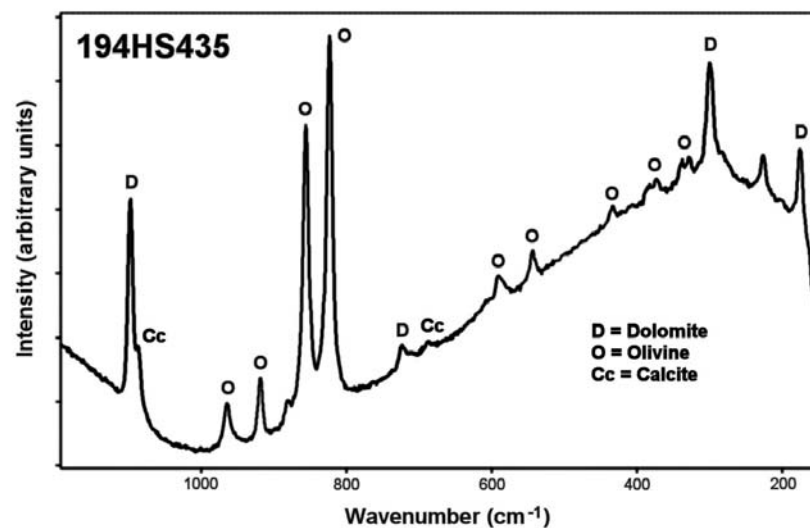


Figure 5.27 *In situ* Raman analysis (785 nm laser) of sample 194HS435 (marble) (after Edwards *et al.*, 2007). The dominant mineralogy evident in all spectra is dolomite (D) but some targets (this spectrum) showed Raman bands assignable to olivine and calcite (Cc). These minerals are likely to be of detrital origin. Instrumentation: UBRAM\$785. Courtesy Prof. Howell Edwards, University of Bradford.

Bulk XRD analysis of powder derived from mostly fresh material showed 194HS435 to be composed of dolomite with some evidence of calcite (Figure 5.29).

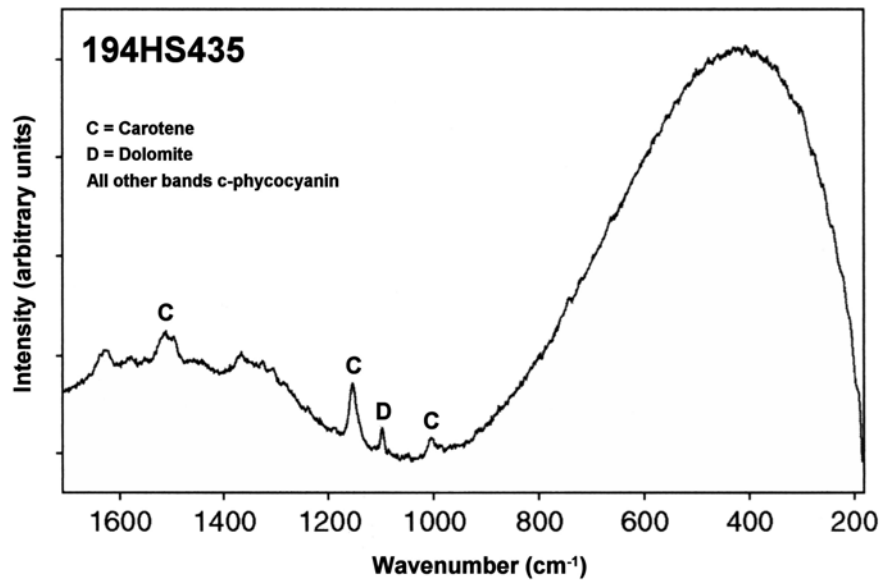


Figure 5.28 *In situ* Raman analysis (514 nm laser) of sample 194HS435 (marble). Spectra acquired from the blue-green areas of 194HS435-1FR20 (Figure 5.24D) show Raman signatures associated with the photosynthetic accessory pigments carotene and c-phycoerythrin. Instrumentation: UBRAM\$514. Courtesy Prof. Howell Edwards, University of Bradford.

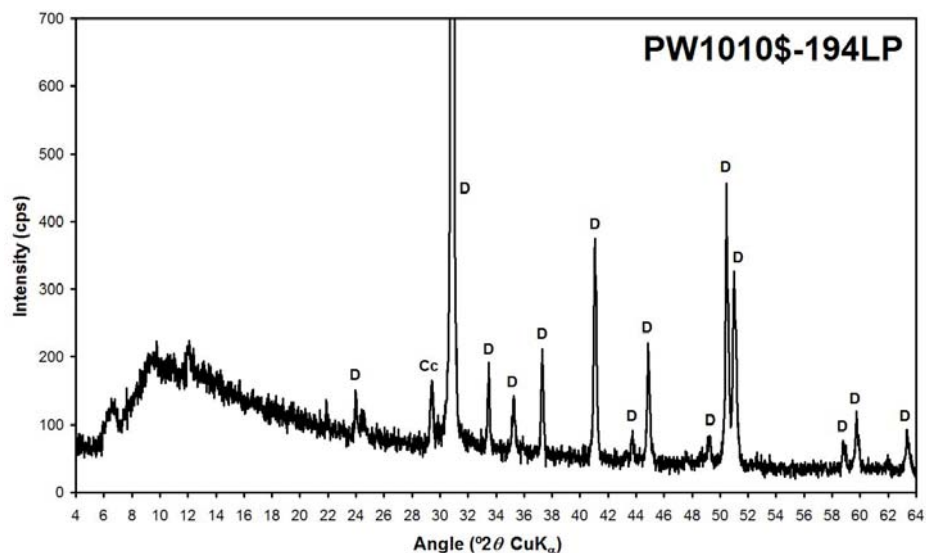


Figure 5.29 Bulk XRD analysis of homogenised powder derived from sample 194HS435 (marble). Most peaks are assignable to dolomite (D) but calcite (Cc) is also identified. Instrumentation: PW1010\$.

5.3.2.3 Geobiological Evaluation

As with sample 114HS353 (orthoquartzite), the identification of a variety of organic components in 194HS435 by Raman spectroscopy constitutes an unambiguous compositional biosignature. Colour and UV imaging allowed for the distribution of the biogenic organic components to be linked to the visible globular clusters on the fracture surfaces (morphological biosignature). Both imaging methods also showed that the chasmoendolithic organisms are more widely distributed than can be seen visually. The nature of the rock and the distribution of the organic biosignatures along fracture surfaces show that these organisms have developed in a chasmoendolithic habitat. In a Mars mission context this rock would be a strong candidate for sampling and further analysis.

5.3.3 Gypsum, Haughton Crater, Devon Island, Canada (44)

Section B.7 describes the geology of Haughton Crater and the samples used for this study. Table 5.13 presents a summary of the *in situ* imaging and analytical results for samples 44HS340 and 44HS419. Semi-quantitative geochemistry data are shown in Table 5.14.

5.3.3.1 Physical Properties

Proximal and macroscopic imaging of 44HS419 revealed a pearly lustrous surface (Figure 5.30A) with a well-defined laminated structure (Figure 5.30B). In places, the sample is highly reflective (especially when imaged parallel to cleavage), but opaque spots and assemblages (chasmoendoliths) could still be readily observed macroscopically (Figure 5.30C).

Due to the clarity of the selenite, the distribution of the chasmoendolithic microbial communities could be determined vertically using the Beagle 2 microscope to an accuracy of ~20 μm by mapping in-focus regions within each image of the stack (Figure 5.30D).

Table 5.13: Summary of *in situ* results for Gypsum, Houghton Crater, Canada (44)

<i>In Situ</i> Techniques¹	Results	Reference
Proximal Imaging (B2SCS\$GEOL\$SOL)	Evidence of layering	Section 5.3.3.1 Figure 5.30A
Macroscopic Imaging (B2SCS\$CUL\$RGB) (B2SCS\$CUL\$UV) (NUVIS\$MAC10\$SOL) (NUVIS\$MIC10\$SOL)	Visible chasmoendoliths Translucency	Section 5.3.3.1 Figure 5.30B Figure 5.30C
Microscopic Imaging (B2MIC\$\$RGB) (B2MIC\$\$UV)	Globular texture of chasmoendoliths Vertical distribution of colonies	Section 5.3.3.1 Figure 5.30D
X-Ray Fluorescence (TN9K\$\$FCA) (AXIOS\$HS)	Sulphate with trace element enrichment Ca, S, Si, Mg, Sr (<i>fresh cleavage surface</i>)	Section 5.3.3.2 Table 5.14
Raman Spectroscopy (UBRAM\$\$488) (UBRAM\$\$514) (UBRAM\$\$785) (UBRAM\$\$1064)	Gypsum (<i>all surfaces</i>) Carotenoid, scytonemin, and chlorophyll (<i>Type I</i>) Parietin, carotenoid, and chlorophyll (<i>Type II</i>)	Section 5.3.3.2 Figure 5.31 Figure 5.32
Mössbauer Spectroscopy	Not analysed due to very little Fe content determined by XRF	
X-Ray Diffraction (PW1010\$)	Not analysed using NHMXRD\$ <i>Note: Powder XRD analysis indicates gypsum only.</i>	Section 5.3.3.2 Figure 5.33

¹ See Table C.1 for explanation of instrument mnemonics

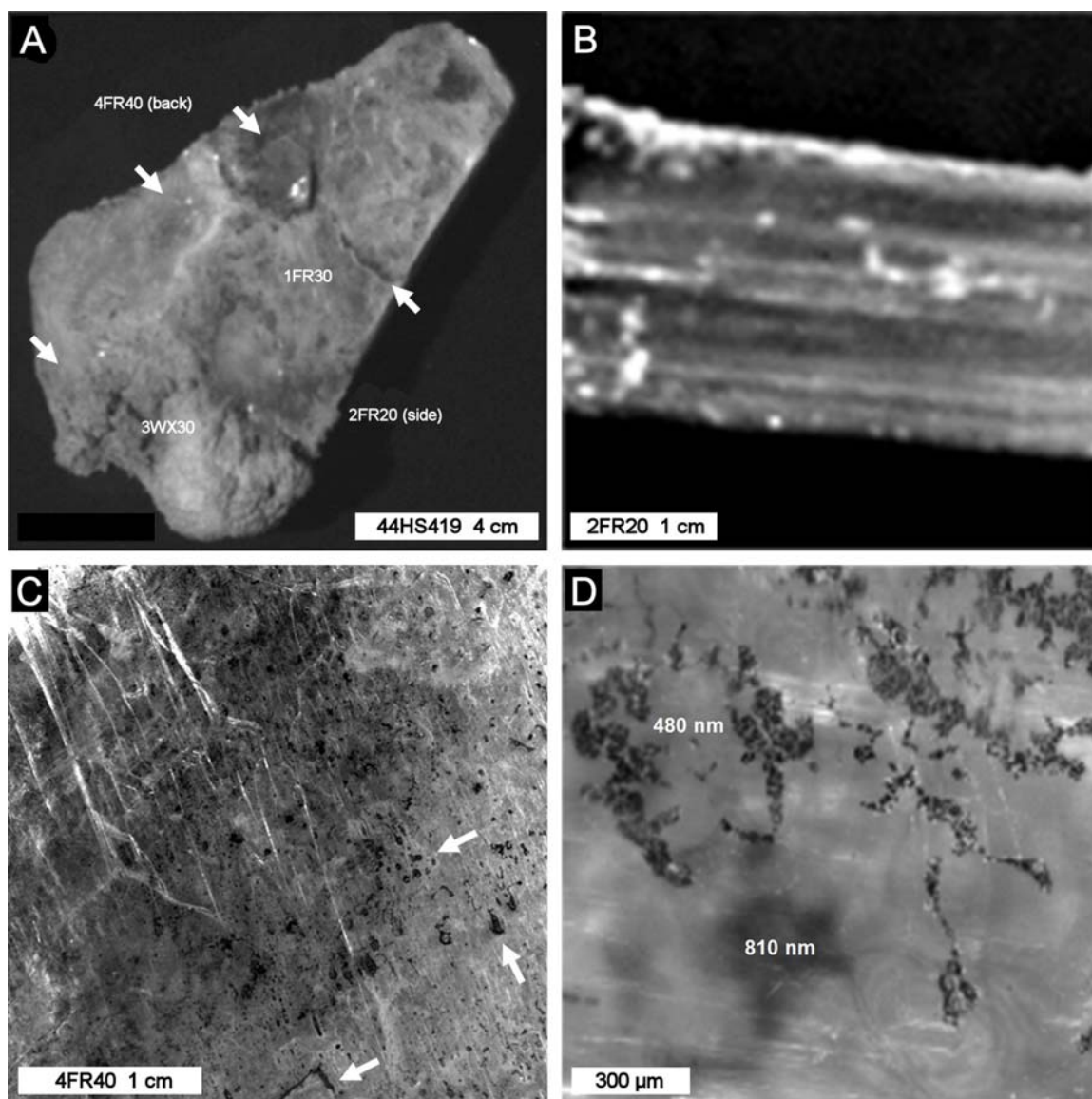


Figure 5.30 Proximal, macroscopic and microscopic imaging of sample 44HS419 (gypsum var. selenite). Imaging at 60 cm shows a lustrous surface with evidence of a laminated fabric in plan view (A) and in cross-section (B). Stereo imaging of the latter (not shown) reveals variable relief associated with very thin cleavage folia. Macroscopic imaging at 8 cm of the reverse side of 44HS419 (C) shows numerous black spots (chasmaendoliths) distributed both laterally and vertically into the specimen (observable due to the transparency and clarity of the gypsum). Microscopic imaging shows the chasmaendoliths to exhibit globular/chain-like morphologies (D). Two vertically spaced colonies are shown, one in focus (480 nm below the surface), and one out of focus (810 nm below the surface). Instrumentation: B2SCS\$670\$SOL (A and B), B2SCS\$CUL\$SOL (C) and B2MIC\$R (D).

5.3.3.2 Chemistry and Mineralogy

In situ WDXRF of fresh, uncolonised selenite (44HS340) confirmed an elemental composition of Mg (0.1 wt % MgO), Si (0.2 wt % SiO₂), S (42 wt % SO₃), Ca (37 wt % CaO) and significant Sr (1240 ppm). *In situ* EDXRF only detected Ca (21 wt % CaO) and Sr (308 ppm), both at lower levels compared to *in situ* WDXRF. Interestingly, EDXRF values for Ca and Sr corresponded better with the bulk composition determined on 44PP581 by WDXRF (29 wt % CaO and 360 ppm Sr). No Fe was detected on fresh surfaces using both *in situ* XRF techniques. Bulk analysis of 44PP581 did report some Fe (0.05 wt % Fe₂O₃).

In situ Raman spectroscopy was performed on similar samples to 44HS340 by Edwards *et al.* (2005). Results using 514 nm laser excitation unambiguously confirmed the presence of gypsum (1142, 1008, 618, 493, 414, 211 and 181 cm⁻¹). Similar results were also obtained with 785 nm excitation. However, Raman spectra from areas associated with observed dark spots exhumed at the surface were characteristic in that they did not contain any gypsum bands at all implying that these spectral signatures were related to the features themselves. A survey of several of these areas was conducted and two different spectral signatures were found (Figure 5.31). The first (later confirmed as *Nostoc commune*) showed well-defined bands associated with a carotenoid (1517, 1157 and 1006 cm⁻¹), scytonemin (1630, 1598, 1552, 1454, 1379 and 1281 cm⁻¹) and chlorophyll (weak feature around 1340 cm⁻¹). The second (later confirmed as *Gloeocapsa alpina*) showed well defined bands associated with parietin (1671, 1575, 1197, and 914 cm⁻¹), a carotenoid (1517 and 1157 cm⁻¹), and chlorophyll (broad, intense feature centred at 1340 cm⁻¹). The prominent band at 464 cm⁻¹ was also assigned to parietin even though this wavenumber would be more commonly assigned to alpha-quartz. However, since quartz was not observed anywhere else in the Raman spectra, and was not reported by XRD, it seemed more likely to be parietin.

Confocal spectroscopic studies of subsurface colonies within similar samples to 44HS340 were also performed by Edwards *et al.* (2005) to test whether the organic signatures could be discriminated from the effects of the host. Figure 5.32 shows a sequence of spectra acquired at various depths from the surface of the gypsum to the interface at which the colony resides (~3 mm depth). By subtracting the gypsum signal the organic signature was enhanced, and in this case successfully matched to organism Type II (Figure 5.31).

Table 5.14 Semi-quantitative geochemical analysis of Gypsum (44)

<i>Instrument</i>	AXIOS\$	TN9K\$	AXIOS\$	PW1K4\$
<i>Sample</i>	44HS340	44HS340	44HS340	44PP581
<i>Target</i>	9XX20 (fresh)	0XX30 (fresh)	10XX10 (colonised)	(bulk)
<u>Major elements</u>				
Na ₂ O	0.01 *	ND	0.11 *	0.03 ± 0.01
MgO	0.11 *	ND	0.44 *	0.12 ± 0.01
Al ₂ O ₃	0.02 *	ND	0.09 *	0.13 ± 0.01
SiO ₂	0.17 *	ND	0.63 *	0.37 ± 0.01
P ₂ O ₅		ND	0.01 *	0.01 *
SO ₃	42.09 ± 0.17	ND	38.23 ± 0.26	41.74 ± 0.42
Cl	0.03 *	ND	0.04 *	
K ₂ O	0.02 *		0.09 *	
CaO	37.4 ± 0.28	22.03 ± 1.65	40.1 ± 0.4	29.53 ± 0.3
TiO ₂				
V ₂ O ₅				
MnO				
Fe ₂ O ₃			0.1 *	0.05 ± 0.01
<u>Trace elements</u>				
Ni				
Cu				
Zn				
Ga				
As				
Rb				
Sr	1241 *	308 ± 63	1392 *	360 ± 4
Y				
Zr				
Mo				
Ba				
Pb				

¹ Concentrations normalised to 80% (sulphate)² Major elements expressed in weight % oxide and trace elements in ppm³ Errors (3σ SD) determined by counting statistics (AXIOS\$) or the Horwitz function (TN9K\$)⁴ Bulk analysis precisions (PW1K4\$) ~1 % (> 10 ppm) and ~10-20% (< 10 ppm)⁵ ND = Not Determined⁶ See Table C.1 for explanation of instrument mnemonics* Errors exceed concentration value (*in situ* analysis) or near LLD (bulk analysis)

In situ Mössbauer spectroscopy was not performed due to low Fe content (0.05 wt % Fe₂O₃).

Bulk XRD analysis provided mineralogical evidence for gypsum only (Figure 5.33) even though the powders were deliberately derived from impure parts of specimen 44HS340.

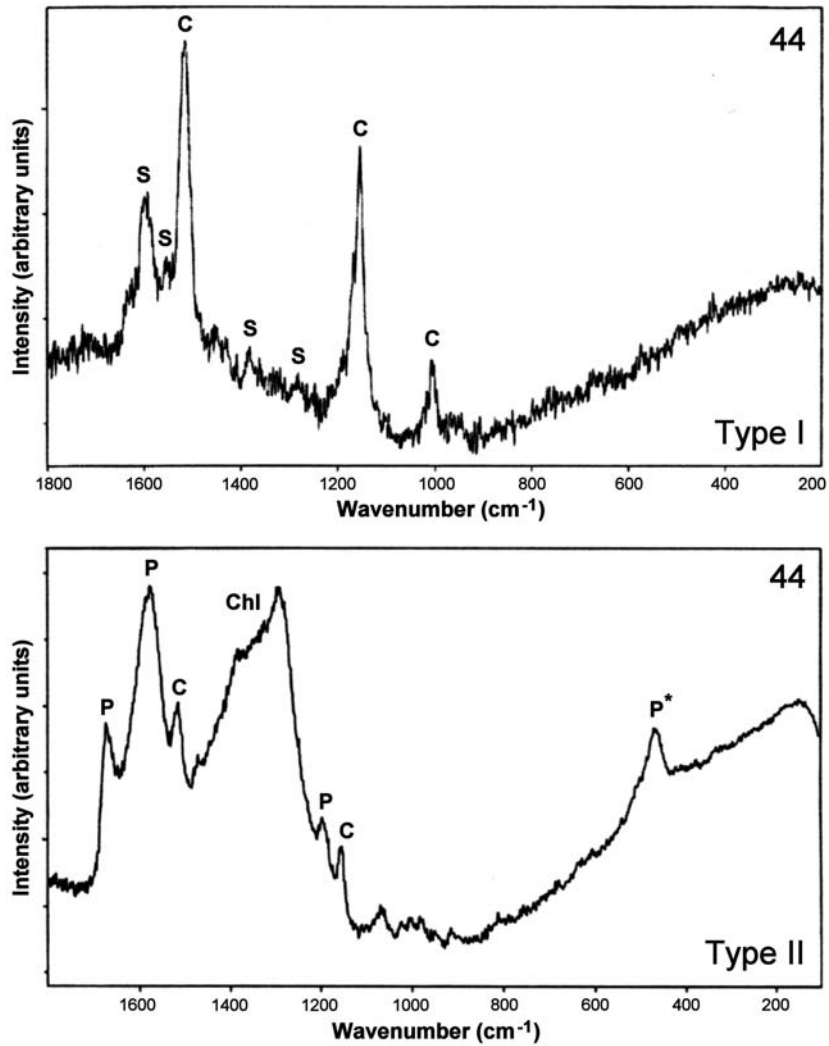


Figure 5.31 *In situ* Raman analysis of a sample similar to 44HS340 (gypsum var. selenite) using 514 nm laser excitation (after Edwards *et al.*, 2005). Two types of halotrophic cyanobacterium can be identified within the same target. Type I (*Nostoc commune*) is characterised by Raman signatures for scytonemin (S) and carotene (C). Type II (*Gloeocapsa alpina*) is characterised by parietin (P), carotene (C) and chlorophyll (Chl). Although the Raman band at 464 cm⁻¹ would normally be assigned to quartz, contextual data supports a parietin assignment in this case. Instrumentation: UBRAM\$514. Courtesy Prof. Howell Edwards, University of Bradford.

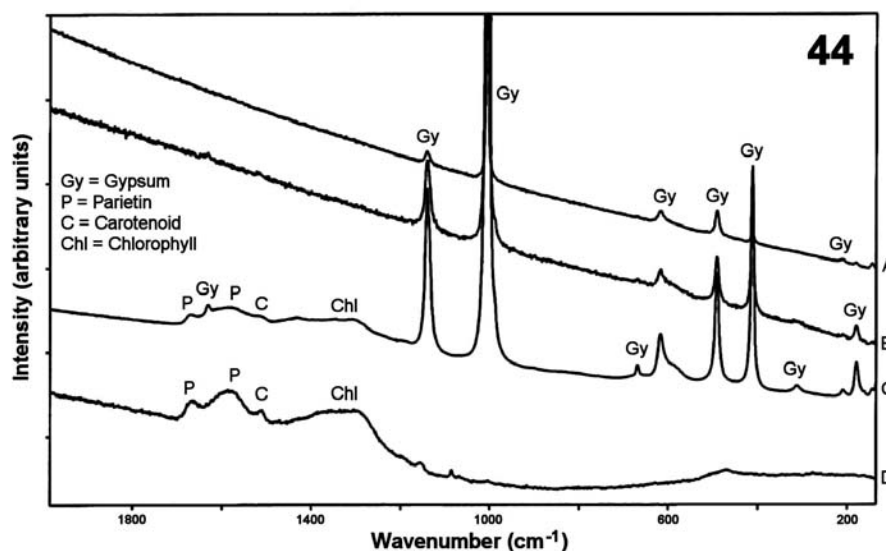


Figure 5.32 *In situ* Raman profile of a sample similar to 44HS340 (gypsum var. selenite) using 514 nm laser excitation (after Edwards *et al.*, 2005). Spectra acquired at the surface of the gypsum (A) and at 1 mm depth (B) show no organic signatures. The spectrum acquired at 3 mm depth (C) represents the interface between the chasmoendolithic microbial community and the gypsum host. Subtracting the gypsum signal reveals an organic signature corresponding to Type II (Figure 5.31). Instrumentation: UBRAM\$514. Courtesy Prof. Howell Edwards, University of Bradford.

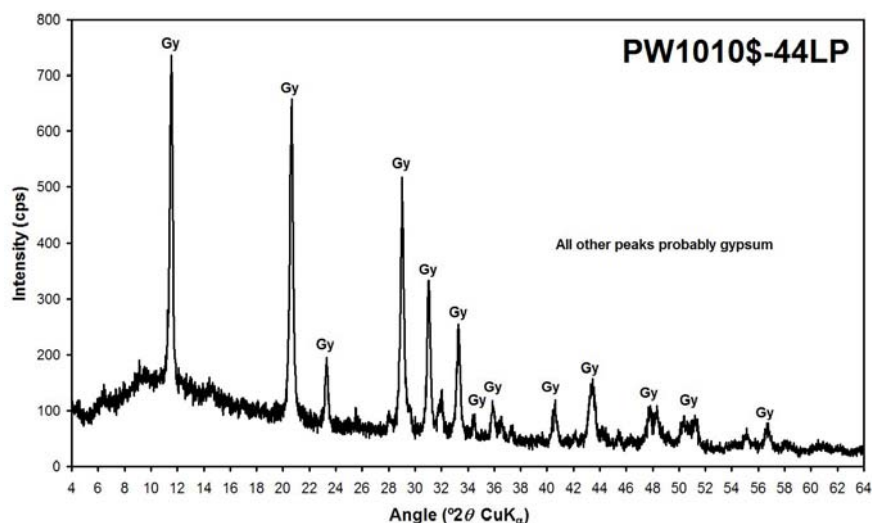


Figure 5.33 Bulk XRD analysis of homogenised powder derived from sample 44HS340 (pure selenite with some clay contamination). All peaks are assignable to gypsum (Gy). Instrumentation: PW1010\$.

5.3.3.3 Geobiological Evaluation

The correlation of biogenic compounds with the black spots observed within the cleavage planes of sample 44HS419 is clear evidence of their biogenicity. Furthermore, the identification of two organisms exhibiting different survival and adaptive strategies is significant. One system uses scytonemin as a UV radiation protective mechanism whereas the other uses parietin. The presence of chlorophyll in both types suggests they are photosynthetic cyanobacteria, and presumably exploit the nature of host medium to the full. The distribution of microbial colonies between the cleavage planes of the colourless gypsum demonstrates a chasmoendolithic habitat.

In a Mars mission context selective sampling and further analysis of these microbial features would be entirely justified. However, given what would be known prior to sampling, based on the above *in situ* results, some consideration would need to be made to avoid potential dilution or loss of any biosignatures.

5.4 Ancient Sedimentary Structures

Visually contrasting features could be discerned at all three scales (<family> = 190). Some however were best viewed at the macroscopic scale due to the size (<family> = 163) or subtlety (<family> = 159) of features. Multi-spectral imaging proved useful for each case, especially where there was a compositional dichotomy (<family> = 163) or where superficial iron staining was evident (<family> = 159). Microscopic 3D imaging was useful in revealing differences in relief associated with thin laminae on natural surfaces (<family> = 190).

5.4.1 Banded Chert, Kitty's Gap, Pilbara, Australia (190)

Section B.8 describes the geology of the Kitty's Gap site and the samples used for this study. Table 5.15 presents a summary of the *in situ* imaging and analytical results for samples 190HS390 and 190RS424. Semi-quantitative geochemistry data are shown in Table 5.16.

Table 5.15: Summary of *in situ* results for Banded Chert, Pilbara, Australia (190)

<i>In Situ</i> Techniques ¹	Results	Reference
Proximal Imaging (B2SCS\$GEOL\$SOL)	Evidence of cross-bedding	Section 5.4.1.1 Figure 5.34A
Macroscopic Imaging (B2SCS\$CUL\$RGB) (NUVIS\$MAC10\$SOL)	Details of lamination style	Section 5.4.1.1 Figure 5.34B
Microscopic Imaging (B2MIC\$RGB)	Surface relief associated with relict laminae	Section 5.4.1.1 Figure 5.35
X-Ray Fluorescence (TN9K\$FCA) (AXIOS\$HS) (PW1K4\$FB)	Silicate with relative trace element enrichment Si, Al, K, Ti, Fe, Ba, Zr, Rb, Sr, Y, Ni, Cu <i>Note: White bands more enriched in K, Al and Fe</i>	Section 5.4.1.2 Table 5.16
Raman Spectroscopy (UBRAM\$488) (UBRAM\$514) (UBRAM\$785) (UBRAM\$1064)	Quartz (<i>all surfaces</i>) Rutile and anatase (<i>isolated spots</i>) Carbon (<i>black bands</i>) Goethite, hematite, calcite, and graphite (<i>coatings</i>) Broad (degraded) organic signature (<i>black particles</i>)	Section 5.4.1.2
Mössbauer Spectroscopy (B2MBSS)	Chalcopyrite? ² <i>Note: Footprint too large to distinguish between laminae</i>	Section 5.4.1.2
X-Ray Diffraction (NHMXRD\$) (PW1010\$)	Quartz plus feldspar and clay (<i>fresh surface</i>) <i>Note: Powder XRD analysis indicates quartz with muscovite.</i>	Section 5.4.1.2 Figure 5.36

¹ See Table C.1 for explanation of instrument mnemonics² Kojima *et al.*, 1998. Compatible IS and QS parameters but B_hf is too low (Vaughan and Craig, 1978)

5.4.1.1 Physical Properties

Laminations, cross-bedding and flaser-linsen structures that characterise this specimen were clearly visible at proximal and macroscopic scales (Figure 5.34). From these observations way-up criteria was unambiguously determined (Figure B.17). Colour macroscopy confirmed Fe-oxide staining to be primarily associated with, and localised to, fracture planes.

Microscopic imaging of selected features revealed details of individual inframillimetric laminae and larger clasts (Figure 5.35A), and depth maps indicated a noticeable distinction in surface relief between the black and white laminae (Figure 5.35B). The latter is probably related to the differences in grain size and chemical composition of the black and white laminae (Orberger *et al.*, 2006; Westall *et al.*, 2006b) which, in turn, influences mechanical resistance to weathering. Individual grains ranging in size from about 20 to > 100 μm were visible in the white layers, especially at the interface with the black layers, where the white grains stood out visually. Black layers appeared to be very fine-grained.

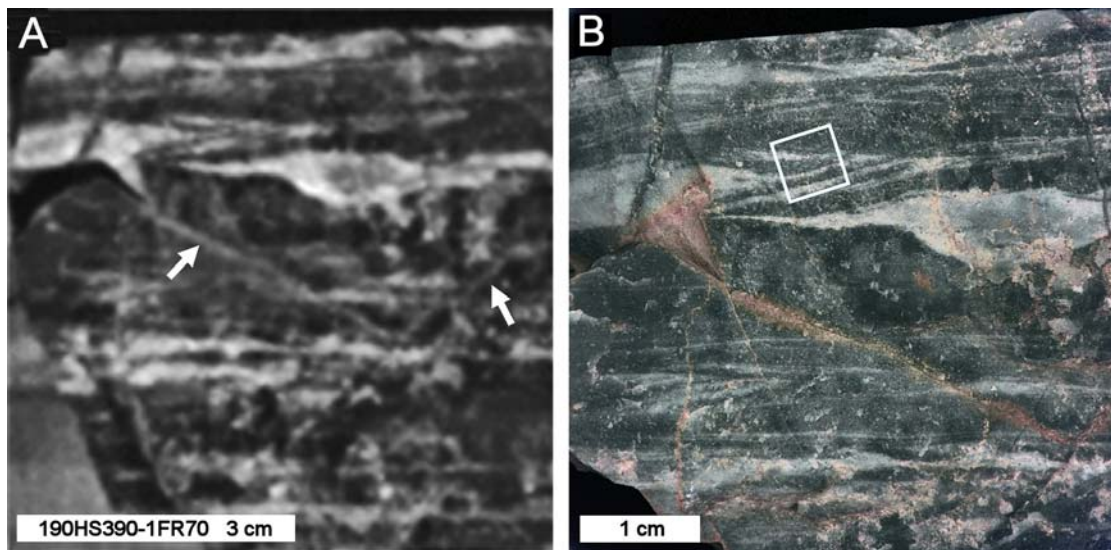


Figure 5.34 Proximal and macroscopic colour imaging of sample 190HS390 (banded chert). Imaging at 60 cm clearly shows alternating light and dark bands that in places exhibit cross-bedding and flaser-linsen structures (A). Fractures are also evident (arrow). Macroscopic colour imaging at 8 cm shows a cryptocrystalline fabric with localised Fe-staining in the vicinity of fractures (B). The individual laminae and sedimentary structures are particularly well defined. The highlighted area (box) represents the microscopic field of view shown in Figure 5.35B. Instrumentation: B2SCS\$530\$SOL (A) and B2SCS\$CUL\$RGB (B).

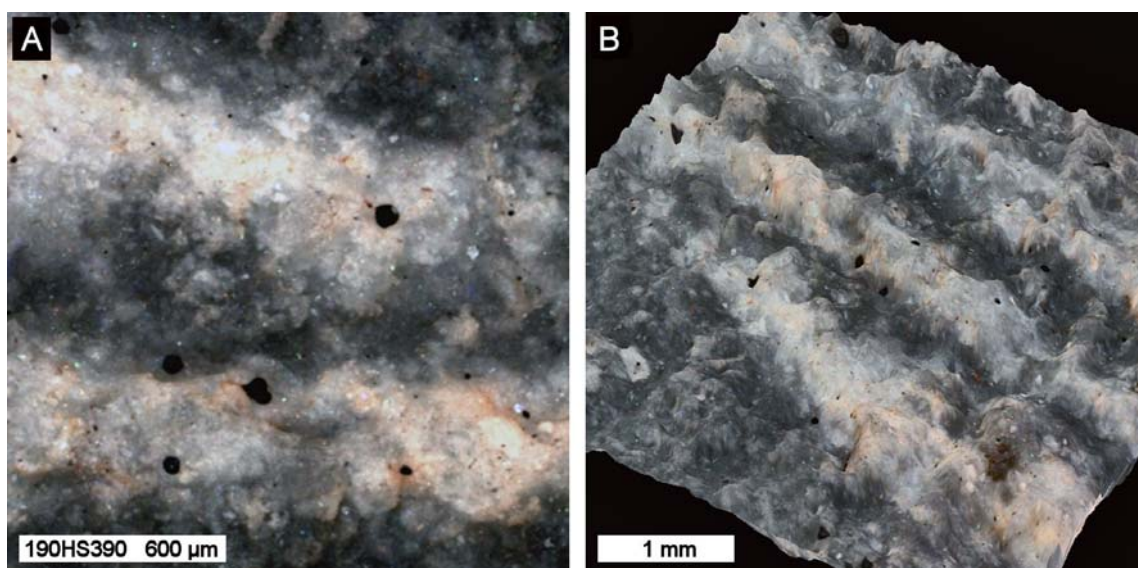


Figure 5.35 Microscopic imaging of sample 190HS390 (banded chert). The central portion of the microscopic field of view highlighted in Figure 5.34B shows individual laminae and cryptocrystalline texture (A). Depth information from image stack provides a means of visualising the surface in 3D (B). Note the undulating relief due to the more mechanically resistant white laminae. Instrumentation: B2MIC\$RGB (A).

5.4.1.2 Chemistry and Mineralogy

As stated previously, white bands are enriched in K, Ti, Rb, Sr, Zr, and Ba, and black bands are enriched in Cu, Zn, and Ni (Oberger *et al.*, 2006). Unfortunately, the measurement footprint of the TN9000 (and Beagle 2 XRS by inference) exceeded the thickness of individual laminae so black and white bands could not be analysed separately to confirm these data. However, both study samples (190HS390 and 190RS424) benefited from prepared surfaces which provided an opportunity to measure predominantly black or white areas.

In situ WDXRF analysis of 190RS424, which is comprised of ~75% white material, confirmed Si (91 wt % SiO₂), with concentrations for Al (5 wt % Al₂O₃), K (1.6 wt % K₂O), Ti (0.5 wt % TiO₂), and Fe (0.2 wt % Fe₂O₃) to be higher than those measured by bulk analysis (190FB579). Si, Al and K were comparable with values reported for white bands by Oberger *et al.* (2006). Trace element concentrations for Rb (82 ppm), Sr (34 ppm) and Y (31 ppm) were probably too statistically uncertain to make a comparison (Table 5.16), but values for Zr (207 ppm) and Ba

(465 ppm) may indicate relative enrichment.

In situ EDXRF analysis of 190HS390-1FR70 confirmed the presence of K (1 wt % K₂O), Ca (0.2 wt % CaO), Ti (0.3 wt % TiO₂), Fe (0.2 wt % Fe₂O₃), Zn (92 ppm), Rb (22 ppm), Sr (39 ppm), Zr (51 ppm), and Ba (96 ppm). The actual area of 1FR70 measured consisted of ~50% white bands and although fresh showed some Fe staining. Results from 190HS390-3SA30, an un-stained surface comprising ~75% black material, were similar to 1FR70 (apart from zero Fe), but Cu (57 ppm) and Ni (111 ppm) were also reported (see Section B.8). Although Zn was not detected, these data also agree with those of Oberger *et al.* (2006).

In situ Raman spectroscopy confirmed the dominance of quartz (especially 465 cm⁻¹) in both black and white layers. Carbon signatures (1314 and 1598 cm⁻¹) were also observed throughout but seemed to be associated more with the black layers than with the white layers. Rutile (447 and 610 cm⁻¹) and anatase (141, 194, 262, 394, 513 and 637 cm⁻¹) were observed in several spectra, frequently appearing together as small nodular masses (probably coated particles) within both the black and white layers. Goethite (246, 299, 386 and 551 cm⁻¹), hematite (225, 295, 411, 504 and 615 cm⁻¹), calcite (156, 281, 712 and 1086 cm⁻¹) and graphite (1368 and 1581 cm⁻¹) were also identified in association with fractures and coatings. Isolated black particles appeared throughout the sample and showed broad Raman signatures indicative of unidentifiable degraded organic compounds.

In situ Mössbauer spectroscopy indicated the possible presence of chalcopyrite (CuFeS₂), though this was not corroborated elsewhere other than in the general literature (Kojima *et al.*, 1998).

In situ XRD confirmed the mineralogy of 190HS390 to be quartz and hydromuscovite (Figure 5.36). These data were further corroborated by XRD analysis of powders selected from separate black and white areas of a fragment of 190HS390. The hydromuscovite signature was more abundant in the white bands thus confirming the results of Oberger *et al.* (2006) and providing an explanation for the XRF data from this study (i.e. K enrichment). Bulk XRD analysis of homogenised powders, consisting of a mixture of black and white material, still showed peaks assignable to hydromuscovite.

Table 5.16 Semi-quantitative geochemical analysis of Banded Chert (190)

<i>Instrument</i>	AXIOS\$	TN9K\$	TN9K\$	PW1K4\$
<i>Sample</i>	190RS424	190HS390	190HS390	190FB579
<i>Target</i>		2FR70	3SA30	
	(75% white)	(interior)	(interior)	(bulk)
<u>Major elements</u>				
Na ₂ O	0.35 *	ND	ND	0.06 ± 0.01
MgO	0.19 *	ND	ND	0.26 ± 0.01
Al ₂ O ₃	5.04 ± 0.63	ND	ND	4.93 ± 0.05
SiO ₂	91.26 ± 0.18	ND	ND	91.09 ± 0.91
P ₂ O ₅	0.1 *	ND	ND	0.02 ± 0.01
SO ₃	0.35 *	ND	ND	0.06 ± 0.01
Cl	0.16 *	ND	ND	ND
K ₂ O	1.56 ± 1.37	1.11 ± 0.12	1.35 ± 0.15	1.22 ± 0.01
CaO	0.19 *	0.2 ± 0.03	0.09 ± 0.03	0.06 ± 0.01
TiO ₂	0.54 *	0.25 ± 0.03	0.25 ± 0.03	0.33 ± 0.01
V ₂ O ₅				
MnO				
Fe ₂ O ₃	0.15 *	0.16 ± 0.03		0.11 ± 0.01
<u>Trace elements</u>				
Ni				ND
Cu				ND
Zn				ND
Ga				ND
As				ND
Rb	82 *	22 ± 6	28 ± 9	ND
Sr	37 *	39 ± 12	25 ± 9	ND
Y	37 *			ND
Zr	256 *	51 ± 15	77 ± 18	ND
Mo				ND
Ba	475 *	96 ± 24	93 ± 24	ND
Pb				ND

¹ Concentrations normalised to 100%

² Major elements expressed in weight % oxide and trace elements in ppm

³ Errors (3σ SD) determined by counting statistics (AXIOS\$) or the Horwitz function (TN9K\$)

⁴ Bulk analysis precisions (PW1K4\$) ~1 % (> 10 ppm) and ~10-20% (< 10 ppm)

⁵ ND = Not Determined

⁶ See Table C.1 for explanation of instrument mnemonics

* Errors exceed concentration value (*in situ* analysis) or near LLD (bulk analysis)

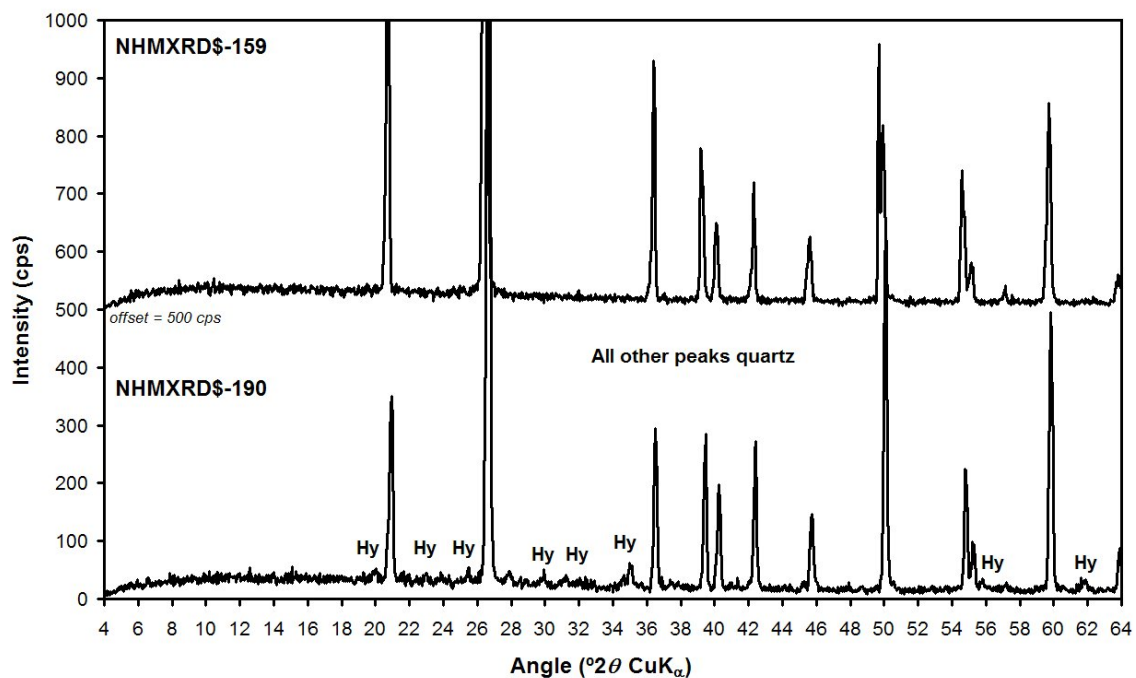


Figure 5.36 *In situ* XRD analysis of samples 190HS390 and 159HS304. Both samples are highly silicified hence the numerous well defined peaks assignable to quartz (Qz). However, the banded chert also shows peaks associated with hydromuscovite (Hy) which indicates aqueous alteration has taken place prior to silicification (see Section 5.4.1.3). Instrumentation: NMHXRD\$. Courtesy Dr. Gordon Cressey, Natural History Museum, London.

5.4.1.3 Geobiological Evaluation

The observed structures are typical indicators of a sedimentary rock that was originally deposited in a shallow, near-shore aqueous environment. Sediments formed in such environments are known to host life on Earth. The presence of muscovite confirms the involvement of water, and suggests the aqueous alteration of a sedimentary protolith had taken place. Heavy trace element concentrations (Cu, Zn) also suggest early diagenetic involvement of hydrothermal fluids. Mineralogical, chemical and textural evidence suggest the original material to be volcanic sand that subsequently underwent aqueous alteration to phyllosilicate, a process relevant to Mars (Poulet *et al.*, 2005). The combination of liquid water and volcanic minerals would have provided important nutrients for anaerobic chemolithotrophic microorganisms. The sediments subsequently underwent rapid hydrothermal silicification, thus preserving the fine palaeoenvironmental features and potentially any microscopic biosignatures associated with

them.

In a Mars mission context and on the basis of these *in situ* observations sampling would be highly justified.

5.4.2 Stromatolitic Chert, North Pole Dome, Pilbara, Australia (159)

Section B.9 describes the geology of the North Pole Dome area and the samples used for this study. Table 5.17 presents a summary of the *in situ* imaging and analytical results for samples 159HS304, 159RS436, and 159RS571. Semi-quantitative geochemistry data are shown in Table 5.18.

5.4.2.1 Physical Properties

Proximal imaging of 159HS304-2WX60 revealed an undulating layered fabric and open cavities (Figure 5.37AB). Iron staining was evident in macroscopic colour images of 159HS304-2WX50 but this did not mask the underlying laminated texture (Figure 5.37CD). Multi-spectral imaging enhanced the stromatolitic texture and differentiated between fresh and coated areas. Microscopic imaging did not provide any useful information apart from confirming the cryptocrystalline texture of 159HS304.

5.4.2.2 Chemistry and Mineralogy

In situ WDXRF analysis of sample 159RS571-1SA30 showed an elemental composition consisting of Si (97 wt % SiO₂) with Na (0.7 wt % Na₂O), Mg (0.1 wt % MgO), Al (0.3 wt % Al₂O₃), P (0.2 wt % P₂O₅), S (0.4 wt % SO₃), Cl (0.4 wt %), K (0.3 wt % K₂O), Ca (0.5 wt % CaO), Fe (0.3 wt % Fe₂O₃), Cu (100 ppm), and Zn (90 ppm). Analysis of 158RS571-2WX30 (external surface) showed a lower abundance of Si (82 wt % SiO₂) and an enrichment in Mg (0.7 wt % MgO), Al (8.7 wt % Al₂O₃), P (0.8 wt % P₂O₅), K (0.9 wt % K₂O), Ti (0.4 wt % TiO₂), and Fe (4 wt % Fe₂O₃). All other elements were relatively consistent for both surface types although Cu was not detected on 2WX20.

Table 5.17: Summary of *in situ* results for Stromatolitic Chert, Pilbara, Australia (159)

<i>In Situ</i> Techniques ¹	Results	Reference
Proximal Imaging (B2SCS\$GEOL\$SOL)	Evidence of layering	Section 5.4.2.1 Figure 5.37A Figure 5.37B
Macroscopic Imaging (B2SCS\$CUL\$RGB) (NUVIS\$MAC10\$SOL)	Stromatolitic texture	Section 5.4.2.1 Figure 5.37C Figure 5.37D
Microscopic Imaging (B2MIC\$RGB)	Cryptocrystalline texture	Section 5.4.2.1
X-Ray Fluorescence (TN9K\$FCA) (AXIOS\$HS)	Silicate Si, Na, Ca, S, Cl, Al, K, Fe, P, Mg, Cu, Zn (<i>fresh surface</i>) Si, Al, K, Fe, P, Mg, Ca, Ti, S, Cl, Zn (<i>weathered surface</i>)	Section 5.4.2.2 Table 5.18
Raman Spectroscopy (UBRAM\$488) (UBRAM\$514) (UBRAM\$785) (UBRAM\$1064)	Quartz (<i>all surfaces</i>) Graphite (<i>dark areas</i>) Dolomite, goethite, hematite, and rutile (<i>weathered surface</i>) No organic signatures (<i>fresh surfaces</i>) Carotenes with scytonemin (<i>weathered surface</i>) Carotenoid with porphyrin (<i>weathered surface</i>) <i>Note: Organic signatures probably recent contamination</i>	Section 5.4.2.2
Mössbauer Spectroscopy (B2MBSS)	Flat response (<i>all surfaces</i>) Red coloration due to very thin Fe coating (<< 0.2 mm). <i>Note: Footprint too large to distinguish between laminae</i>	Section 5.4.2.2
X-Ray Diffraction (NHMXRD\$) (PW1010\$)	Quartz (<i>fresh surface</i>) Quartz (<i>weathered surface</i>) <i>Note: Powder XRD analysis indicates quartz only.</i>	Section 5.4.2.2 Figure 5.36B

¹ See Table C.1 for explanation of instrument mnemonics

In situ EDXRF analysis of sample targets 159RS436-1SA50 and 159HS304-3WX50 did not produce any significant results apart from the tentative presence of Zn (close to the LLD) within 159RS436-3WX50.

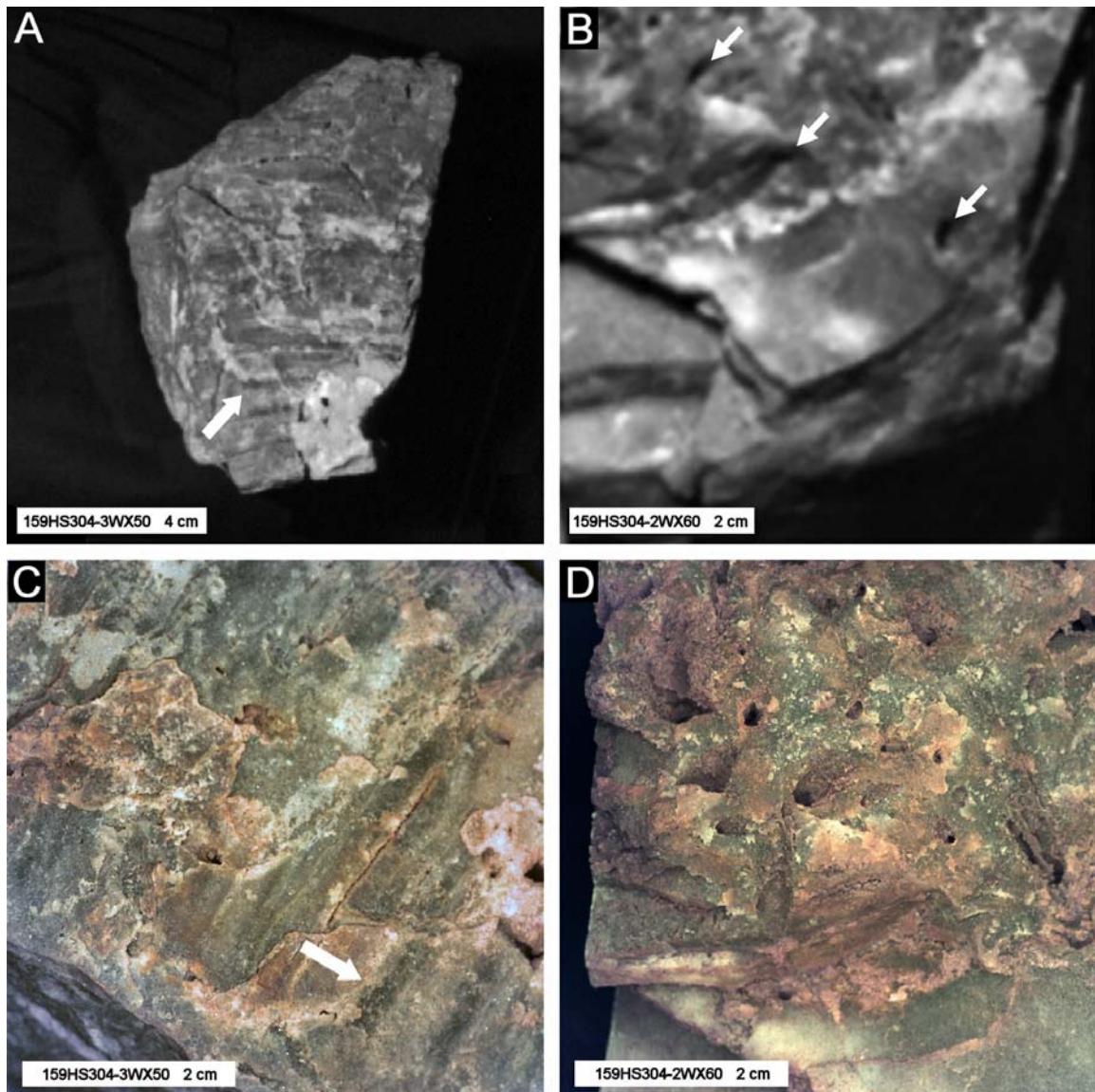


Figure 5.37 Proximal and macroscopic imaging of sample 159HS304 (stromatolitic chert). Imaging at 60 cm shows undulating layers on surface 3WX50 (A) and an open layered fabric on surface 2WX60 (B). Colour imaging of both surfaces at 8 cm shows a cryptocrystalline texture and well defined laminae in both cross-section (C) and plan view (D). The smooth, broadly curved layers and localised cavities shown in B (arrows) and D are characteristic of a basal unit of a stromatolite. Instrumentation: B2SCS\$530\$SOL (A), B2SCS\$670\$SOL (B) and B2SCS\$CUL\$RGB (C and D).

Table 5.18 Semi-quantitative geochemical analysis of Stromatolitic Chert (159)

<i>Instrument</i>	AXIOS\$	TN9K\$	AXIOS\$	TN9K\$
<i>Sample</i>	159HS571	159HS304	159RS571	159HS436
<i>Target</i>	2WX30	3WX50	1SA30	1SA50
	(exterior)	(exterior)	(interior)	(interior)
<u>Major elements</u>				
Na ₂ O	0.64 *	ND	0.74 *	ND
MgO	0.72 *	ND	0.13 *	ND
Al ₂ O ₃	8.74 ± 0.58	ND	0.28 *	ND
SiO ₂	82.33 ± 0.23	ND	96.72 ± 0.18	ND
P ₂ O ₅	0.79 *	ND	0.22 *	ND
SO ₃	0.32 *	ND	0.36 *	ND
Cl	0.4 *	ND	0.39 *	ND
K ₂ O	0.94 *		0.31 *	
CaO	0.48 *	0.18 ± 0.03	0.47 *	0.19 ± 0.03
TiO ₂	0.42 *	0.02 ± <0.01	0.02 *	
V ₂ O ₅				
MnO	0.03 *		0.03 *	
Fe ₂ O ₃	4.18 ± 0.81	0.25 ± 0.03	0.33 *	
<u>Trace elements</u>				
Ni				
Cu			100 *	
Zn	104 *		90 *	
Ga				
As				
Rb				
Sr				
Y				
Zr				
Mo				
Ba				
Pb				

¹ Concentrations normalised to 100%

² Major elements expressed in weight % oxide and trace elements in ppm

³ Errors (3σ SD) determined by counting statistics (AXIOS\$) or the Horwitz function (TN9K\$)

⁴ ND = Not Determined

⁵ See Table C.1 for explanation of instrument mnemonics

* Errors exceed concentration value (*in situ* analysis) or near LLD (bulk analysis)

In situ Raman spectroscopic analysis of sample target 159RS571-1SA30 identified quartz (106, 128, 264, 354, 393, 402, 464, 696, 808, 1064, 1081, 1161 and 1227 cm^{-1}). Spectra obtained from darker areas of this surface also indicated the presence of highly crystalline graphite (1307 and 1601 cm^{-1}). Analysis of sample target 159RS571-2WX30 and similar coated areas of 159RS571-1SA30 also revealed signature bands for dolomite (175, 300, 724 and 1098 cm^{-1}), goethite (250, 300, 387, 478 and 548 cm^{-1}), hematite (224, 297, 407, 500, 611 and 650 cm^{-1}) and rutile (447 and 606 cm^{-1}). The association of these minerals with weathered areas is corroborated by the elemental composition determined by *in situ* WDXRF and is almost certainly recent contamination rather than related to deposition.

Several organic signatures were unambiguously identified by *in situ* Raman spectroscopy on sample target 159RS571-2WX30 and similar coated areas of 159RS571-1SA30. No organic signatures were identified on un-weathered areas of 159RS571-1SA30. Beta-carotene (1004, 1155 and 1516 cm^{-1}) and another carotenoid (1006, 1144 and 1535 cm^{-1}), were identified in association with scytonemin (several distinct bands between 450 and 1714 cm^{-1}). A third carotenoid (1007, 1144 and 1530 cm^{-1}) was identified in association with a porphyrin (several bands between 483 and 1592 cm^{-1}). These distinct groupings may be indicative of two or more epilithic and chasmoendolithic microorganisms that have inhabited the sample fairly recently.

In situ Mössbauer spectroscopic analysis of sample target 159RS571-1SA30 did not produce a sufficient response due to insufficient Fe content. Despite its oxidised appearance and measured Fe content (4 wt % Fe_2O_3), analysis of target 158RS571-2WX30 only produced a weak signal. This implies that the Fe-oxide content represented by the octahedral Fe^{3+} doublet and presumably responsible for the red-brown colouring observed by the camera systems, is very thin compared to the sampling depth of the instrument.

In situ XRD analysis of a relatively fresh thumbnail sample removed from 159HS304 identified only quartz (Figure 5.36).

5.4.2.3 Geobiological Evaluation

Although the unambiguous organic signatures identified by *in situ* Raman spectroscopy are an interesting observation, given the extreme age of the sample they should not be considered relevant in the context of this investigation.

The regular, slightly unconformable wavy laminations observed at a variety of scales on exposed surface 159RS436-1SA50 are suggestive of a sedimentary rock but unlike the Kitty's Gap samples (see Section 5.4.1) these do not provide independent morphological evidence for aqueous deposition. However, the cavities seen on surface 159HS304-2WX60 resemble ghost crystals and are similar to those observed by the MER Opportunity in Eagle Crater, Meridiani Planum, Mars (Knoll *et al.*, 2005). These features suggest aqueous dissolution of a pre-existing mineral phase (in this case, gypsum, but this cannot be corroborated from the *in situ* data directly).

Chemical and mineralogical analysis confirmed the samples to be highly silicified but, unlike the Kitty's Gap example, no aqueous-formed minerals were evident. The Fe-oxide staining on the weathered surface is an indication of relatively recent aqueous alteration of the exterior surface and therefore not relevant to this study. The identification of graphite on the other hand is potentially significant and may provide justification for sampling.

As mentioned in Section B.9, these samples were collected from an exposure that exhibited larger domal stromatolitic structures and therefore only represent a small, cross-sectional perspective. Taking the entire exposure into context would provide sufficient morphological evidence to suspect that the sediment was formed in an aqueous environment and to provide important way-up criteria for sample 159HS304. The domal features themselves would be of immediate exobiological interest, given the relationship between such structures and microbial mats on Earth (Walter, 1978). The texture observed on 159RS436-1SA50 could potentially be an indication that sticky microbial mats influenced the precipitation of minerals onto these substrates to form the domal structures.

From other work, silicified microbial remains in the form of isolated filaments and small colonies of coccoidal microorganisms have been observed in samples from the Trendall locality (Dr. Frances Westall, unpublished data) but these are below the resolution of the imaging instruments used in this investigation.

The *in situ* evidence gathered from samples 159HS304 and 159RS436 alone, although informative, is incomplete. Given the scale and 3D nature of the feature of which these samples form a part, other samples from the same outcrop are clearly required to formulate a more representative *in situ* assessment. In a Mars mission context sampling would be deferred until

further evidence was obtained.

5.4.3 Banded Iron Formation (BIF), Barberton, South Africa (163)

Section B.10 describes the geology of the Barberton area and the samples used for this study. Table 5.19 presents a summary of the *in situ* imaging and analytical results for samples 163HS303, 163RS585 and 163HS586. Semi-quantitative geochemistry data are shown in Table 5.20.

Table 5.19: Summary of *in situ* results for BIF, Barberton, South Africa (163)

<i>In Situ</i> Techniques ¹	Results	Reference
Proximal Imaging (B2SCS\$GEOL\$SOL)	Evidence of layering	Section 5.4.3.1 Figure 5.38A
Macroscopic Imaging (B2SCS\$CUL\$RGB) (NUVIS\$MAC10\$SOL)	Evidence of layering within oxidised zone Spectral dichotomy	Section 5.4.3.1 Figure 5.38B
Microscopic Imaging (B2MIC\$\$RGB)	No useful information from surfaces imaged	Section 5.4.3.1
X-Ray Fluorescence (TN9K\$\$FCA) (AXIOS\$HS)	Silicate and Fe-oxide Si, Fe (<i>white band</i>) Fe, Si, Mn, Al, Mg, S, Na (<i>brown band</i>)	Section 5.4.3.2 Table 5.20
Raman Spectroscopy (UBRAM\$\$785) (UBRAM\$\$1064)	Quartz (<i>white band</i>) Goethite (<i>brown band</i>) No organic signatures (<i>both bands</i>) <i>Note: Incomplete survey performed</i>	Section 5.4.3.2
Mössbauer Spectroscopy (B2MBS\$)	Minor amounts of goethite and hematite (<i>white band</i>) Crystalline and chemically pure goethite (<i>brown band</i>) <i>Note: Effect is low ~0.15% (white band)</i>	Section 5.4.3.2 Figure 5.39
X-Ray Diffraction (NHMXRD\$) (PW1010\$)	Quartz (<i>white band</i>) Goethite and quartz (<i>brown band</i>) <i>Note: Powder XRD analysis indicates quartz and goethite.</i>	Section 5.4.3.2 Figure 5.40

¹ See Table C.1 for explanation of instrument mnemonics

5.4.3.1 Physical Properties

The alternating light and dark bands within 163HS303 were clearly visible at the proximal scale (Figure 5.38A). The lighter units appeared to be less physically weathered than the darker units,

suggesting a more resistant material. Macroscopic imaging revealed subtle layering within the dark unit, accentuated due to weathering, and appeared to be pisolitic in places (Figure 5.38B). Multi-spectral imaging produced contrasting spectral signatures and suggested a degree of homogeneity within each unit. Due to the macro texture of 163HS303, *in situ* microscopy did not provide any useful additional information.

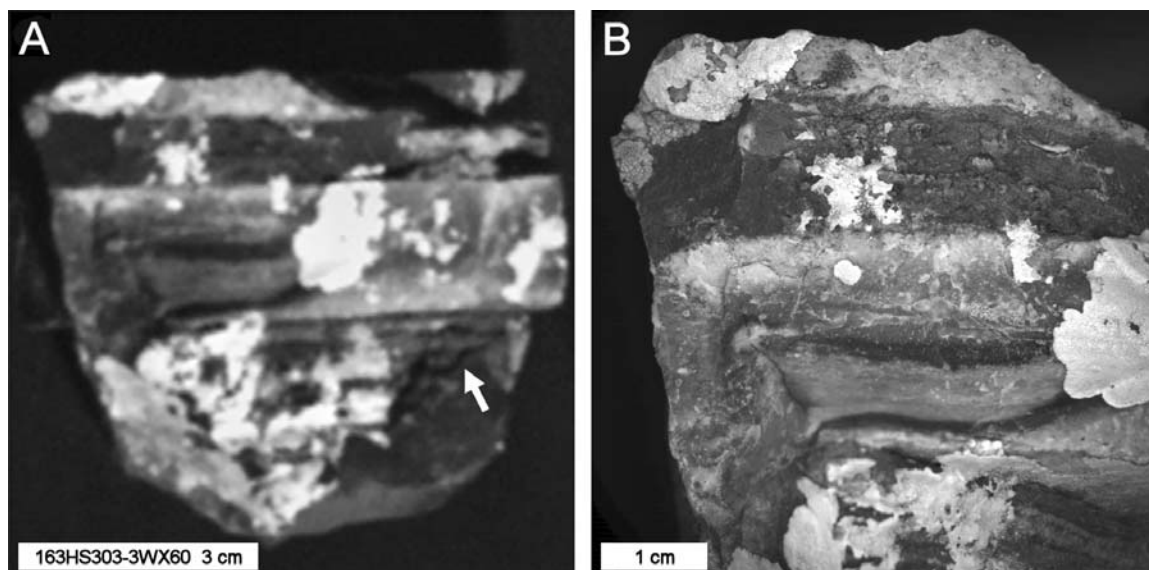


Figure 5.38 Proximal and macroscopic imaging of sample 163HS586 (BIF). Imaging at 60 cm shows relatively thick alternating light and dark bands (A). The light bands appear to be more resistant to weathering. Imaging at 8 cm shows a more detailed layered structure (B) and a pisolitic texture within the dark bands (accentuated by weathering). Note that the epilithic lichens visible on the surface of 163HS586 are recent and not relevant to this work so should be ignored. Instrumentation: B2SCS\$530\$SOL (A) and B2SCS\$CUL\$R (B).

5.4.3.2 Chemistry and Mineralogy

In situ WDXRF analysis of sample 163HS586A-1SA20 (chert band) revealed a composition of Si (98 wt % SiO_2) and Fe (2 wt % Fe_2O_3) only. Analysis of sample 163HS586B-1SA15 (oxidised band) showed lesser but still significant levels of Si (41.5 wt % SiO_2) and more Fe (56.6 wt % Fe_2O_3), plus minor Na (0.1 wt % Na_2O), Mg (0.3 wt % MgO), Al (0.5 wt % Al_2O_3), S (0.2 wt % SO_3), and Mn (0.7 wt % MnO). No trace elements were detected within either sample.

In situ EDXRF analysis of sample 163RS585 only confirmed the Fe and Mn content of the

oxidised band (41 wt % Fe₂O₃ and 0.3 wt % MnO) to be higher than that of the chert band (6 wt % Fe₂O₃ and zero MnO).

Only a limited *in situ* Raman spectroscopic survey was performed on sample 163HS586 which confirmed the presence of goethite (163HS586B) and quartz (163HS586A). No organic signatures were identified.

In situ Mössbauer spectroscopy (Figure 5.39) confirmed the brown bands (163HS586B) to be highly crystalline and chemically pure goethite. Small amounts of goethite and hematite were also identified within the chert bands (163HS586A) but these were not detected by *in situ* XRD.

In situ XRD analysis of thumbnail samples derived from 163HS303 showed the chert band to be comprised of quartz and the oxidised band to be a mix of goethite and quartz (Figure 5.40). Hematite was not identified.

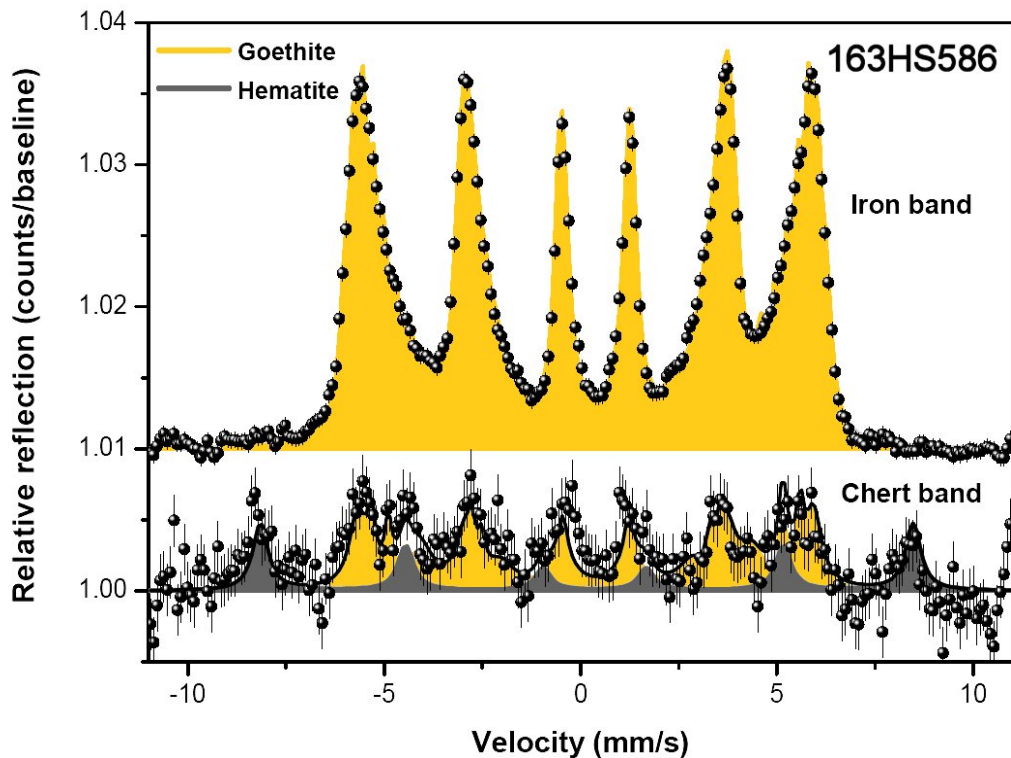


Figure 5.39 *In situ* Mössbauer analysis of sample 163HS586 (BIF). The strong signal from the oxidised band is characteristic of goethite. Although substantially weaker, the signal from the siliceous band shows the presence of goethite and hematite. Shaded areas are reference fits for goethite and hematite. Instrumentation: B2MBSS. Courtesy Dr. Christian Schröder, NASA JSC.

Table 5.20 Semi-quantitative geochemical analysis of BIF (163)

<i>Instrument</i>	AXIOS\$	TN9K\$	AXIOS\$	TN9K\$	AXIOS\$
<i>Sample</i>	163HS586A	163RS585	163HS586B	163RS585	163HS586B
<i>Target</i>	1SA20	1FR40	1SA15	1FR40	2FR15
	(Si band)⁴	(Si band)	(Fe band)	(Fe band)	(Fe band)⁴
<u>Major elements</u>					
Na ₂ O		ND	0.11 *	ND	
MgO		ND	0.25 *	ND	
Al ₂ O ₃		ND	0.46 *	ND	0.51 *
SiO ₂	97.8 ± 2.47	ND	41.55 ± 0.24	ND	32.79 ± 4.15
P ₂ O ₅		ND	0.08 *	ND	
SO ₃		ND	0.15 *	ND	
Cl		ND	0.04 *	ND	
K ₂ O			0.03 *		
CaO			0.08 *	0.03 ± 0.01	
TiO ₂			0.02 *		
V ₂ O ₅					
MnO			0.68 *	0.3 ± 0.03	0.87 *
Fe ₂ O ₃	2.24 *	5.74 ± 0.54	56.56 ± 0.17	40.64 ± 2.79	65.83 ± 2.38
<u>Trace elements</u>					
Ni					
Cu					
Zn					
Ga					
As					
Rb					
Sr					
Y					
Zr					
Mo					
Ba					
Pb					

¹ Concentrations normalised to 100%

² Major elements expressed in weight % oxide and trace elements in ppm

³ Errors (3σ SD) determined by counting statistics (AXIOS\$) or the Horwitz function (TN9K\$)

⁴ Sampling area reduced to 6 mm diameter

⁵ ND = Not Determined

⁶ See Table C.1 for explanation of instrument mnemonics

* Errors exceed concentration value (*in situ* analysis) or near LLD (bulk analysis)

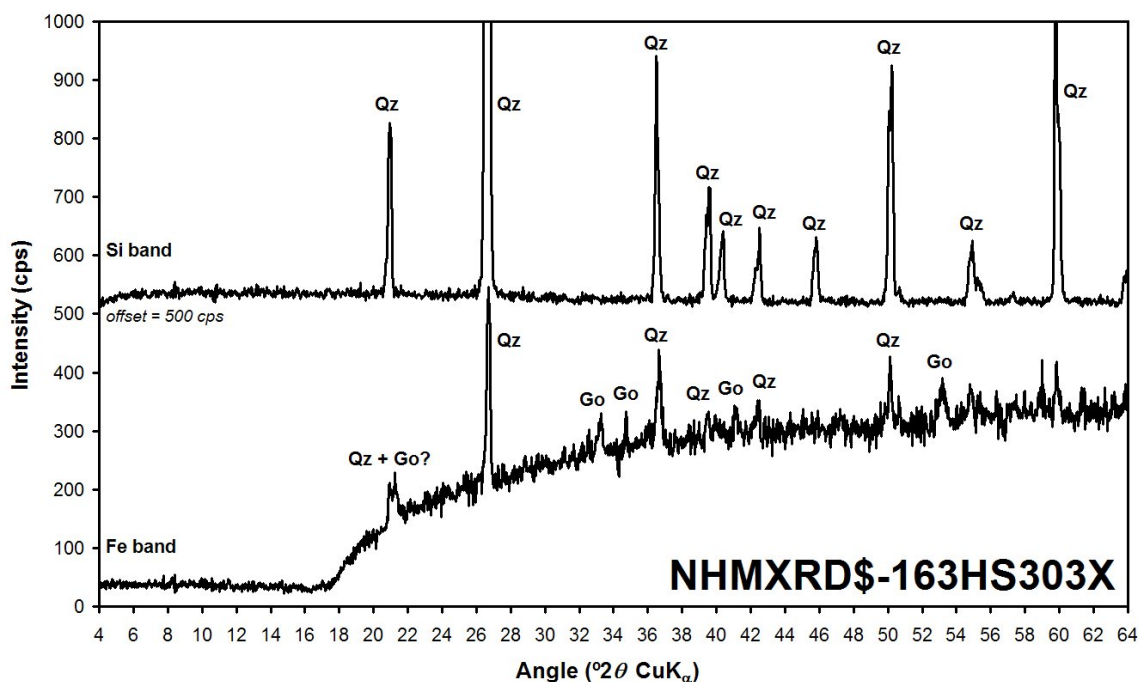


Figure 5.40 Bulk XRD analysis of sample 163HS303 (BIF). The siliceous band (upper trace) shows well-defined peaks assignable to quartz (Qz) only. The oxidised band (lower trace) shows several peaks assignable to goethite (Go) but quartz is also present. Hematite was not identified (see Mössbauer spectra in Figure 5.39). Instrumentation: PW1010\$.

5.4.3.3 Geobiological Evaluation

The combination of alternating siliceous and Fe-rich material in these samples is immediately suggestive of a BIF sediment, i.e., a chemical deposit precipitated under quiescent aqueous conditions within oceanic or shallow basin environments. Whether or not microbial activity was the primary influence in the formation of such a precipitate is still the subject of debate on Earth. However, evidence of a BIF on Mars for example would indicate formation in the presence of free standing water and therefore suggest the possibility of a microbial habitat.

From other work it is known that filamentous microbial fossils occur in the siliceous layers within 163HS303 (Dr. Frances Westall, unpublished data), but these are below the resolution of the imaging instruments used in this investigation. However, relatively high levels of C are also reported to be associated with the Fe-rich layers which could be detectable by Raman spectroscopy assuming suitable targets could be located (see results for the Kitty's Gap chert). In

a Mars mission context further detailed scrutiny by Raman spectroscopy would be desirable before sampling could be justified.

5.5 Summary

The results from two experimental studies using the analogue samples described in Appendix B have been presented. The first study focused on the ability of a combination of representative *in situ* techniques, including multi-scale/multi-spectral imaging and spectroscopy (XRF, Raman, Mössbauer and XRD), to unambiguously identify morphological biosignatures (i.e., biologically mediated structures) exhibited by these samples. The second study focused on the ability of these techniques to assess the biogenic potential of visible sedimentary structures as palaeo-environmental indicators of conditions once favourable to life. All experiments were conducted using the instrumentation and mission-like constraints described in Appendix C.

Overall the results showed that the combination of imaging and analytical techniques adopted proved sufficient to make reasonable geobiological assessments of the samples. In most cases, data from one technique was corroborated by at least one other, although observations did occasionally conflict. No *in situ* analytical technique proved to be ideal with respect to the determination of composition, although Raman proved invaluable for organic chemistry. The importance of field representative measurements was clearly demonstrated. Of paramount importance was the ability to image at a variety of scales and to have access to a combination of unprepared and prepared surfaces.

The conclusions from this work will be discussed and placed into overall context in Chapter 7.

Chapter 6

Field Applications and Scientific Autonomy

"We prefer self-government with danger to servitude in tranquillity"

Kwame Nkrumah (1909-1972)

Ghanaian Prime Minister (1952-1960) and President (1960-1966)

This Chapter describes some fundamental aspects of terrestrial geological field practice and discusses how they could be implemented into a robotic planetary mission equipped with a payload such as described in Appendix C. A novel approach to autonomous science operations is defined and the requirements for in-field and planetary yard evaluation specified.

The information contained in this Chapter has been incorporated into a research council-funded study entitled "The Autonomous Robot Scientist" (Shaw *et al.*, 2007). Results from this work are presented here.

6.1 Introduction

Planetary surface exploration is becoming increasingly constrained by uplink/downlink bandwidth, due in part to improved mobility and data acquisition capabilities of mobile robotic elements and the limitations of interplanetary communications. Currently, robots require frequent ground-based intervention, often days apart, which inevitably slows up a mission and restricts overall potential scientific output. There is now a strong case to empower planetary robots, especially rovers, with scientific decision-making capability in order to progress key tasks more efficiently. Depending on risk strategy, these autonomous tasks could range from remote target selection to complete traverse-sampling scenarios. In addition, there is particular value in undertaking opportunistic science during traverses between waypoints (WP).

Autonomous systems for planetary exploration are currently very topical and include studies in rock detection and target prioritisation (Pedersen, 2000; Castaño *et al.*, 2003, 2006, 2007), feature detection (Gulick *et al.*, 2001; Thompson *et al.*, 2005), novelty detection (Thompson *et al.*, 2006), compositional evaluation (Gazis and Roush, 2001), and life detection (Wettergreen *et al.*,

2005). These studies focus on isolated or float rocks as potential science targets with the aim of assigning basic scientific parameters to them such as albedo, basic texture and colour, and in some cases consider analytical input such as spectral signature and fluorescence. Some employ techniques common to navigation and locomotion work where landscape features such as rocks and slopes are considered “obstacles” thereby requiring some detailed autonomous assessment of physical parameters such as shape and size.

The development of these robotic systems can learn much from terrestrial field geology. Many aspects of fieldwork undertaken by humans are taken for granted, especially in terms of dexterity, experiential learning, subliminal observation and complex decision processes. Fundamentally, two aspects are common to both human and robotic fieldwork, the ability to identify and classify geological features and the ability to interpret their relevance within a broader scientific context.

On Earth, the search for exploitable resources such as oil, gas, water, minerals, geothermal energy etc., although specific objectives, rely heavily on an initial understanding of the fundamental geology of the region being explored. Prior to any field campaign it is important to accumulate all previous data in order to establish local and regional context. This is usually achieved via survey data (including geological maps, satellite remote sensing, geophysical surveys and analysis of samples collected on previous expeditions).

On Mars (and other planets), orbital data from previous missions are likely to be the only source of contextual information prior to landing although some ground truth (albeit inferred) may be available. Surface missions to new sites therefore have to undertake basic site investigation *in situ* with whatever payload assets are available (Allen *et al.*, 1995), usually a limited suite of instruments but likely to include what a human field geologist would consider essential (discussed later). Once the landing site has been characterised, human scientists can then place detailed observations into appropriate context and subsequently make revisions throughout the mission.

Autonomous robots should adopt the same approach using the ability to identify key attributes and scoring them as to scientific value. A working contextual model should be maintained as part of the “learning” process.

For this study, and to maintain continuity with the topics covered in previous chapters, a mission

model based on the ESA ExoMars rover is considered. ExoMars (due to launch in 2016) envisages a single rover that relies on existing in-orbit assets (i.e., NASA MRO or successor). The Pasteur payload consists of a complementary suite of imaging, analytical and geotechnical instrumentation (ExoMars Project Team, 2007b, and Section 2.1.1.3). Surface operations will be constrained by complex communications windows, more similar to the Beagle 2 model than that of the NASA Mars Exploration Rovers, Spirit and Opportunity. ESA mission engineers are therefore considering implementing as much *engineering autonomy* into the “experimental cycle” elements of surface operations as possible (ExoMars Project Team, 2007a). This could potentially involve some limited *scientific autonomy*.

At the time of writing, the ExoMars operational requirements remain fluid so some latitude is applied in formulating the concepts described in this study. Given this, and based on the current ExoMars model (Catullo and Acquaroli, 2006; ExoMars Project Team, 2007a and 2007b), crucial Decision Points (DP) requiring scientific ground-based intervention are assumed to include:-

- DP1: Post Wide Angle Camera (WAC) survey (select ~10 targets of interest)
- DP2: Post High Resolution camera (HRC) survey (select ~3 targets for close-up survey)
- DP3: Post close-up survey (select 1 target for sampling)
- DP4: Post sampling (microscopic survey of core prior to sample preparation)

DP1 and DP2 follow remote sensing activities and likely require assessment by the mission team (scientists and engineers). Given the potential complexity of the broad vista observed beyond several tens of metres, it is not feasible at this stage to autonomously characterise a scene that could contain thousands of widely varying objects. There may be cases however when DP1 and DP2 could be combined into a single DP although this would depend on the nature of the landing site, or the use of object filtering (i.e., anomaly recognition).

DP3 has the potential to be replaced by an on-board autonomous sequence based on scientific rationale since the rover is already stationed. At DP2, the scientific rules and parameters required for DP3 could be modified to reflect the contextual data obtained from the remote imaging surveys. Depending on the spatial distance, terrain type and other risk parameters between the targets chosen for close-up inspection, the objective would be to perform all manoeuvres, measurements and scientific assessments as an autonomous sequence (constrained of course by engineering in order to maintain rover safety/integrity at all times).

DP4 provides the only opportunity to study an acquired sample in its natural form before crushing, homogenising and distributing to the analytical laboratory. In this respect it is an important stage of the experiment cycle. The possibility of acquiring an intact core displaying characteristic micro-fabric/structure should not be discounted. Similarly, a heterogeneous unconsolidated material may also be informative. The bottom line is that if the sample is destroyed before fully scrutinising it, the entire mission is at risk of losing both potential science and essential context for other instruments. Consider the possibility, albeit remote, of an intact core that is clearly fossiliferous yet contains no biogenic organic signatures, a common occurrence on Earth. Ideally DP4 should have the capability of at least two iterations, evaluation of the highly compressed/partial view “quick look data” (DP4.1), and acquisition of a best-resolution image set of the full sample (DP4.2) if this was appropriate. Assessing the physical state of the sample (from no material present to fragment/powder mix to solid intact core) is an obvious and necessary non-scientific autonomous task. Scientific autonomy could be exploited for DP4 by using similar algorithms designed for macroscopic feature detection (i.e., layering, discontinuities, spectral distribution, etc.) described later.

6.2 A Methodology for Autonomous Science

Geological features often appear complex and are influenced by a huge number of variables. In the field, human geologists mentally deconstruct what they see and draw on broader contextual input (the bigger picture) to help classify geological materials and the processes that act on them. Observations made in the field, aided by effective use of a hammer and a hand lens, provide an assessment of structure, texture and composition, the basic ingredients for interpretation. As mentioned above, this should also be the objective of a robot undertaking planetary geological fieldwork. In either case, interpretation relies on iteration since features seen from afar often look very different when viewed close up (sometimes unexpectedly so). This emphasises both the importance of detailed close-up observations (payloads must be equipped with appropriate deployable instruments and tools for *in situ* work), and the need to incorporate re-evaluation into the onboard autonomous routines.

For the purpose of this study, the following were considered necessary to establish a framework for a first generation system based on autonomous science:-

- Definition of the fundamental attributes applicable to geological features

- Mechanism for assigning scientific value to these attributes
- Methodology for constraining scientific value due to external factors (i.e., context)
- Requirements for rule-based algorithms
- Facility for testing and evaluating the concept

It is beyond to scope of this thesis to create a fully working model based on this framework. What is presented in the remainder of this section is a concept which can be used to design and build such a system. However, a simple model has already been implemented and demonstrated, and this will be discussed in Section 6.4.

6.2.1 Fundamental Attributes

As mentioned previously, the basic attributes used in field classification of rocks are structure, texture and composition. It is unlikely that an adequate scientific evaluation could be made using any one of these in isolation even though there may be cases where this might apply (e.g., exceptionally well-preserved complex metazoan fossils). Nevertheless, it is appropriate to first consider each attribute independently by performing a feature recognition assessment. Feature lists associated with each attribute would be initially pre-defined and allocated Science Value Scores (SVS) based on potential significance, whether they appear in isolation or in association with other features.

The total SVS derived for each attribute is only an indicator of “feature richness” and does not necessarily reflect the overall SVS of the target. The SVS of the target itself is derived by evaluating all the matching features for each attribute and biasing the assessment using the contextual model (see Section 6.2.3). At the start of the mission, the contextual model is primed using pre-landing data (regional geology from orbital mapping) and mission objective criteria (search for signatures of life). Following landing, the contextual model is enhanced using ground truth from panoramic landing site surveys and *in situ* analytical measurements. As the mission proceeds the contextual model is updated by human “mentoring”.

The following sections describe each fundamental attribute in detail. The feature lists are incomplete but are sufficiently populated and varied to exercise any recognition routines that may be written to generate a target SVS. Note that all SVS assignments are arbitrary at this time.

6.2.1.1 Structure

For simplicity, basic geometric forms will be considered here. The most obvious form is layering or stratification, a term used in reference to sedimentary deposits but applicable to volcanic and metamorphic rocks exhibiting layered structures. Where thickness is implied, units display either “bedding” (> 1 cm) or “lamination” (< 1 cm). At all scales the basic geometric parameters are the same.

Depending on the material, bedding can often be readily identified remotely, especially if enhanced due to differential weathering and natural illumination geometry. Closer up, thin beds and laminations sometimes require additional aids such as controlled illumination and surface preparation (i.e., splitting, grinding and sometimes polishing). Combined geometries can be very informative and in some cases have high scientific value. A particular challenge for the autonomous system will be to interpret macroscopic features in 3D.

In its simplest form, stratified rock or soil can appear in cross section as linear, parallel units. The interface between each unit can be due to a variety of factors including difference in grain size or composition or both. Furthermore, the units could be homogeneous or graded (due to variation in grain size within each unit). Unit boundaries could be equidistant or graduated (due to thinning or thickening units). Nonlinearity could be expressed as wavy, turbulent, converging or diverging units. Discontinuities are highly characteristic. For example, cross-bedding/lamination (two layered units inclined to one another) would be an interesting target. When combined with other attributes such as texture, planar (and perhaps irregular) structures can also yield vertical orientation.

Table 6.1 lists some examples of structural attributes observed in cross section (or oblique section) applicable at all scales from remote to microscopic. Structures observed in plan view are not considered at the moment.

Table 6.1: Structural feature list (all scales, incomplete)¹

Parameter	Fuzzy Assignment ²	GSPARC ³	SVS ⁴	Notes ⁵
Signature	None		0	No structure
Signature	Indistinct		10	Poorly defined or blurred by drift
Signature	Well defined	190HS390	15	Chert (cross-bedding) (Figure 5.34)
Signature	Distinct		25	Cape Verde, Mars (Figure 2.6)
Extent	Continuous		20	Traceable until terminated
Extent	Discontinuous		10	Traceable with gaps
Form	Planar	44HS340	10	Selenite (cleavage) (Figure 5.30B)
Form	Lenticular	190HS390	40	Chert (linsen structures) (Figure 5.34)
Form	Nodular	158HS318	50	Iron ore (concretions in matrix)
Orientation	Parallel		10	Equidistant or cyclic
Orientation	Multiple		50	Differently orientated parallel units
Orientation	Non-parallel		30	Diverging and converging
Scale	Very thick bedding		100	> 100 cm
Scale	Thick bedding		100	30 cm to 100 cm
Scale	Medium bedding		10	10 cm to 30 cm
Scale	Thin bedding		10	3 cm to 10 cm
Scale	Very thin bedding		10	1 cm to 3 cm
Scale	Thick lamination		10	0.6 cm to 1 cm
Scale	Medium lamination		10	0.3 cm to 0.6 cm
Scale	Thin lamination		50	0.1 cm to 0.3 cm
Scale	Very thin lamination	44HS340	100	Selenite (< 0.1 cm) (Figure 5.30B)

¹ Could be implemented as a C data type where “parameter” is a member of a C++ class.² Defined within a membership function (see Section 6.2.4). End members not necessarily shown here.³ Typical GSPARC specimen (or field exposure) exhibiting the feature.⁴ Values are arbitrary and for illustrative purposes only. In practice these will depend on the application.⁵ With reference to the example given, or in the absence of such, more generalised criteria.

6.2.1.2 Texture

The textural properties of rocks are dependent on particle grain size and distribution, grain morphology and overall fabric, i.e., how grains are orientated and packed. Although these properties can only be determined macroscopically or microscopically, some generic aspects are

applicable to remote observation of larger geological features.

Table 6.2 lists some examples of generic textural attributes that can be applied to all scales from remote to microscopic. Table 6.3 and Table 6.4 list examples of textural attributes applicable for close-up assessment only.

Table 6.2: Textural feature list (all scales, incomplete) ¹

Parameter	Fuzzy Assignment ²	GSPARC ³	SVS ⁴	Notes ⁵
Signature	None		20	No texture (perfectly smooth)
Signature	Indistinct		5	Poorly defined or blurred by dust
Signature	Distinct	163HS303	10	BIF (Figure B.21B)
Extent	Homogeneous	139HS347	10	Tuff (volcanic ash)
Extent	Heterogeneous	163HS303	50	BIF (Figure B.21B)
Fabric	Random	179HS367	5	Goethite (localised) (Figure B.9B)
Fabric	Orientated	179HS367	50	Goethite (general) (Figure B.9A)
Fabric	Imbricated		100	Overlapping clasts/pebbles
Lustre	Earthy	168HS131	5	Iron ore (phyllosilicate matrix)
Lustre	Pearly	175HS363	50	Chert (desert polished)
Lustre	Vitreous	24HS237	100	Obsidian (fresh)
Lustre	Metallic	150HS280	100	Iron meteorite (un-oxidised)
Relief	Rough	115HS215	10	Basalt (weathering rind)
Relief	Striated	121HS243	50	Impactite (shatter cone)
Relief	Conchoidal	24HS237	100	Obsidian (glassy fracture)
Relief	Vesiculated	112HS214	10	Basaltic lava (gas bubbles)
Relief	Pitted	168HS131	40	Iron ore (concretion casts)
Relief	Bumpy	168HS131	50	Iron ore (concretions in matrix)

¹ Could be implemented as a C data type where “parameter” is a member of a C++ class.

² Defined within a membership function (see Section 6.2.4). End members not necessarily shown here.

³ Typical GSPARC specimen (or field exposure) exhibiting the feature.

⁴ Values are arbitrary and for illustrative purposes only. In practice these will depend on the application.

⁵ With reference to the example given, or in the absence of such, more generalised criteria.

Table 6.3: Textural feature list (fine scales, general, incomplete) ¹

Parameter	Fuzzy Assignment ²	GSPARC ³	SVS ⁴	Notes ⁵
Matrix	Clastic	145HS273	20	Conglomerate (felsic)
Matrix	Crystalline	204HS456	50	Gabbro (interlocking crystals)
Shape	Spherical	168HS131	20	Iron ore (concretions)
Shape	Tabular	44HS340	100	Selenite (Figure B.14)
Shape	Bladed	23HS49	200	Amphibolite (oriented crystals)
Shape	Geometric	140HS333	1000	Limestone (gastropods)
Roundness	Very angular		10	
Roundness	Angular		10	
Roundness	Sub-angular		10	
Roundness	Sub-rounded		20	
Roundness	Rounded		20	
Roundness	Well rounded	113RS212	40	Stony meteorite (condrules)

¹ Could be implemented as a C data type where “parameter” is a member of a C++ class.

² Defined within a membership function (see Section 6.2.4). End members not necessarily shown here.

³ Typical GSPARC specimen (or field exposure) exhibiting the feature.

⁴ Values are arbitrary and for illustrative purposes only. In practice these will depend on the application.

⁵ With reference to the example given, or in the absence of such, more generalised criteria.

Table 6.4: Textural feature list (fine scales, grain size and sorting, incomplete) ¹

Parameter	Fuzzy Assignment ²	GSPARC ³	SVS ⁴	Notes ⁵
Size	Medium gravel		10	8 mm to 16 mm
Size	Fine gravel		10	4 mm to 8mm
Size	Very fine gravel		10	2 mm to 4 mm
Size	Very coarse sand		10	1 mm to 2 mm
Size	Coarse sand		10	0.5 mm to 1 mm
Size	Medium sand	114HS353	10	0.25 mm to 0.5 mm (Figure 5.20A)
Size	Fine sand		10	0.125 mm to 0.25 mm
Size	Very fine sand		50	0.0625 mm to 0.125 mm
Size	Mud		100	< 0.0625 mm (includes silt and clay)
Sorting	Very well sorted		50	$\sigma < 0.35$
Sorting	Well sorted		40	$\sigma = 0.35$ to 0.5
Sorting	Moderately sorted		30	$\sigma = 0.5$ to 0.7
Sorting	Poorly sorted		20	$\sigma = 0.7$ to 2.0
Sorting	Very poorly sorted		10	$\sigma > 2.0$

¹ Could be implemented as a C data type where “parameter” is a member of a C++ class.

² Defined within a membership function (see Section 6.2.4). End members not necessarily shown here.

³ Typical GSPARC specimen (or field exposure) exhibiting the feature.

⁴ Values are arbitrary and for illustrative purposes only. In practice these will depend on the application.

⁵ With reference to the example given, or in the absence of such, more generalised criteria.

6.2.1.3 Composition

The geochemical and mineralogical make-up of rocks is perhaps the most demanding of attributes to define visually yet one of the easiest to classify and index by quantitative analysis. Weathering and alteration processes can subtly or radically change both the chemistry and/or mineralogy of rocks and soils so there is much reliance on contextual data to assist in the interpretation of analytical measurements. Thankfully, initial clues regarding composition can be obtained using imaging and remote sensing. In fact target selection relies on a combination of imaging and spectral techniques since only close-up surveys of pre-selected targets will benefit from *in situ* analytical measurement.

Table 6.5 and Table 6.6 list some examples of compositional attributes applicable to all scales

from remote to microscopic. Note that mineralogy and petrology require specific measurement and subsequent analytical processing and are included to indicate what type of information will be required eventually.

Table 6.5: Compositional feature list (general, all scales, incomplete) ¹

Parameter	Fuzzy Assignment ²	GSPARC ³	SVS ⁴	Notes ⁵
Signature	None		0	Indeterminable or beyond resolution
Signature	Indistinct	194HS435	50	Near resolution (Figure 5.24A)
Signature	Distinct	194HS435	100	Spatial coverage (Figure 5.24D)
Extent	Homogeneous	139HS347	10	Tuff (volcanic ash)
Extent	Heterogeneous	193HS402	50	Impact breccia (polymict)
Albedo	Low	113RS212	10	Stony meteorite
Albedo	Medium		50	Ice (~35%)
Albedo	High	169HS330	100	Light toned deposits
Specularity	Low	75HS136	10	Sandstone (coating) (Figure A.2)
Specularity	Medium	51RS69	50	Granite (quartz, mica)
Specularity	High	44HS340	100	Selenite (mirror-like) (Figure 5.30C)
Colour	Reddish	64HS120	5	Hematite
Colour	Greenish	81HS124	20	Olivine (phenocrysts)
Colour	Bluish	194HS435	200	c-phyco cyanin (Figure 5.24)
Colour	Black	24HS237	50	Basalt (fresh)
Colour	White	34HS252	100	Gypsum (also salt or ice)

¹ Could be implemented as a C data type where “parameter” is a member of a C++ class.

² Defined within a membership function (see Section 6.2.4). End members not necessarily shown here.

³ Typical GSPARC specimen (or field exposure) exhibiting the feature.

⁴ Values are arbitrary and for illustrative purposes only. In practice these will depend on the application.

⁵ With reference to the example given, or in the absence of such, more generalised criteria.

Table 6.6: Compositional feature list (mineralogy/petrology, all scales, incomplete) ¹

Parameter	Fuzzy Assignment ²	GSPARC ³	SVS ⁴	Notes ⁵
Signature	Indistinct	114HS353	5	Near resolution (Figure 5.22)
Signature	Distinct	44HS340	50	Unambiguous (Figure 5.33)
Mineralogy	Dolomite	140FE570	9999	First discovery of a carbonate?
Mineralogy	Jarosite	214HS562	50	Acid aqueous formation
Mineralogy	Goethite	179HS367	5	Weathered Fe-minerals (Figure 5.39)
Mineralogy	Hematite	64HS120	10	Aqueous formation
Mineralogy	Gypsum	34HS252	5	Evaporite facies?
Mineralogy	Phyllosilicate	168LP415	200	Neutral/alkaline formation?
Mineralogy	Quartz	159HS304	50	Chert (Figure B.19)
Mineralogy	Kamacite	150HS280	200	Iron meteorite
Petrology	Basalt	112HS214	5	Mafic volcanism
Petrology	Andesite	202HS454	50	Intermediate volcanism
Petrology	Carbonaceous chondrite	113HS212	400	Chondritic meteorite

¹ Could be implemented as a C data type where “parameter” is a member of a C++ class.

² Defined within a membership function (see Section 6.2.4). End members not necessarily shown here.

³ Typical GSPARC specimen (or field exposure) exhibiting the feature.

⁴ Values are arbitrary and for illustrative purposes only. In practice these will depend on the application.

⁵ With reference to the example given, or in the absence of such, more generalised criteria.

6.2.2 Target Scoring

Deriving the overall SVS for a target is potentially complex. For this study it is important to demonstrate a mechanism by which this could be achieved for a variety of situations using the most basic parameters. The robustness of the method can then be assessed as more complex parameters are introduced.

In general terms the SVS of the target is a function of a number of derived parameters:-

$$SVS = f(As, At, Ac, Ax, Q, B) \quad 6.1$$

where

As is the overall structural attribute score

A_t is the overall textural attribute score
 A_c is the overall compositional attribute score
 A_x is the composite attribute score
 Q is a quality factor
 B is a bias factor

A simple method of calculating overall SVS could be expressed as follows:-

$$SVS = (\sum A_s + \sum A_t + \sum A_c + A_x) \cdot Q \cdot B \quad 6.2$$

The composite score (A_x) is applied when certain attributes occur in combination (See Table 6.7). Note that the quality and bias factors Q and B are intended to enhance or diminish the overall score in much the same way a human geologist may apply these criteria in the field. Q is derived from the recognition algorithms and instrument parameters such as focus, resolution, and illumination. B is derived from the contextual model (Section 6.2.3).

Table 6.7 lists some examples of how one could derive a SVS for a target based on features described in the previous sections and using the above expression. The interpretation assigned to each observation (feature set) is compared with table entries within the contextual model in order to associate the appropriate bias factor. How the observation maps to the interpretation is the subject of further study into the requirements of rule sets and context.

Table 6.7 illustrates some interesting potential outcomes. Example 1 (cross-bedded sandstone) has a predictably high SVS of 1245 due to its compound feature set and distinctiveness. Example 2 (salt deposit) has fewer features and would normally have an SVS of 210. In this case, however, a bias factor of 10 is currently assigned in the contextual model to “salt deposits” as these have yet to be found but are expected at the landing site. Thus the salt deposit scores higher than the cross-bedded sandstone. Example 3 (carbonate) is not expected at the landing site so has a bias factor of unity. However, the detection of carbonate overrides the previous two examples even though the data quality is poor. This is due entirely to the high SVS assigned to the carbonate composition (i.e., 9999). Example 4 (vesicular basalt) scores lower than all previous examples even with an unambiguous petrological interpretation. This is due to a combination of uniqueness and feature-richness of the previous examples.

Table 6.7: Examples of composite features

Feature	Ax ¹	Attributes (As, At, Ac) ²	Q ³	B ³	SVS ⁴
Cross-bedded sandstone	1000	structure.signature = “distinct” = 25 structure.extent = “continuous” = 20 structure.form = “planar” = 10 structure.orientation = “multiple” = 50 texture.matrix = “clastic” = 20 texture.roundness = “sub-rounded” = 20 texture.size = “medium sand” = 10 texture.sorting = “well sorted” = 40 composition.mineralogy = “quartz” = 50	1	1	1245
Salt deposit	0	structure.signature = “none” = 0 texture.extent = “homogeneous” = 10 composition.albedo = “high” = 100 composition.colour = “white” = 100	1	10	2100
Carbonate	0	structure.signature = “none” = 0 texture.signature = “indistinct” = 5 composition.mineralogy = “dolomite” = 9999	0.25	1	2501
Vesicular basalt	0	texture.relief = “vesiculated” = 10 composition.signature = “distinct” = 50 composition.petrology = “basalt” = 5	1	1	65

¹ Composite score due to combination of attributes highlighted in bold.

² Fuzzy assignments and values derived from the feature database (i.e. As, At and Ac).

³ Adjustment based on quality (Q) and bias (B) (see Equation 6.2).

⁴ Final (modified) SVS (see Equation 6.2).

6.2.3 Contextual Model

Put simply, the contextual model describes the geological environment in which the robot explores. For example, if the rover landed in a volcanic region then the contextual model would start off with a presumption that the rocks should be volcanic. If the robot subsequently observes fine layering then this would be assumed to be due to ash deposition or aeolian (or aqueous) reworking of volcanic materials. On the other hand, if the landing site was a lacustrine deposit or an aeolian sand sheet then different interpretations would result. An on-board capability is required in order to either confirm the current contextual model or revise it as a result of “discovery”. In addition to being guided by geological context we need to bias autonomous

decisions toward the mission objectives. So if a robot searching for evidence of water cannot decide which of two candidate targets should be considered prime, and following autonomous assessment one is shown to contain hydrated minerals and the other is a basaltic ash then a positive bias would be applied to the former. To take things further, if during a mission a rock turns out to be comprised of carbonate, this would be treated as a “discovery” (assuming it had yet to be found) and subsequently override any mission objective. The contextual model could also be used to recognise rare rock types found previously during the mission during opportunistic science excursions.

The detailed design of the contextual model is beyond the scope of this thesis. However, it is important to factor such things into the methodology from the very beginning.

6.2.4 Fuzzy Logic

Fuzzy logic is based on reasoning that is approximate rather than precise (Hajek, P., 2006). Consider the classical logic example of hot and cold. In fuzzy logic, the difference between these end members (i.e., “slightly warm”, “moderately warm”, “slightly cool”) may be described by a membership function based on a linear trend, Gaussian distribution, quadratic polynomial, or some other relationship. Fuzzy rules can deal with diverse spatial and temporal data of varying degrees of confidence. In geology, absolute values such as major element concentration (weight % oxide) can be transformed into fuzzy values (i.e., “high Ca content”) and incorporated into rule sets that handle concepts requiring varying confidence levels. The definition of “high Ca content” may differ from one geological scenario to another and probably be influenced by context. Other examples pertaining to structure/texture could (for robotic simplicity) include “slightly weathered”, “distinct fabric”, “rounded grains” and so on.

The application of fuzzy logic in planetary exploration is currently the subject of study (Furfaro *et al.*, 2007). Although the emphasis is focused on tier-scalable planetary reconnaissance, the concept is entirely valid for detailed (and potentially more challenging) *in situ* robotic fieldwork. Fuzzy logic provides a suitable mechanism for resolving rules associated with feature detection (see Section 6.3) and will therefore be considered in future work when the rule-set algorithms are designed. Tables 6.1 to 6.7 list some fuzzy assignments associated with the attributes introduced in Section 6.2.1.

6.2.5 Example Scenarios

The following is based on a rover stationed at an initial waypoint (WP1) and three pre-selected candidate targets (A, B and C) located some distance away on higher ground (Figure 6.1). The primary mission objective is the search for life (i.e., ExoMars) and the contextual model describes the site as a volcanic plain with debris fields adjacent to ridges. The targets were selected from WAC and HRS survey data on the basis of the following:-

- Small vertical promontory, dark (black), mottled texture (Target A)
- Large boulder, smooth, rounded, high albedo, otherwise featureless (Target B)
- Potential outcrop, bluish, slight evidence for bedding (Target C)

Each target is a potential final waypoint (WP_a, WP_b or WP_c) for this excursion and the final choice will depend on the outcome of close-up scientific assessment and engineering requirements made autonomously. The sequence is A-B-C. WP2 is defined by the navigation team as a suitable intermediate waypoint in the case of an unresolved outcome (i.e., the robot is unable to decide between targets on grounds of both science and engineering). Otherwise the rover will remain at or return to the prime target following scientific scrutiny.

Two routes are considered viable in order to reach the location of the targets due to the presence of a large boulder field. Route 1 tracks to the north and Route 2 tracks to the south. The decision which route to take is autonomously confirmed at the new vantage point (?). Remote sensing from WP1 suggests the boulder field to be of no scientific interest. However, an optional WAC/HRC survey at the decision point (targeted towards the boulder field) may enhance a decision based on navigation/engineering grounds only. Whatever route is chosen the rover is programmed to initiate a localised survey along occluded regions of either route. In other words the rover goes into “opportunistic science mode” along segments as shown. In addition, the rover’s “brief” on this occasion is to restrict activities to imaging and only store data that pass the feature-recognition algorithms. An extreme “discovery threshold” is assigned whereby only a high opportunistic SVS would cause the rover to curtail the traverse and await instructions. If this does not happen then the rover proceeds to the target locality and performs close-up evaluation as described in the previous section.

OS = Opportunistic Science

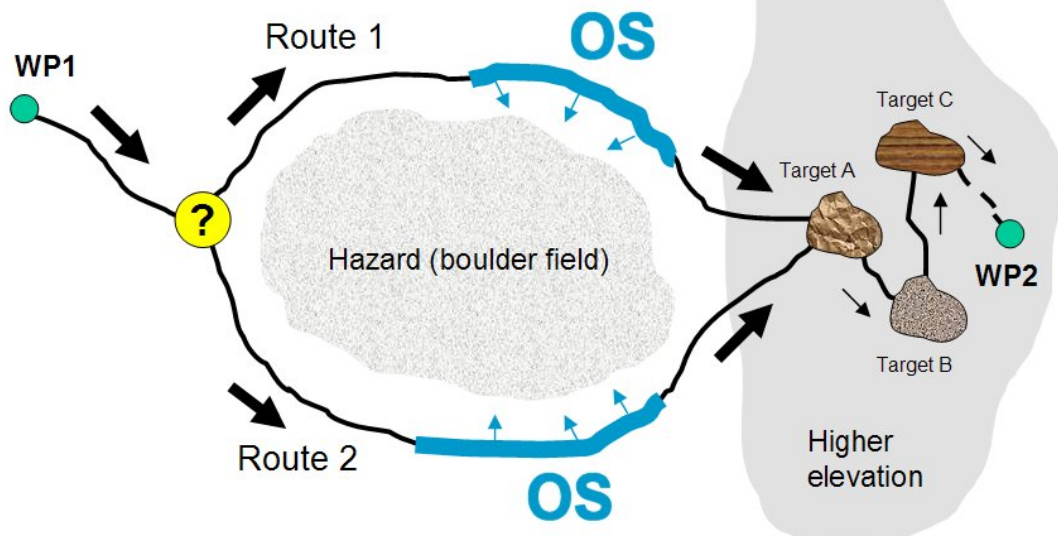


Figure 6.1 Proposed scenario for the evaluation of opportunistic science using an autonomous rover. Scale is arbitrary but the distance between waypoints (WP1 and WP2) could be small (~5 m) in the case of a planetary yard (see Section 6.4.1), or large (~50 m) in the case of a field locality (Figure 3.2E). Targets A, B and C are pre-selected as possible candidates from data acquired at the initial waypoint (WP1). The final target is determined autonomously using scientific criteria (i.e., presence of layering etc.) following close-up investigation. In addition, the traverse includes periods where opportunistic science can be performed en-route to test a variety of outcomes (i.e., halt the traverse following detection of a carbonate signature). For added complexity, the decision point shown can also be used to autonomously select the most appropriate route.

Possible scenarios that could be demonstrated using this example include:-

- A salt deposit is detected (rover stores data and continues towards A, B, and C)
- A carbonate is detected (rover safes itself and waits for instruction)
- Target C displays fine cross-bedding (rover stays at C)
- Target A, B and C are the same volcanic material as WP1 (rover proceeds to WP2)
- Target A is confirmed as an outcrop and is rich in hematite (rover returns to A)

All these scenarios are capable of being evaluated within the controlled environment of a planetary “yard” (see Section 6.7), or at a suitable analogue field site (Table 3.1).

6.3 Feature Detection

Features are “regions of interest” within an image which exhibit spatially related properties such as form, texture, colour, or a combination of all three. The ability to recognise and characterise features within an image using such criteria is perfectly compatible with the objective of this study. In addition, features may also be associated with non-imaging information (i.e., spectral signature). Given the scope of this work, only spatial aspects of feature detection are discussed in the following sections. More complex feature detection involving complementary analytical and geotechnical input will be addressed in future work.

6.3.1 Image Processing

A number of well-established image processing techniques can be employed to recognise structural, textural and compositional features contained within a scene. The order in which each technique is applied will depend on which of these attributes is being sought. In practice, several recursive processing operations will be required since the outcome of one may reveal further, previously hidden attributes (i.e., structure highlighted by differences in texture) and relationships (i.e., composition associated with structure).

The basic image processing techniques considered useful for this application are described in the following sections.

6.3.1.1 Segmentation

Segmentation is a process whereby an image is compartmentalised into regions of interest that share common properties (i.e., texture, intensity, colour, etc.) that differ from neighbouring regions characterised using the same criteria (Gonzalez and Woods, 2007). The technique enables complex scenes to be broken down into simpler entities that can be more effectively analysed. Segmentation is both a closed region boundary detection technique and a classification technique

making it a powerful method for geological application. For example closed regions (segments) are useful for determining the size and shape of individual grains, rocks, or exposures, depending on the scale of the image. Segment properties are also useful in the assessment of texture, fabric, and even composition especially if similar regions map to similar analytical data.

There is no general solution to image segmentation. Edge detection techniques such as described in Section 6.3.1.3 can be used to delineate boundaries but since regions need to be closed, some interpolation is required to infer between disconnected parts of the perimeter. More effective methods for textural analysis (i.e., granularity in geological specimens) include the watershed transformation (Farfan *et al.*, 2004).

An example of image segmentation is shown in Figure 6.2B.

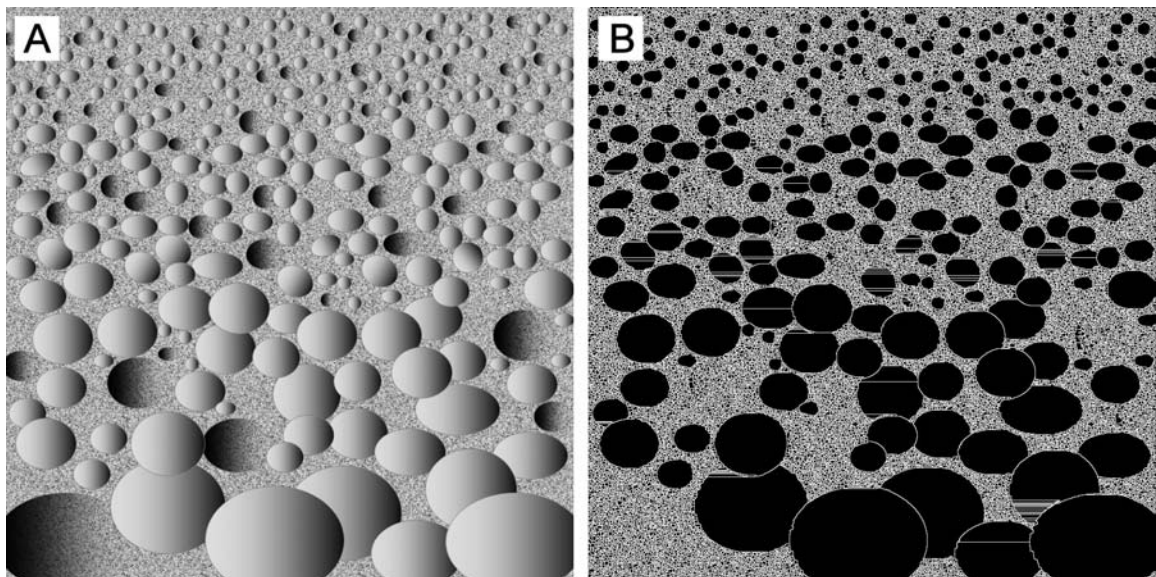


Figure 6.2 An example of image segmentation. The test image A is a cartoon representation of a graded bedding sequence (fining upwards) with added noise and shading (illumination from the left). By applying a segmentation algorithm to A, all the positive elements (“clasts”) are identified as closed regions (B). These regions can be subsequently processed to determine important data such as size, shape and distribution. Note that the negative features (“casts”) are treated as part of the matrix.

6.3.1.2 Morphological Smoothing

Gaussian filters are commonly used in image processing as smoothing functions to reduce high spatial frequencies such as detail and noise (Gonzalez and Woods, 2007). When visualised in two dimensions, a Gaussian surface (filter) is a matrix with circular symmetry and a normal distribution of values radiating from the centre of the matrix. Such a filter is used to calculate and perform a weighted transformation on each pixel and its neighbours resulting in a blurring of the original image whilst still preserving boundaries and edges. This is a necessary pre-stage to edge detection (see Section 6.3.1.3). In theory, such a matrix would be infinite in size and contain non-zero values. However, in practice, values beyond 3σ are considered insignificant allowing the size of the filter to be usually much smaller than the image itself.

An example of morphological smoothing is shown in Figure 6.3B.

6.3.1.3 Edge Detection

Edge detection determines the parts of an image where neighbouring pixel intensities change abruptly thereby indicating a discontinuity or an edge (Gonzalez and Woods, 2007). Two approaches are common in image processing, the Sobel operator (Fisher *et al.*, 2003) and the Canny edge detector (Canny, 1986). Both require morphological smoothing as a pre-processing step to reduce noise.

The Sobel operator calculates the local intensity gradient for each pixel in an image using two 3×3 convolution masks (see Fisher *et al.*, 2003), one to estimate the gradient in the X direction and the other in the Y direction. The resulting magnitude is used as an indicator of the likelihood of an edge at that position. The Sobel filter is straightforward to implement and computationally efficient making it an attractive technique for planetary robots. However, the gradient determination (and direction) is rather crude and heavily dependent on effective pre-smoothing.

The Canny edge detector uses four filters (these could be Sobel operators) to determine gradient maxima for horizontally, vertically and diagonally orientated edges. The directional information is approximated to one of the four principal directions (i.e., 0° , 45° , 90° , 135°). Enhanced versions of the Canny algorithm make provision for smaller angular increments thus producing

higher directional fidelity. The assigned vector is determined from a search of all the gradients calculated for each direction. This process is called non-maximum suppression and results in a binary image comprised of pixels that either correspond or do not correspond to edges for a particular direction.

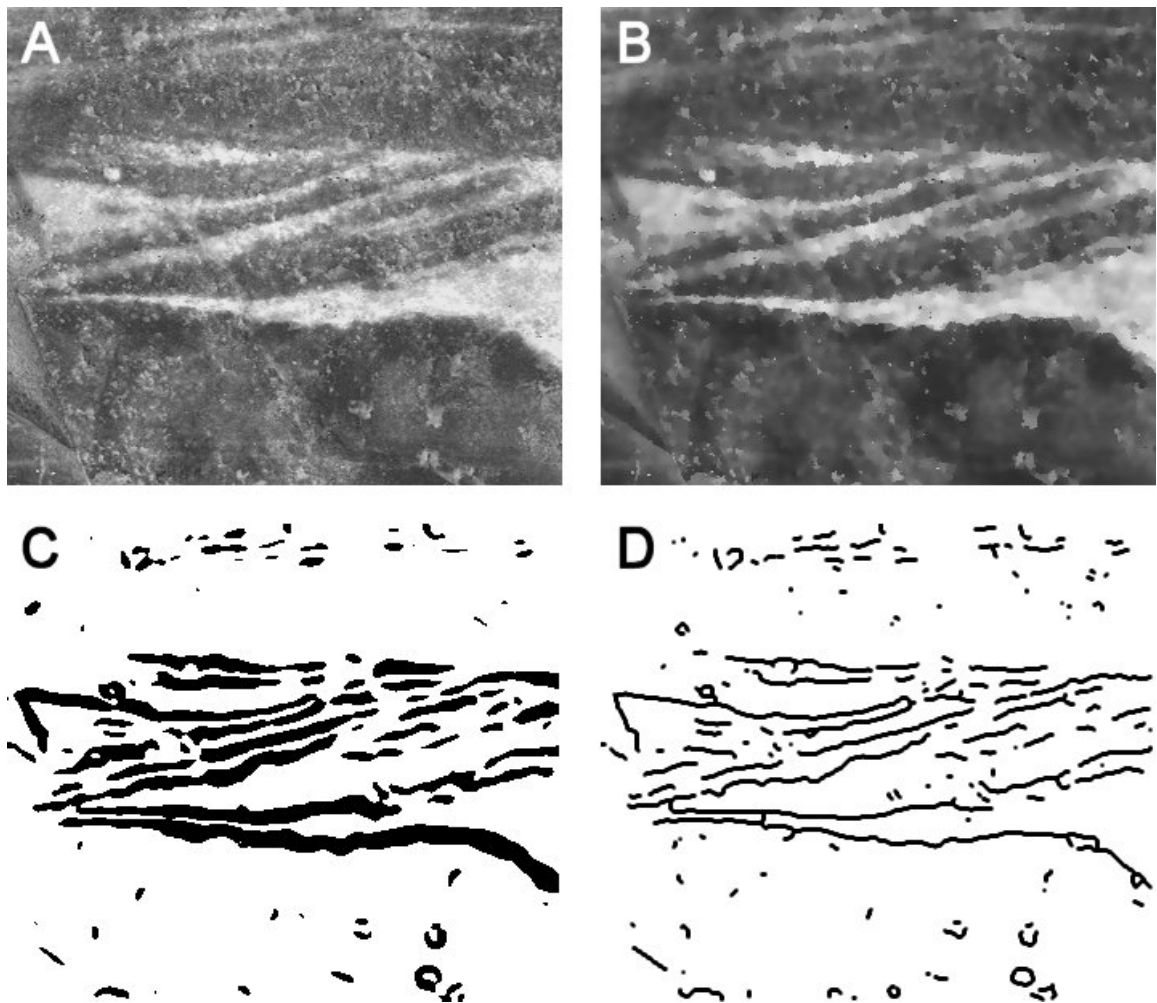


Figure 6.3 Edge detection techniques applied to robotic field geology. Image A is a macroscopic view of sample 190HS390, an Early Archaean banded chert from the Pilbara, Western Australia (see Section B.8). Image scale is ~2 cm across. The features of interest include cross-bedding and lenticular structures. The image is initially processed using a morphological smoothing function which results in a blurring of the image whilst preserving key edges (B). The edge detection algorithm (i.e., Canny) is then applied to B resulting in C. The lines are then reduced to a single pixel thick (D) using a skeletonise technique so further computation can be performed on the result (i.e., orientation). Note that D has been re-thickened for presentational clarity. Instrumentation: B2SCS\$CUL\$R (A).

Line thinning (or skeletonisation) is usually performed as a post-processing step following edge detection, although non-maximum suppression naturally performs this function. Edge tracing and thresholding with hysteresis can then be applied to ensure isolated pixels with large gradients are discarded whilst traceable pixels (i.e., part of an extended line) with small gradients are retained. This is particularly important for geological applications since it could be used to quantifiably delineate bedding features and unconformities.

An example of edge detection is shown in Figure 6.3C and line thinning in Figure 6.3D.

6.4 The Autonomous Robot Scientist (ARS)

The Autonomous Robotic Scientist (ARS) addresses the need for greater rover autonomy in the areas of data analysis/interpretation, science planning, responsive manoeuvres and instrument placement. At a more abstract level, the ARS provides rovers with the ability to opportunistically detect targets of scientific interest and rank them accordingly, this would both enable additional science activity and improve the turn-around time for nominal mission goals.

The initial phase of ARS was funded under the UK STFC CREST initiative in order to establish and demonstrate a prototype of a system based on the ESA ExoMars model (rover design and operational philosophy), since this was seen as a potential route to early implementation. However, much of the scientific requirements of the ARS are generic and transferable to robotic and robo-assisted human missions to other Solar System bodies including the Moon.

Within the limited funding and time constraints of this initial phase, the ARS project implemented and fulfilled the following requirements:-

- A methodology for the scientific assessment of fundamental geological parameters
- A prototype system architecture which can support the concept of autonomous science
- Prototype elements of the scientific model in order to demonstrate and assess the feasibility of the methodology
- Multi-scenario demonstrations of the prototype system within a representative environment using an ExoMars-like rover equipped with tricloptic vision (stereo WAC and HRC system)

Details of the overall ARS system architecture, operations framework and the results of early trials are given in Woods *et al.* (2008b). At the core of the ARS system architecture is the Science Assessment and Response Agent (SARA). This module processes scheduled input data from the science instruments and performs a science assessment using an implementation of the rules outlined in Section 6.2. If the assessment is positive (i.e., the targets are considered scientifically “interesting” and worthy of deviation from the nominal timeline), SARA makes a request to the planning system to insert a new sequence into the schedule (i.e., stop and acquire a HRC image). The planner evaluates the feasibility of this request (in terms of system resources), and modifies the sequence to accommodate the new activity if this is possible. Subsequent outcomes may result in an escalation of opportunistic science (i.e., HRC images reveal more scientific interest) or simply a reversion to the nominal plan.

The current version of SARA (post CREST) is limited to processing 2D greyscale images and uses the basic image processing methods described in Section 6.3.1. Nevertheless, the software is capable of demonstrating basic feature detection and classification based on structure (see Section 6.4.3). Future versions will incorporate other visual attributes and ultimately analytical data.

To assist in the design and verification of the SARA software, a library of images was specified and compiled by the author. Each image needed to be representative of geological features exhibiting a number of attributes and degrees of complexity. The first step was to produce very simple synthetic images (cartoons) in 2D greyscale representing individual attributes such as structure (Figure 6.4A), texture (Figure 6.4B) and composition (Figure 6.4C). Complexity was systematically introduced to each basic image by adding noise and shading (Figure 6.4D). Further realism was achieved by representing a variety of attributes within the same field of view (Figure 6.4E). As a final validation step, images of real geological features were prepared (Figure 6.4F), including those related to the study specimens described in Chapter 4 and Appendix B.

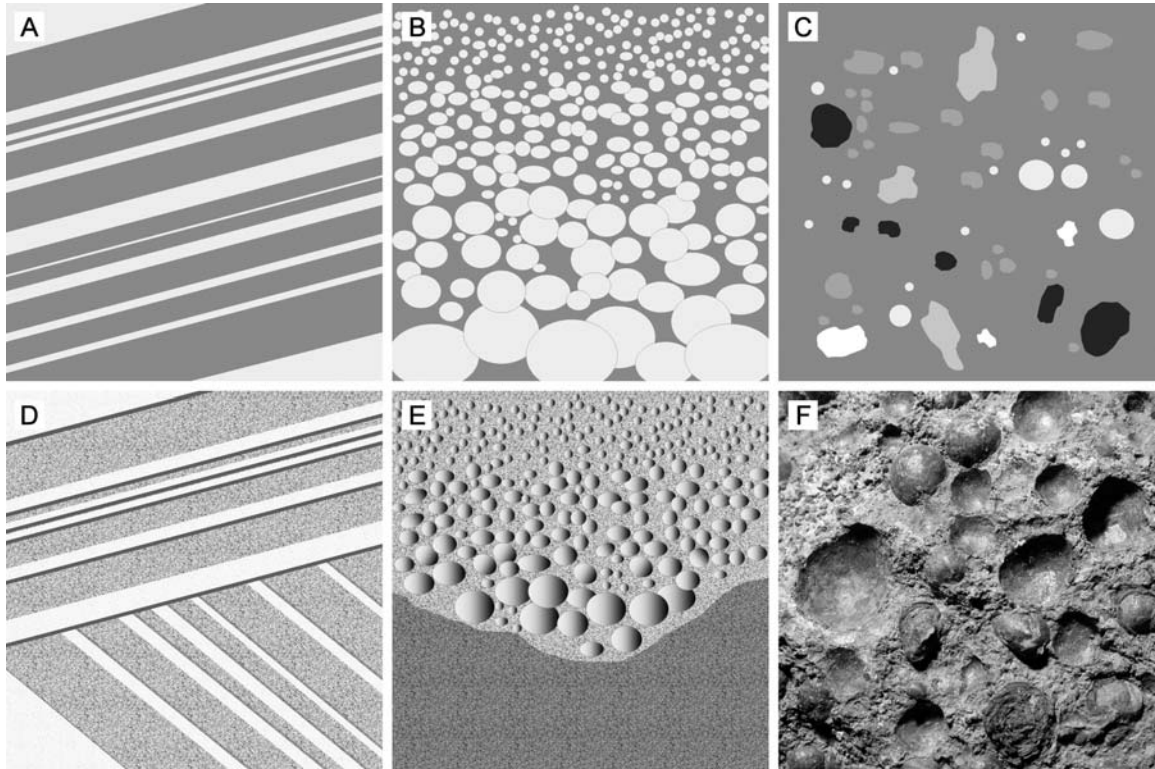


Figure 6.4 Selection of test images from the image library prepared for the Autonomous Robot Scientist (ARS) project (see Section 6.4). Images ranged from simple cartoons representing individual attributes pertaining to structure (A), texture (B) and composition (C), to more complex composite cartoons (D and E), and to images of real rocks (F). Key: A = planar bedding, B = graded bedding, C = albedo, D = cross-bedding, E = buried channel, and F = hematite concretions (168HS131).

All these images are 2D representations of 3D scenes so depth perception relates to texture rather than the location of objects in physical space. Nevertheless, there are many situations in field geology where 2D imagery is relevant such as vertical exposures or horizontal pavements. Furthermore, proving the concept in 2D is an essential prerequisite to the more complex world of 3D. Future versions will ultimately be expected to interpret stereo data, derived Digital Terrain Models (DTMs), and the results of shape from shading analysis (Cryer *et al.*, 1995). In preparation for 3D, stereo image pairs were also included in the library.

Prior to the hardware demonstrations (see Section 6.4.3) selected images were processed by SARA using the techniques described in Section 6.3.1. Some results are shown in Figure 6.5.

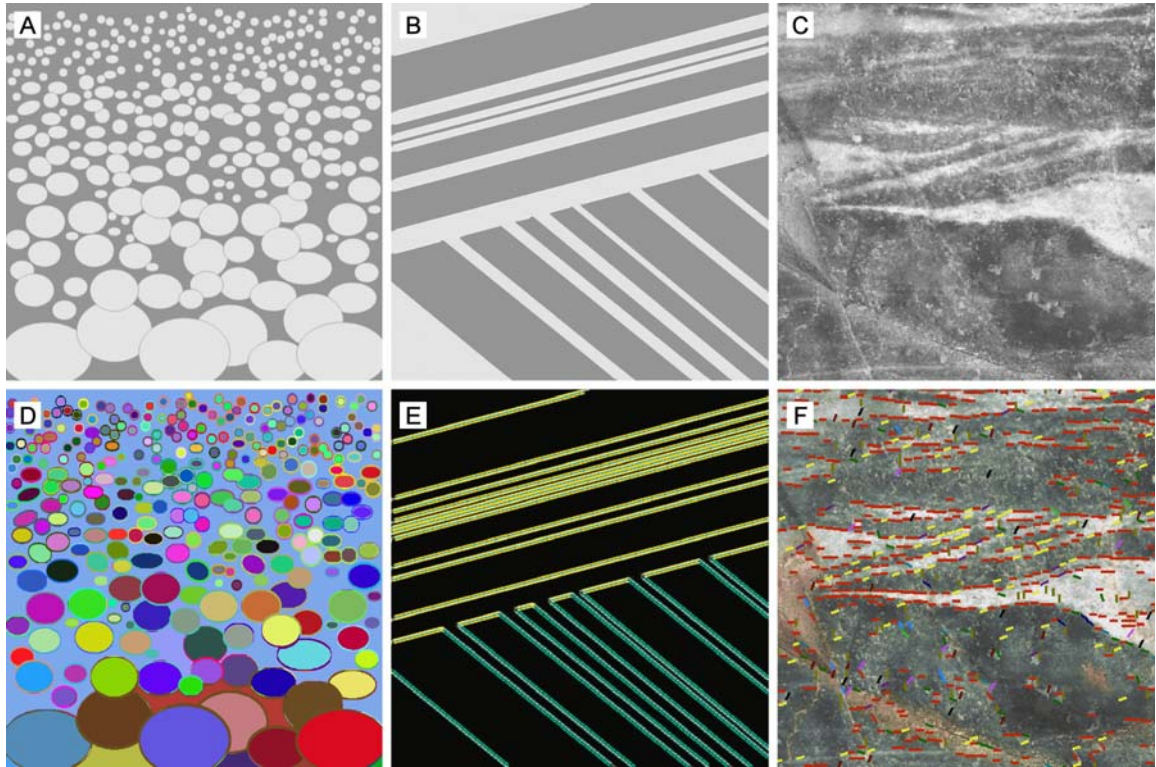


Figure 6.5 Evaluation of the Science Assessment and Response Agent (SARA) software developed for the Autonomous Robot Science (ARS) project (see Section 6.4). The segmentation routine was first tested on simple cartoons (A and D) and subsequently used during the rover trials to detect rocks within the terrain (Figure 6.8B). Colour coding in D is a consequence of the test routine and not relevant. The edge detection routine also underwent similar testing (B and E) prior to being used to recognise layering in science targets (C and F, and Figure 6.8B). The colour coded line segments in images E and F represent edges sharing the same orientation. Image C is ~2 cm across. Courtesy Dr. Andy Shaw, SciSys Ltd (DEF).

6.4.1 The Planetary Analogue Terrain (PAT) Laboratory

The Planetary Analogue Terrain (PAT) is an 8 m x 5 m simulated Martian surface situated in the Department of Computer Science laboratory at Aberystwyth University and is designed specifically for robotic rover simulations (Figure 6.6). The surface material is a grey geotechnical analogue of Martian “soil” and is comprised of a Flintag-quartz sand mixture (USDA classification 91% sand, 6% silt, 3% clay). Although useful for locomotion, the monochromatic nature of the simulant imposes some limitations on visual science operations beyond the proximal scale (> 1 m). The material is approximately 15 cm thick and overlies a solid coarsely

contoured substrate. The topographic profile is based on the author's generic design shown in Figure 6.1, consisting of an elevated area which can accommodate removable science targets (i.e., synthetic outcrops or real large rocks) and column inserts for sub-surface sampling operations using other analogue materials such as Mars soil stimulant JSC Mars1 (Figure A.4). Given the limited size of the PAT, activities that require traversing between waypoints are constrained to half-scale robotic vehicles equipped with commercial imaging systems. However, "at station" activities such as sub-surface sampling, arm placement manoeuvres or close-up/contact science measurements can be conducted using full size representative instrumentation.

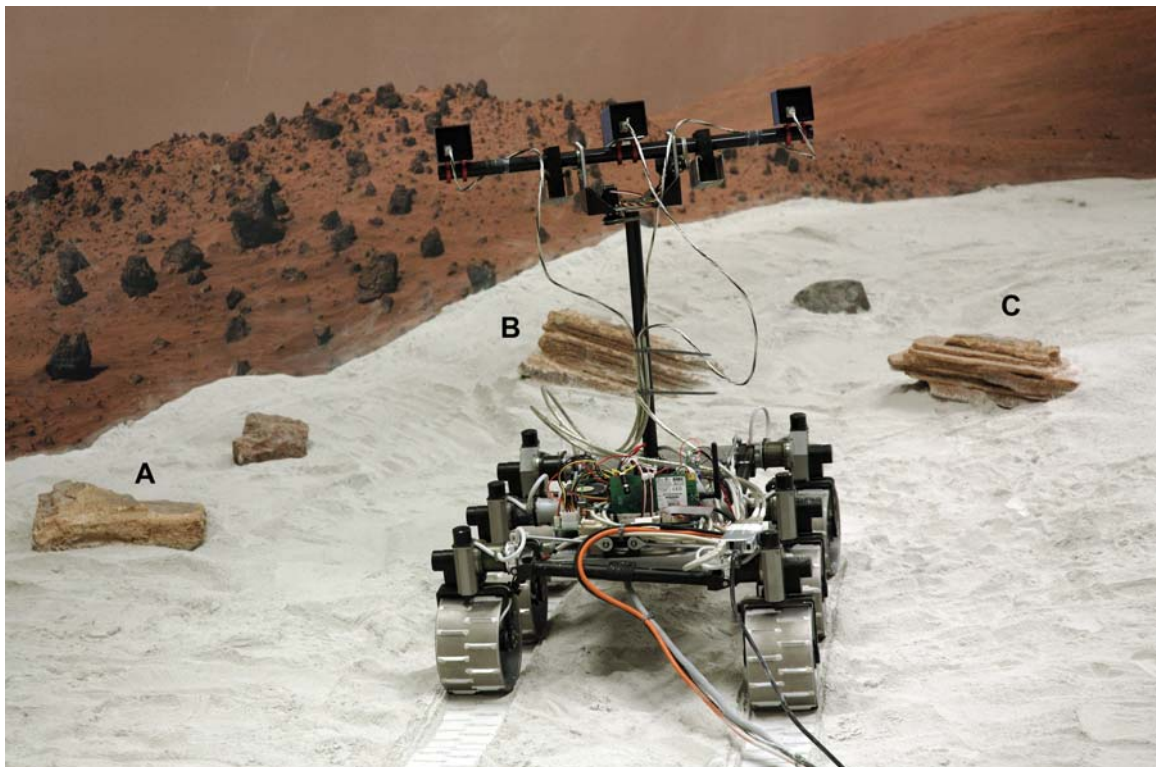


Figure 6.6 Half-scale rover equipped with camera systems performing a science assessment of candidate targets during autonomous trials at the Planetary Analogue Terrain (PAT) laboratory, Aberystwyth University. See Figure 6.7 for a closer view of the synthetic science targets.

6.4.2 Science Targets

For the CREST ARS rover trials (July-October 2007), synthetic science targets were prepared by the author and integrated into the PAT (Figure 6.7). No analytical or representative contact operations were planned, therefore the use of real rocks for scientific purposes was discounted.

Furthermore, the feature recognition algorithms were at a very early stage of development so relatively simple 3D targets were required. Geological samples were used during the rover trials but these were restricted to featureless specimens to provide context and obstacles for navigation.

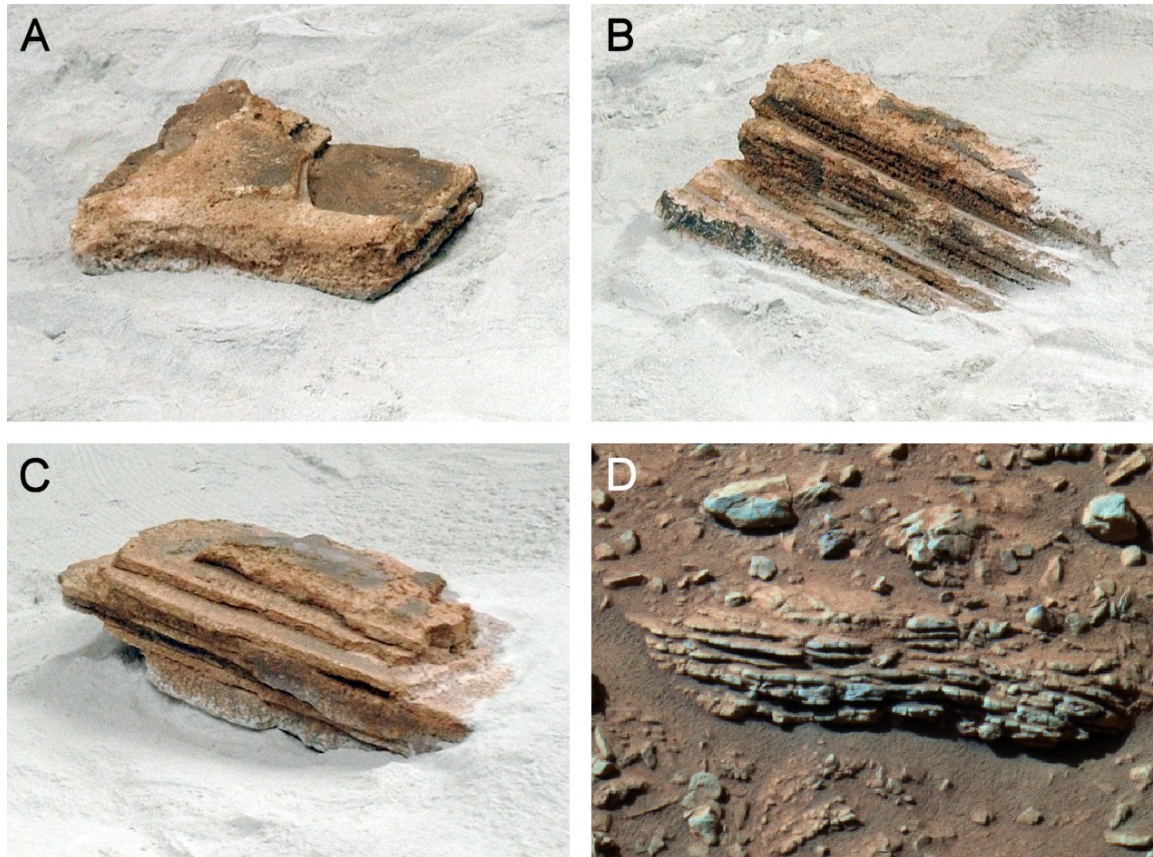


Figure 6.7 Three-dimensional science targets (A, B, and C) created by the author for use in the Planetary Analogue Terrain (PAT) laboratory at Aberystwyth University (see Section 6.4.1). The targets were designed to exhibit simple layering similar to exposures observed on Mars (D). Refer to Section 6.4.2 for a description of how the targets were made. Each target measures about 30 cm across. Key: A = 117FE575, B = 117FE576, C = 117FE577, and D = 04-SS1-04-Color_Rock-A268R1. Courtesy NASA (D).

Expanded polystyrene was used to fabricate three appropriately scaled and visually realistic science targets, each illustrating a combination of primary attributes including layered structure, granular texture and colour heterogeneity. Two of the prepared targets were designed as outcrops (117FE576 and 117FE577) which required that they be inserted into the terrain (Figure 6.7B/C). The other (117FE575) was also designed as an outcrop, but could be used as a float rock which revealed layering only when viewed from a certain rover position (Figure 6.7A). Once carved and

physically distressed for morphological realism, each target was painted using a “wet-on-wet” technique. The base hue was determined from Spirit images of layered light toned rocks such as Tetl (04-SS1-04-Color_Rock-A268R1) (Figure 6.7D) and the saturation level adjusted to minimise excessive greyscale-equivalent contrast between the colour targets and the grey geotechnical surface. The final stage involved “dry brushing” in order to accentuate the natural granular texture of the material and simulate a compositionally contrasting rock coating similar to the sandstone sample 75HS136 shown in Figure A.2. These synthetic targets remain a resident feature of the PAT surface.

6.4.3 Rover Trials

Autonomous science using the prototype ARS, and a half-scale rover equipped with WAC and HRC cameras, was demonstrated using a simple traverse shown in Figure 6.8A. The planned sequence was to proceed in a straight line from the WP1 (current location of rover) and assess WAC images at strategic intermediate points en-route with SARA. Science richness was based simply on the presence of layers within objects detected in the WAC images using segmentation (see Section 6.3.1.1). Geological targets without layering were located at intermediate positions 1 and 2 (group 1), and with layering (117FE576 and 117FE577) near intermediate position 3 (group 2). The pre-planned response following positive detection was to first request a HRC image and, if more detailed layering was detected, to subsequently request an ARM placement manoeuvre on the target rock. Figure 6.8CD illustrates the successful outcome for this particular scenario. Significantly, by inverting the assessment criteria (i.e., no layering is more interesting than layering) it was possible to demonstrate a different outcome for the same nominal traverse.

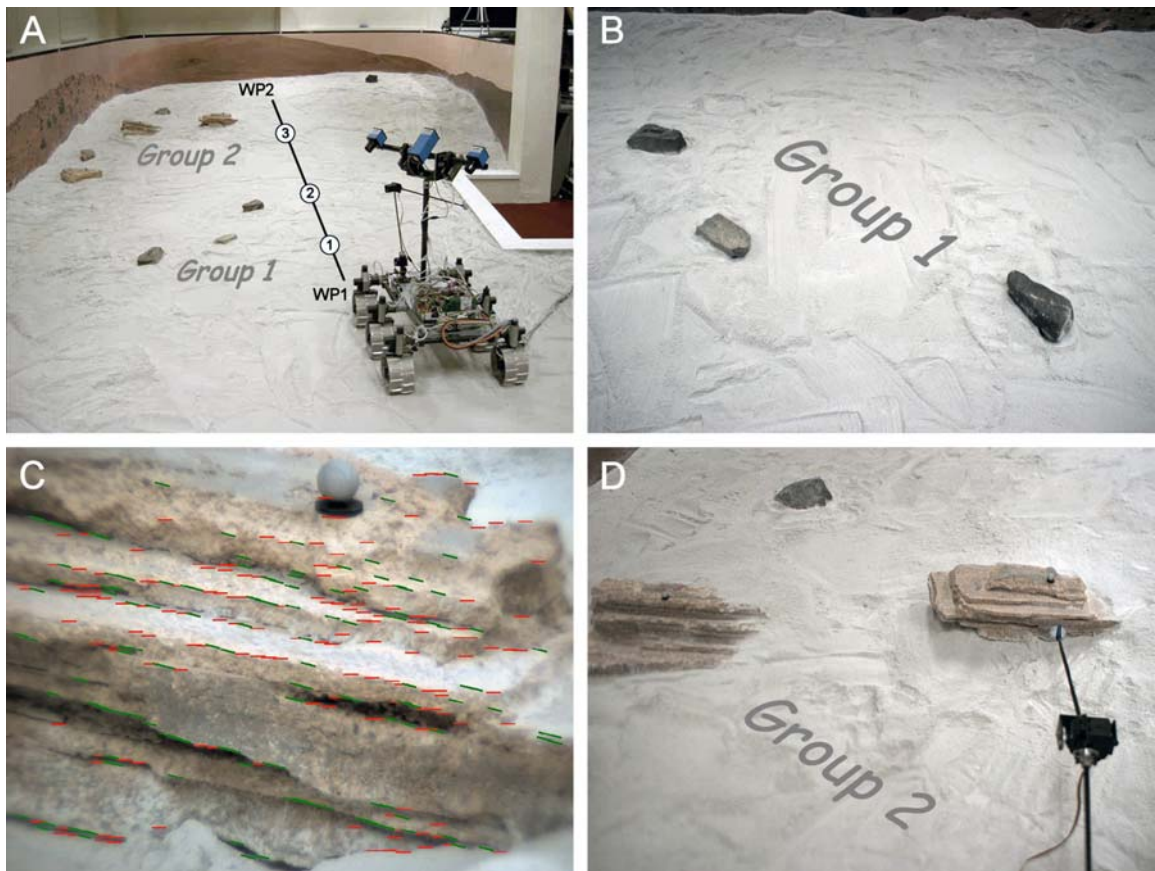


Figure 6.8 Demonstration of opportunistic science with the Autonomous Robot Scientist (ARS) at the Planetary Analogue Terrain (PAT) laboratory, Aberystwyth University (see Section 6.4). The nominal plan consisted of a single linear traverse from WP1 to WP2 with three intermediate points at which imaging and science assessment would be performed (A). Two groups of science targets were positioned along the route as shown. Group 1 consisted of dark rocks without layering (B) and group 2 consisted of the samples shown in Figure 6.7 expressing well defined layering (C and D). For this traverse, the SARA software was programmed to consider layering of high scientific value and if detected (C) request a deviation from the nominal plan to perform an ARM placement manoeuvre (D). Other traverses with different scientific criteria (i.e., homogeneous rocks higher priority the layered rocks) produced different successful outcomes. Courtesy CREST ARS.

6.5 Summary

Some fundamental aspects of terrestrial field geology have been described in this Chapter, in particular the ability to characterise structure, texture and composition. These attributes are routinely assessed by terrestrial field geologists in the interpretation of geological features and therefore have the potential to form the basis of a framework suitable for robotic applications. As a result, a novel methodology for autonomous science is outlined in detail which is based on assigning a numerical science richness score to geological features exhibiting these attributes in both simple and complex combinations. Examples given include planar-bedding, cross-bedding and graded-bedding. In addition to assigning a basic score, external factors such as the influence of bias (based on geological context) and quality (based on observation parameters) are also considered at this stage but not fully defined since this is beyond the scope of this thesis. The current work is restricted to 2D imaging but this will necessarily evolve to incorporate 3D and analytical data in the future. Considerations for these more advanced concepts were discussed.

Proposed mechanisms for implementation and verification of the concept include fuzzy logic (for non-precise calculations), feature detection techniques (for identification of targets and fundamental attributes) and evaluation scenarios (testing with robots).

A basic implementation of the concept was successfully demonstrated as part of the CREST Autonomous Robot Scientist project.

Chapter 7

Conclusions and Further Work

This Chapter summarises the outcomes and conclusions drawn from the topics covered in preceding chapters, namely the specimen archive, payload experiments and scientific autonomy. The need for further work within each of these areas is argued and recommendations are made to ensure the continuation of an integrated programme of analogue studies. Spin-off potential to other areas of science is also discussed, including the transfer of technologies and methodologies described herein to the field of forensic science.

7.1 Introduction

Analogue studies importantly underpin planetary missions and can provide essential continuity between early concept and design through to actual mission operations. This has been demonstrated within the US space programme since the Apollo era but is only recently being considered in Europe. Nevertheless, no established coordinated analogue programme exists that combines all the necessary elements together in the form of resources, context, community and outreach. In recognition of this, the author proposes the following with which to establish such a programme:-

- An extensive archive of well characterised, and appropriately formatted geological analogue specimens and associated experimental data for use by the planetary science, space engineering, and outreach communities (Chapter 3)
- A network of multidisciplinary specialists with an interest in planetary exploration, including adjunct scientists and engineers not directly associated with missions or payload development (Chapter 3)
- A programme of themed laboratory and field analogue studies designed to address the practical aspects of *in situ* planetary exploration from payload experiments (Chapter 5) to autonomous science (Chapter 6)

7.2 The Planetary Analogue Archive

The need for a shared archive of well characterised and appropriately formatted planetary analogue specimens to support planetary exploration was envisaged at the beginning of this project in late 2001. A novel combination of physical specimen archive and experiment database (GSPARC) began in 2003, initially biased to the geological and astrobiological needs of the Beagle 2 mission, and later expanded to cater for future missions such as ExoMars. The concept also proved to be a way of linking planetary-related research with the requirements of education and outreach via initiatives such as SpaceROX (see Section 3.2.4.1).

As described in Chapter 3, the analogue support programme for Beagle 2 was limited due to lack of both project funds and time. Some useful experiments with GSPARC specimens and Beagle 2 instrumentation were conducted prior to the failure of the mission and subsequently incorporated into a more substantial study programme in support of ExoMars and beyond (Chapter 5). Lessons learned from the failure of Beagle 2, although primarily concerned with spacecraft engineering (Sims *et al.*, 2004), also highlighted a lack of adequate overall scientific readiness for surface operations. In response to the concerns of the Beagle 2 science team expressed during the latter part of 2003, the Planetary Analogue Field Studies Network (PAFS-net) was founded in 2004 (see Section 3.2.3.2). In addition to coordinating analogue studies in association with GSPARC (Chapter 5 and Chapter 6), the author and other members of PAFS-net have been active in drafting major proposals for future missions such as the Mars Origins Mission (Westall and Klingelhöfer, 2007; Klingelhöfer *et al.*, 2008).

7.2.1 Future Work

The GSPARC physical archive continues to expand with more analogue themes being added to the collections. At the time of writing, the total number of <items> exceeds 600. The project remains unfunded although there are plans to finance a central repository of physical specimens within France (Dr. Frances Westall, Centre de Biophysique Moléculaire, CNRS, personal communication). The PAFS-net membership also continues to expand, partly due to active targeted recruitment and partly as a result of exposure to the activities of the network via international conferences and workshops (for example Pullan, 2007).

For some of the experiments described in this thesis the quantity and variety of study sample material was clearly restrictive. For example, only one small specimen of chasmoendolithic marble from Antarctica was available (Appendix B.6), and no domical stromatolites in plan section from the Trendall locality (Appendix B.9), thus imposing limitations on what could be achieved with these analogues. If possible, future studies should aim to incorporate a field component whereby samples can be both collected and contextualised according to long-term need prior to the laboratory phase. Sample collection can be achieved either as a dedicated, funded part of a study, or via special requests to the PAFS-net membership who plan to visit analogue sites to pursue their own research. Recent examples include sampling at sites near Barberton, South Africa (komatiite), and near Krafla, Iceland (hyaloclastite). Another advantage of the expanding PAFS-net membership will be to provide wider access to institutional sample collections, instrumentation and niche expertise.

The on-line version of GSPARC is already under development and currently includes a working search interface (Figure 3.7). The intention is to incorporate all the functionality of the standalone version described in Section 6.2.2.1 and implement the different access requirements for researchers, educators and the public. The database currently contains the results of experiments undertaken within the scope of this thesis and the work in progress shown in Table 3.3. It is planned to add the results of previous studies performed by PAFS-net members where relevant specimens can be made available for inclusion into the physical archive *post facto*. This will greatly enhance the database with minimal effort.

7.3 Astrobiology Studies

The work carried out in both experimental studies described in Chapter 5 was by no means exhaustive, given the limited number of samples chosen (Chapter 4), and the array of potential techniques available (Appendix C). It was possible, however, with such an inventory, to investigate a number of fundamental sample attributes and methods applicable to *in situ* measurement within the constraints of current space instrument technology, and establish an approach upon which to build further.

Unambiguous identification of biologically related features on Earth or Mars requires substantiating evidence from a multitude of techniques. One should not posit a biosignature or palaeo-environmental indicator based on evidence from one technique without corroboration

from at least one other. This applies equally to the various features observable within the range of physical scales employed within this work (~100 μm to ~10 cm). Examples include detectable organic signatures (i.e., Figures 5.21 and 5.31), residual biofabrics formed as a result of mineral encrustation (i.e., Figures 5.2 and 5.14), or preserved sedimentary structures indicative of potential habitable environments (i.e., Figures 5.34 and 5.38), all of which are very common processes observed on Earth and entirely plausible for Mars (Banfield *et al.*, 2001). Corroborating evidence in support of morphological expression could come from a number of viable *in situ* observations, including physical properties, elemental chemistry, molecular chemistry, and mineralogy (see Section 2.3).

Collectively, all imaging, analytical and geotechnical techniques that were employed confirmed their effectiveness for *in situ* astrobiology and geology (Table 7.1). By adopting a sample-centred philosophy (as would be the case during mission operations) and utilising a combination of spaceflight hardware (where appropriate) and commercial instrumentation (acting as emulators), synergies, interdependences, and practical issues could be experienced first hand. Scientifically, these studies have also advanced the level of understanding about which techniques (that were available for this investigation and are technologically viable for space missions) can be used in concert to evaluate the potentially biogenic nature of certain morphological features. Based on the results, some strategic criteria can be formulated (Table 7.2). A more detailed philosophy will emerge following the outcome of *in situ* studies within a broader programme, in particular in-field experiments involving robotic sampling.

A practical scaling philosophy was introduced that defined radial working distances for *in situ* operational activities of stationed rovers, static landers and “instrumented” humans: proximal (~100 cm), macroscopic (~10 cm) and microscopic (~1 cm). The adoption of the term “proximal” corresponded with the lower bounds of the microfacies scale (metres to centimetres) advocated by Cady *et al.* (2003). Strategies differed at each scale, with finer scales being dependent on the interpretations made at coarser scales. As such, imaging is recommended to be as seamless as possible within this range of distances and to have high spectral capability (bandwidth and resolution) to support each scale. Controlled illumination was found to be extremely useful for *in situ* macroscopy and absolutely essential for *in situ* microscopy. Such techniques provided a way of obtaining the true colour of targets and a means for identifying and discriminating bio-fluorescent features (via UV excitation).

Table 7.1 Suitability of selected instrumentation for *in situ* analysis of study samples^{1,2,3,4,5}

Samples: ⁶	Microbial filaments				Endoliths			Sedimentary structures		
	Limestone (140)	Opaline sinter (169)	Chalcedony (45)	Goethite (179)	Ortho-quartzite (114)	Marble (194)	Gypsum (44)	Banded chert (190)	Stromatolitic chert (159)	Banded Iron Formation (163)
Beagle 2 camera (<i>geology filters</i>)	MC	MC	MC	MC	MC	MC	MC	MC	MC	MC
Beagle 2 camera (<i>close-up mode</i>)	MC	MC	MC	MC	MC	MC	MC	MC	MC	MC
Beagle 2 camera (<i>close-up + UV mode</i>)	-	-	-	-	-	B	-	-	-	-
Multi-spectral imager	MC	MC	MC	MC	MC	MCB	MC	MC	MC	MC
Beagle 2 microscope	MC	MC	MC	MC	MCB	MC	MCB	MC	MC	MC
Beagle 2 microscope (<i>UV mode</i>)	-	-	-	-	B	B	-	-	-	-
Laboratory XRF	C	C	C	C	C	C	C	C	C	C
Field portable XRF	C	C	C	C	C	C	C	C	C	C
Laboratory Raman	C	C	C	C	CB	CB	CB	C	CB	C
Beagle 2 Mössbauer	C	C	C	C	C	n/a	n/a	C	C	C
Laboratory XRD	C	n/a	n/a	n/a	C	n/a	n/a	C	C	C
Beagle 2 soil sampler (<i>rock splitting mode</i>)	✓	✓	✓	? ⁷	✓	✓	✓	✓	✓	✓
Beagle 2 rock corer	✗	✗	? ⁷	✗	✗	✗	✗	? ⁷	? ⁷	? ⁷

¹ Characteristics observed based on morphological (M), compositional (C), and biological (B) indicators.

² All samples were unprepared, natural hand specimens. Measurements made on reference powders are not shown here.

³ Shaded entries indicate significant or influential results (see Chapter 5).

⁴ A dash (-) indicates no effect was observed and n/a = not analysed.

⁵ The technique would likely be beneficial (✓) or detrimental (✗) in the case of morphological features.

⁶ Number refers to the GSPARC <family> ID (see Appendix A for details). All samples are fully described in Appendix B.

⁷ Tests on similar materials are required to assess whether the technique would be advantageous.

Table 7.2: Summary of key features observed at each working scale

Activity ^{1,3,4,5}	Key Features (sample <family> IDs)
Proximal (~ 100 cm)	
Ambient (solar) illumination only Stereo imaging (using pairs) Multi-spectral classification of candidate targets Target selection for macroscopy	Spectral anomalies (194, 114) Layering (169, 114, 44, 159, 163) Sintered surfaces (140) Aligned textures (140, 179) Cross-bedding (190)
Macroscopic (~ 10 cm)	
Ambient (solar) or self illumination (RGB, UV) Stereo and 3D imaging (using translation) Multi-spectral classification of observed features True colour imaging (RGB) UV fluorescence (biological or mineralogical) Target selection for <i>in situ</i> microscopy Target selection for <i>in situ</i> XRF Target selection for <i>in situ</i> Mössbauer	Open fabric (140, 169, 179) Tubular morphology (140) Mineralogy with morphology (140) Visible filaments (45, 179) Visible cryptoendoliths (114) Visible chasmoendoliths (44) Bio-fluorescence (194) Stromatolitic texture (159)
Microscopic ² (~ 1 cm)	
Self illumination (RGB, UV) Stereo and 3D imaging (using translation) True colour imaging (RGB) UV fluorescence (biological or mineralogical) Target selection for <i>in situ</i> Raman Geochemistry (XRF) Mineralogy (Raman and Mössbauer) Organic compounds (Raman) Physical properties (geotechnics)	3D morphology of tubes (140) 3D morphology of clusters (169) Morphology of encrusted filaments (45) 3D distribution of chasmoendoliths (44) Globular texture (194, 44) Distribution of bio-fluorescence (194) Surface relief of relict laminae (190) Trace element enrichment (140, 45, 190) Fe-coated grains (114) Identification of scytonemin (194, 114, 44, 159) Identification of carotenes (194, 114, 44, 159, 140) Identification of chlorophyll (194, 114, 44) Identification of parietin (194, 44) Identification of c-phycoyanin (194) Identification of porphyrin (159) Crystallinity and chemical purity of goethite (163)

¹ Distance between observer (instrument) and target (feature on sample)² May involve physical contact to ensure correct standoff distance between detector and target³ Imaging footprints are 4 cm x 4 cm (macroscopy) and 4 mm x 4 mm (microscopy)⁴ Analytical footprints are ~ 20 mm \varnothing (XRF), ~ 14 mm \varnothing (Mössbauer), ~ 2 μ m to 100 μ m \varnothing (Raman)⁵ XRD is not included as this is a post-sampling activity. However, *in situ* XRD used in this work examined an elliptical spot of area ~ 0.13 mm² so could be classed as a microscopic activity here.

The Nuance multi-spectral system was extremely useful for macroscopic imaging (Figures 5.1D, 5.19B, and 5.25B) and has the potential to be exploited across the scale range using suitable optics. LCTFs are probably not suitable for space applications (due to thermal constraints) but are convenient for analogue studies. Microscopic imaging of some study samples with the Beagle 2 microscope produced impressive results but often required additional care when fine-positioning over a target identified at the macroscopic scale. This was particularly challenging when visible biosignatures were small and spatially distributed (Figure 5.24C). 3D imaging using stereo techniques proved invaluable for open fabric materials (Figures 5.7A and 5.15), as did those using incremental focusing for seemingly flat surfaces exhibiting subtle relief (Figure 5.35B). Specular reflection was more of a problem for the Beagle 2 camera than the Beagle 2 microscope due to a combination of non-diffused projected light from the commercial ring-light and high reflectivity of some targets (Figure 5.30C). Enhancements are being implemented to minimise this effect using a polarised light source and a polarising filter, similar to what is being proposed for MicrOmega on ExoMars (Bibring *et al.*, 2006b). The Beagle 2 microscope performed exceptionally well and produced some spectacular results (Figures 5.2, 5.7C, 5.11, 5.14B, 5.20, 5.26B, 5.30D, and 5.35B), which confirmed the usefulness of a true “deployable” field microscope.

The portable XRF (TN9000), though limited in terms of elemental coverage, provided some supportive evidence with which to assist in material classification but clearly showed that for serious *in situ* field geology a full range of major elements (as listed in Table 5.X) and selective trace elements was crucial. Analysis of natural specimen surfaces using WDXRF (Axios system) provided a means of emulating a potential future *in situ* XRF instrument loosely based on the combined capability of the MER APXS and Beagle 2 XRS. Indeed it remains to be seen what the new Mössbauer instrument (MIMOS IIa) being developed for ExoMars and MSL delivers in terms of elemental coverage. Although *in situ* XRF was occasionally constrained by measurement footprint, it was considered preferable to post-sampling bulk powder analysis since *in situ* measurement provides essential context for the Mössbauer and Raman data. Reducing the footprint to determine the composition of individual laminae within the Kitty’s Gap chert (Figure 5.35A) yielded significant information that assisted geobiological interpretation.

Raman spectroscopy proved to be a valuable *in situ* technique due to its ability to identify and map both organic compounds and mineralogy precisely to the imaging data (Figure 11 in Pullan *et al.*, 2008). However, the small size of the measurement spot (2 to 20 μm diameter) is both an

advantage and a drawback of the Raman technique. Heterogeneity at the microscopic scale is perhaps inevitable so many measurements are needed, each requiring spatial context to associate target with spectra. This, together with the choice of excitation wavelength(s), will be a major consideration for the proposed Raman-LIBS instrument on ExoMars (Rull and Martinez-Frias, 2006).

Mössbauer spectroscopy, already a proven technique on Mars (Morris *et al.*, 2004; Klingelhöfer *et al.*, 2004; Morris *et al.*, 2006), was important for all samples containing significant iron. The technique was also useful, in association with the multi-spectral imaging data (Figure 5.19B), in confirming the nature and distribution of iron at low levels (< 0.5%) in cryptoendolithic siliceous sediments (i.e., granular coatings).

XRD generally confirmed the composition of each host material already determined by *in situ* Raman spectroscopy. Targeted measurements made on unprepared samples using the NHM instrument provided more relevant detail than general powder analysis (Figure 5.5), but the technique used (i.e. spinning stage) is not viable for robotic planetary field geology. CheMin on MSL (<http://chemin.janl.gov/> and Table 2.6) will agitate samples to help align as many crystal surfaces as possible but these samples will already have been supplied to the instrument in powdered form. XRD analysis of prepared homogenised powders relies heavily on the efficiency of the sample-processing system and the results are dependent on the original quantity of material that was sampled, how it was sampled, and from where it was sampled. Based only on the astrobiology studies undertaken here, it is questionable whether an XRD instrument would have been of any additional benefit assuming a Raman-LIBS spectrometer was part of the payload and capable of performing *in situ* targeted measurements.

Although geotechnics did not factor directly into the experimental work, related studies showed that splitting rocks was preferable to grinding or coring some samples exhibiting observable biogenic features (Figure C.5).

7.3.1 Future Work

The experimental work presented in this thesis marks an initial step in acquiring practical experience with multiple *in situ* techniques for astrobiology-focused planetary exploration, which will inevitably be of benefit to planetary scientists, instrument designers and mission engineers.

Further work will be essential in order to build on this experience and maximise readiness for future missions to Mars.

Follow-on studies will inevitably require experiments to be conducted in the field, at analogous sites, where measurement and sampling strategies can be emulated within a wider operational zone (i.e., beyond proximal). Where possible, new commercially available field-robust instruments will be exploited to complement the laboratory instrumentation used to date.

In addition to the fundamental *in situ* techniques required for planetary field geology (Chapter 2), post-sampling laboratory experiments such as autonomous microscopy of sample cores, mass spectrometry and radiometric dating will be included for more complete end-to-end simulations. Blind tests will be an important feature of the programme, providing a mechanism to assess the ability of the science teams to conduct geological interpretations from evolving mission-like data sets. Geotechnics will also feature in follow up work assuming sufficient material can be sourced for destructive testing. New techniques or instrument prototypes under development (such as PanCam, CLUPI, Mars-XRD and MIMOS IIa for ExoMars), will be included as they become available. Collaborative links to missions are already in place (via PAFS-net) to ensure continuity and potential access to any appropriate space hardware.

From a planetary analogue perspective, other specimens are being sourced to extend the scope of the studies described in Chapter 5. Samples of coniform stromatolites (159) in plan section are now available via GSPARC and these will provide more appropriate geological context for further laboratory work on these analogues, especially if access to the Trendall field site is not possible. In addition, fossilised examples of endolithic biosignatures are being sourced to compare with the extant samples from the Canadian Arctic (44) and Antarctica (114 and 194).

Additional studies using the same experimental philosophy adopted by the author in this thesis, but with different planetary analogues, are currently in progress or being proposed (Table 3.3). These include bleached and unbleached sandstones from Utah (156, 157, 158, 164, 165, 166, and 167), and pisolitic iron ores from Switzerland (155 and 168), all potential analogues of concretionary processes and iron mobilisation on Mars (Chan *et al.*, 2004).

7.4 Scientific Autonomy

The CREST study (Shaw *et al.*, 2007) has been an important first step in empowering planetary robots with scientific autonomy. Early trials have shown that some basic geological parameters can be recognised, appropriately scored and used to influence operations. However, extensive further development and field testing are now required before any autonomous system based on science would be accepted by the planetary community.

Due to the short duration of the CREST project (one year) and limited industrial manpower assigned to the development of the Science and Response Agent (SARA), only very basic criteria were used for scientific assessment, i.e., 2D greyscale images exhibiting simple layering. Furthermore, the need to incorporate the planning agent and other system architecture components within the development and testing prevented more time from being devoted to generic science evaluation.

7.4.1 Future Work

The next phase beyond CREST is to develop a standalone software application with which to test the methodologies set out in Chapter 6 more thoroughly. Such an application would be independent of any system architecture or planning software and concentrate on the generic concepts of scientific evaluation and contextualisation. At the core of the application would be a relational database populated with a broad and diverse library of structural, textural and compositional reference data ranging from simple greyscale cartoon images (as described in Chapter 6) through to multi-spectral image cubes and compositional spectra. Objectivist Bayesian probability may provide a basis for the interpretation algorithms and the contextual model (Storrie-Lombardi, 2005). In addition to the scientific content the database would also include engineering and environmental information relevant to the mission, instrumentation and planetary body. Suitable data have already been accumulated from existing missions (Chapter 2), GSPARC (Chapter 3) and analogue studies (Chapter 5 and Table 3.3).

Front end application software in the form of a GUI would provide a link to the database. User data in the form of images, spectra and other relevant information (i.e. geotechnics) would be prepared as input to simulate partial or complete mission data sets. The GUI would specifically

be used to manipulate pre-conditions such as geological context, traverse objectives, mission objectives and science value scores in order to test the robustness and versatility of the scientific evaluation of these data sets. The standalone model would be used to prove the concept of autonomous science prior to implementation within a planning system, subsequent use in rover field trials and exploitation in flight systems thereafter. In addition it would also provide an ideal tool for conducting controlled blind tests for mission scientists in preparation for real operations (as per Section 7.1.2.1).

The software and database would draw heavily on the design already developed by the author to manage the GSPARC planetary analogue archive (see Chapter 3 and Appendix A). Indeed, data products from GSPARC would provide all the necessary multi-thematic input. Specific to the autonomous application would be routines for feature analysis (based on a variety of methods), science evaluation (scoring and weighting) and contextual modelling.

7.5 The Analogue Study Programme

The US planetary exploration programme is well supported in terms of analogue research, ranging from laboratory and in-field instrument studies through to integrated rover operations at analogue sites (Figure 3.2E). All these generic and mission-specific activities, although not centrally coordinated, contribute to current and future missions within the NASA programme. The situation in Europe however is somewhat different. Analogue-related studies within the ESA planetary exploration programme are mostly limited and confined to the final stages of instrument development and calibration. Simulated operations using these instruments as part of a payload suite, either under controlled laboratory conditions, or as part of fully integrated rover trials, are rarely considered due to the lack of funding to support such activities within the mission budgets.

PAFS-net and GSPARC provide the essential components for an integrated and coordinated analogue research programme within Europe. However, funding for integrated analogue research in support of planetary exploration in general is not available although Europlanet (<http://www.europlanet-eu.org/>) does provide a framework for networking.

7.6 Applications in Forensic Science

The spin-off potential of the database described in Chapter 3 has already been recognised. Techniques and procedures used in forensic science, both at the scene of crime or on items returned to the laboratory, are very similar to those employed in planetary field geology. Both involve systematic evidence gathering, often at trace levels, under challenging conditions and are constrained by the environment (i.e., limited access to target evidence). As part of a forensics project performed by the author in association with the Forensic Science Service, multi-spectral imaging has been shown to be effective in the *in situ* identification of human body fluids on cloth in much the same way as extant cyanobacteria in rocks (Figure 5.25).

7.7 Summary

Conclusions and recommendations originating from the three main themes of this thesis, the specimen archive, payload experiments, and scientific autonomy, have been presented and collectively reviewed. The planetary analogue specimen archive and experiment database (GSPARC) and the Planetary Analogue Field Studies Network (PAFS-net) were both established during the course of this project following early recognition of the need for such facilities. Together they form a unique framework in which to conduct coordinated analogue research studies that collectively benefit a broad spectrum of planetary scientists, mission engineers, and the public via an outreach component. Two examples of analogue studies of relevance to astrobiology were conducted as part of this work. The results of mission-like experiments performed on a variety of analogue samples using representative instrumentation demonstrated the usefulness of combined interpretation. Acquiring practical experience of appropriate measurement strategies well in advance of a real mission was also shown to be important. The experimental studies also naturally link to autonomous robotic field operations. A novel methodology for the implementation of scientific autonomy in planetary rovers has been specified and partially demonstrated during the course of this project.

A large number of follow-on studies are recommended as an outcome of this thesis. Some extend the experimental work related to *in situ* astrobiology by incorporating other examples of biological signatures, and others consider more generic geological themes such as sedimentary processes, robotic sampling and remote sensing. A software model to verify the concept of

scientific autonomy is also proposed. Fundamentally, all individual studies will be conducted within a coordinated and shared analogue research programme. In addition, other spin-offs are actively being pursued, in particular the use of autonomous robotic field strategies in forensic science.

Appendix A

Geological Specimen Archive (GSPARC) Specification

This Appendix presents a detailed coding specification for the Geological Specimen Archive (GSPARC) introduced in Chapter 3. The scheme described herein is used throughout the thesis.

A.1 Basic Sample Identification

Physical specimens are referred to as *items*, and are distinguished by a unique numeric identifier (i.e., can only occur once). Multiple items of the same material are referred to as *families* and assigned a non-unique family identifier (i.e., can occur many times). Individual specimens exist in a variety of *formats* as required by different instruments and experimental techniques. These three terms are used to form the basic sample identifier.

The generic expression (in a version of standard software notation) of the basic sample identifier, `<sample>`, is as follows:-

$$\langle \text{family} \rangle \{ [.] [\langle \text{format} \rangle] [.] \} \langle \text{item} \rangle [\langle \text{part} \rangle]$$

where

`< >` is a field¹

`[]` is an optional field

`{ }` is a compulsory field (at least one field must be specified)

`.` is a fixed delimiter (period)

¹ Fields are expressed in one of the following coded formats:-

*numeric***n* is a string of numbers of length *n* (or a positive integer if *n* is omitted)

*character***n* is a case sensitive string of letters of length *n*

*alphanumeric***n* is a case sensitive string of letters and numbers of length *n*

Each field is described as follows:-

- `<family>` Sample family identifier. Format is *numeric*. This number must be unique to an associated group (or family) of samples. Usually a family of samples is simply a set of items derived from specimens obtained from a common source (i.e. a particular rock, outcrop, horizon etc). However, if there is sufficient variation in properties to jeopardise "commonality" then a separate family must be created. It is entirely feasible for a family to consist of a single item, and therefore only appear once in the database. Note that the field can be padded with leading zeros if this is deemed appropriate (i.e., filenames may benefit from this).
- `<format>` Sample format identifier. Format is *character*2*. Valid codes are FE (Field Exposure), HS (Hand Specimen, RS (Rock Slab), LP (Loose Powder), PP (Powder Pellet), FB (Fusion Bead) and TS (Thin Section). Full details of these formats, and their requirements, are described in Section A.2. In some circumstances this field can be omitted (see the example at the end of this section). A two parameter search of the database based on `<format>` plus `<family>` would return all items (samples) in a family of this format type.
- `<item>` Item identifier. Format is *numeric*. A number unique to the database (i.e. can occur once only). Searching the GSPARC database for this parameter would always return this particular item (sample) irrespective of other attributes. It is possible to pad this field with leading zeros as in the case of `<format>`.
- `<part>` Optional part identifier. Format is *character*1*. Used to distinguish items which are made up of more than one piece, i.e., due to breakage. Maximum number is 26 (i.e., A-Z). Can also be used to identify removed fragments that may or may not be retained.

Example: Consider a sample with `<family>` = 23 (amphibolite), `<format>` = HS, and `<item>` = 49. It is entirely feasible to express this specimen as 23.49 if it obvious that the sample is a hand specimen (i.e., in the case of an image caption), or as 23HS49 (or 23.HS.49) if

the format is relevant or not obvious (i.e., when describing data for siblings of different formats). Similarly, a folder containing data for this specimen could also be expressed as 23HS49, but it may be more appropriate to use 0023HS0049 instead to optimise sequential sorting of all specimen folders.

Note that `<item>[<part>]` can be omitted when there is a need to describe samples that can not, or do not need to, be retained (i.e., powders that have been destroyed/contaminated, or simply discarded after analysis).

The basic sample identifier `<sample>` forms the root of more complex identifiers containing a wide variety of additional sample attributes and experimental parameters. These will be described in Section A.3.

A.2 Sample Formats

The most common formats of interest to geologists are field exposures, hand specimens, rock slabs, loose powders, powder pellets, fusion beads, and thin sections. These therefore form the basis of the format classification scheme for GSPARC.

Field Exposures (`<format> = FE`) are outcrops or other geological features at a locality where sampling is undertaken, or is impractical (i.e., too large or too friable), or not possible (i.e., a preservation order is in place). Field exposures are essentially “large natural specimens” that remain *in situ*, and exploited during field-based experiments (Figure A.1). Their inclusion into the physical archive is important since they can often be associated with, and be the source of, the smaller formats discussed next. Field exposures also apply to natural or synthetic, semi permanent, objects utilised in planetary yards during simulated operations (Chapter 6).

Hand Specimens (`<format> = HS`) are the usual form of physical samples collected during field work (Figure A.2). They should be as field representative as possible by maintaining all natural features, form and texture (both fresh and weathered). Practical sizes are commonly ~15 cm x ~15 cm, but this would depend on heterogeneity, grain size and application. For example geotechnical studies require more resource than non-destructive experiments (Chapter 5). Distinguishing features should be preserved (i.e., phenocrysts, veins, cryptoendoliths, etc.). Given

all these criteria, a number of samples may be required to be representative.

Rock Slabs (<format> = RS) are mineralogically and petrologically intact samples but geometrically constrained (Figure A.3). Thick sections and chips (from the manufacture of thin sections) fall into this category. Samples are ideally ~5 cm x ~5 cm x ~1 cm, but can be larger, or smaller, depending on application and the ability of material to be sawn and remain intact. The number of slabs required depends on grain size, heterogeneity, etc. Ideal surfaces include sawn and polished. Rock slabs can act as suitable substrates for simulated alteration rind and rock coating studies and are particularly useful for instruments that require prepared surfaces.

Loose Powders (<format> = LP) include natural soils and unconsolidated material (Figure A.4), and homogenised powders derived from crushed rock. Powders can be used as is, but are also required for manufacturing other formats as described below. Several hundred grams should be prepared for this purpose. Larger quantities of geotechnical analogue material can be used to fabricate planetary surfaces for robotic studies (Chapter 6).

Powder Pellets (<format> = PP) are homogenised powders derived from crushed samples, that have been bound and pressed into disks (Figure A.4). The ideal standard size is ~35 mm diameter and ~5 mm thick, but this can vary depending on the quantity of powder available and the ability to bind (Watson, 1995). Powder pellets are used to determine bulk major and trace element geochemistry (Chapter 5).

Fusion Beads (<format> = FB) are homogenised powders derived from crushed samples, that have been vitrified in a furnace and pressed into disks (Figure A.4). The ideal standard is ~35 mm diameter and ~2 mm thick. Fusion beads are usually produced in association with Power Pellets, and are used to determine bulk major element geochemistry (Chapter 5).

Thin Sections (<format> = TS) are 30 µm thick slices of rock used for definitive mineralogical and petrological characterisation, and electron microprobe analysis. Microscopically anisotropic materials may require more than one thin section to be representative.

It would seem logical that each family of specimens should contain examples of at least one of these formats. However, unless sufficient material is collected specifically for the archive as part of a field campaign this will not usually be the case. The current physical archive contains many

examples of individual specimens in a variety of formats originating from, or belonging to, existing institutional or private collections. These include unique and valuable specimens such as meteorites. Many of the larger terrestrial items are also not suitable for formatting since they exhibit unique qualities that have to be preserved (i.e., ancient sedimentary structures).



Figure A.1 Microbial algal stromatolite structures (209FE569) in mildly-metamorphosed sandstones from the Torridonian Stoer Group (1.2 Ga) exposed at Clachtoll, Lochinver, Sutherland, Scotland (Upfold, 1984). ID: 058110682N005201880W0-209FE569.



Figure A.2 Hand specimen of sandstone (75HS136) with characteristic manganese coating from Erie Barge Canal, Middleport, New York, USA.

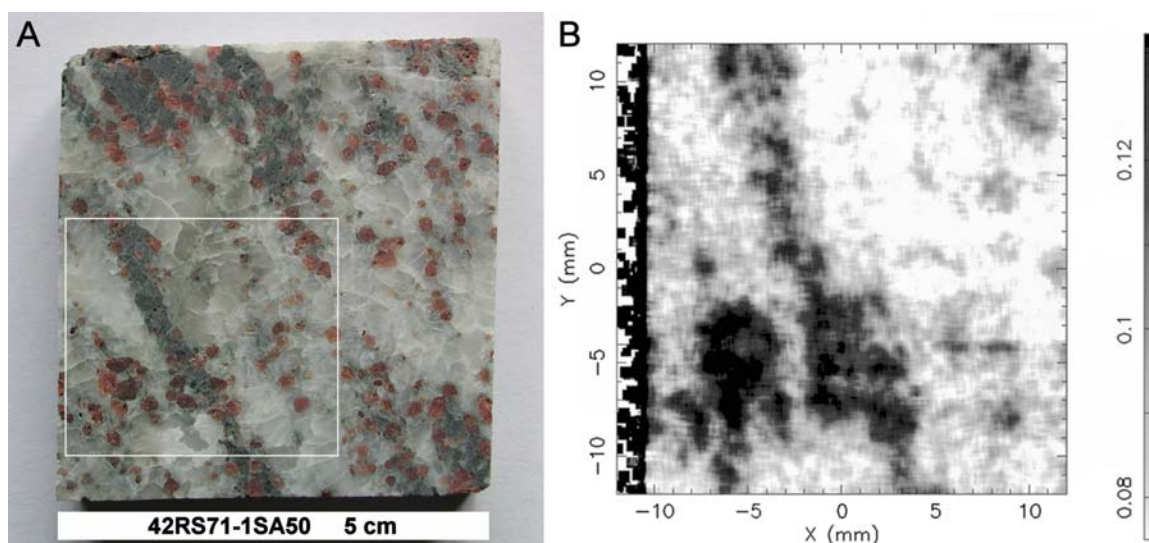


Figure A.3 Rock slab of garnetiferous anorthosite (42RS71-1SA50) from Bergen, Norway (A). Elemental map of highlighted area (B) obtained with an Imaging X-ray Fluorescence Spectrometer (IXRFS) showing distribution of Mg (dark areas). Courtesy Price *et al.*, 2004 (B).

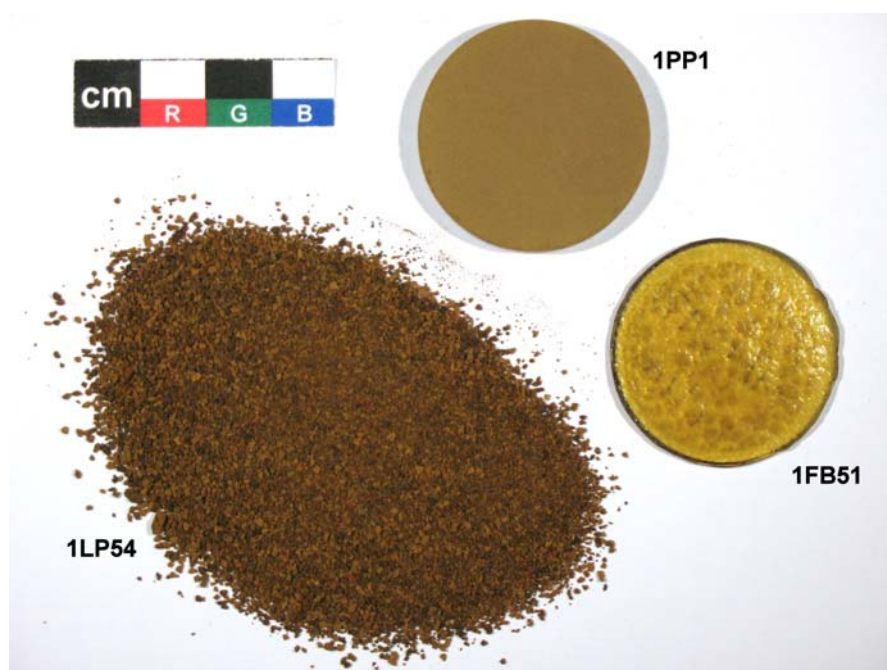


Figure A.4 Martian soil simulant JSC Mars-1 (Allen, 1998) as supplied (1LP54), as a pressed powder pellet (1PP1), and as a fusion bead (1FB51).

A.3 Sample Identifier Extensions

Where appropriate, specimens may need to be precisely associated with a locality by specifying the original site coordinates. This is particularly important in the case of field exposures (<format> = FE) but can apply to any format type. Specimen <items> may also exhibit a number of features that require documenting. For example, rock slabs will need a number to designate each face, and hand specimens will need to distinguish between fresh and weathered surfaces. In addition, specimens may exhibit special features of interest (i.e., endolith). The documenting procedure is to assign such basic features during the photo-cataloguing process (i.e., side 1, side 2, patch 1, patch 2, etc.). Other areas of the specimen such as instrument measurement footprints are designated when required for the first time. To keep things simple, all features of interest are referred to as *targets*.

Experiments also need to be associated with samples, and subsequently targets, and *vice versa*. This is achieved by combining the basic sample identifier <sample> (described in Section A.1) with two optional extensions, one describing an experiment and the other describing a target. The generic expression is as follows:-

```
[ <experiment> ] [ <site> ] <sample> [ <target> ]
```

where

< > is a field

[] is optional

<experiment> is the experiment prefix extension string

<site> is the site prefix extension string

<sample> is the basic sample identifier string (see Section A.1)

<target> is the target suffix extension string

The fields can be used in combination to form encoded mnemonics. Alternatively, each field can be used independently. This system is extremely useful for annotating data and organising folders (see later). Notice that the convention is for <experiment> to precede <site> if these appear together as a combined prefix.

The generic expression of the <target> suffix extension is as follows:-

[-<targetnumber><targettype><targetsize>]

where

- is a fixed delimiter

Each field is described as follows:-

<targetnumber> Target identifier. Format is *numeric*. This should be unique with respect to this particular <sample> to avoid ambiguity. It is possible to pad this field with leading zeros if appropriate.

<targettype> Target type. Format is *character*2*. Valid codes currently assigned are FR (fresh surface), WX (weathered surface), CH (chipped surface), SA (sawn surface), PO (polished surface), AB (abraded surface), XX (removed fragment), BH (borehole), EN (endolith), and UN (undefined).

<targetsize> Diameter of the target (i.e., footprint). Format is *numeric* and expressed in millimetres. For three dimensional targets, a plan view or equivalent can be assumed.

Example: Consider the identifier 23HS49-2WX10. The target extension describes a 10 mm diameter weathered patch on a hand specimen of family 23 (amphibolite). Searching a collection in the GSPARC database for all hand specimens with weathered targets would require just two parameters, <format> and <targettype>.

The generic expression of the <site> prefix extension is as follows:-

[<coordinates>[<elevation>]-]

where

- is a fixed delimiter

The fields are described as follows:-

- <coordinates> Coordinates of the site locality. Format is *alphanumeric*20* expressed as *dddmmssssYdddmmssssX* where *ddd* is degrees (000 to 360), *mm* is arc minutes (00 to 59), *ssss* is arc seconds (00.00 to 59.99), *Y* is latitude (N or S), and *X* is longitude (E).
- <elevation> Elevation of the site locality. Format is *numeric* expressed as metres above datum.

Example: Consider the mnemonic 048571792N010375977E473-140HS493. The sample is a hand specimen of freshwater limestone (140) collected from a disused quarry SE of Hainsfarth Ries Crater, Germany at field exposure 140FE570 (48° 57' 17.92" N, 10° 37' 59.77" E). The elevation of the sampling site is 473 m (in this case 2 m above ground level). See Figure B.2 for an image of this field exposure.

The generic expression of the <experiment> prefix extension is as follows:-

[<date><sequence><instrument>\${ <mode> } [\${<stim> }] -]

where

\$ and - are fixed delimiters

Each field is described as follows:-

- <date> Experiment date. Format is *numeric*6* expressed in date format *yymmdd*.
- <sequence> Experiment sequence number. Format is *numeric*2*. For each day specified by the field <date>, the sequence should start from 1 (zero being reserved to specify undefined or not applicable).
- <instrument> Instrument code. Format is *alphanumeric*n* where *n* is variable. It is recommended to keep this field as short as possible. Any combination of letters and numbers (no spaces or symbols) to identify instrument used to perform experiment. Valid codes are contained in a database look up table. Examples from the database lookup tables include B2MIC (Beagle 2 QM microscope) and B2SCS (Beagle 2 DM stereo camera). See Table

C.1 for a complete list of codes used in the context of this thesis.

`<mode>` Optional instrument mode. Format is *alphanumeric*n* where *n* is variable. It is recommended to keep this field as short as possible. Examples include 440 (440 nm filter) and CUL (close-up lens). See Table C.1 for a complete list of codes used in the context of this thesis.

`<stim>` Optional stimulation code. Format is *alphanumeric*n* where *n* is variable. It is recommended to keep this field as short as possible. Examples include SOL (Solux illumination) and RGB (RGB illumination). See Table C.1 for a complete list of codes used in the context of this thesis.

Example: Consider the mnemonic 05072701B2SCSSCUL\$RGB-114HS353A. The sample is a hand specimen of orthoquartzite (114), and one of two parts. The experiment prefix extension describes the first experiment performed on the 27th July 2005 using the Beagle 2 DM stereo camera. The camera was used in macroscopic mode (as indicated by the close-up filter), and imaging was performed under separate red, green and blue illumination. No target information is specified in this particular case. However, if we add the target extension to give 05072701B2SCSSCUL\$RGB-114HS353A-01FR20, the string now states the imaging experiment was performed on the 20 mm diameter fresh patch designated number 1.

A.4 Sample Documentation

The identifiers `<sample>`, `<target>`, `<site>`, and `<experiment>` are sufficiently versatile and detailed for use as an “everyday language” to describe the physical specimens and the experiments performed on them. These identifiers plus additional information on samples, experiments, and other related topics are stored as data in indexed *tables*. The core data are referred to as *parameters* and are described below. A full list of tables is shown in Figure 3.3, but for clarity some are introduced here. To maintain continuity with other sections in this Appendix, the `<field>` notation is used to describe each parameter.

The additional parameters associated with <family> are as follows:-

- <descriptor> Sample descriptor. Format is *alphanumeric*n*, where *n* is variable. Example for <family> 140 is “Freshwater limestone”.
- <locality> Locality where the sample was collected, or originated (if known). Format is *alphanumeric*n*, where *n* is variable. Example for <family> 140 is “Hainsfarth, Ries Crater, Germany”.
- <site> Coordinates and elevation of the site locality (if known). Format is *alphanumeric* expressed as *dddmmssssYdddmmssssXe* where *ddd* is degrees (000 to 360), *mm* is arc minutes (00 to 59), *ssss* is arc seconds (00.00 to 59.99), *Y* is latitude (N or S), *X* is longitude (E), and *e* is elevation in metres. This parameter is identical to the external identifier <site> (see Section A.3)
- <class> Sample classification. Format is *alphanumeric*n*, where *n* is variable. Valid codes are selected from the lookup table *LUTclass* (see Section A.1). Example for <family> 140 is “Sedimentary rock”.
- <mineralogy> Mineralogical classification. Format is *alphanumeric*n*, where *n* is variable. A parsable string of concatenated mineral species codes selected from the lookup table *LUTmineralogy* (see Section A.1). Only the principal minerals are used to compile the list. Example for <family> 140 is “%Dol%Cal”.
- <entrydate1> Date family was first entered into the database. Format is *numeric*8*. Expressed in date format *ddmmyy*. Example for <family> 140 is “141203”.
- <comments1> Supplementary comments. Format is *alphanumeric*n*, where *n* is variable. Example for <family> 140 is “Crater lake deposit”

The additional parameters associated with `<item>` are as follows:-

<code><dimensions></code>	Physical dimensions of the specimen. Format is <i>alphanumeric*n</i> , where <i>n</i> is variable. Dimensions expressed in millimetres. Example for sample 140RS464 is “50x50x10”.
<code><size></code>	Size classification. Format is <i>alphanumeric*n</i> , where <i>n</i> is variable. Valid codes are selected from the lookup table <i>LUTsize</i> (see Section A.1). Example for sample 140RS464 is “Miniature”.
<code><mass></code>	Mass of the specimen. Format is <i>numeric</i> and expressed in grams. Example for sample 140RS464 is “46”.
<code><collection></code>	Collection the specimen belongs to. Format is <i>alphanumeric*n</i> , where <i>n</i> is variable. Valid codes are selected from the lookup table <i>LUTcollection</i> (see Section A.1). Example for sample 140RS464 is “Planetary Analogue Library”.
<code><originator></code>	Originator of the sample. Format is <i>alphanumeric*n</i> , where <i>n</i> is variable. Valid codes are selected from the lookup table <i>LUTname</i> (see Section A.1) containing names of institutes or individuals participating in GSPARC. Example for sample 140RS464 is “Derek Pullan”.
<code><provider></code>	Provider of the sample. Format is <i>alphanumeric*n</i> , where <i>n</i> is variable. May not be the actual originator of the sample. Valid codes are selected from the lookup table <i>LUTname</i> (see Section A.1). Example for sample 140RS464 is “Derek Pullan”.
<code><preparer></code>	Preparer of the sample. Format is <i>alphanumeric*n</i> , where <i>n</i> is variable. Applicable in cases where formats have been produced such as pressed powder pellets etc. Valid codes are selected from the lookup table <i>LUTname</i> (see Section A.1). Example for sample 140RS464 is “University of Leicester, Geology Department”.
<code><owner></code>	Owner of the sample. Format is <i>alphanumeric*n</i> , where <i>n</i> is variable. Although part of the GSPARC physical archive, the actual sample may still be owned by an institute or an individual. Valid codes are selected from the lookup table <i>LUTname</i> (see Section A.1). Example for sample 140RS464 is “European Space Agency, ESTEC Sci-A”.

<custodian>	Custodian of the sample. Format is <i>alphanumeric*n</i> , where <i>n</i> is variable. This status can change as samples migrate between laboratories. Valid codes are selected from the lookup table <i>LUTname</i> (see Section A.1). Example for sample 140RS464 is “European Space Agency, ESTEC Sci-A”.
<status>	Current status of the specimen. Format is <i>alphanumeric*n</i> , where <i>n</i> is variable. Valid codes are selected from the lookup table <i>LUTstatus</i> (see Section A.1). Example for sample 140RS464 is “Default”.
<extrefs>	External references or alternate identifier(s) assigned to this <item> by other institutions. Format is <i>alphanumeric*n</i> , where <i>n</i> is variable. Example for sample 140RS464 is “Not applicable”.
<entrydate2>	Date the specimen was entered into the database. Format is <i>numeric*8</i> . Expressed in date format <i>ddmmyy</i> . Example for sample 140RS464 is “250207”.
<comments2>	Supplementary comments. Format is <i>alphanumeric*n</i> , where <i>n</i> is variable. Example for sample 140RS464 is “ESA Sci-A procurement via University of Leicester, Department of Geology”.

Appendix B

Sample Descriptions

This Appendix provides a summary of the geological specimens used in the experimental studies presented in Chapter 5. Details of the GSPARC coding conventions can be found in Appendix A.

B.1 Freshwater limestone, Hainsfarth, Ries Crater, Germany (140)

The Ries and Steinheim craters of the Jurassic Alb plateau in Southern Germany represent well-studied examples of terrestrial impact structures (Pohl *et al.*, 1977; Pache *et al.*, 2001). As early as 1970, the area was recognised as an analogue field site for Apollo 17 astronauts (Margolin, 2000). Topographically, the Ries crater is characterised by an almost circular, relatively flat inner basin of 12 km diameter surrounded by a system of concentric normal faults and an outer tectonic ridge (outer diameter 25 km as shown in Figure B.1). The Steinheim crater is smaller (3.8 km diameter) with a disrupted rim and eroded central peak. Both were formed by hypervelocity impacts of separate bolides (~ 1 km and ~ 100 m diameter respectively) during the Mid-Miocene (14.4 ± 0.4 Ma) (Bruchner, 2003).

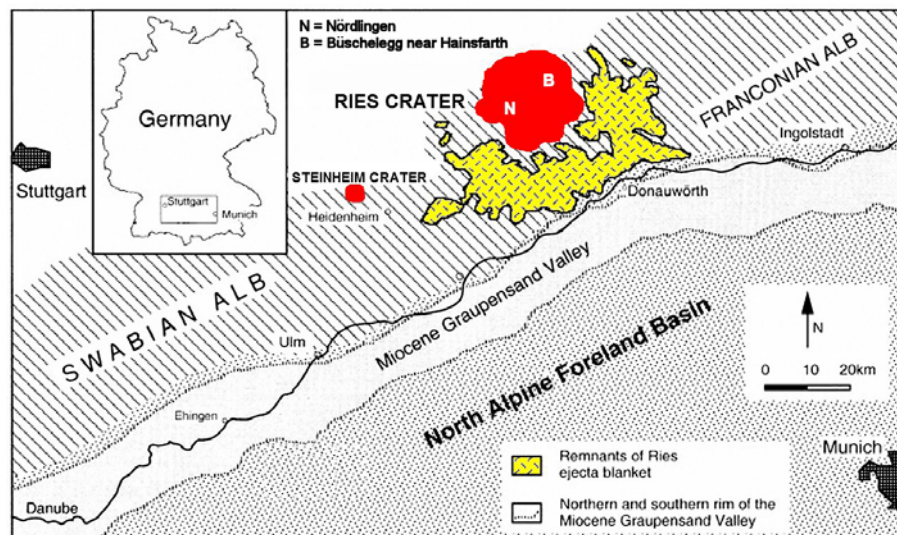


Figure B.1 Simplified context map of the Ries and Steinheim impact sites (modified after Bruchner *et al.*, 2002).

The Ries bolide was sufficiently massive to penetrate through the Jurassic/Triassic limestones and marls into the basement granites, gneisses and amphibolites. The extruded mixture of basement melt and shocked crystalline material produced a polymict breccia known as suevite, a proportion of which fell back into the crater. The Central European tektites (impact glasses), known as moldavites, are thought to be associated with the Ries event.

Following impact both the Ries and Stenheim sites experienced a short (2 Ma) period of crater lake development (due to the disruption of the local drainage system). The lacustrine phase was curtailed when the depressions became completely filled with sediments. Subsequent uplift and erosion has exposed thick sequences of carbonates at several localities.

Near-shore crater lake carbonates are well exposed at Büschelberg near Hainsfarth (48° 57.15' N, 10° 38.1' E), 2.5 km east of Öttingen (Figure B.1) and have been extensively studied (Arp, 1995). The site (a former quarry) is the highest elevation above the eroded flat plains of the inner basin which lies 60 m below. The carbonate sequence is thick (>8 m) and consists of extensive bioherms of *Cladophorites* (green algae) with minor stromatolites and carbonate sands composed of gastropods and ostracods. The carbonates lie directly on basal suevite.

Samples of freshwater limestone were collected from outcrop by the author in 2005 during a field excursion to the area (Hofmann *et al.*, 2005). The exposure displays a combination of well-preserved (fresh) and weathered calcified remnants of *Cladophorites* cemented in a dolomite matrix (Figure B.2). The tubular morphology is due to an accumulation of carbonate veneers around the original *Cladophorites* threads, which were subsequently completely oxidised, thus leaving a void (*cf.* Cady and Farmer, 1996). This together with sinter-like crusts on associated algal constructions within the bioherm suggest that temporal vadose conditions prevailed where evaporation may have led to impregnation of carbonate into the biofilms (Dr. Gernot Arp, Göttingen, personal communication). Subsequent phreatic conditions during the Upper Miocene dolomitized these carbonates and most surfaces are veneered with dolomite cement. Although the visible calcified tubes are abiogenic, their morphology (resulting from mineralization over a *Cladophorites* substrate) classifies these features as a biosignature.

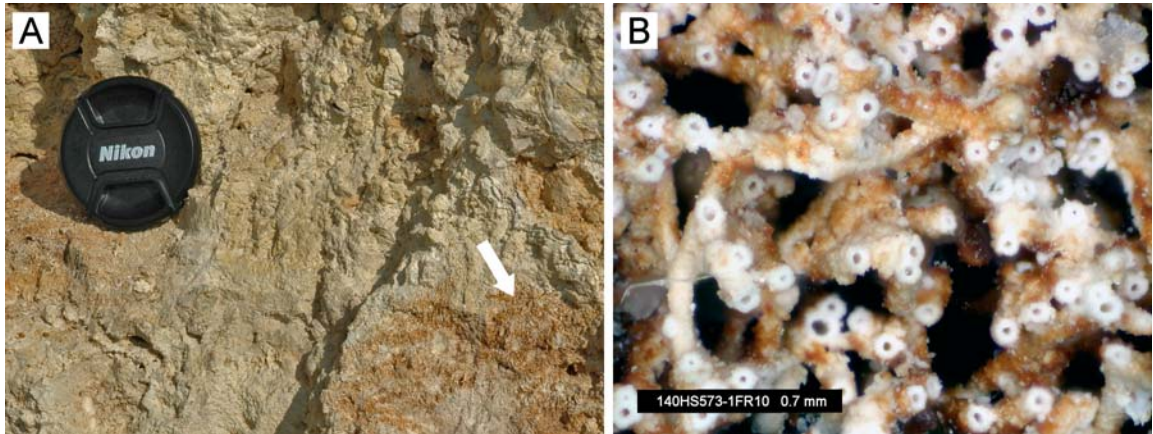


Figure B.2 Freshwater limestone in outcrop (140FE570) at Büschelberg near Hainsfarth (A) on the northeast rim of Ries Crater (048571792N010375977E473). See Figure B.1 for general location. Well preserved filamentous fabric (after *Cladophorites*) is exposed in sections of the outcrop (arrow) and in hand specimen 140HS573 (B).

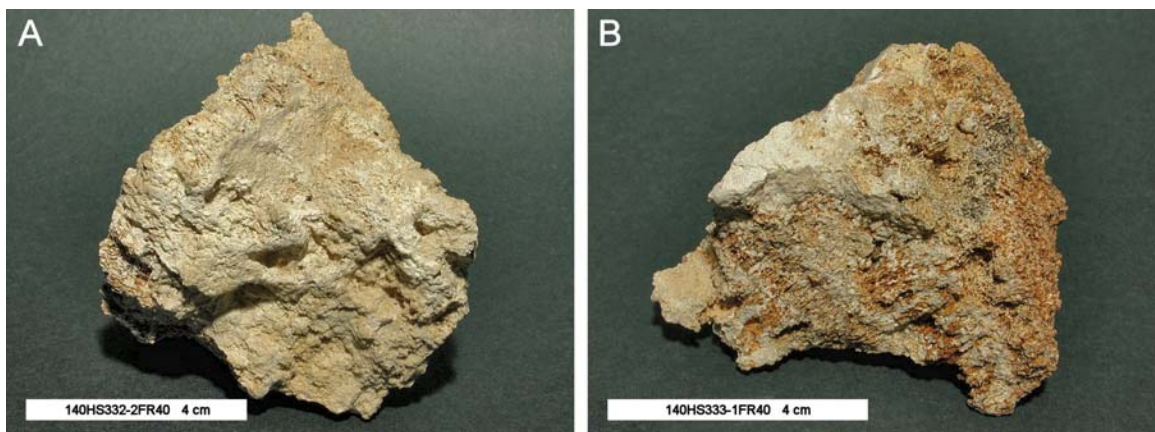


Figure B.3 Study specimens 140HS332 (A) and 140HS333 (B). Two surface textures are represented, smooth dolomitic veneers (A), and rougher, darker areas (B) comprised of oxidised remnants of calcified tubes originally laid down over *Cladophorites* (see Figure B.2B).

Samples 140HS332, 140HS333, 140HS420, 140HS573 and 140HS584 exhibit a combination of open fabric surfaces (high microscopic relief), and sintered surfaces (low microscopic relief) (Figure B.3). Dolomite makes up the matrix and veneers. The calcified *Cladophorites* filament structures have a hollow tubular morphology, and are aligned and clustered. Individual tubes range in length from millimetres to centimetres and have average outer diameters of ~100 µm. Tube masses extend to centimetres.

Geochemically, the specimens are simple lacustrine Mg-carbonates (WDXRF of 140PP431). Lake waters in which this limestone was deposited are reported to be enriched in Sr²⁺ (Arp, 1995), and fall within a well-defined range between 2140 and 2940 ppm (Pache *et al.*, 2001). Trace element analysis of 140PP431 reveals a Sr concentration that is within this range (2327 ppm). In contrast, pre-impact marine carbonates of Jurassic age (pre-impact) in the Ries area have lower Sr concentrations (< 200 ppm).

B.2 Opaline Sinter, Yellowstone Park, Wyoming, USA (169)

Yellowstone Park is well known for geysers, fumaroles, hot springs and associated thermophilic life (Cady and Farmer, 1996; Fouke *et al.*, 2000; Rothschild and Mancinelli, 2001; Lowe and Braunstein, 2003; Walker *et al.*, 2005). Hillside Springs (44° 28.30' N, 110° 51.8' W) is located 3.5 km northwest of Old Faithful geyser in the Upper Geyser Basin area (Figure B.4). Unusually, the springs discharge from a steep mountain slope approximately 20 m above the valley floor (hence the name). Discharge temperatures of 82 to 85 °C were recorded in September 1996 (Dr. Beda Hofmann, Natural History Museum, Bern, personal communication). Fluids are rich in silica and carbonate, which precipitate out to form siliceous and carbonate-rich deposits. Minor constituents also include montmorillonite group clay minerals (nontronite) and hollandite (Ba-rich Mn-hydroxide). Inevitably, microbial communities living at the surface/fluid interface can become preserved as relict micro-fabric within the rock.

The study specimens were collected by a research team led by Prof. Jack Farmer (then NASA Ames Research Center, currently Arizona State University) in 1995. They are representative of a hot spring precipitate that is comprised mostly of silica (> 95%) and has replaced a microbial mat. Pore space is very high with voids (up to 10 mm) that are occupied by fibrous assemblages similar in microfabric to *Phormidium*, a sheeted cyanobacterium that usually forms flat, slimy mats of tangled filaments at temperatures between 35 °C and 59 °C at some distance from the

spring (Cady and Farmer, 1996). The observed “threads” are not thought to be the individual filaments themselves (which are usually $< 5 \mu\text{m}$ across) but are considered to be representative of a larger preserved biofabric that consists of bundles of filaments. Nevertheless, the morphology can be considered as a preserved biosignature.

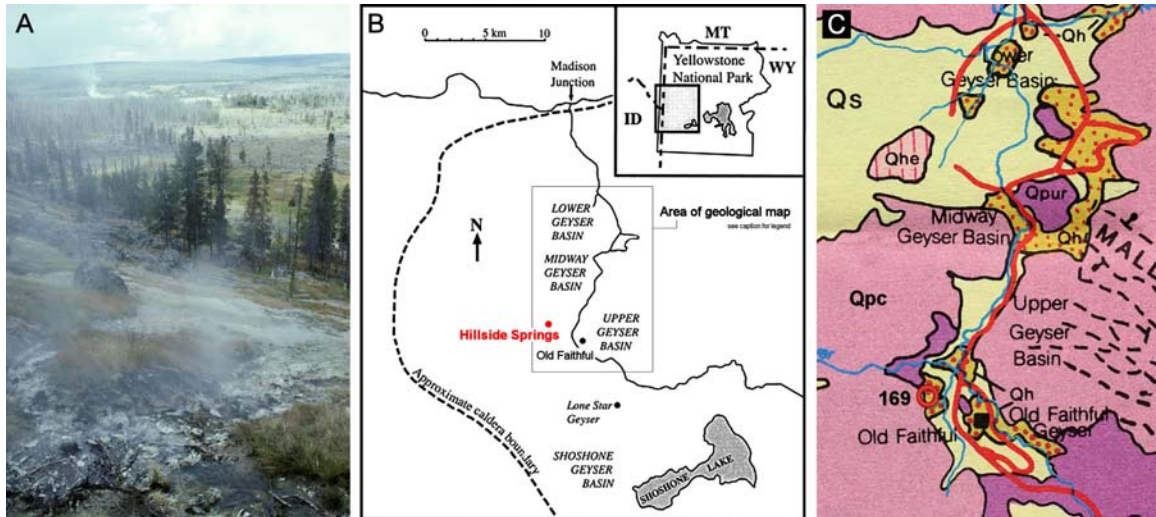


Figure B.4 Geology of Hillside Springs, Yellowstone National Park, Wyoming, USA (A). Context map (B) and geological map (C) of the Geysers Basin area showing the location of the sampling site at Hillside Springs (169). Legend: Qs (river/lake/glacial sediments), Qh (hot spring deposits), Qhe (hydrothermal explosion deposits), Qpur (canyon rhyolite), Qpc (central plateau rhyolites). Courtesy Dr. Beda Hofmann, NMBE (A) and Taylor *et al.*, 1989 (C).

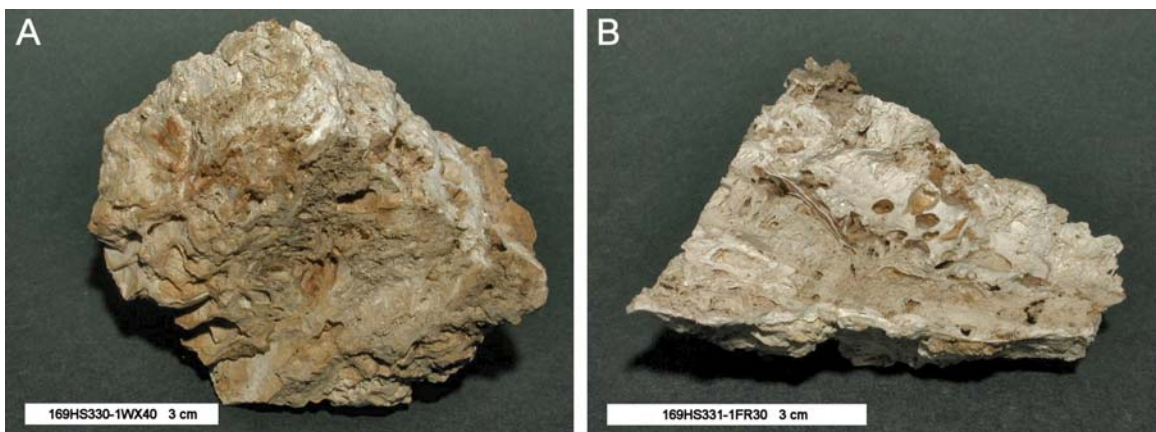


Figure B.5 Study specimens 169HS330 (A) and 169HS331 (B). Relic micro-fabric representative of the original microbial mat development is well preserved in the form of open layering (A). Fine networks of silicified filaments are also preserved within void spaces (B).

Specimens 169HS330 and 169HS331 show an amorphous texture, and macroscopically have a distinct layered fabric that consists of alternating flat parallel layers, and layers with a vertical texture (Figure B.5). Consequently the samples have high microscopic relief. Filament bundles are typically ~15 µm wide and < 500 µm long.

Insufficient material was available for bulk powder geochemistry but analysis of fresh surfaces of 169HS331 by WDXRF confirms a high silica content of 97 wt % SiO₂ and minor Fe (< 1 wt % Fe₂O₃). Analysis of un-discriminated powder (i.e. mixture of fresh and weathered material) by XRD confirms the sample to be comprised of amorphous silica.

B.3 Chalcedony, Cady Mountains, California, USA (45)

The Lower Miocene volcanic and sedimentary sequence of the Sleeping Beauty Ridge region of the Cady Mountains, San Bernardino County, California, USA (Figure B.6) has been mapped in detail (Glazner, 1988). The volcanic sequence comprising basalts, dacites and rhyolites exceeds 3 km thick and was extruded between 23-21 Ma during a volcanotectonic event that migrated northward across the region. Intercalated with the volcanics are well-sorted red bed sandstones. Following tectonic tilting, the volcanic sequence was capped by rhyolitic tuff (18.5 ± 0.2 Ma) and subsequent lake sediments. The area is dissected by NW to N trending faults, some of which are still active. The volcanic rocks of the region are a well-known source of various types of agate and jasper (Henry, 1957).

Veining within the dacites and basalts extends to over 2 km. The silica-rich veins, up to 50 cm thick, are resistant to weathering and occur as aligned blocks within the weathered country rock. Veins that contain Subsurface Filamentous Fabric (SFF) are mainly composed of chalcedony, Fe-hydroxides and calcite and are strongly enriched in trace elements Sb, As, Mo, Pb, Be, and Ag. Filamentous chalcedony or “moss agate” is commonly known as Lavic Jasper. The study specimens were collected in 2000 by Dr. Beda Hofmann (Natural History Museum, Bern, Switzerland) from a well preserved silica-rich vein (34° 45.65' N, 116° 16.17' W) within weathered volcanic country rock (Figure B.7A) (Hofmann and Farmer, 2000).

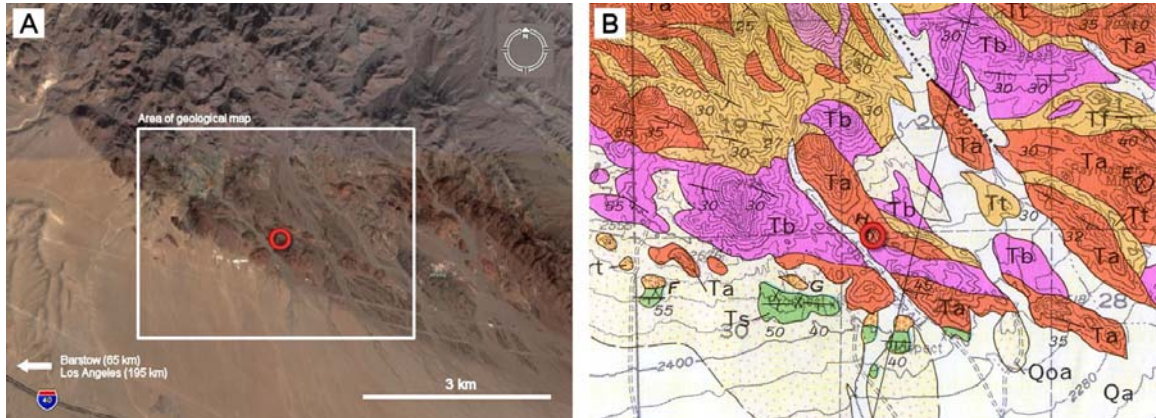


Figure B.6 Satellite image of the Sleeping Beauty Ridge region of the Cady Mountains, California, USA (A). Geological map (B) of the area highlighted in the satellite image. Samples of vein chalcedony (45HS265 and 45HS325) were collected at the location shown. Legend: T (Tertiary), Q (Quaternary), Ta (andesite), Tb (basalt), Tt (tuff, breccia), Tf (fanglomerate). Courtesy Digitalglobe (A) and Dibblee and Bassett, 1966 (B).

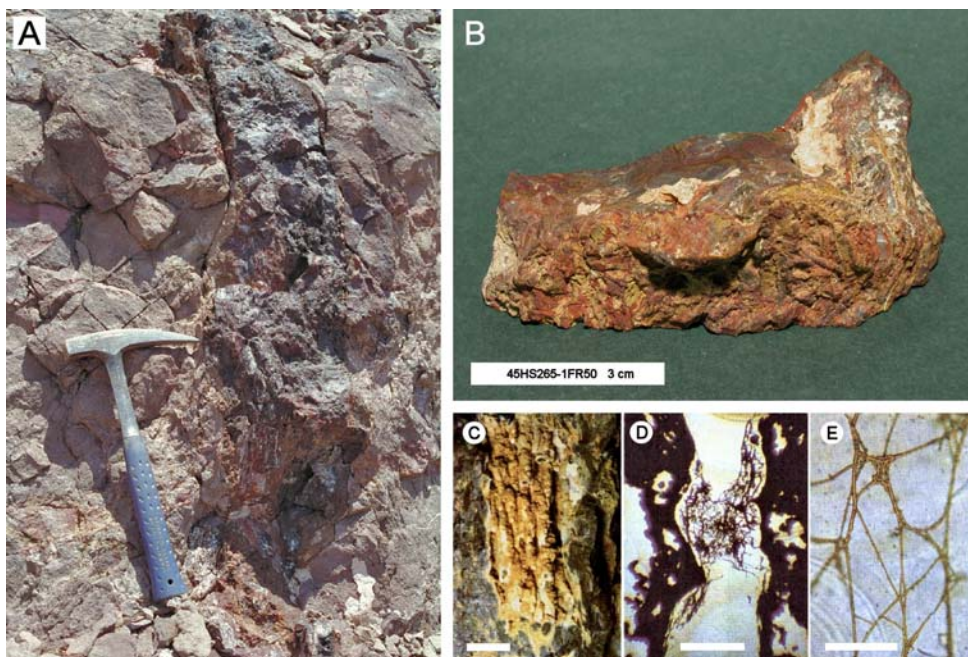


Figure B.7 Well preserved vein of chalcedony at location highlighted in Figure B.6 (A). Sample 45HS265 (B). Goethite- and quartz-encrusted filament bundles with vertical orientation due to gravity draping (C). Filament orientation is similar to that shown in Figure B.8 and tubular morphology similar to that shown in Figure B.2. Mineralised filaments embedded in quartz (chalcedony) as seen in thin section (D). Detailed view of individual mineralised filament (E). Scale bars are 1 cm (C), 500 μm (D) and 50 μm (E). Courtesy Dr. Beda Hofmann, NMBE (A) and Hofmann and Farmer, 2000 (CDE).

The originally biogenic filaments were formed within a hydrothermal regime a few hundred metres below the palaeosurface. The filament-bearing zones were originally porous and served by nutrient-rich fluids that provided a suitable subterranean habitat. Late stage infilling of these voids with chalcedony and calcite preserved the filaments. The oldest filamentous fabric is heavily Fe-encrusted and macroscopically preserved, but no individual filament details are discernible (Figure B.7E and in Hofmann *et al.*, 2002). Subsequent generations of filaments exhibit less Fe-cementation and show preserved individual morphology, including visible cores. The sub-micron size of these individuals prohibits detection within this study.

Natural surfaces of samples 45HS265 and 45HS325 exhibit moderate microscopic relief. Individual Fe-encrusted filaments are ~200 µm wide and extend to centimetres (Figure B.7D).

Geochemical analysis of 45FB583 by WDXRF reveals a dominance of Si (~65 wt % SiO₂) and Fe (~25 wt % Fe₂O₃) with minor Ca. Trace element analysis of 45PP428 confirms the presence of Cu, Zn, As, Mo, Ba, and Pb. The WDXRF system was not primed to measure Be, Ag or Sb.

B.4 Goethite, Cerro de Pasco, Peru (179)

The Matagente orebody is part of the Quaternary magmatic-hydrothermal Zn-Pb-Ag-Bi-(Cu) ore complex of Cerro de Pasco, which is situated 170 km NNE of Lima (10° 38.5' S, 76° 10.5' W) (Figure B.8). Prior to exploitation, the maximum extent of the orebody was 480 m x 200 m. Mining of the Pb-Ag deposit took place predominantly within the oxidation zone (Sangameshwar and Barnes, 1983), which reached a depth of approximately 100 m.

Within such near-surface ore bodies, sulphides of Fe, Cu, Pb, Zn, and Fe-rich carbonates are commonly transformed into highly porous Fe-hydroxide minerals. This environment provides an energy source, usually from pyrite, for chemosynthetic organisms (Melchiorre and Williams, 2001) that originally formed below a palaeosurface (Hofmann and Farmer, 2000). These filamentous microbes often display parallel orientation due to gravitational draping (pseudostalactites), and potentially act as substrates for subsequent growth of oxidation zone minerals.

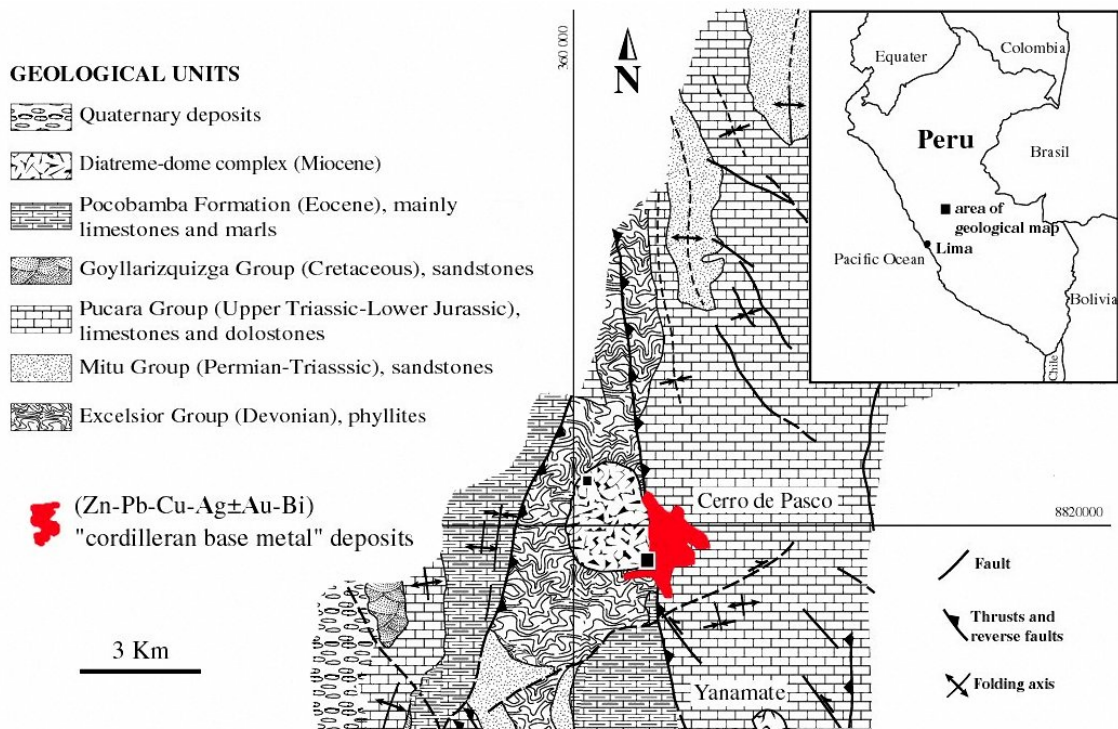


Figure B.8 Geological map of the Cerro de Pasco district (modified after Bendezú and Fontboté, 2002). Filamentous goethite samples (including 179HS367) were collected from the oxidation zone of the Cordilleran base metal deposit shown.

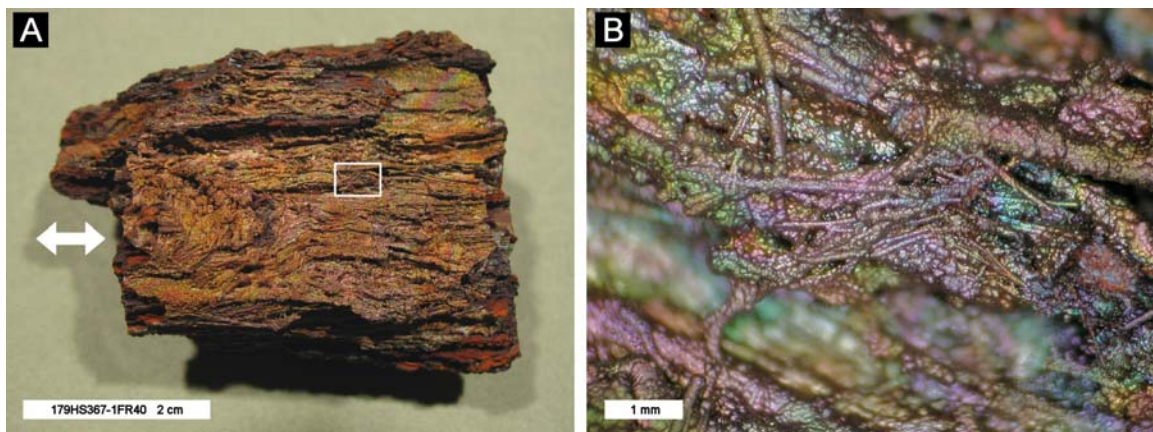


Figure B.9 Outer surface of study specimen 179HS367 (A). The orientated texture is caused by gravity-induced draping of the original microbial filaments. Way-up is either to the left or right as indicated. Close-up view of the highlighted area showing the encrusted filament bundles and their aligned, occasionally chaotic distribution (B).

The study specimens were originally collected in 1955 by G. Christian Amstutz, mine geologist at Cerro de Pasco. Externally, they exhibit linear texture that is similar in appearance to

“fossilised wood” (Figure B.9A) and have a high porosity (> 50%). Fe-hydroxides drape the surface in curtain-like laminae approximately 1 mm to 3 mm thick. The surface is festooned with macroscopic filamentous assemblages. Individual filaments are also preserved with core diameters of about 0.3 μm when observed by SEM (Dr. Beda Hofmann, Natural History Museum, Bern, personal communication).

Samples 179HS367 and 179HS588 have high microscopic relief. The outer surface has a metallic lustre and the inner surface is dull and oxidised. Filaments are generally aligned (as mentioned previously) but occasionally occur as intersecting chaotic assemblages (Figure B.9B). Individual encrusted filaments are typically 100 μm wide, and occasionally extend to centimetres long.

Bulk elemental geochemistry performed on 179PP578 and 179FB582 by WDXRF at both the Open University and the University of Leicester confirm the samples to be ~70 wt % Fe_2O_3 and heavily enriched in Pb (~5 %), Zn (~3 %), Ba (~3700 ppm), As (~2400 ppm), and Cu (~2000 ppm).

B.5 Orthoquartzite, McMurdo, Victoria Land, Antarctica (114)

The dry valleys of Southern Victoria Land, Antarctica extend across an area of 5000 km^2 and lie between 76° 30' S and 78° 30' S and 160° E and 164° E. Geomorphologically they are a system of gouged glacial valleys with a predominant east-west trend (Figure B.10). During the summer air temperatures range between -15 °C and 0 °C and can fall to almost -60 °C in the winter. Less than 10 mm water equivalent of precipitation occurs annually. The Upper Devonian orthoquartzites of the Beacon Sandstone Formation outcrop throughout the dry valleys and contain well-studied examples of cryptoendolithic lichens and micro-algal communities (Friedmann, 1982; Friedmann *et al.*, 1988; Siebert *et al.*, 1996).



Figure B.11 Exfoliating orthoquartzite at Battleship Promontory, Alatna Valley, McMurdo Dry Valleys, Antarctica (A). The clasticity, porosity and translucency of these rocks offer a favourable biohabitat for cryptoendolithic development. Specimen 114HS380 from Linnaeus Terrace (Figure B.10, locality A) showing case hardened exterior and exposed lichen layer (B). Cross sectional view of specimen 114HS353 showing typical distribution of cryptoendolithic communities (C). Note: Battleship Promontory is located 75 km N of Linnaeus Terrace. Courtesy Dr. David Wynn-Williams/British Antarctic Survey (A) circa 1992.

Specimens of exfoliated orthoquartzite that contain cryptoendoliths were collected by the British Antarctic Survey (BAS) in 1995 from Wright Valley at Linnaeus Terrace (Figure B.10, locality A). Linnaeus Terrace ($77^{\circ} 36' S$, $161^{\circ} 05' E$ elevation 1600 m) is an elevated bench of weathered Beacon Sandstone approximately 1.5 km long and 1 km wide, located at the east end of the Asgaard Range, 10 km from the terminus of the Wright Upper glacier. Much research has already been done on these sandstones and other rocks of the region (Friedmann, 1982; Wierzbosch *et al.*, 2003; Blackhurst *et al.*, 2005) including analysis by way of techniques employed in this work (Edwards *et al.*, 1997; Edwards *et al.*, 2004). As such, these specimens provide an appropriate benchmark from which to draw comparison with other types of endolithic biosignature.

Rocks from Linnaeus Terrace are colonised by photosynthesizing cryptoendolithic lichens that form by symbiotic association between unicellular green algae (phycobionts) and filamentous fungi (mycobionts). The physical makeup of the interior of this orthoquartzite (translucency and porosity) provides a favourable protective environment for these organisms. Grain size is typically between 0.2 mm and 0.5 mm. The outer surface is case hardened and oxidised (though the brown coloration belies the low bulk iron content). Over time, oxalic acid secretions from the lichens dissolve the intergranular cement of the host rock, which leads to bioweathering and exfoliation of the rock surface (Sun and Friedmann, 1999).

By their nature cryptoendolithic (subsurface dwelling) and chasmoendolithic (fissure dwelling) organisms live within rocks and are not necessarily associated with epilithic (surface dwelling) varieties (Dr. Wynn-Williams, BAS, personal communication). To make matters worse not all samples within a given area may contain endolithic colonies. External indicators of the likely presence of such colonies being present within rocks would be an important parameter to look for. One possible indicator is colour change which given the capabilities of imaging technology could be subtle. In-field observations at Mars Oasis, Alexander Island, Antarctica (Plate 2 in Edwards, 2004) seems to show a correlation between external surface colour and colonisation of boulders. Darker rocks at the site were inevitably un-colonised whereas those with an orange-yellow hue yielded endoliths. Although a statistical survey was not done, experienced geologists found the technique effective enough to adopt as a sampling strategy.

Communities typically occur as distinct layers within the rock fabric (Friedmann *et al.*, 1988). Figure B.11C shows the sequence in one of the study samples. The upper (near surface) black band is commonly 1 mm thick and close to the exfoliation interface. The coloration is due to UV-protective pigments, such as scytonemin, which are produced by these organisms. Below this layer is a white zone between 1 mm and 4 mm thick, where the lichens have mobilized iron compounds and leached the rock of iron-bearing minerals (Sun and Friedmann, 1999), concentrating them in a red zone at the base of the white zone. A green algal layer is typically found between these zones. Growth and development of these cryptoendolithic communities is extremely slow.

Specimens 114HS353, 114HS354, 114HS380 and 114HS587 are fine examples of the classic layering described by Friedmann *et al.* (1988) (Figure B.11). Vertical zonation extends to a few

centimetres, and both Fe-mobilisation bands and lichen layers are particularly well pronounced. In places the lichen layer can be observed in plan section where recent exfoliation has occurred. The samples exhibit low microscopic relief.

Bulk geochemistry (WDXRF on 114PP430 and 114FB580) confirms the samples to consist of 99 wt % SiO₂ with detectable trace levels of Ba (~25 ppm) and Zr (~90 ppm).

B.6 Marble, McMurdo, Victoria Land, Antarctica (194)

In parts of the McMurdo Dry Valley system, crystalline rocks host examples of chasmoendolithic cyanobacteria (Jorge Villar *et al.*, 2003). Some specimens were collected by the late Dr. David Wynn-Williams (BAS) during a field campaign from a talus slope in the vicinity of the Long Term Ecological Research (LTER) site on Andrews Ridge (77° 38' S, 162° 52' S) near Lake Hoare, Taylor Valley (Figure B.10, locality B). The study sample (194HS435) is a weathered marble colonised by *Chroococidiopsis*, a desiccation resistant, radiation resistant cyanobacterium (Erokhina *et al.*, 2002).

Sample 194HS435 generally has low microscopic relief. Fresh surfaces are almost white and have a crystalline fabric (Figure B.12). Weathered surfaces are off-white to light brown. Microbial growth occurs along fracture planes on both fresh and internal weathered surfaces, which suggests chasmoendolithic behaviour. Colonies are distinct due to their blue-green coloration and penetrate deep (~centimetres) into the rock. Under high magnification they appear as a patchwork of “globules” (Figure B.12E) 50 µm to 100 µm in diameter, typical of cyanobacteria containing c-phycoyanin in association with chlorophyll. Insufficient material was available for bulk geochemistry but XRD analysis on derived powders confirms a dolomite with calcite mineralogy. 194HS435 is included in the inventory of morphological biosignatures on the basis of crystalline fabric, biofluorescent properties, and comparison with other cryptoendolithic samples from the same region (<family> ID 114).

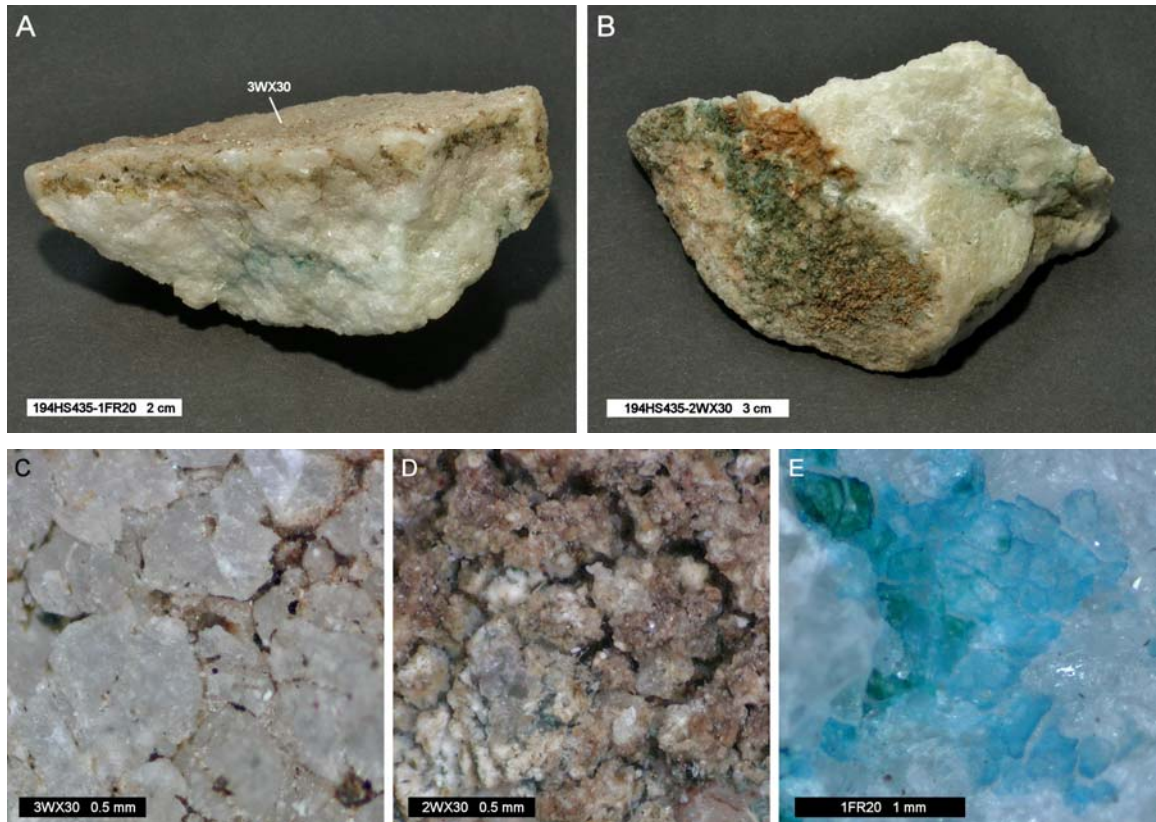


Figure B.12 Study specimen of marble (194HS435) collected from Andrews Ridge, Taylor Valley, Antarctica (Figure B.10, locality B). The sample is colonised by the cyanobacterium *Chroococcidiopsis* on fresh surfaces (A and E) and weathered surfaces (B and D). The exterior of the sample (C) is discoloured and un-colonised.

B.7 Gypsum (var. selenite), Houghton Crater, Devon Island, Canada (44)

The Houghton impact structure is located in the western region of Devon Island in the Canadian High Arctic (75° 22' N, 89° 41' W) (Figure B.13A) and was formed during the late Eocene (~39 Ma) (Sherlock *et al.*, 2005). Surface mapping and the local gravity signature confirm a crater of approximately 24 km in diameter (Grieve, 1988; Pohl *et al.*, 1988; Scott and Hajnal, 1988). The impacting asteroid (or comet) penetrated target rocks composed of a thick carbonate sequence (~1.8 km) that is underlain by Precambrian granites and gneisses. Allochthonous polymict impact breccia dominates the central portion of the crater (~10 km diameter), which is largely made up of target rock clasts from the carbonate sequence plus basement gneisses. Evidence for impact-induced hydrothermal activity is well preserved within the structure, including sulphate mineralization and mobilization (Osinski *et al.*, 2003). Microbial colonization within these

sulphate deposits has recently been described (Parnell *et al.*, 2004).

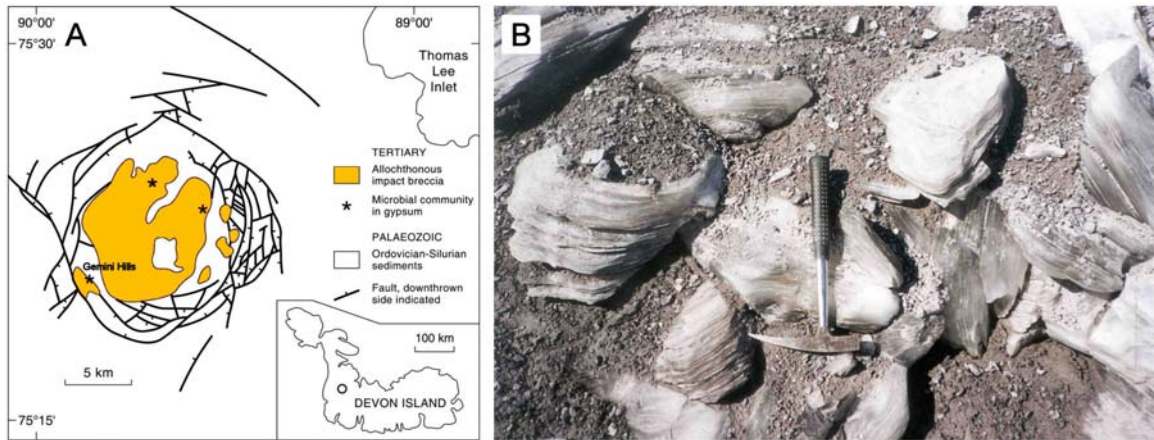


Figure B.13 Geological sketch map of the Haughton impact crater, Devon Island, Canada (A) showing the extent of the brecciated region (modified after Parnell *et al.*, 2004). Microbe-bearing sulphates (gypsum var selenite) occur throughout the allochthonous impact breccia zone (B) including Gemini Hills, the location of the study samples. These microbial colonies exhibit chasmoendolithic behaviour (Figure B.14). Courtesy Prof. John Parnell, University of Aberdeen.

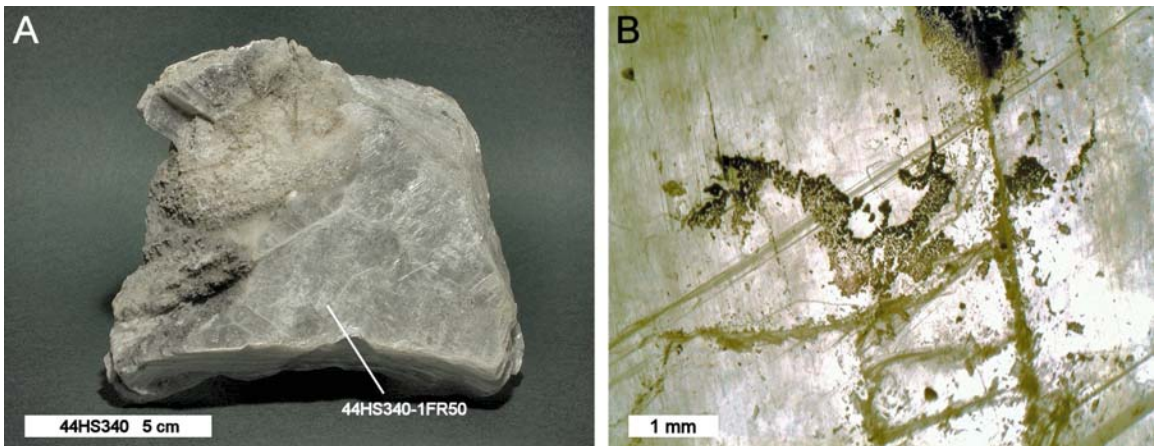


Figure B.14 Study specimen 44HS340 (A) of microbe-bearing gypsum collected from Gemini Hills area of Haughton Crater (for location see Figure B.13). This variety of gypsum (selenite) is characterised by well developed, transparent cleavage folia which are evident in the lower part of the image. Such an environment provides a favourable habitat for photosynthetic, halotrophic micro-organisms (B, black areas).

Specimens of microbe-bearing gypsum were collected by Prof. John Parnell (University of Aberdeen) from sites within the impact breccia unit adjacent to the Palaeozoic basement strata. The gypsum is in the form of *selenite*, a highly pure variety of hydrous calcium sulphate ($\text{CaSO}_4 \cdot 2\text{H}_2\text{O}$) with large transparent cleavage folia (Figure B.13B and in Osinski and Spray, 2003). The microbes inhabit the interlaminar space between crystals and appear up to a few centimetres from the external margins. The clarity of the selenite crystals provides a “window” through which to observe the microbial communities at successive levels. Two species of cyanobacteria have been identified, *Gloeocapsa alpina* (Nägeli) Brand and *Nostoc commune* Vaucher (Parnell *et al.*, 2004). Given the nature of their host, these photosynthesizing chasmoendoliths are halotrophic (salt tolerant) and have been shown to be dependent on photo-protective pigment synthesis (Edwards *et al.*, 2005b).

Samples 44HS340 and 44HS419 exhibit characteristically large cleavage folia (Figure B.14A). Fresh surfaces have extremely low relief, but due to the transparency of the selenite, these samples can be described as having high relief in the context of this study. Interlaminar chasmoendoliths (*Nostoc* and *Gloeocapsa*) are well distributed both horizontally (centimetres) and vertically (millimetres). Individual clusters are typically a few millimetres across and often chained together as larger communities (Figure B.14B).

Geochemical analysis of 44PP581 by WDXRF confirms the samples to be almost pure calcium sulphate with high levels of Sr (360 ppm), a typical palaeosalinity indicator in gypsum, and trace levels (< 10 ppm) of Cu, Ni, and Rb. The Cu and Ni may be attributable to host rock contamination since 44PP581 was not derived from pure selenite.

B.8 Banded Chert, Kitty’s Gap, Pilbara, Australia (190)

The oldest part of the Pilbara craton of Western Australia lies to the east within the 3.72 Ga to 2.85 Ga granite-greenstone terrane (Figure B.15) and includes the Warrawoona Group of volcanics and cherts (Figure B.16). The Panorama Formation of the Warrawoona Group is characterised by volcanoclastic sediments grading from rhyolitic to dacitic towards the top of the sequence. These sediments are thought to have formed in a shallow marine to subaerial environment (Nijman *et al.*, 1998; de Vries, 2004). The sediments were rapidly silicified owing to the high silica content of the sea water and pore water, as well as the rapid silification of the biogenic organic remains within the sediments (Westall *et al.*, 2006b; Orberger *et al.*, 2006).

Radiometric studies date these rocks at $3.446 \text{ Ga} \pm 5 \text{ Ma}$ (de Vries, 2004).

The morphological signatures contained in these sediments are small, subtle, and generally beyond the limits of detection in the context of this work. Individual microfossils are comprised of filaments ($0.25 \mu\text{m}$ diameter and 10s of μm long), rods, and coccoids. Colonies of coccoids ($0.5 - 1 \mu\text{m}$ diameter) containing 10^2 to 10^3 individuals can reach $> 100 \mu\text{m}$ in diameter. Occasionally very fine but laterally extensive biofilms consisting of consortia of different microfossils are present. Although these larger manifestations could theoretically be detected by *in situ* microscopy, the microfossils themselves are carbonaceous and, although they appear optically dark, they cannot be distinguished from other dark particles, such as Ti-oxide coated particles.

Specimens of black and white laminated chert from the Coppin Gap locality rocks of the Panorama Formation exposed at Kitty's Gap ($120^\circ 5' \text{ E}$, $20^\circ 53' \text{ S}$) were collected by Dr. Westall in 2000. Field exposures (Figure B.17AB) exhibit well preserved macroscopic bedding structures and micro-laminae (Westall *et al.*, 2004, 2006b). Laminations are $< 1 \text{ mm}$ thick and extend linearly to centimetres. Individual volcanic clasts range in size from 30 to $500 \mu\text{m}$, with the coarser fraction being more associated with the white laminations. Geochemical analysis (Orberger *et al.*, 2006) confirms enrichment of Al, K, Ti and Fe in the white laminae compared to the black laminae owing to the relative abundance of hydromuscovite-replaced volcanic clasts in the former. Trace element analysis (*op. cit.*) also shows that the white bands are more enriched in Rb, Sr, Y, Zr, Ba, Nb, Ta, and W, whilst the black bands are more enriched in Ni, Cu, Zn, and Sb.

Sample 190HS390 is an excellent example of Kitty's Gap chert with well preserved black and white laminae, cross-bedding and flaser-linsen bedding structures (Figure B.17C). The sample is fresh with occasional, localised, fractures and associated iron coatings. Surfaces of interest have low microscopic relief. Sample 190RS424 provides examples of coarser banding up to 9 mm thick.

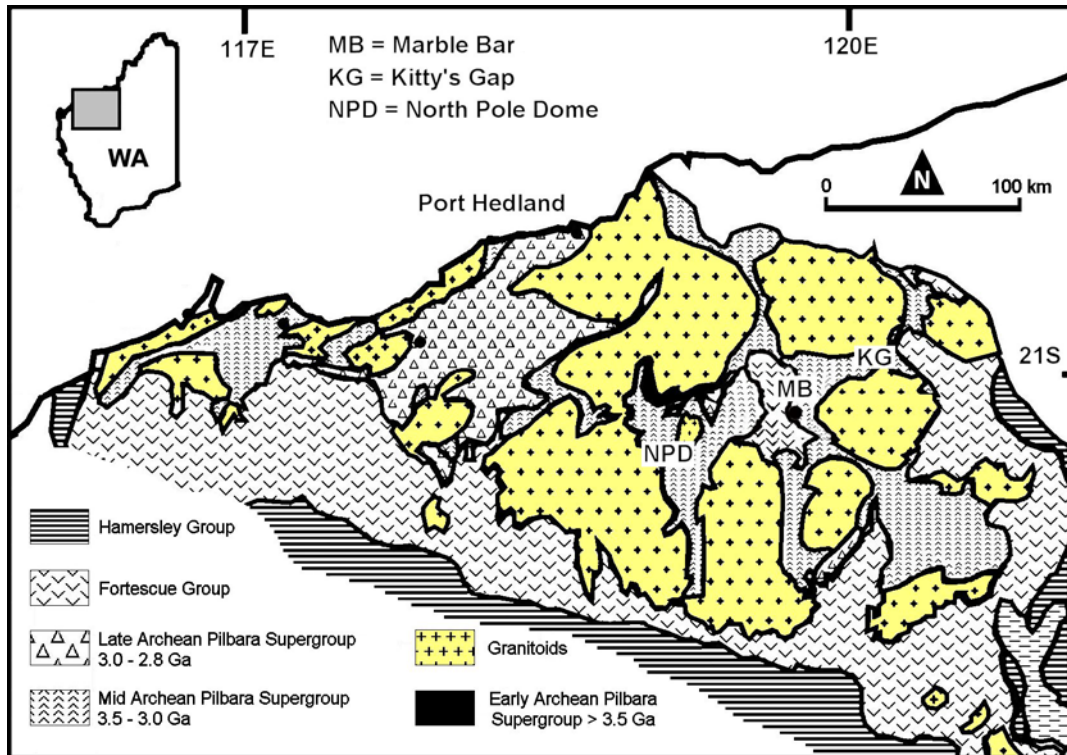


Figure B.15 Geological sketch map of the Pilbara craton, Western Australia. The approximate locations of Kitty's Gap (Section B.8) and North Pole Dome (Section B.9) are indicated. Courtesy NASA Astrobiology Institute/GSWA (modified by the author).

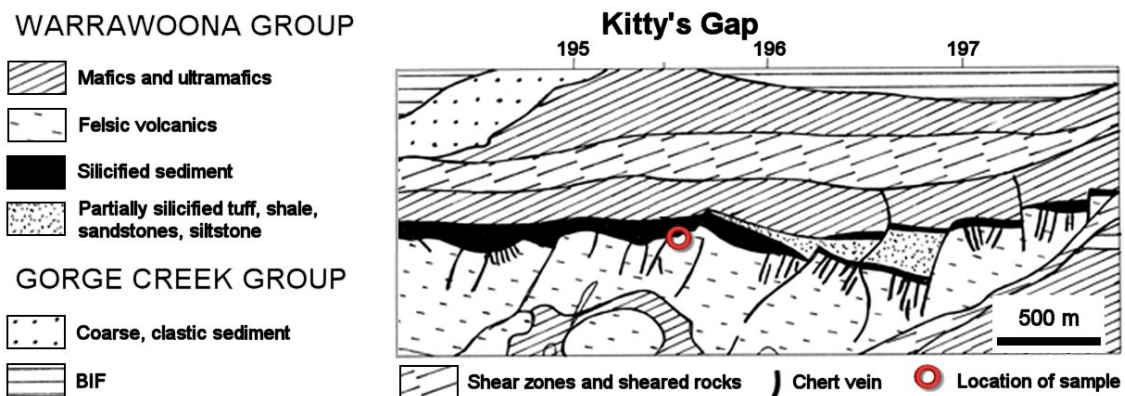


Figure B.16 Geological sketch map of the Kitty's Gap locality (modified after Westall *et al.*, 2006b). For general location see Figure B.15. Samples of banded chert (including 190HS390) were collected from the location shown.

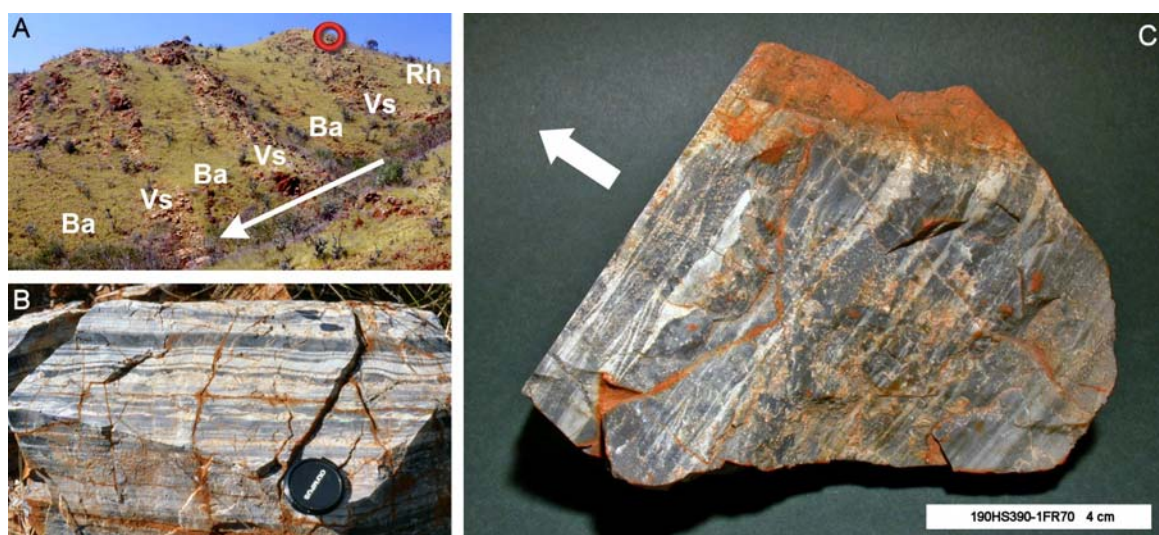


Figure B.17 Stratigraphic sequence visible in the topography at Kitty's Gap (A). Legend: Rh (rhyolite), Vs (volcaniclastic sediment), Ba (basalt). Large blocks of fresh banded chert (B) yield well preserved sedimentary features such as black and white laminae, cross-bedding and flaser-linsen bedding structures. These are particularly well represented in study specimen 190HS390 (C). Courtesy Dr. Frances Westall, Centre de Biophysique Moléculaire, CNRS (AB) circa 2000.

Bulk major element analysis by WDXRF on 190FB579 (derived from 190HS390) confirms the sample to be predominantly Si (91 wt % SiO₄), with minor K (1.2 wt % K₂O) and Ti (0.33 wt % TiO₂). Insufficient material was available to perform representative bulk trace element chemistry, but analysis of 190RS424 (80% white bands) by *in situ* WDXRF reveals the presence of Rb (~80 ppm), Sr (~35 ppm), Y (~30 ppm), Zr (~210 ppm) and Ba (~470 ppm).

B.9 Stromatolitic Chert, North Pole Dome, Pilbara, Australia (159)

Well-preserved coniform and columnar stromatolites in silicified carbonate sediments (3.443 Ga) occur in the North Pole Dome area of the Pilbara craton (Figure B.15 and Hofmann *et al.*, 1999). Allwood *et al.*, (2006) suggest microbial mediation in their formation and Westall (personal communication) has observed microfossils in these rocks. Specimens of domical stromatolites from the Strelley Pool Chert on the SW perimeter of North Pole Dome (Figure B.18) were acquired by Dr. Frances Westall in 2000, before the site was considered for protection.

Samples 159HS304, 159RS435, and 159RS571 display stromatolitic texture in cross-section (Figure B.19A). Laminae range from planar to convoluted, and are < 1 mm thick. No examples of domical features in plan view were available for this study (see Chapter 8). However, basal stromatolitic features are particularly well preserved in sample 159HS304 with fine examples of pseudomorphs after gypsum (Figure B.19B). Natural surfaces on all samples have low microscopic relief with the exception of the lower portion of 159HS304 which is moderate to high. Fracturing is more evident in this chert compared to the sample from Kitty's Gap (190HS390).

Geochemical analysis by WDXRF confirms the dominance of Si (~97 wt % SiO₂) plus minor (< 1 wt %) components of Na₂O, CaO and Fe₂O₃. Traces of Cu (100 ppm) and Zn (~100 ppm) are also present.

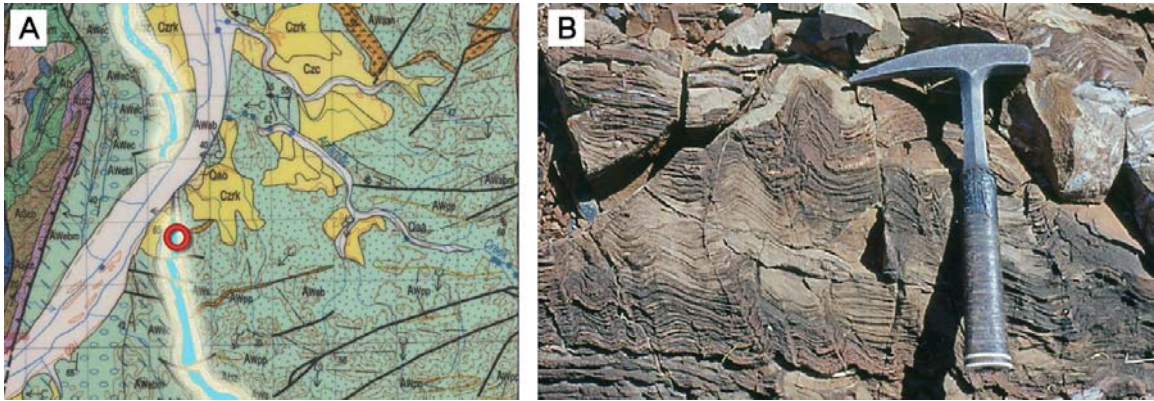


Figure B.18 Geological map of a section of the North Pole Dome region of the NE Pilbara craton (A) showing the extent of the Strelley Pool Chert (highlighted) and the Trendall locality (circled). Apex basalts (east) and Euro basalts (west) of the Warrawoona Group lie either side of the chert ridge. Recent, unconsolidated deposits are prefixed C and Q. Well preserved stromatolites are exposed in outcrop at the Trendall locality (B). Courtesy GSWA (A) and Dr. Frances Westall, Centre de Biophysique Moléculaire, CNRS (B) circa 2000.

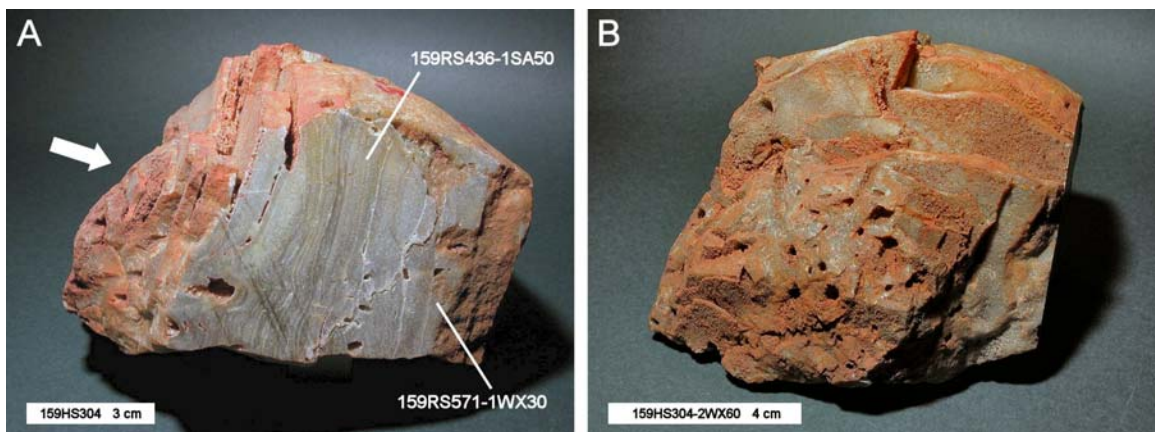


Figure B.19 Study specimen 159HS304 of Strelley Pool Chert from the Trendall locality (Figure B.18A). Well defined stromatolitic texture is visible on the sawn face (A), now 159RS435 and 159RS571. Way-up is indicated by the arrow. Sample 159HS304 represents a basal unit of the stromatolite as indicated by the occurrence of pseudomorphs after gypsum (B).

B.10 Banded Iron Formation (BIF), Barberton, South Africa (163)

The Barberton Greenstone Belt (BGB) is a remnant of an Early Archaean orogenic belt (de Wit *et al.*, 1982; de Ronde *et al.*, 1994) located near the Transvaal-Swaziland border (Figure B.20A). The Swaziland Supergroup sequence in the BGB consists of mainly mafic and ultramafic rocks

of the Onverwacht Group (~3.45 Ga), overlain by pyroclastic and epiclastic sediments of the Fig Tree Group (~3.2 Ga) followed by conglomerates and siltstones of the Moodies Group (3.22 Ga to 3.1 Ga). Low grade regional metamorphism (lower greenschist facies) has had no effect on the preserved textures, especially within the older units of the sequence (Onverwacht and Fig Tree Groups) where preservation is exceptional. This has led to much interest in the search for evidence of endogenous early life within these rocks (Byerly *et al.*, 1986; Walsh, 1992, 2004; Westall and Folk, 2003; Westall *et al.*, 2001, 2006a; Tice and Lowe, 2004; Banerjee *et al.*, 2004; Westall and Walsh, 2006; Hofmann and Bolhar, 2007). Specimens of Banded Iron Formation (BIF) from the Fig Tree Group were collected by Dr. Frances Westall in 1999 from the Msauli River (Figure B.20B).

Samples 163HS303, 163RS585 and 163HS586 have a prominent siliceous band exhibiting a well defined (linear) contact with a massive Fe-oxide layer (Figure B.21). The interface is a potential zone of weakness and extends to centimetres. The siliceous bands have low microscopic relief and the oxidised bands range from low to moderate relief. Generally smooth surfaces featuring both units (163RS585, 163HS586-1FR30 and 163HS303-1WX50) provide useful targets for analytical measurements requiring contact, whereas differentially weathered surfaces (163HS303-2WX60) aid imaging.

Geochemical analysis of 163HS586A (siliceous band) confirms a composition of predominantly Si (98 wt % SiO₂) with minor Fe (2 wt % Fe₂O₃). No other elements were detected. Likewise, analysis of 163HS586B (oxidised band) confirms a high concentration of Fe (66 wt % Fe₂O₃), with some associated Mn (1 wt % MnO), but still significant Si (33 wt % SiO₂).

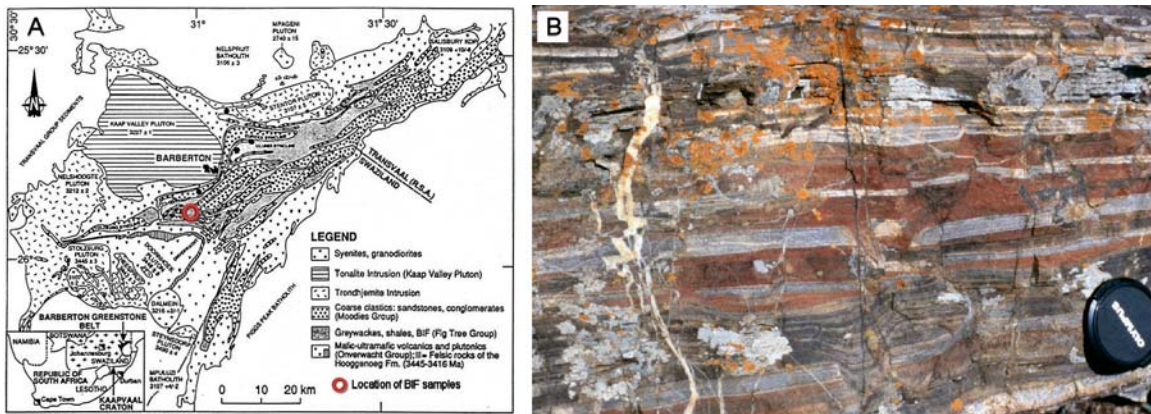


Figure B.20 Geological map of the Barberton Greenstone Belt, South Africa (A) (modified after de Ronde *et al.*, 1994). The mafic-ultramafic rocks of the Onverwacht Group (~3.45 Ga) are overlain by sediments of the Fig Tree Group (3.2 Ga). The latter contain well preserved BIFs from the Fig Tree Group (B). Courtesy Dr. Frances Westall, Centre de Biophysique Moléculaire, CNRS (B) circa 1999.

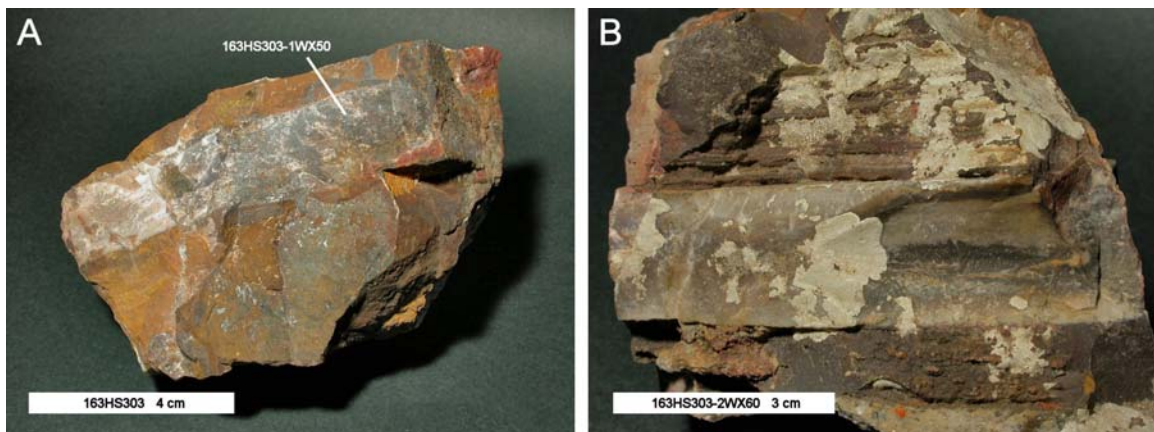


Figure B.21 Specimen of BIF (163HS303) collected from the locality shown in Figure B.20A. The interface between the siliceous band and the oxidised iron layer is well pronounced on fresh surfaces (A). Differential weathering accentuates the more resistant siliceous band from the weaker oxidised iron layers (B).

Appendix C

Experimental Setup and Instrumentation

This Appendix describes the experimental setup and instrumentation used to conduct the *in situ* astrobiology experiments presented in Chapter 5. The analytical methods used are also explained. The combination of imaging, analytical and geotechnical techniques outlined is intended to represent a suite of payload elements considered fundamental yet viable for *in situ* geological exploration at the planetary surface. Field-like procedures described below are relevant to the autonomous robot studies discussed in Chapter 6.

C.1 Introduction

From practical experience, geological activities conducted in the field can be classified on the basis of three working distances between observer and target: *proximal* (~100 cm), *macroscopic* (~10 cm) and *microscopic* (~1 cm). These are not formal definitions but will be used throughout this thesis to define the immediate radial “working zone” of a stationary human field geologist who is suitably equipped with vision and the tools of the trade such as a hammer, a field lens, portable analysers and sampling devices. The terms are adopted to distinguish from distances to targets beyond the physical reach of the observer (i.e. “remote”) that require mobility to reach. The use of the term proximal also naturally fits within the lower bounds of the microfacies scale (metre to centimetre size targets) described by Cady *et al.* (2003). In the planetary context, the analogy applies equally to static planetary landers or stationed mobile vehicles equipped with robotic arms (Golombek, 1997; Baglioni, 2003; Pullan *et al.*, 2004; Squyres *et al.*, 2003; Vago *et al.*, 2003).

All imaging, analytical, and geotechnical activities for this study were performed within an open laboratory since there were no requirements on the instruments for strict cleanliness. Although designed for use on Mars, the instruments and tools from the Beagle 2 PAW could be used under these circumstances without significant degradation in performance. Each device was removed from the PAW (Figure 5 in Pullan *et al.*, 2004) and operated in standalone mode. Unfortunately the Flight Spare XRS (FS-XRS) was not available during the course of this work since it was

committed to a calibration and performance study (Talboys, 2006).

In the field (i.e. at the planetary surface), one would systematically acquire, analyse and interpret the collective data at each scale by proceeding from coarse (far from target) to fine (close to or in contact with target). For the purposes of this work the reverse was adopted to enable the relatively small microbial relict features to lie within a field of view at each scale (if this was achievable). Where possible, both weathered and fresh examples of each sample were compared and in some cases sawn (unpolished) surfaces were also investigated. Thus external surfaces (pre-splitting), internal surfaces (post-splitting) and prepared surfaces (post-grinding) were represented. Instrument positioning with respect to sample targets (i.e. emulating robotic placement) was achieved manually by way of retort stands, mechanical translation stages, articulating arms (as used in studio photography) and tripods.

Since the identification of morphological features is the dominant theme of this investigation, spatial imaging is the obvious primary technique. In the framework of these studies, and of planetary fieldwork in general, analytical data provide essential context with which to constrain the interpretation of images, and geotechnics provide the means by which to access the features.

Even though all samples were imaged, some could not be analysed by all methods due to either a paucity of material available for destructive analysis or non-availability of some of the instrumentation. As this study is part of an ongoing programme it was considered undesirable to commit unique specimens that display visual features of interest to the rock crusher. Nevertheless, the majority of the study samples benefited from the complete array of techniques.

Instrumentation made available for this work included selected flight spare instruments from the Beagle 2 Mars lander (Pullan *et al.*, 2004), and an array of commercial equipment serving as emulators of potential future instruments and of techniques currently being developed for space. The Beagle 2 instruments (Figure 2.3) included one stereo camera (Griffiths *et al.*, 2005) with a full complement of geological filters and the close-up lens (Table 2.3), the microscope (Thomas *et al.*, 2004), the Mössbauer spectrometer (Klingelhöfer *et al.*, 2003), the sampling Mole (Richter *et al.*, 2002) and the rock corer (Pullan *et al.*, 2004). The commercial instruments included a high fidelity multi-spectral imager (visible band) (<http://www.cri-inc.com/products/nuance-vx.asp>), a field portable energy dispersive X-ray fluorescence (EDXRF) spectrometer (Potts *et al.*, 1995), a wavelength dispersive X-ray fluorescence (WDXRF) spectrometer (see the Axios Advanced page

at <http://www.panalytical.com/>), a micro-Raman spectrometer (see Raman Spectroscopy pages at <http://www.renishaw.com/> and <http://www.brukeroptics.com/>), and a custom built X-Ray diffractometer (Menzies *et al.*, 2003). Importantly, all the imaging and analytical instruments were capable of making *in situ* measurements on field representative geological specimens without the need for sample preparation.

Other instruments were also used in support of the *in situ* studies. These included a laboratory WDXRF spectrometer for determination of bulk major and trace elemental composition (Philips PW1400), and a laboratory X-ray powder diffractometer for determination of bulk mineralogy (Philips PW1010). Both involved the preparation of homogenised powders from the study specimens and were used to establish compositional benchmarks in advance of the *in situ* experimental work.

Table C.1 lists the GSPARC codes used to describe each instrument and operational mode.

C.2 Imaging

Imaging was performed at the three working distances described previously. Dark enclosures, translation stages and controlled illumination were specifically constructed and utilized for all the imaging work (Figure C.1). Both Beagle 2 cameras (stereo camera and microscope) also benefited from reduced ambient room temperatures. For example reducing the lab temperature from 25 °C to 17 °C approximately halved the dark current and therefore improved the signal to noise ratio (SNR) (Dr. Andrew Griffiths, MSSL, personal communication).

C.2.1 Proximal and macroscopic imaging

The Development Model (DM) of the Beagle 2 stereo camera (Figure C.1A) was used for both proximal imaging at 60 cm range with a near-complete set of geological filters (B2SCSS\$GEO) and macroscopic imaging at 8 cm range with the x6.4 close up lens filter (B2SCSS\$CUL). Stereo was achieved in the latter mode using lateral displacement of the camera using a translation stage. For the laboratory experiments a spare filter wheel was populated with eleven geology filters (440 nm, 530 nm, 600 nm, 670 nm, 750 nm, 800 nm, 860 nm, 900 nm, 930 nm, 965nm, and 1000 nm), plus the close-up lens (Griffiths *et al.*, 2005). The 480 nm filter was excluded due to the lack

of space in the filter wheel assembly. Spectral imaging was possible at room temperature with all filters with the exception of 440 nm (blue) due to lower responsivity of this filter compared to the rest of the set (see Table 5 in Griffiths *et al.*, 2005).

Illumination was provided by a Solux 4700 K daylight halogen lamp for proximal imaging (B2SCS\$GEOL\$SOL), and RGB filtered light via a cold ring light system for macroscopic work (B2SCS\$CUL\$RGB) (Figure C.1A). For macroscopic fluorescence imaging, UV illumination was provided by an 8W off-axis UV lamp operating in either UVA (B2SCS\$CUL\$365), UVB (B2SCS\$CUL\$302) or UVC (B2SCS\$CUL\$254). Prior to the experiments on the study samples, initial results using samples of fluorite (184HS379) and amber (178HS369) confirmed the usefulness of UV fluorescence for mineral identification in field macroscopy (Figure C.2B) and microscopy (Figure C.2D).

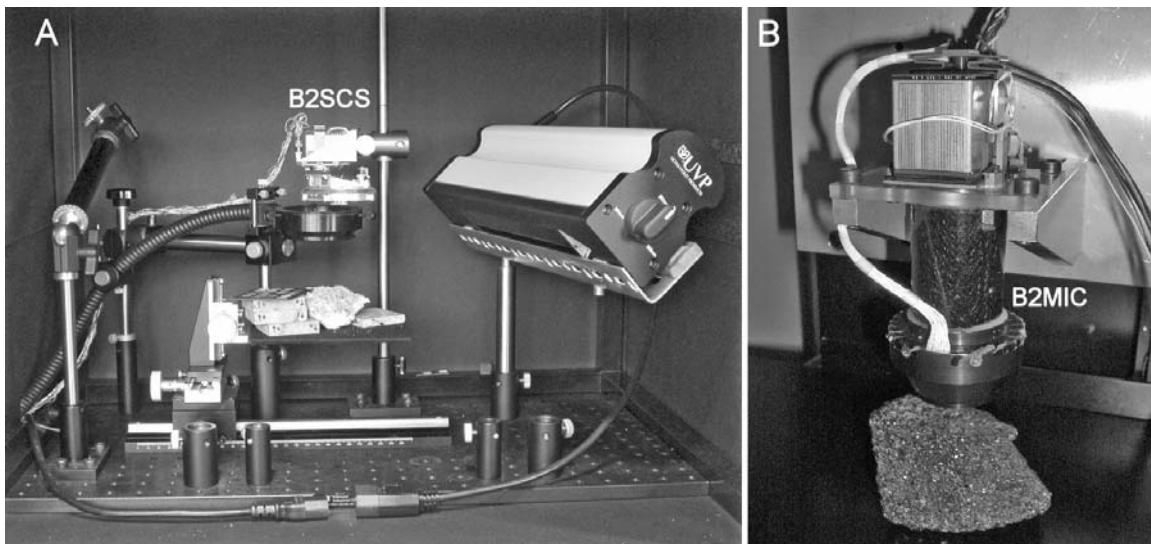


Figure C.1 Experimental set up for proximal, macroscopic, and microscopic imaging using the Beagle 2 cameras. For proximal and macroscopic imaging (A), specimens were secured to a triaxial stage and moved vertically (for focusing), and horizontally (for stereo displacement). The Beagle 2 stereo camera (B2SCS) remained in a fixed position either 10 cm or 60 cm above the sample depending on the imaging mode. For macroscopic imaging (close up filter) a cold ring light provided controlled illumination from a light source outside the enclosure and a UV lamp was used for fluorescence work. For proximal imaging (geology filters) the ring light was removed and replaced with an off axis daylight lamp. Imaging with the Beagle 2 microscope (B2MIC) utilised a standalone motorised translation table for precision focusing (B). In this arrangement the sample remained stationary and the camera moved.

Table C.1: List of GSPARC instrument related codes relevant to this work ¹.

Instrument	Modes and Stimuli	Section
B2SCS (Beagle 2 DM stereo camera)	\$GEOL (all geology filters) \$n (specified filter wavelength in nm) ² \$CUL (close-up lens) \$W (unfiltered ring light, white illumination) \$RGB (filtered ring light, RGB illumination) \$UV (UV illumination) \$365 (8W UV lamp, UVA illumination) \$302 (8W UV lamp, UVB illumination) \$254 (8W UV lamp, UVC illumination) \$SOL (Sohlux lamp, daylight illumination)	C.2.1
NUVIS (Nuance multi-spectral camera)	\$MAC10 (macro optics, 10 nm passband)	C.2.1
	\$MIC10 (micro optics, 10 nm passband)	C.2.2
	\$SOL (Sohlux lamp, daylight illumination)	
B2MIC (Beagle 2 QM microscope)	\$RGB (all red, green and blue LEDs)	C.2.2
	\$W (all white LEDs)	
	\$UV (all UV LEDs)	
PW1K4 or AXIOS or ARL8K42 (Laboratory WDXRF spectrometer)	\$HS (hand specimen, in situ analysis)	C.3.1
	\$PP (powder pellet, bulk analysis)	
	\$FB (fusion bead, bulk analysis)	
TN9K (Portable EDXRF spectrometer)	\$FCA (⁵⁵ Fe, ¹⁰⁹ Cd, ²⁴¹ Am excitation)	C.3.1
UBRAM (Laboratory Raman spectrometer)	\$488 (488 nm laser, Renishaw system)	C.3.2
	\$514 (514 nm laser, Renishaw system)	
	\$785 (785 nm laser, Renishaw system)	
	\$1064 (1064 nm laser, Bruker system)	
	\$40X (40X objective)	
	\$50X (50X objective)	
B2MBS (Beagle 2 QM Mössbauer spectrometer)	Not specified (default ⁵⁷ Co source)	C.3.3
NHMXRD (In situ X-Ray diffractometer)	Not specified (default Microsource [®] Cu-K α)	C.3.4
PW1010 (Laboratory XRD)	Not specified (default X-ray tube Cu-K α)	C.3.4
B2PLUTO (Beagle 2 QM PLUTO soil sampler)	\$SPLIT (rock splitter)	C.4
B2RCG (Beagle 2 QM rock corer/grinder)	\$CORE (coring)	C.4

¹ Refer to Appendix A for a detailed explanation of GSPARC coding conventions² Valid filter peak values are 440, 530, 600, 670, 750, 800, 860, 900, 930, 965 and 1000 (expressed in nm)

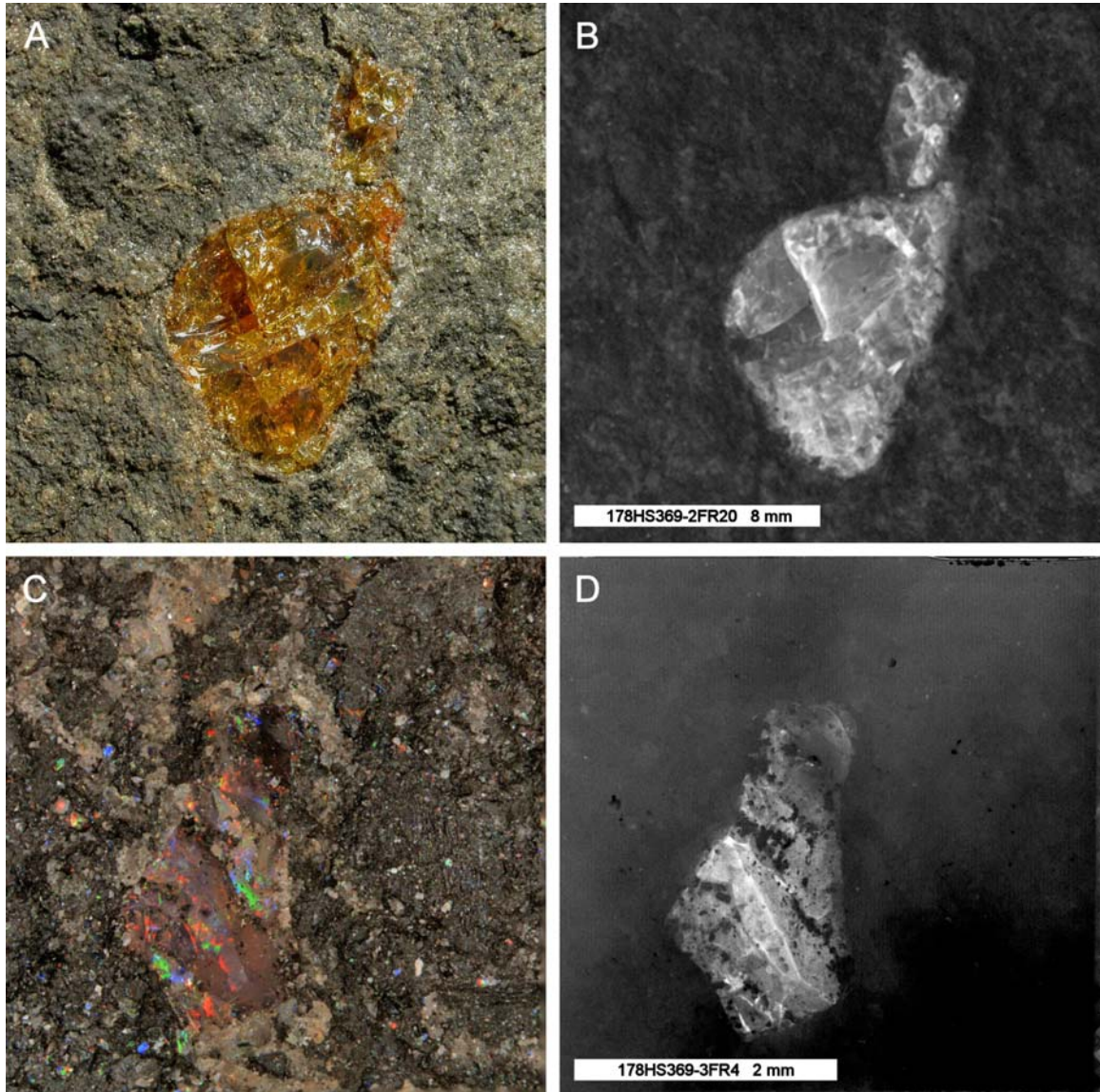


Figure C.2 Demonstration of macroscopic and microscopic fluorescence imaging using the Beagle 2 camera systems and a specimen of amber (178HS369). Composite image acquired with the Beagle 2 stereo camera and external RGB illumination (A) and equivalent view under UVA (365 nm) illumination (B). Colour composite image acquired with the Beagle 2 microscope and integral RGB illumination (C) and equivalent view using UVA (373 nm) illumination only (D). Instrumentation: B2SCSSCUL\$RGB (A), B2SCSSCUL\$365 (B), B2MIC\$RGB (C), B2MIC\$SUV (D).

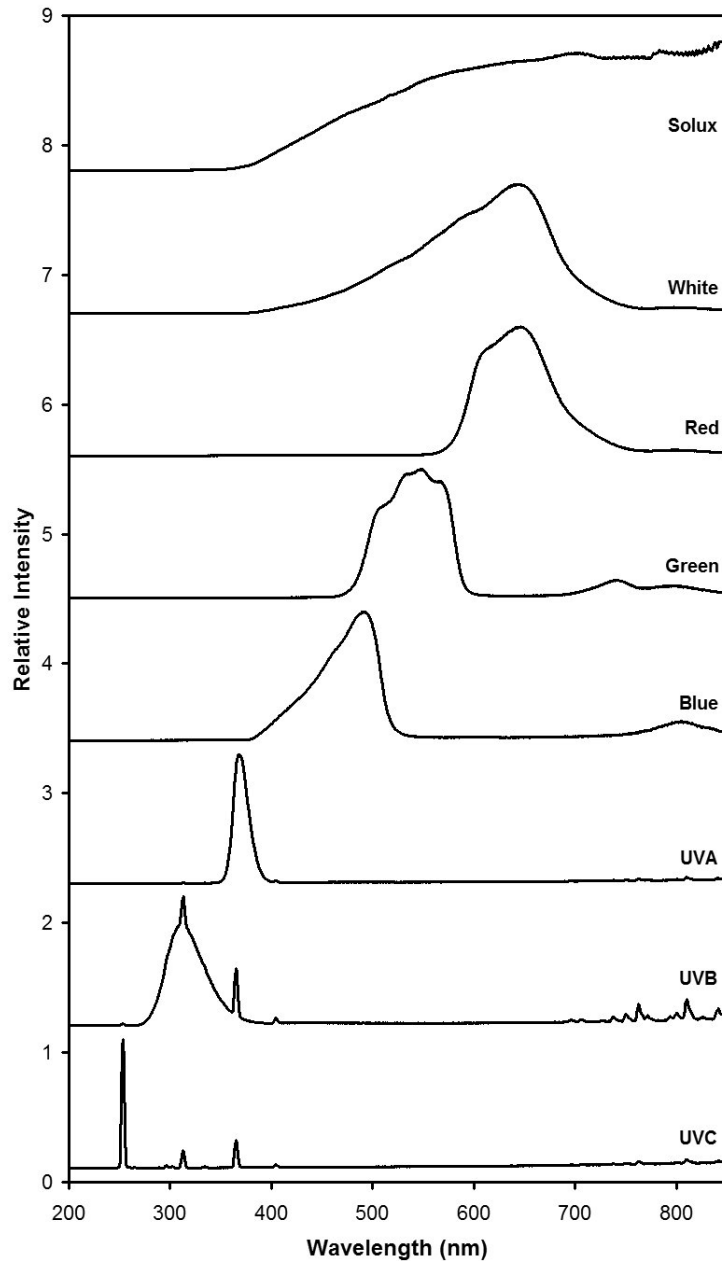


Figure C.3 Spectral characteristics of the light sources used for proximal and macroscopic imaging with the Beagle 2 stereo camera (B2SCSS). Close approximation to natural daylight was achieved with a Solux 4700 K halogen lamp. Red, green and blue light was provided by a Mille Luce illuminator equipped with a halogen white light source and removable filters for each channel. UV illumination was provided by an 8W lamp with selectable output for UVA, UVB and UVC. All spectra were characterised with a Hamamatsu UV-VIS spectrometer at 1 nm spectral resolution.

The spectral characteristics of all the above light sources were recorded with a Hamamatsu C10082CA UV-VIS spectrometer with 2.7 to 4.3 nm typical spectral resolution across the range 200 to 800 nm (Figure C.3). Illumination standoff distances were comparable to those for the camera (80 mm and 600 mm as mention above). The typical geometry for off-axis illumination (Solux and UV sources) was 45°.

All DM camera images were partially calibrated (bias and dark current) and cropped to a square field of view (FOV) (Figure C.4) in order to be compliant with other imaging formats and more useful for stereoscopic viewing. Cropping also removed the slight fall-off in CCD flat field response observed at the peripheral regions in the DM camera.

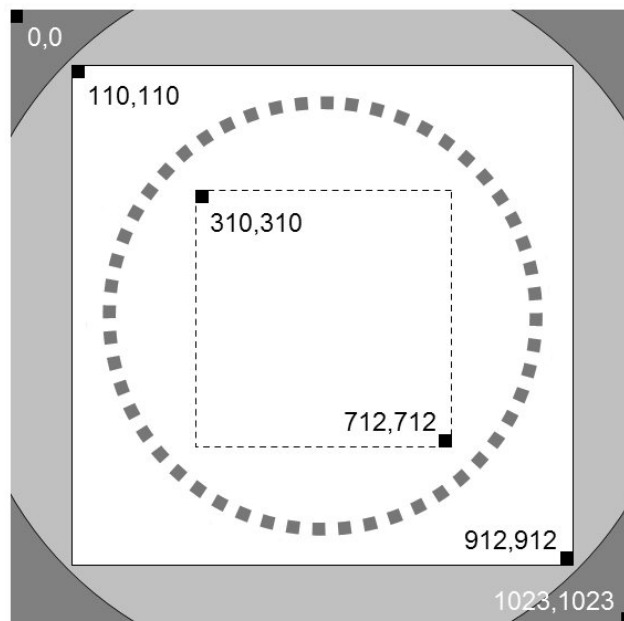


Figure C.4 Cropping procedure for all Beagle 2 stereo camera (B2SCSS) images. The optical arrangement of the SCS results in a circular field of view (FOV) slightly larger than the 1024 x 1024 pixel CCD at the focal plane. For convenience, and to benefit from the relatively uniform flat field response of the central region, images are cropped to an approximate 800 x 800 pixel FOV. For most experiments this is adequate. However, for some highly reflective samples imaged in macroscopic mode, the working FOV requires cropping further (dashed box) to avoid deleterious effects caused by the ring light (dashed circle). CCD pixel coordinates are shown for reference.

Multi-spectral imaging was performed with a Nuance VIS-10 system (420 nm to 720 nm at 10 nm spectral resolution) (<http://www.cri-inc.com/products/nuance-vx.asp>). The Nuance system is

based on a stack of Lyot liquid crystal filters (see Glossary) placed in front of a 1.3 Mpixel scientific grade CCD. Each filter can be “tuned” by applying an appropriate electric field, which thus alters the overall transmission characteristics of the stack. The system is controlled via a supplied software interface.

The Nuance camera was equipped with a standard Nikon 60 mm lens for macroscopic brightfield imaging (NUVIS\$MAC10). Samples were illuminated with the Solux daylight lamp as described above. Imaging with the Nuance was conducted using a commercial photographic copy stand (within a dark enclosure), and a similar triaxial specimen stage to that shown in Figure C.1A. All acquired image cubes (i.e. collections of images acquired at each filter value across the range) were corrected for flat fielding and optical density (OD) to ensure quantitative spectral analysis was performed. Where necessary individual images were exported from the stack and examined separately (i.e. for contrast enhancement).

C.2.2 Microscopic imaging

The Beagle 2 microscope is a fixed focus monochromatic camera with integral illumination LEDs for RGB colour (642 nm, 523 nm and 466 nm peak) and UVA (373 nm peak) imaging (Thomas *et al.*, 2004). Focusing is achieved by mechanically translating the entire microscope incrementally along its optical axis (Pullan *et al.*, 2004) and combining all the in-focus portions of each image into a single image. As a consequence, depth information is also obtained. At a nominal standoff distance of 12 mm (range 9 mm to 15 mm \pm 3mm), the FOV is 4.1 mm x 4.1 mm (naturally square due to optics/CCD arrangement). This equates to a scale of 4 μ m pixel⁻¹.

The Qualification Model (QM) of the Beagle 2 microscope was used as a flight-ready example of a deployable instrument for field microscopy (Figure 2.3). No external light sources were required since the instrument uses its own array of switchable LEDs (B2MIC\$RGB and B2MIC\$UV).

All microscopic imaging was performed within a dark enclosure to eliminate stray environmental light. To emulate *in situ* microscopic operations at the planetary surface (Pullan *et al.*, 2004), the microscope was mounted to a computer-controlled motorised stage (Figure C.1B) capable of precision movements with respect to the sample. Increments of 40 μ m were used, being equivalent to the depth of field of the instrument (see Section 2.3.1.3).

Specimens with high relief at this scale required up to 160 individual images for colour/UV compositing. Samples needed to be firmly secured to avoid any movement throughout the imaging process, which could, in some cases, last several hours. Once acquired, all images were fully calibrated (bias, dark current, flat field and alignment). No image cropping was necessary since the QM microscope had undergone full pre-flight calibration, and by virtue of the optical design, had a square footprint.

The Nuance multi-spectral camera was also equipped with an Edmunds Optics dual tube inspection head for additional microscopic imaging (NUVIS\$MIC10).

C.3 Analytical

C.3.1 X-Ray Fluorescence (XRF)

X-ray fluorescence is concerned with the emission of characteristic secondary (i.e. fluorescent) X-rays from a material that has been bombarded with energetic photons or particles (Schlotz and Uhlig, 2006). High energy X-rays or γ -rays impinging on the atomic structure of a material can induce ionisation (through photoelectric absorption) and result in the ejection of electrons from K-, L- or M-shell orbits. The loss of an electron causes instability within the atom which is rectified by an electron of a higher orbit filling the vacancy created at a lower orbit. A photon is emitted as a consequence of this state transition the energy of which is equal to the difference in energies between orbits. A number of transitions are possible, for example L-shell electrons replacing K-shell electrons are called $K\alpha$ transitions and M-shell electrons replacing K-shell electrons are called $K\beta$ transitions. Similar transitions between L- and N-shells result in $L\alpha$ and $L\beta$ transitions. The characteristics of the fluorescent X-rays are unique to each element (Table 1 in Thompson and Vaughan, 2001) and are governed by Moseley's Law (Moseley, 1913) which relates wavelength (λ) to atomic number (Z) as:

$$\lambda^{-1} = k \cdot (Z - \sigma)^2 \tag{C.1}$$

where k and σ are constants particular to the transition line and electron shell respectively.

In energy dispersive XRF (EDXRF) systems photons fall directly onto a detector such as a Si-PiN diode which outputs a pulsed voltage that is proportional to the input photon energy. This signal is processed by a Multichannel Analyser (MCA) that constructs an energy spectrum in the form of a histogram. In wavelength dispersive XRF (WDXRF) system secondary photons are separated by diffraction (see Section C.3.4) before reaching the detector (i.e. a scintillation counter). Different crystals such as Ge-111 or LiF-220 are used to allow a wide range of elements to be determined (see Section 1.8 in Schlotz and Uhlig, 2006).

The concentration of elements in a sample is derived from the intensities of the fluorescing X-rays (Potts, 1987). For geological specimens quantitative analysis is complicated by matrix effects whereby the incident X-rays or the secondary X-rays are attenuated by other elements in the sample. In some cases secondary fluorescence can also occur where fluorescing X-rays emitted from one element excite atoms of another. Accuracy is determined using reference materials or “geostandards” in the form of homogeneous powders with elemental compositions known to a high level of accuracy (Potts *et al.*, 1992).

In place of the Beagle 2 FS-XRS, the studies employed a TN Technologies Spectrace 9000 commercial EDXRF spectrometer (TN9K\$) designed for field use (Figure C.5), which utilizes the same excitation method as the Beagle 2 system (^{55}Fe and ^{109}Cd) plus ^{241}Am (Potts *et al.*, 1995; Ramsey *et al.*, 1995). The ^{241}Am source is used to excite the K-lines of higher Z elements rather than the L-lines as would normally be the case with conventional X-ray tube based instruments (Potts *et al.*, 1995). The TN9000 had previously been used to conduct an analytical performance comparison with the Beagle 2 XRS (Talboys *et al.*, 2006).

The TN9000 is designed for terrestrial applications and uses an HgI_2 detector (resolution 260 eV at Mn-K α). Useful elements determined with this spectrometer include K, Ca, Ti, Mn, Fe, Sr, Zr, Mo, Pb, Rb, and Ba, plus Cu, Ni, Zn, and As if these are present in relative abundance (>100 ppm). The XRS is designed specifically for Mars and uses a Si-PiN diode detector (resolution 390 eV at Mn-K α for the FS-XRS and 340 eV for the flight model). Useful elements determined by the FS-XRS are Mg, Al, Si, K, Ca, Ti, Fe, Rb, Sr, Y, and Zr (Talboys *et al.*, 2006).

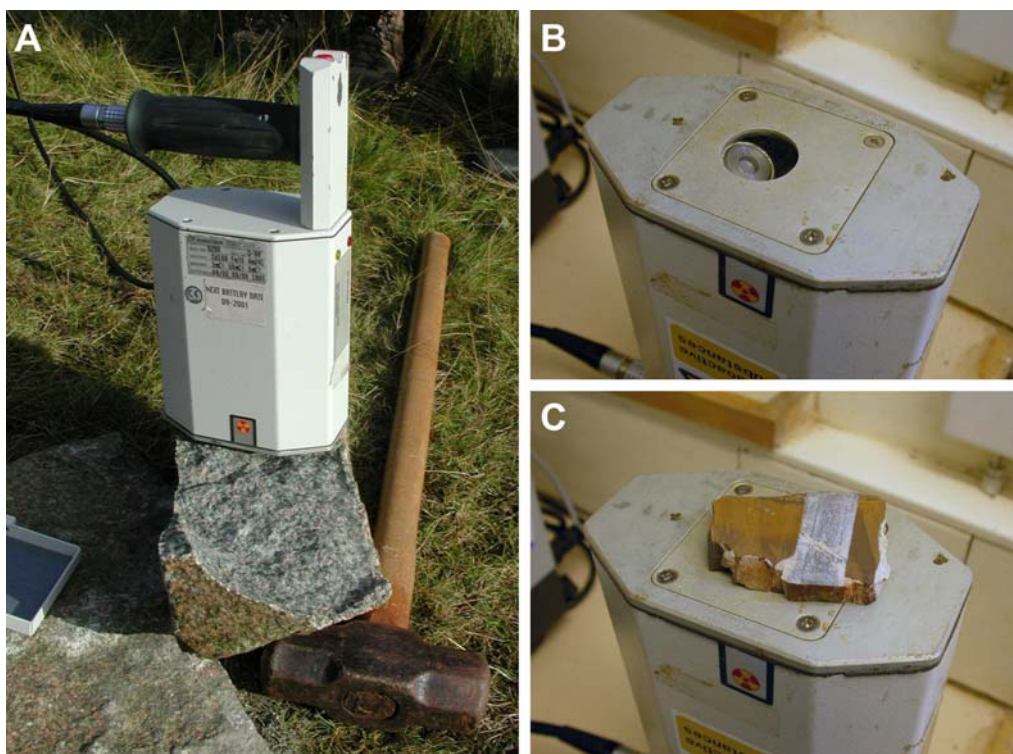


Figure C.5 TN Technologies Spectrace 9000 portable X-Ray spectrometer (TN9K\$). Early field trials at Markfield Quarry, Leicestershire demonstrated the practicalities of field measurement (A). For the experimental work described in Chapter 5, the instrument was configured upside down (B) and study samples placed over the aperture (C).

Clearly, the excitation methods used by the TN9000 does not allow for all major elements to be determined, especially Si and Mg. This is a serious limitation since most of the study samples are either siliceous sediments or Mg-carbonates. In order to complete the elemental coverage necessary for effective *in situ* field geochemistry, and thus emulate the capability of current space technology (i.e., MER APXS plus Beagle 2 XRS), a PANalytical Axios Advanced laboratory WDXRF spectrometer (AXIOSS) was used on smaller examples of the study specimens. Most samples could be accommodated in holders with a 26 mm diameter aperture, thus representing the measurement footprint of the MER APXS (25 mm \varnothing FOV) or the Beagle 2 XRS (22 mm \varnothing FOV). A few specimens were too small and required holders with a 6 mm diameter aperture instead.

Measurements made with the TN9000 were more straightforward. The instrument was configured vertically with the ~25 mm window facing upward (Figure C.5C). Samples were presented face down over this aperture for the duration of the measurements (100 s).

Bulk geochemistry was also determined by laboratory WDXRF in order to set a benchmark of elemental concentrations prior to the field-representative measurements. Bulk data are not necessarily representative of field data since there is no discrimination between surface coatings, fresh material, weathered surfaces, and other heterogeneities. Nevertheless bulk data provide a handle on what elements are present. Where sufficient sample material was available, standard methods were used to prepare fusion beads and pressed powder pellets (Watson, 1996 and Figure A.4), for the determination of major and trace element composition respectively. In the absence of fusion beads, major element concentrations were determined from pressed powder pellets. This work was undertaken within the Department of Geology at the University of Leicester. XRF data were obtained using a Philips PW1400 X-Ray Fluorescence spectrometer (PW1K4S) operating a 3 kW Rhodium (Rh) anode side window X-Ray tube powered by a standard Philips PW 1730 series generator. Detection limits achieved were typically 0.01 % yielding precisions of 1 % for concentrations greater than 10 ppm (Nick Marsh, Geology Department, University of Leicester, personal communication). For the trace elements of interest to this study, the detection limits were better than 3 ppm (8 ppm for Ba). Concentrations of less than 10 ppm were generally precise to 10 or 20 %.

All *in situ* XRF data analysis involved a number of steps. Data acquired with the TN9000 were corrected using elemental calibration curves based on geostandards (i.e., measured versus recommended linear trend lines). A broad range of recommended values were available (courtesy Dr. Phil Potts, Open University) for K, Ca, Fe, Zr, Sr, and Ba, whereas Mn, Cu, Zn, Mo, Pb, and Rb did not have such good spread (see Figure 2 in Potts *et al.*, 1995). Nevertheless, usable trend lines were determined for all these elements. Unfortunately, no calibration data were available for Ni or As so a 1:1 relationship had to be assumed. Depending on the samples, standard loss corrections for sulphates (80 %) and carbonates (50 %) were also applied following calibration. Concentration errors (3σ standard deviation) for each element were subsequently determined using the Horwitz function which relates the concentration to the relative standard deviation of reproducibility (RSDR) (see Glossary and Thompson, 2004).

Data acquired with the PANalytical Axios Advanced WDXRF spectrometer on unprepared (i.e., field representative) samples, were examined for each of the ten scans across the entire range of interest to this study (Mg to Ba). Peaks not automatically recognised by the scan software were manually assigned with the aid of an in-built database of elements and X-ray emission lines. Sulphates and carbonates were normalised as previously described. Major and trace element

concentrations were then determined using the in-built software. Concentration errors (3σ standard deviation) for each element were subsequently derived from counting statistics (based on the number of counts reported by the software for each peak assignment).

C.3.2 Raman Spectroscopy

Raman spectroscopy is a form of vibrational spectroscopy (Lewis, 2001). Photons from a beam of light impinging on a sample are absorbed by the material and subsequently scattered. Scattering is the result of photonic emissions from electrons returning from a higher virtual energy state following excitation by incident photons. The vast majority of scattered photons have the same wavelength as the incident radiation (Rayleigh “elastic” scattering). However, a tiny proportion of photons (1 in 10^7) undergo a wavelength shift (Raman “inelastic” scattering). Most of these Raman scattered photons are shifted to longer wavelengths (Stokes shift) since at any given time, electrons are more likely to be at the lowest virtual energy state (at least for the more common temperature ranges). A small proportion of Raman scattered photons however are shifted to shorter wavelengths (anti-Stokes shift) when electrons return to a lower state following excitation.

A Raman spectrum is a plot of intensity of Raman scattered radiation as a function of wavelength difference, or Raman shift, expressed as a wavenumber (cm^{-1}). Raman spectra are thus independent of the frequency of incident radiation. However, in some applications it may be advantageous to avoid certain wavelengths where adverse effects may arise such as induced fluorescence in the material.

Raman spectroscopy exhibits high specificity since the method detects fundamental molecular vibrations. In other words, peaks (bands) in a Raman spectrum are non-overlapping. The spectral range of Raman spectroscopy covers approximately the same information rich portion of the mid-IR spectrum (400 nm to 4000 nm). Although signals are weak compared to IR spectroscopy, signal to noise ratios are particularly high. The technique requires no special sample preparation and is entirely non-destructive (assuming experimental precautions are observed). Data acquisition times are typically short (seconds to minutes).

The Raman technique is sensitive to both organic and inorganic components of a heterogeneous system. This makes it an invaluable method for identifying biological markers and determining

mineralogical composition. Measurements can be performed without physical contact with the target, and irregular surfaces or polished surfaces (i.e. core samples) are equally suitable for spectral analysis. Raman is therefore particularly useful for *in situ* applications involving natural geological specimens or exposures.

As mentioned previously, the wavelength of incident light (usually provided by a laser) is an important consideration for Raman spectroscopy. Induced fluorescence emission from the material can dominate the weaker Raman signal so choice of wavelength is dependent on the target being analysed and the application. For example, in the context of this work, 785 nm excitation provides a good balance between organic and inorganic constituents of rocks, but 514 nm excitation is particularly effective for identifying photosynthetic pigments such as carotene, even in small concentration.

Another important parameter for Raman spectroscopy is spectral resolution. Laboratory-based Raman spectrometers are currently highly specified in terms of spectral resolution (typically 4 cm^{-1}), but miniaturised systems for field use are inevitably compromised (typically 8 cm^{-1}). With reduced spectral resolution, overlapping bands become increasingly difficult to discriminate resulting in potentially erroneous identification of compounds.

Standard wavenumber reference tables and spectral databases used with existing laboratory systems for compound identification (i.e., <http://rruff.info/>) are not appropriate for planetary Raman instrumentation (Edwards *et al.*, 2004). A more appropriate approach is to utilise data compiled from analogue studies with geological specimens containing molecular biosignatures (Jorge Villar *et al.*, 2003).

Raman spectroscopy has long been advocated as a technique for *in situ* planetary exploration (Israel *et al.*, 1997; Wynn-Williams and Edwards, 2000; Tarcea *et al.*, 2002; Ellery and Wynn-Williams, 2003; Sharma *et al.*, 2003; Wang *et al.*, 2003; Edwards *et al.*, 2005a; Jorge Villar and Edwards, 2006). A Raman instrument is proposed for the ExoMars mission in 2016 (see Section 2.3.2.2).

A portable Raman spectrometer designed for field use was not available for this work but is being planned to be incorporated into follow-on studies (see Chapter 7). Standard laboratory instruments were therefore used for all *in situ* Raman measurements on the study samples.

A Bruker IFS66 IR spectrometer with FRA 106 Raman module and an Nd³⁺:YAG laser operating at 1064 nm was used in conjunction with a Raman non-confocal microscope fitted with a 40X objective (UBRAM\$40X\$1064). This configuration provided a sample footprint of approximately 20 µm diameter. Spectra were recorded between 50 and 3500 cm⁻¹ in increments of 4 cm⁻¹. In addition, a Renishaw *InVia* confocal Raman microscope operating at 514 nm (UBRAM\$50X\$514) and 785 nm (UBRAM\$50X\$785) was used with a 50X objective, which results in a smaller target footprint of 2 µm diameter. Typical laser power ranged between 0.5 mW and 50 mW.

Raman data were analysed in collaboration with colleagues from the Department of Chemical and Forensic Sciences at the University of Bradford. In addition, access was also provided to an unpublished Raman database of geobiological organic signatures compiled by Dr. Susana Jorge Villar at the University of Burgos in Spain.

C.3.3 Mössbauer spectroscopy

Mössbauer Spectroscopy is concerned with the recoilless emission and resonant absorption of γ -rays by certain nuclei in solid materials (Greenwood and Gibb, 1971). Iron Mössbauer Spectroscopy is specifically concerned with Fe-bearing materials and is the most studied example in this type of γ -ray spectroscopy, and the most relevant to this work.

⁵⁷Co decays by electron capture to the second excited state of ⁵⁷Fe at 136.4 keV with ~99.8% probability. This second excited state of ⁵⁷Fe subsequently decays to the first excited state at 122.0 keV with ~91% probability, or the ground state with ~9% probability. The first excited state rapidly decays to the ground state mostly by electron conversion and the emission of a ~6.4 keV X-ray, but importantly for the Mössbauer effect, also decays to the ground state (with 10% probability) by emission of a 14.4 keV γ -ray.

Resonance is achieved by modulating the γ -ray excitation beam (i.e., ⁵⁷Co source) with respect to the sample. The resulting Mössbauer spectrum is the relative number of γ -rays per second scattered back from the absorbing sample as a function of the relative velocity of the source. The nuclear energy structure of the absorber (i.e., rock) usually differs from the ⁵⁷Co source due to oxidation state, chemical makeup, and magnetic properties of the target. Iron phase and oxidation

states can be determined from peak locations in the spectrum and concentration can be derived from peak areas.

Iron is abundant at the surface of Mars (Knudsen 1989; Knudsen *et al.*, 1990, 1992; Rieder *et al.*, 1997). Mossbauer Spectroscopy cannot determine the total amount of iron in a sample relative to other elements but in recent years the technique has contributed much to our understanding of the properties of martian rocks and soils (Morris *et al.*, 2004, 2006; Klingelhöfer *et al.*, 2004).

The Beagle 2 QM Mössbauer spectrometer (B2MBSS) (Klingelhöfer *et al.*, 2003) was used to determine Fe-bearing mineralogy and Fe oxidation states for most of the study samples (Figure C.6). The instrument is located at the University of Mainz, Germany, where it has been used extensively to support the NASA Mars Exploration Rovers mission since 2003 (Schröder *et al.*, 2004).



Figure C.6 Beagle 2 Qualification Model (QM) Mössbauer sensor head (B2MBSS) in contact with test sample (not a GSPARC specimen). This configuration (backscatter mode) was used for all laboratory measurements. Sample is ~7 cm across. Courtesy Dr. Christian Schröder, NASA JSC.

Many of the study samples are depleted in, or devoid of, Fe-bearing minerals. However, flight heritage, synergy with other techniques such as XRF/XRD, and consistency within the overall analogue programme make it important to include the Mössbauer technique. As will be seen, samples that appear visually and spectrally oxidised, yet yield null Mössbauer spectra, can

benefit from measurement.

Study samples were shipped to the University of Mainz with required targets clearly defined. Data acquisition and reduction was performed by Dr. Christian Schröder (NASA JSC) using software designed for analysis of MER data.

C.3.4 X-Ray Diffraction (XRD)

X-ray diffraction is concerned with the constructive interference of incident monochromatic X-rays and a crystalline lattice (Bragg, 1914). Constructive interference (and diffraction of the incident beam) occurs when Bragg's Law is satisfied:

$$n \cdot \lambda = 2d \cdot \sin\theta \qquad \text{C.2}$$

where n is the reflection order

Knowing the wavelength of the incident beam (λ) and by measuring the angle at which diffraction occurs (2θ), one can determine d , the spacing (in Å) between the planes in the atomic lattice of the sample being measured. All minerals are characterised by a unique set of d -spacings and by comparing the observed d -spacings with standard reference data (i.e. <http://rruff.info/>) one can identify the mineral species present.

For laboratory XRD the incident beam is usually generated by an X-ray tube (i.e. a source of electrons and a target to bombard them onto). A crystal filter is used to produce a monochromatic beam. Copper is commonly used for the target material to emit Cu-K α radiation ($\lambda = 0.5418 \text{ \AA}$). The collimated X-ray beam is directed at the sample to be measured and the intensity of reflected X-rays recorded at different angles by a detector (such as a proportional counter). The sample is rotated with respect to the X-ray beam by θ while the detector rotates by 2θ . This geometry is achieved using a goniometer.

Samples are usually prepared as homogenised powders so that all crystallographic planes are represented and diffracted by the incident X-rays. Some instruments are capable of analysing unprepared samples and rely on spinning the specimen about 3 axes in order to orientate all the

crystallographic planes (see Section C.3.4.1). Whatever measurement technique is used mineral identification is usually determined on the basis of several peaks with different d-spacings.

In situ determination of mineralogy by XRD of some of the study samples was made using a laboratory instrument located at the Natural History Museum, London (NHMXRD\$) (Figure C.7). The instrument records data from small areas ($< \text{mm}^2$) of unprepared samples by way of an INEL 120° curved Position Sensitive Detector (PSD) (see X-ray detectors page at <http://inel-xrd.com/>). The PSD has an output array of 4096 digital channels and permits the simultaneous measurement of diffracted X-ray intensities at all angles of 2θ across 120° with a static beam-sample-detector geometry.

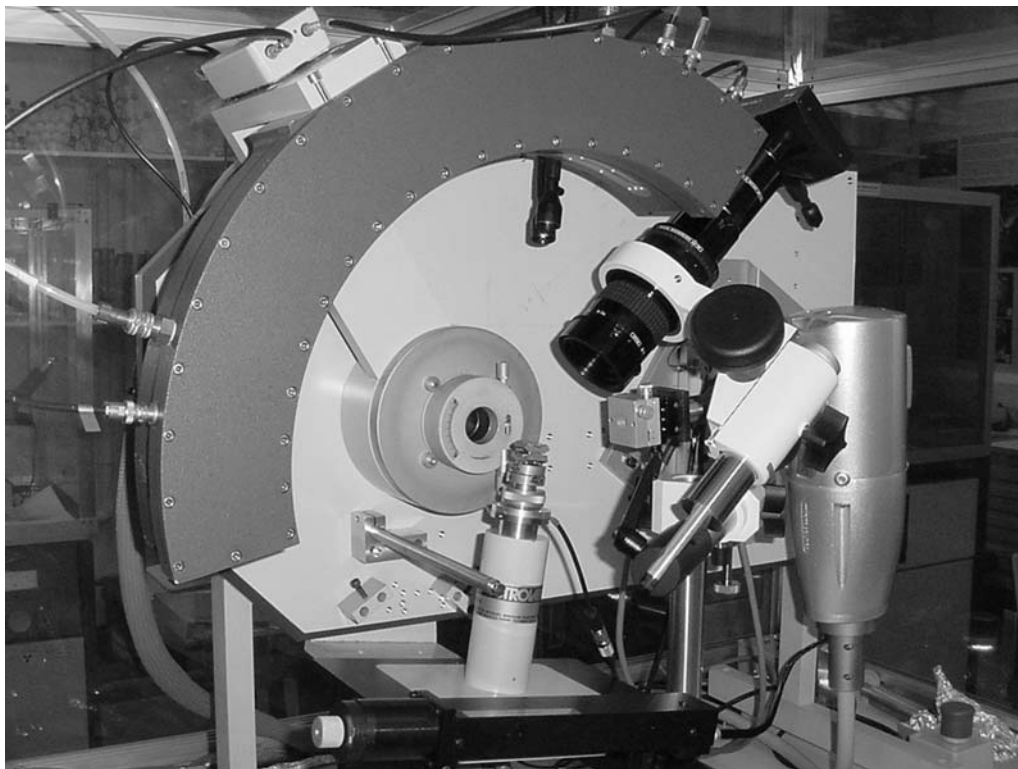


Figure C.7 Laboratory X-Ray Diffractometer (NHMXRD\$) used for *in situ* analysis of natural (unprepared) specimens. Thumbnail sized samples are secured on a spinning triaxial stage (foreground centre). High brightness Cu-K α radiation is generated by a Microsource® (right) and the beam restricted to a micro-area ($< \text{mm}^2$) on the target sample (see Figure 5.5B). A CCD camera (top right) images the same micro-area. The curved Position Sensitive Detector (PSD) (top left) has an arc of 120° 2θ for simultaneous measurement across the range. Courtesy Dr. Gordon Cressey, Natural History Museum, London.

A Microsource[®] is employed to generate high brightness Cu-K α radiation and horizontal and vertical slits are used to restrict the beam to a chosen size appropriate to the dimensions of the micro-area selected on the solid sample; the micro-area on the sample is viewed with a CCD image capture system, and the whole sample is manipulated by a triaxial stage. The limited focus depth of field of the optical system is used to bring the sample to the correct height to be intercepted by the X-ray beam, whose position is predetermined by way of a fluorescent screen with a fiducial mark in focus at the point where the beam is also in focus on the screen. In this mode, microdiffraction experiments are performed *in situ*, without destructive sampling. Measurements are made in reflection geometry. Data collection times are only a few minutes for each sample, and the angular range recorded is 4° to 120° 2 θ .

For this work, thumbnail fragments of some of the study specimens were prepared and secured to the spinning triaxial stage located at the beam focus. Where appropriate, witness images were acquired of the specimens showing the beam footprint with respect to the surfaces being measured. Such an example is shown in Figure 5.5B.

Standard laboratory X-ray diffraction was also performed on homogenised powders previously prepared for XRF (or smaller quantities of material if these did not exist) using a Philips PW1010 diffractometer (PW1010\$) within the Department of Geology at the University of Leicester. A long fine focus X-ray tube, fitted with a Ni filter, was used to generate Cu-K α radiation at 40 kV (30 mA). A step size of 0.02° 2 θ was used over a scan range of 4° to 64° 2 θ at 1° 2 θ min⁻¹. All XRD data were analysed using peak fitting software CrystalSleuth (available from <http://rruff.info/>), and international standard d-spacing reference tables (Bayliss *et al.*, 1986).

The NHM system was chosen for this work in order to compare the results of *in situ* XRD with powder diffraction methods. Both ExoMars and MSL will analyse prepared powders by XRD (see Table 2.6). Since many geological materials are mineralogically heterogeneous and the quantity of material available for analysis is likely to be small (see Table 2.5), it is important for planetary fieldwork to know whether the lack of spatial content in the case of powder diffraction is an issue.

C.4 Geotechnics

Due to the paucity of study sample material available for destructive testing, no *in situ* preparation method was employed as an integral part of either the morphological biosignature study or relict sedimentary structure study. However, geotechnics is an important consideration in the context of planetary field work. As discussed in Section 2.3.3, tools provide a means of sample acquisition (Richter *et al.*, 2002; Pullan *et al.*, 2004) and surface preparation (Gorevan *et al.*, 2003b). Apart from these primary functions, physical property data can help identify rocks and soils and determine preservation state (Richter *et al.*, 2002; Arvidson *et al.*, 2004a; Arvidson *et al.*, 2004b). Grinders and samplers are inherently destructive devices that would likely destroy any morphological biosignature preserved as an endolith or relict structure inside a rock (Figure C.8A). Splitting a rock with a hammer, a tried and tested technique used by every field geologist, would be a more appropriate method of sample preparation, especially for *in situ* astrobiology (Figure C.8CD).

Ideally, geotechnical elements of a payload would consist of a hammer, a grinder and a rock/soil sampler or some device that is capable of performing all these functions (Figure C.8B). For this work, it was assumed that this was the case, and targets were presented in formats that would have been available to the field geologist (i.e., fresh, weathered, and abraded surfaces).

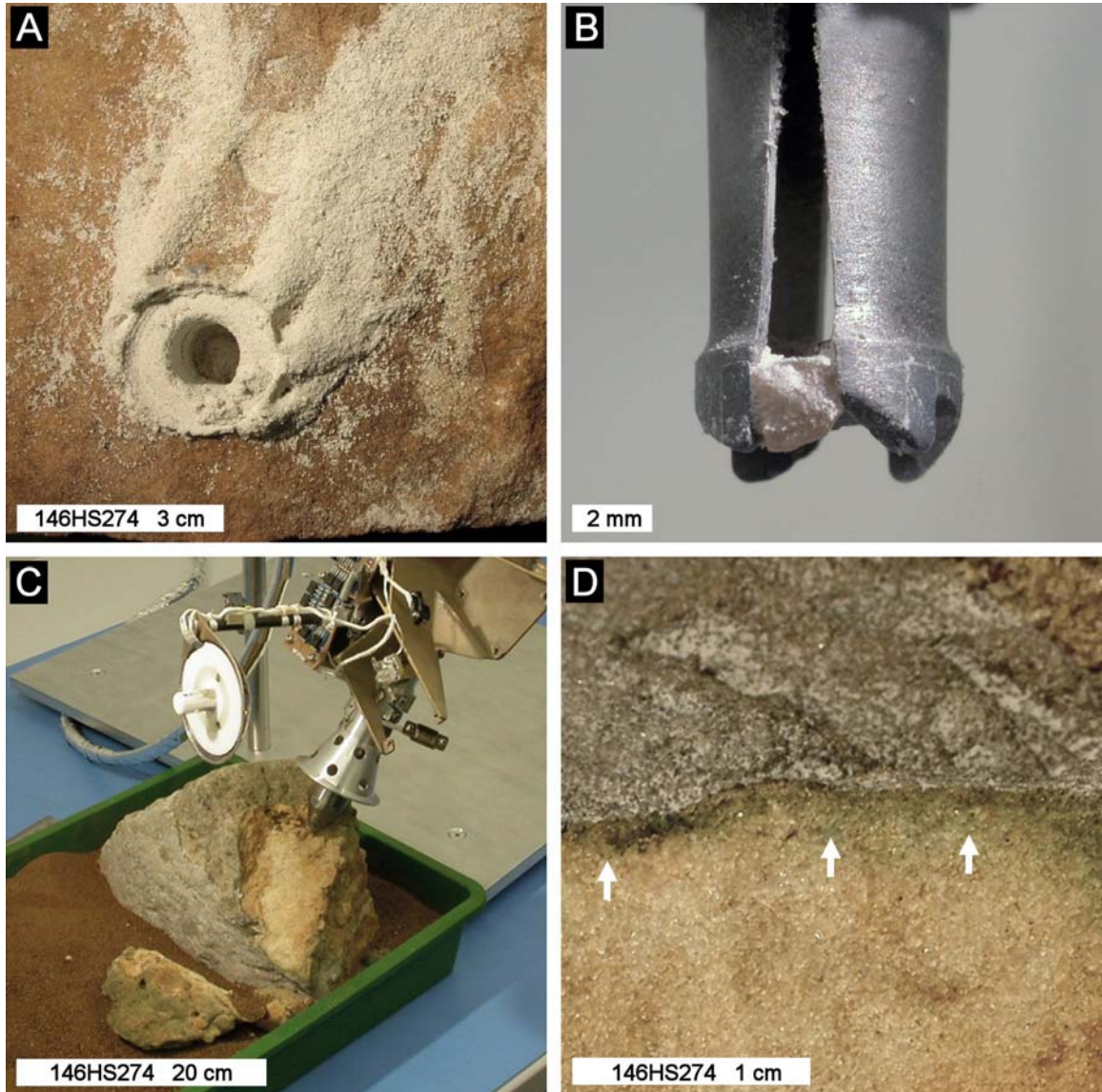


Figure C.8 *In situ* coring and rock splitting of sample 146HS274, an orthoquartzite from Montana, USA, with similar physical and geobiological properties to Beacon Sandstone from Antarctica (see Section B.5). Sampling experiments with the Beagle 2 rock corer (A) (B2RCG\$CORE) destroyed all morphological evidence of life and distributed any potential biomarkers within the extruded debris. In addition, the corer had a tendency to jam open when used on clastic rocks, rendering the tool useless (B). Splitting the rock (C) with the Beagle 2 soil sampler (B2PLUTO\$SPLIT) proved more effective in revealing the cryptoendolithic biosignatures (D).

Glossary of Terms and Acronyms

AFL	Astrobiology Field Laboratory
AMASE	Arctic Mars Analog Svalbard Expedition
Amazonian	Martian epoch ~1.8 Ga to present according to an established chronological scheme based on crater density analysis. Characterised by late stage volcanism including development of Olympus Mons.
APS	Active Pixel Sensor
APXS	Alpha Proton X-ray Spectrometer (on MFP) or Alpha Particle X-ray Spectrometer (on MER)
ARM	Anthropomorphic Robotic Manipulator. Robotic arm on Beagle 2.
ARS	Autonomous Robot Scientist. See Chapter 6.
ASP.NET	Environment for developing dynamic web pages using Active Server Pages and the .NET programming language.
BAS	British Antarctic Survey
Bayesian network	A graphical model representing a set a variables and their probabilistic inter-dependencies. For example, a Bayesian network could represent the probabilistic relationships between indicators of life and mineralogy, trace element chemistry and structural geometry. Given these observations, the network can be used to compute the probabilities of the presence of life.
Bayesian probability	Probability based on “state of knowledge”. Objectivist Bayesian probability is justified on the basis of rationality and consistency. Used in machine learning. See Bayesian network
Beta-carotene	$C_{40}H_{56}$. Orange pigment important for photosynthesis. This is the most common form of carotene having β -rings at both ends.
BGS	British Geological Survey
B_hf	Hyperfine field value (Mössbauer spectroscopy). Splitting of excited and ground state energy levels as a result of an internal or external magnetic field produces a sextet spectrum. B_hf is measured between the two end peaks of the sextet and expressed in

	Tesla (T)
BIF	Banded Iron Formation
Bioherm	A mound-like mass of rock built by sedentary organisms such as colonial corals or calcareous algae.
Ca-oxalate monohydrate	Metabolic by-product of the reaction between oxalic acid and calcareous material within rocks
CCD	Charge Coupled Device
ChemCam	Remote sensing instrument on MSL. See Section 2.3.1.1.
Chlorophyll	$C_{55}H_{72}O_5N_4Mg$. Blue-green-yellow pigment compound important for photosynthesis. Characteristic absorption bands for chlorophyll-a (blue-green) are at 400-450 nm and 650-700 nm, and for chlorophyll-b (yellow-green) at 450-500 nm and 600-650 nm.
<i>Chroococcidiopsis</i>	A genus of cyanobacterium of order <i>Pleurocapsales</i> , characterised by its desiccation resistant and radiation resistant properties
CLUPI	Close Up Imager
CNRS	Centre National de la Recherche Scientifique (Orléans, France)
c-phycocyanin	$C_{36}H_{38}O_6N_4$. Water soluble accessory pigment to chlorophyll which characteristically aggregates into clusters in order to adhere to the membrane. Absorbs orange and red light at 620 nm and fluoresces at 650 nm.
CREST	Collaborative Research in Exploration Systems and Technology
CW	Continuous Wave (pertaining to lasers)
DEM	Digital Elevation Model. Mathematical or virtual context. See DTM.
DLR	Deutsches Zentrum für Luft- und Raumfahrt (German Aerospace Centre)
DOF	Depth of Field (optics) or Degrees of Freedom (robotics)
DP	Decision Point
DM	Development Model
DTM	Digital Terrain Model. Physical, natural world context. See DEM.
EDXRF	Energy Dispersive X-Ray Fluorescence
Engineering autonomy	Autonomous operations concerned with the prescribed aspects of navigation, instrument deployment and placement, sample acquisition, sample processing, instrument control etc.

EPS	Extracellular Polymeric Substances
Erg	Sand sea. Large aeolian dune field.
EVA	Extra Vehicular Activity (“Moon walk”).
Facies	<i>In sedimentology</i> : The sum total of features such as sedimentary rock type, mineralogy, sedimentary structures, fossils etc. which characterise a sediment as having been deposited in a given environment. The term microfacies expresses small spatially scaled facies less than 1 m.
Flaser-linsen	Lenticular bedding structures. Flaser refers to mud infilled troughs preserved in sandy sediment, whereas linsen structures are sand ripples isolated in muddy sediment. Both are characteristic of shallow tidal flow regimes. See Figure B.17C, Figure 5.34 and Figure 6.3.
Flintag	An industrial powdered aggregate comprised of angular grains of crushed and dried blue flint. Rheologically similar to cement powder. GSPARC example is 189LP398.
FM	Flight Model
FOV	Field Of View
GAP	Gas Analysis Package. Isotopic chemistry experiment on Beagle 2.
GCMS	Gas Chromatograph and Mass Spectrometer
<i>Gloeocapsa alpina</i>	Species of genus <i>Gloeocapsa</i> , a cyanobacterium of the order <i>Chroococcales</i> .
GPR	Ground Penetrating Radar. Geophysics instrument on ExoMars.
Greenschist facies	A metamorphic facies of low-grade regional metamorphism of moderate pressure (~0.3 GPa to ~0.6 GPa) and moderate temperature (~300 °C to ~500 °C) in which the primary minerals of basic rocks are replaced by albite, epidote, chlorite and actinolite.
GSPARC	Geological SPecimen ARChive. See Chapter 3 and Appendix A.
GSWA	Geological Survey of Western Australia
Gypsiferous	Containing gypsum
Gypsum	Hydrous calcium sulphate (CaSO ₄ ·2H ₂ O). Evaporite.
Hesperian	Martian epoch ~3.5 Ga to ~1.8 Ga according to an established chronological scheme based on crater density analysis.

	Characterised by extrusive volcanism and development of extensive lava plains.
HiRise	High Resolution Imaging Science Experiment. Camera system on MRO with 30 cm resolution.
Horwitz function	The relationship between the analysed concentration of an element and the relative standard deviation of repeatability (RSDR) (Thompson, 2004). Mathematically the function can be expressed as $\sigma_H = 0.02C_i^{0.8495}$ where σ_H is the standard deviation (g/g) and C_i is the concentration of element (g/g). For error analysis the Horwitz function can be expressed as RSDR :-
	$\text{RSDR}(\%) = 2C_i^{-0.1505} \qquad \text{G.1}$
HPGP	Hydrogen Peroxide (H ₂ O ₂) Gas Plasma. A common technique used in medicine for sterilising surgical instruments.
HRC	High Resolution Camera. Part of the PanCam system for ExoMars.
Hydromuscovite	An altered muscovite in which K has been leached out. Also known as Illite.
IDD	Instrument Deployment Device. Robotic arm on MER.
IMP	Imager for Mars Pathfinder
IPA	Isopropanol Alcohol. Cleaning agent commonly used on space hardware. Also used to sterilise components where other techniques such as HPGP or heat treatment may not be appropriate.
IR	Infra Red
IS	Isomer Shift (Mössbauer spectroscopy). A measure of the energy difference between the source and the absorber transition. Provides information on the character of chemical bonds such as valence and covalence. IS is measured between the peak and zero velocity and expressed in mm s ⁻¹ .
JPL	Jet Propulsion Laboratory (Pasadena, California, USA)
JSC	Johnson Space Center (Houston, Texas, USA)
LCTF	Liquid Crystal Tunable Filter
LIBS	Laser Induced Breakdown Spectrometer. Part of the <i>in situ</i> and laboratory payload on ExoMars.

LLD	Lower Limit of Detection
LMC	Life Marker Chip. Assay-based biomarker instrument on ExoMars.
LUT	Look Up Table
Lyot filter	Type of optical filter that uses birefringence (i.e., double refraction) to produce a narrow pass band of transmitted wavelengths. A complete filter is made up of alternating polarisers and birefringent plates (each plate being half the thickness of the previous one). The relative phase delay between the two polarisation components of light passing through each stage of the filter are wavelength dependent. Tuning is achieved by rotating each element with respect to its “entrance” polariser. The narrowness of the transmission peak exiting the final polariser in the Lyot stack is dependent on the number of plates used (i.e. the thickness of the thinnest element). Electrically tunable filters utilise liquid crystals for the birefringent elements as in the case of the Nuance imaging system described in Section C.2.1.
MA_MISS	Mars Multi-spectral Imager for Subsurface Studies. IR spectrometer associated with the ExoMars drill system.
Macroscopic	Operational working distance for close-up activities in <i>in situ</i> robotic field geology. Approximately 10 cm between observer and target. May require physical contact to establish correct standoff distance. Analogous to a human geologist examining a hand specimen with the naked eye (i.e., FOV $\sim 5 \text{ cm}^2$ and features $> 100 \mu\text{m}$). See also remote, proximal and microscopic.
MAHLI	Mars Hand Lens Imager. Close-up and microscopic imager on MSL.
MARTE	Mars Astrobiology Research and Technology Experiment
MBS	Mössbauer Spectrometer. Instrument to identify Fe-bearing minerals on MER, Beagle 2 and ExoMars.
MCA	Multi-Channel Analyser
MDI	Multiple Document Interface. See SDI.
MER	Mars Exploration Rover
MI	Microscopic Imager. Close-up imager on MER.
Microfacies	See facies.

Microscopic	Operational working distance for microscopic activities in <i>in situ</i> robotic field geology. Approximately 1 cm between observer and target. Usually requires physical contact to establish correct standoff distance. Analogous to human geologist examining a hand specimen with a high power field lens (i.e., FOV ~5 mm ² and features < 100 μm). See also remote, proximal and macroscopic.
MIMA	Martian Infra-Red Mapper. Remote sensing instrument on ExoMars.
MIMOS	Miniature Mössbauer Spectrometer
Mini-TES	Miniature Thermal Infrared Spectrometer. Remote sensing instrument on MER.
MOD	Mars Organic Detector. Part of Urey experiment on ExoMars.
MOI	Mars Oxidant Instrument. Part of Urey experiment on ExoMars.
MOM	Mars Origins Mission
MOMA	Mars Organic Molecule Analyser. Part of the analytical laboratory on ExoMars.
MRO	Mars Reconnaissance Orbiter
MSL	Mars Science Laboratory
MSSL	Mullard Space Science Laboratory
MSR	Mars Sample Return
Nd ³⁺ :YAG	Neodymium-doped Yttrium Aluminium Garnet (Y ₃ Al ₅ O ₁₂).
NHM	Natural History Museum (London)
NIR	Near Infra Red
NMBE	Natural History Museum (Bern, Switzerland)
Noachian	Martian epoch ~4.6 Ga to ~3.5 Ga according to an established chronological scheme based on crater density analysis. Characterised by development of the Tharsis bulge and catastrophic flooding towards the end of the epoch.
<i>Nostoc commune</i>	Species of genus <i>Nostoc</i> , of the order <i>Nostocales</i> , a fresh water cyanobacterium characterized by spherical colonies of filaments of moniliform cells in a gelatinous sheath.
NSC	National Space Centre (Leicester, UK)
OMEGA	Observatoire pour la Minéralogie, l'Eau, les Glaces, et l'Activité. VNIR spectrometer (500-5200 nm) on Mars Express.

Orthoquartzite	A clastic sedimentary rock composed almost entirely of detrital quartz grains
Oxalic acid	$\text{H}_2\text{C}_2\text{O}_4$. An organic acid $\sim 10^4$ stronger than acetic acid.
PAFS-net	Planetary Analogue Field Studies Network. See Chapter 3.
PAH	Polycyclic Aromatic Hydrocarbons. Chemical compounds consisting of fused aromatic rings. Have been observed in comets and meteorites.
PAT lab	Planetary Analogue Terrain laboratory at Aberystwyth University. See Chapter 6.
Parietin	$\text{C}_{16}\text{H}_{12}\text{O}_5$. Blue (UV) light protective pigment.
PanCam	Panoramic camera system for ExoMars. See WAC and HRC.
PAW	The deployable instrument package at the end of the ARM on Beagle 2 (Figure 2.3). Occasionally used as an acronym for Position Adjustable Workbench.
Phyllosilicate	Clay. Compound in which silicate atomic structures are arranged in sheets. Examples include talc and mica.
Phyllocian	Martian epoch ~ 4.6 Ga to ~ 4 Ga according to an alternative chronological scheme based on mineralogy (Bibring <i>et al.</i> , 2006a). Characterised by dominance of phyllosilicates and presence of alkaline water.
Pisolitic	Texture characterised by small, spherical, accretionary particles
Planetary Yard	A simulated planetary surface on which to conduct locomotion, navigation and science activities with robotic vehicles. Examples include the JPL Mars Yard and the PAT laboratory at Aberystwyth University (see Chapter 6).
PLUTO	Planetary Underground Tool. Soil sampling device on the Beagle 2 PAW (Figure 2.3).
Polymict	Comprised of more than one minerals or rock types
Porphyrin	Macromolecular pigment with distinctive ring structure that can bind a metal ion within it. Chlorophyll is a primary example comprising a central Mg ion.
Prehnite-pumpellyite facies	Metamorphic facies characterised by formation of prehnite, pumpellyite and quartz in basic igneous rocks under moderate pressure (~ 0.2 GPa to ~ 0.6 GPa) and low temperature (~ 150 °C to

	~300 °C), usually during burial metamorphism.
Proximal	Operational working distance for near-field activities in <i>in situ</i> robotic field geology. Typically ~1 m between observer and target or dictated by the reach of a robotic arm. For example, mast mounted panoramic cameras observing targets reachable by the arm would be conducting proximal imaging. Analogous to a human geologist scrutinising an exposure prior to close-up (macroscopic) examination. See also remote, macroscopic and microscopic.
PSA	Photosensor Array. Imaging detector system used on the Viking landers.
PSD	Position Sensitive Detector (instrumentation) or Particle Size Distribution (geology)
Pyrolysis	Chemical decomposition of organic materials by heating in the absence of oxygen or other reagents
QM	Qualification Model
QS	Quadrupole Splitting (Mössbauer spectroscopy). The spin of the excited state is invariably different from the ground state. This leads to one or more quadrupole moments interacting with local electric field gradients. The result is a doublet spectrum where QS is the peak separation and expressed in mm s^{-1} .
RAC	Robotic Arm Camera. Close-up imager on Phoenix.
RAT	Rock Abrasion Tool. Sample preparation device on MER (Figure 2.3).
RCG	Rock Corer Grinder. Sampling device on the Beagle 2 PAW (Figure 2.3)
Remote	Operational working distance for remote activities in <i>in situ</i> robotic field geology. Typically everything further away than the reach of a robotic arm (> 1 m). Analogous to a human geologist scrutinising the local terrain beyond physical reach. See also proximal, macroscopic and microscopic.
RMI	Remote Micro-Imager. Imaging device associated with ChemCam on MSL.
ROI	Region Of Interest

RSDR	Relative Standard Deviation of Reproducibility. See Horwitz function.
SAM	Sample Analysis at Mars. Instrument suite on MSL that includes a sample manipulation and processing facility, a GCMS and a tunable laser spectrometer.
SARA	Science Assessment and Response Agent
Scientific autonomy	Autonomous operations concerned with decision making based on on-board interpretation of data (visual, analytical, physical) using programmed scientific (geological) rule sets, contextual modelling and objective bias.
Scytonemin	$C_{36}H_{20}N_2O_4$. UV screening pigment found in many species of cyanobacteria.
SD	Standard Deviation
SDI	Single Document Interface. Application client form and all instantiated forms appear as independent windows. SDI is an alternative to MDI (Multiple Document Interface), an application environment based on a parent control form and child forms contained within it.
Serpentinization	The process of hydrothermal alteration by which Mg-rich silicate minerals (i.e., olivine, pyroxenes, and/or amphiboles in dunites, peridotites, and/or other ultramafic rocks) are converted into or replaced by serpentine minerals (i.e., antigorite, chrysotile and lizardite).
SFF	Subsurface Filamentous Fabric
Siderikan	Martian epoch ~3.5 Ga to present according to an alternative chronological scheme based on mineralogy (Bibring <i>et al.</i> , 2006a). Characterised by anhydrous ferric oxides, no (or insignificant) water, no (or insignificant) volcanism.
Sinter	Smooth incrustation as a result of precipitation by fluids rich in Si (siliceous sinter) or $CaCO_3$ (calcareous sinter).
Si-PiN	Silicon PiN diode. Photons entering the intrinsic region (i) free charge carriers. Under reverse bias conditions, photons will therefore induce current flow.
SNC	Shergottites Nakhilites Chassignites. Class of meteorites generally

thought to have originated from Mars. Shergottites resemble terrestrial dolerites in terms of texture and mineralogy. Two sub-classes are recognised, basaltic shergottites (resembling terrestrial basalts) and lherzolitic shergottites (resembling terrestrial lherzolites and harzburgites). Nakhilites resemble terrestrial clinopyroxenites and wehrlites. Shock metamorphism is not evident since maskelynite is totally absent. Cumulus augite ($\text{En}_{38}\text{Fs}_{23}\text{Wo}_{39}$) predominates, but minor coarse-grained cumulus olivine (Fa_{65-67}) is also present. Chassignites resemble terrestrial dunites consisting mainly of homogenous fayalitic olivine (Fa_{32}) with inclusions of silicate melt glass. Augite and poikilitic orthopyroxene are also present.

SNR	Signal to Noise Ratio
Sol	Martian solar day. Equivalent to 1.027346 Earth days (24h 39m 35.244s).
SQL	Structured Query Language
SSI	Surface Stereo Imager. Panoramic camera system on Phoenix.
STFC	Science and Technology Facilities Council. Previously known as the Particle Physics and Astronomy Research Council (PPARC).
Suevite	A polymict impact breccia with a matrix that contains shocked and unshocked clasts and cogenetic melt particles (glassy or crystallized).
Super-oxide	Anion O_2^- . Free radical. Highly reactive and paramagnetic.
SVS	Scientific Value Score. See Chapter 6.
Theiikian	Martian epoch ~4 Ga to ~3.5 Ga according to an alternative chronological scheme based on mineralogy (Bibring <i>et al.</i> , 2006a). Characterised by sulphates, acidic water, volcanism and SO_2 .
TRESSA	Teamed Robots for Exploration and Science on Steep Areas
UB	University of Bradford (used as a prefix)
UL-GEOL	University of Leicester, Geology Department
Urey	Instrument on ExoMars to identify organic compounds. Includes a sub-critical water extractor and the MOD and MOI experiments.
USDA	United States Department of Agriculture
USGS	United States Geological Survey

VB6	Visual Basic 6. Microsoft application development environment.
VIS	Visible
VL	Viking Lander (as VL1 or VL2)
VNIR	Visible Near Infra Red
WA	Wide Angle
WAC	Wide Angle Camera. Part of the PanCam system for ExoMars.
WAM	Wide Angle Mirror. Parabolic mirror associated with the right-hand stereo camera on the Beagle 2 PAW (Figure 2.3). Initially positioned in the FOV for panoramic imaging of the landing site prior to ARM/PAW deployment.
WDXRF	Wavelength Dispersive X-Ray Fluorescence
Whewellite	A type of Ca-oxalate monohydrate
WP	Waypoint
WUSTL-EPS	Washington University St Louis, Department of Earth and Planetary Science
XRD	X-Ray Diffraction
XRF	X-Ray Fluorescence
XRFS	X-Ray Fluorescence Spectroscopy
XRS	X-Ray Spectrometer

Bibliography

- Ai-Chang, M., Bresina, J., Charest, L., Chase, A., Cheng-jung Hsu, J., Jonsson, A., Kanefsky, B., Morris, P., Rajan, K., Yglesias, J., Chafin, B.G., Dias, W.C., and Maldague, P.F. (2004) MAPGEN: Mixed-Initiative Planning and Scheduling for the Mars Exploration Rover Mission, *IEEE Intelligent Systems*, vol. 19, no. 1, pp. 8-12.
- Allen, C.C. and Oehler, D.Z. (2008) Sample return from ancient hydrothermal springs. *Ground Truth from Mars: Science Payoff from a Sample Return Mission, April 21-23, Albuquerque, New Mexico*, abstract 4011.
- Allen, C.C., Morris, R.V., Jager, K.M., Golden, D.C., Lindstrom, D.J., Lindstrom, M.M., and Lockwood, J.P. (1998) Martian regolith simulant JSC Mars-1. *LPSC XXIX*.
- Allen, C.C., Jakeš, P., Jaumann, R., Marshall, J., Moses, S., Ryder, G., Saunders, S., and Singer, R. (1995) Field Geology/Processes. In *Planetary Surface Instruments Workshop*, edited by C. Meyer, A.H. Treiman and T. Kostiuk, LPI technical Report 95-05.
- Allwood, A.C., Walter, M.R., Kamber, B.S., and Burch, I.W. (2006) Stromatolite reef from the Early Archaean era of Australia, *Nature* 441, 714-718.
- American Astronomical Society (2001) Terrestrial Analogs to Mars: Planetary Decadal Study Community White Paper Solar System Exploration Survey, 2003-2013. *American Astronomical Society*.
- Arp G. (1995) Lacustrine bioherms, spring mounds, and marginal carbonates of the Ries-impact-crater (Miocene, southern Germany). *Facies* 33, 35-90.

- Arvidson, R.E., Anderson, R.C., Bartlett, P., Bell III, J.F., Blaney, D., Christensen, P.R., Chu, P., Crumpler, L., Davis, K., Ehlmann, B.L., Fergason, R., Golombek, M.P., Gorevan, S., Grant, J.A., Greeley, R., Guinness, E.A., Haldemann, A.F.C., Herkenhoff, K., Johnson, J., Landis, G., Li, R., Lindemann, R., McSween, H., Ming, D.W., Myrick, T., Richter, L., Seelos IV, F.P., Squyres, S.W., Sullivan, R.J., Wang, A., and Wilson, J. (2004a) Localization and Physical Properties Experiments Conducted by Spirit at Gusev Crater. *Science* 305, 821-824.
- Arvidson, R.E., Anderson, R.C., Bartlett, P., Bell III, J.F., Christensen, P.R., Chu, P., Davis, K., Ehlmann, B.L., Golombek, M.P., Gorevan, S., Guinness, E.A., Haldemann, A.F.C., Herkenhoff, K., Landis, G., Li, R., Lindemann, R., McSween, H., Ming, D.W., Myrick, T., Parker, T., Richter, L., Seelos IV, F.P., Soderblom, L.A., Squyres, S.W., Sullivan, R.J., and Wilson, J. (2004b) Localization and Physical Properties Experiments Conducted by Opportunity at Meridiani Planum. *Science* 306, 1730-1733.
- Arvidson, R. E., Guinness, E. A., Moore, H. J., Tillman, J., and Wall, S. D. (1983) Three Mars years: Viking Lander 1 imaging observations, *Science* 222, 463-468.
- Awramik, S. M. and Grey, K. (2005) Stromatolites: biogenicity, biosignatures, and bioconfusion. *Proc. SPIE Vol. 5906*, 227-235, *Astrobiology and Planetary Missions*; Richard B. Hoover, Gilbert V. Levin, Alexei Y. Rozanov, G. Randall Gladstone; Eds.
- Baglioni, P. (2003) Pasteur Payload Package. Instrument Definition Document (IDD), European Space Agency.
- Banfield, J.F., Moreau, J.W., Chan, C.S, Welch, S.A., and Little, B. (2001) Mineralogical biosignatures and the search for life on Mars. *Astrobiology* 1, 447-465.
- Banerjee, N.R., Muehlenbachs, K., Furnes, H., Staudigel, H., and de Wit, M. (2004) Potential for early life hosted in basaltic glass on a wet Mars. *Second Conference on Early Mars: Geologic, Hydrologic, and Climatic Evolution and the Implications for Life, October 11-15, 2004, Jackson Hole, Wyoming*, abstract 8048.

- Barbieri, R., Stivaletta, N., Marinangeli, L., and Ori, G.G. (2006) Microbial signatures in sabkha evaporate deposits of Chott el Gharsa (Tunisia) and their astrobiological implications. *Planet. Space Sci.* 54, 726-736.
- Bar-Cohen, Y., Chang, Z., Sherrit, S., Badescu, M., and Bao, X. (2005) The Ultrasonic/Sonic Driller/Corer (USDC) as a Subsurface Drill, Sampler and Lab-On-A-Drill for Planetary Exploration Applications. *Proc. of the SPIE Smart Structures Conference, San Diego, CA., SPIE Vol. 5762-22, March 7-10, 2005.*
- Barlow, N. (2008) Mars: An Introduction to its Interior, Surface and Atmosphere. *Cambridge Planetary Science Series*, Cambridge University Press, ISBN 978-0-521-85226-5.
- Bayliss, P., Erd, D.C., Mrose, M.E., Sabina, A.P., and Smith D.K. (1986) Mineral Powder Diffraction File Data Book. *International Centre for Diffraction Data.*
- Bell III, J.F., Squyres, S.W., Herkenhoff, K.E., Maki, J.N., Arneson, H.M., Brown, D., Collins, S.A., Dingizian, A., Elliot, S.T., Hagerott, E.C., Hayes, A.G., Johnson, M.J., Johnson, J.R., Joseph, J., Kinch, K., Lemmon, M.T., Morris, R.V., Scherr, L., Schwochert, M., Shepard, M.K., Smith, G.H., Sohl-Dickstein, J.N., Sullivan, R.J., Sullivan, W.T., and Wadsworth M. (2003) Mars Exploration Rover Athena Panoramic Camera (Pancam) investigation. *J. Geophys. Res.* 108(E12), 8063, doi: 10.1029/2003JE002070
- Bendezú, R. and Fontboté, L. (2002) Late timing for high sulfidation cordilleran base metal lode and replacement deposits in porphyry-related districts: the case of Colquijirca, central Peru. *SGA News* 13, 9-13.
- Bibring, J-P., Langevin, Y., Mustard, J.F., Poulet, F., Arvidson, R., Gendrin, A., Gondet, B., Mangold, N., Pinet, P., Forget, F., and the OMEGA team (2006a) Global Mineralogical and Aqueous Mars History Derived from OMEGA/Mars Express Data. *Science* 312, pp 400-403.

- Bibring, J-P., Thomas, N., Westall, F. and the MicrOmega Team (2006b) MicrOmega: Visible and Infrared Microscope, Instrument Information Package (IIP) Part A, In *Pasteur Instrument Payload for the ExoMars Mission, ESA Mission Documentation*.
- Bishop J.L., Murad E., Lane M.D., and Mancinelli R.L. (2004) Multiple techniques for mineral identification on Mars: A study of hydrothermal rocks as potential analogues for astrobiology sites on Mars. *Icarus* 169, 331-323.
- Blackhurst, R.L., Genge, M.J., Kearsley, A.T., and Grady, M.M. (2005) Cryptoendolithic alteration of Antarctic sandstones: Pioneers or opportunists? *J. Geophys. Res.* 110, E12S24, doi: 10.1029/2005JE002463.
- Boston, P.J., Spilde, M.N., Northup, D.E., Melim, L.A., Soroka, D.S., Kleina, L.G., Lavoie, K.H., Hose, L.D., Mallory, L.M., Dahm, C.N., Crossey, L.J., and Schelble, R.T. (2001) Cave biosignature suites: Microbes, Minerals and Mars. *Astrobiology* 1, 25-55.
- Bragg, W.L. (1914) The Diffraction of Short Electromagnetic Waves by a Crystal. *Proceedings of the Cambridge Philosophical Society* 17, 43–57.
- Brasier, M.D., Green, R.G., and McLoughlin, N. (2004) Characterization and critical testing of potential microfossils from the early Earth: the Apex “microfossil debate” and its lessons for Mars sample return. *Int. J. Astrobiology* 3, 139-150.
- Bridges, J.C., Seabrook, A.M., Rothery, D.A., Kim, J-R., Pillinger, C.T., Sims, M.R., Golombek, M.P., Duxbury, T., Head, J.W., Haldermann, A.F.C., Mitchell, K.L., Muller, J-P., Lewis, S.R., Moncrieff, C., Wright, I.P., Grady, M.M., and Morley, J.G. (2002) Selection of the Landing Site in Isidis Planitia of Mars Probe Beagle 2. *J. Geophys. Res.* 108(E1), 5001, doi: 10.1029/2001JE001820.

- Büdel, B., Weber, B., Kühl, M., Pfan, H., Sültemeyer, D., and Wessels, D. (2004) Reshaping of sandstone surfaces by cryptoendolithic cyanobacteria: bioalkalization causes chemical weathering in arid landscapes. *Geobiology* 2, 261-268.
- Burridge, R., Graham, J., Shillcutt, K., Hirsh, R., and Kortenkamp, D. (2003) Experiments with an EVA Assistant Robot. In *The 7th International Symposium on Artificial Intelligence, Robotics and Automation in Space (i-SAIRAS-03)*.
- Byerly G.R., Walsh, M.M., and Lowe, D.L. (1986) Stromatolites from the 3300-3500 Myr Swaziland Supergroup, Barberton Mountain Land, South Africa. *Nature* 319, 489-491.
- Cabrol, N.A. and Grin, E.A (2005) Ancient and Recent Lakes on Mars, In *Water on Mars and Life*, edited by Tokano, T., *Adv. Astrobiol. Biogeophys*, Springer, Berlin Heidelberg, pp 235-259.
- Cady, S.L. and Farmer, J.D. (1996) Fossilization processes in siliceous thermal springs: Trends in preservation along the thermal gradient. In *Evolution of Hydrothermal Ecosystems on Earth (and Mars?)*, *Ciba Foundation Symposium 202*, edited by G.R. Bock and J.A. Goode, John Wiley and Sons, Inc., Chichester UK, pp. 150-173.
- Cady, S.L., Farmer, J.D., Grotzinger, J.P., Schopf, J.W., and Steele, A. (2003) Morphological biosignatures and the search for life on Mars. *Astrobiology* 3, 351-368.
- Cannon, H.N., Stoker, C.R., Dunagan, S.E., Davis, K., Gómez-Elvira, J., Glass, B.J., Lemke, L.G., Miller, D., Bonaccorsi, R., Branson, M., Christa, S., Rodríguez-Manfredi, J.A., Mumm, E., Paulsen, G., Roman, M., Winterholler, A., and Zavaleta, J.R. (2007) MARTE: Technology Development and Lessons Learned from a Mars Drilling Mission Simulation. *J. Field Robotics* 24(10), 877-905.
- Canny, J. (1986) A Computational Approach to Edge Detection, *IEEE Trans. Pattern Analysis*

and Machine Intelligence, 8:679-714.

Cargel, J.S., Delmelle, P., and Nash, D.B. (1999) Volcanogenic sulfur on Earth and Io: Composition and Spectroscopy. *Icarus* 142, 249-280.

Carr, M.H. and Head III, J.W. (2003) Oceans on Mars: an assessment of the observational evidence and possible fate. *J. Geophys. Res.* 108(E5): 5042, 10.1029/2002JE001963.

Castaño, R., Anderson, R.C., Estlin, T., DeCoste, D., Fisher, F., Gaines, D., Mazzoni, D., and Judd, M. (2003) Rover Traverse Science for Increased Mission Science Return. *IEEE*.

Castaño, R., Estlin, T., Anderson, R.C., Gaines, D., Castaño, A., Bornstein, B., Chouinard, C., and Judd, M. (2007) OASIS: Onboard Autonomous Science Investigation System for Opportunistic Rover Science. *J. Field Robotics* 24(5), 379-397.

Castano, R., Estlin, T., Gaines, D., Castano A., Bornstein, B., Chouinard, C., Anderson, R.C., and Judd M. (2006) Automated target selection for opportunistic rover science. *LPSC XXXVII*

Catullo, A. and Acquaroli, B. (2006) ExoMars MRO Visibility, Alcatel Alenia Space, EXM-MS-TNO-AI-0014.

Chan, M.A., Beitler, B., Parry, W.T., Ormö, J., and Komatsu, G. (2004) A possible terrestrial analogue for hematite concretions on Mars. *Nature* 429, 731-734, doi: 10.1038/nature02600.

Chapman, M.G. (ed.) (2007) The Geology of Mars: Evidence from Earth-based Analogs. *Cambridge Planetary Science Series*, Cambridge University Press, ISBN 978-0-521-83292-2.

Cheng, A.F. and Farmer, J.D. (1997) Planetary Surface Sample Collection: Rock Chipper. *LPSC XXVII*.

- Clark, B.C., Baird, A.K., Rose, H.J., Toulmin III, P., Christian, R.P., Kelliher, W.C., Castro, A.J., Rowe, C.D., Keil, K., and Huss, G.R. (1977) The Viking X Ray Fluorescence Experiment: Analytical Methods and Early Results. *J. Geophys. Res.* 82, 4577-4594.
- Clark, B.C., Baird, A.K., Weldon, R.J., Tsusaki, D.M., Schnabel, L., and Candelaria, M.P. (1982) Chemical composition of Martian fines. *J. Geophys. Res.* 87, 10059-10067.
- Clark, B.C., Morris, R.V., McLennan, S.M., Gellert, R., Jolliff, B., Knoll, A.H., Squyres, S.W., Lowenstein, T.K., Ming, D.W., Tosca, N.J., Yen, A., Christensen, P.R., Gorevan, S., Brückner, J., Calvin, W., Dreibus, G., Farrand, W., Klingelhöfer, G., Wänke, H., Zipfel, J., Bell III, J.F., Grotzinger, J., McSween, H.Y., and Rieder, R. (2005) Chemistry and mineralogy of outcrops at Meridiani Planum. *Earth Planet. Sci. Lett.* 240, 73-94.
- Clifford, S.M. (1987) Polar basal melting on Mars. *J. Geophys. Res.* 92, 9135-9152.
- Clifford, S.M. and Parker, T.J. (2001) The Evolution of the Martian Hydrosphere: Implications for the Fate of a Primordial Ocean and the Current State of the Northern Plains. *Icarus* 154, 40-79.
- Coates, A.J., Jaumann, R., Josset, J-L., and the PanCam Team (2006) PanCam: Wide Angle Stereo Pair and Monoscopic High Resolution Colour Imager, Instrument Information Package (IIP) Part A, In *Pasteur Instrument Payload for the ExoMars Mission, ESA Mission Documentation*.
- Cockell, C.S. (2000) The ultraviolet history of the terrestrial planets – Implications for biological evolution. *Planet. Space Sci.* 4, 203-214.
- Cockell, C.S. and Lee, P. (2002) The biology of impact craters – a review. *Biol. Rev.* 77, 279-310.

- Cockell, C.S., Lee, P., Osinski, G., Horneck, G., and Broady, P. (2002a) Impact-induced microbial endolithic habitats. *Meteoritics Planet. Sci.* 37, 1287-1298.
- Cockell, C.S., Rettberg, P., Horneck, G., Patel, M., Lammer, H., and Cordoba-Jóbonero (2002b) Ultraviolet protection in microhabitats – lessons from the terrestrial poles applied to Mars. *Proc. of the Second European Workshop on Exo/Astrobiology, Graz, Austria, 2002, ESA SP-518*, 215-218.
- Crisp, J.A, Grotzinger, J.P., Vasavada, A.R., Karcz, J.S., and the MSL Science Team (2008) Mars Science Laboratory: Science Overview. *Workshop on Ground Truth from Mars: Science Payoff from a Sample Return Mission*, 21-23 April 2008, Albuquerque, NM, abstract 4016.
- Cryer, J.E., Ping-Sing Tsai, and Shah, M. (1995) Integration of Shape from Shading and Stereo. *Pattern Recognition* 28, 7, 1033-1043.
- Date, C.J. (1997) A guide to the SQL Standard: A user's guide to the standard database language SQL. Fourth Edition, Addison-Wesley.
- Des Marais, D.J., Clark, B.C., Crumpler, L.S., Farmer, J.D., Grotzinger, J.P., Haskin, L.A., Knoll, A.H., Landis, G.A., Moersch, J., Schröder, C., Wdowiak, T., Yen, A.S., Squyres, S.W., and the Athena Science Team (2005) Astrobiology and the basaltic plains in Gusev Crater. *Lunar and Planetary Science XXXVI*, abstract 2353.
- de Ronde, C.E.J., de Wit, M.J., and Spooner, E.T.C. (1994) Early Archaean (> 3.2 Ga) Fe-oxide-rich, hydrothermal discharge vents in the Barberton greenstone belt, South Africa. *Geol. Soc. Amer. Bull.* 196, 86-104.
- de Vries, S.T. (2004) Early Archaean sedimentary basins: Depositional environment and hydrothermal systems. *Geologica Utraiectina* 244, 160 pp.

- de Wit, M.J., Hart, R., Martin, A., and Abbott, P. (1982) Archaean abiogenic and probable biogenic structures associated with mineralised hydrothermal vent systems and regional metasomatism with implications for greenstone belt studies. *Econ. Geol.* 77, 1783-1802.
- Dibblee, T.W. (1967) Geologic map of the Broadwell Lake quadrangle, San Bernardino County, California. *U.S. Geol. Survey*, Washington, DC.
- Dibblee, T.W. and Bassett, A.M. (1966) Geologic map of the Cady Mountains quadrangle, San Bernardino County, California. *U.S. Geol. Survey*, Washington, DC.
- Downs, R.T. and Hall-Wallace, M. (2003) The American Mineralogist Crystal Structure Database. *American Mineralogist* 88, 247-250.
- Edgett, K.S., Bell III, J.F., Herkenhoff, K.E., Heydari, E., Kah, L.C., Minitti, M.E., Olson, T.S., Rowland, S.K., Shieber, J., Sullivan, R.J., Yingst, R.A., Ravine, M.A., Caplinger, M.A., and Maki, J.N. (2005) The Mars Hand Lens Imager (MAHLI) for the 2009 Mars Science Laboratory. *LPSC XXXVI*, abstract 1170.
- Edwards, H.G.M., Jorge Villar, S.E., Parnell, J., Cockell, C.S., and Lee, P. (2005a) Raman spectroscopic studies of cyanobacterial gypsum halotrophs and their relevance for sulphate deposits on Mars. *Analyst* 130, 917-923.
- Edwards, H.G.M., Moody, C.D., Jorge Villar, S.E., and Wynn-Williams, D.D. (2005b) Raman spectroscopic detection of key biomarkers of cyanobacteria and lichen symbiosis in extreme Antarctic habitats: Evaluation for Mars Lander missions. *Icarus* 174, 560-571.
- Edwards, H.G.M., Russell, M.C., and Wynn-Williams, D.D. (1997) Fourier transform Raman spectroscopic and scanning electron microscopic study of cryptoendolithic lichens from Antarctica. *J. Raman Spectrosc.* 30, 685-690.

- Edwards, H.G.M., Jorge Villar, S.E., **Pullan, D.**, Hargreaves, M.D., Hofmann, B.A., and Westall, F. (2007) Morphological biosignatures from relict fossilised sedimentary geological specimens: a Raman spectroscopic study, *J. Raman Spectrosc.* 38, 1352-1361, doi: 10.1002/jrs.1775
- Edwards, H.G.M., Wynn-Williams, D.D., and Jorge Villar, S.E. (2004) Biological modification of haematite in Antarctic cryptoendolithic communities. *J. Raman Spectrosc.* 35, 470-474.
- Ehlmann, B.L., Mustard, J.F., Murchie, S.L., Poulet, F., Bishop, J.L., Brown, A.J., Calvin, W.M., Clark, R.N., Des Marais, D.J., Milliken, R.E., Roach, L.H., Roush, T.L., Swayze, G.A., and Wray, J.J. (2008) Orbital Identification of Carbonate-Bearing Rocks on Mars. *Science* 322, 1828-1832.
- Eisele, L.E., Bakhru, S.H., Liu, X., MacColl, R., and Edwards, M.R. (2000) Studies on C-phycoyanin from *Cyanidium caldarium*, a eukaryote at the extremes of habitat, *Biochim. Biophys. Acta* 1456, 99-107.
- Ellery, A. and Wynn-Williams, D.D. (2003) Why Raman spectroscopy on Mars? A case for the right tool for the right job. *Astrobiology* 3, 565-579.
- Erokhina, L.G., Shatilovich, A.V., Kaminskaya, O.P., and Gilichinskii, D.A. (2002) The absorption and fluorescence spectra of the cyanobacterial phycobionts of cryptoendolithic lichens in the high-polar regions of Antarctica. *Microbiology* 71, 5, 601-607.
- ExoMars Project Team (2007a) Reference Surface Mission. *European Space Agency*, EXM-PL-RS-ESA-00002.
- ExoMars Project Team (2007b) Scientific Payload Requirements Document. *European Space Agency*, EXM-PL-RS-ESA-00001.

- Farfan, C., Salinas, R.A., and Cifuentes, G. (2004) Rock segmentation and measures on gray level images using watershed for sizing distribution in particle systems. Available from <http://cabierta.uchile.cl/revista/19/articulos/pdf/paper2.pdf>.
- Farr, T.G. (2004) Terrestrial Analogs to Mars: The NRC Community Decadal Report. *Planet. Space. Sci.* 52, 3-10.
- Farr, T.G., Arcone, S., Arvidson, R.W., Baker, V., Barlow, N.G., Beaty, D., Bell, M.S., Blankenship, D.D., Bridges, N., Briggs, G., Bulmer, M., Carsey, F., Clifford, S.M., Craddock, R.A., Dickerson, P.W., Duxbury, N., Galford, G.L., Garvin, J., Grant, J., Green, J.R., Gregg, T.K.P., Guinness, E., Hansen, V.L., Hecht, M.H., Holt, J., Howard, A., Keszthelyi, L.P., Lee, P., Lanagan, P.D., Lentz, R.C.F., Leverington, D.W., Marinangeli, L., Moersch, J.E., Morris-Smith, P.A., Mouginiis-Mark, P., Olhoeft, G.R., Ori, G.G., Paillou, P., Reilly, J.F., II, Rice, J.W., Jr., Robinson, C.A., Sheridan, M., Snook, K., Thomson, B.J., Watson, K., Williams, K., and Yoshikawa, K. (2002) Terrestrial Analogs to Mars. In *The Future of Solar System Exploration, 2003-2013*, edited by M.V. Sykes, *ASP Conference Series 272*, 35-76.
- Farmer, J.D. and Des Marais, D.J. (1999) Exploring for a record of ancient Martian life. *J. Geophys. Res.* 104 (E11), 26977-26995 (1998JE000540).
- Feldman, W.C., Boynton, W.V., Tokar, R.L., Prettyman, T.H., Gasnault, O., Squyres, S.W., Elphic, R.C., Lawrence, D.J., Lawson, S.L., Maurice, S., McKinney, G.W., Moore, K.R., and Reedy, R.C. (2002) Global distribution of neutrons on Mars: results from Mars Odyssey. *Science* 287: 75-78.
- Fernández-Remolar, D.C. (2006) The subsurface and surface acidic system of Río Tinto: Sulfur and iron transfer from underground weathering to subaerial precipitation. *Geochim. Cosmo. Acta* 70, A171, doi: 10.1016/j.gca.2006.06.343.

- Fink, W., Dohm, J.M., Tarbell, M.A., Hare, T.M., and Baker, V.R. (2005) Next-generation robotic planetary reconnaissance missions: A paradigm shift. *Planet. Space. Sci.* 53, 1419-1426.
- Fisher, R., Perkins, S., Walker, A., and Wolfart, E. (2003) Sobel Edge Detector. *Hypermedia Image Processing Reference*, <http://homepages.inf.ed.ac.uk/rbf/HIPR2/sobel.htm>
- Formisano, V., Atreya, S., Encrenaz, T., Ignatiev, N., and Giuranna, M. (2004) Detection of Methane in the Atmosphere of Mars. *Science* 306, 1758-1761.
- Fouke, B.W., Farmer, J.D., Des Marais, D.J., Pratt, L., Sturchio, N.L., Burns, P.C., and Discipulo, M.K. (2000) Depositional facies and aqueous-solid geochemistry of travertine-depositing hot springs (Angel Terrace, Mammoth hot springs, Yellowstone National Park, U.S.A.). *J. Sedimentary Research* 70(3), 565-585.
- Friedmann, E.I. (1982) Endolithic microorganisms in the Antarctic cold desert. *Science* 215, 1045-1053.
- Friedmann, E.I., Hua, M.S., and Ocampo-Friedmann, R. (1988) Cryptoendolithic lichen and cyanobacterial communities of the Ross Desert, Antarctica. *Polarforschung* 58, 251-259.
- Furfaro, R., Dohm, J.M., Fink, W., Kargel, J., Schulze-Makuch, D., Fairén, A.G., Palmero-Rodriguez, A., Baker, V.R., Ferré, P.T., Hare, T.M., Tarbell, M.A., Miyamoto, H., and Komatsu, G. (2007) The search for life beyond Earth through fuzzy expert systems. *Planet. Space. Sci.*, doi: 10.1016/j.pss.2007.09.006.
- Furnes, H., Banerjee, N.R., Muehlenbachs, K., and Kontinen, A. (2004) Preservation of biosignatures in metaglassy volcanic rocks from the Jormua ophiolite complex, Finland. *Precamb. Res.* 136, 125-137.

- Gautsch, S. (2002) Development of an Atomic Force Microscope and measurement concepts for characterising Martian dust and soil particles. PhD Thesis, University of Neuchâtel, Switzerland.
- Gazis, P.R. and Roush, T. (2001) Autonomous identification of carbonates using near-IR reflectance spectra during the February 1999 Marsokhod field tests, *J. Geophys. Res.* 106, pp. 7765-7773.
- Gellert, R., Rieder, R., Anderson, R.C., Brückner, J., Clark, B.C., Dreibus, G., Economou, T., Klingelhöfer, G., Lugmair, G.W., Ming, D.W., Squyres, S.W., d'Uston, C., Wänke, H., Yen, A., and Zipfel, J. (2004) Chemistry of Rocks and Soils in Gusev Crater from the Alpha Particle X-ray Spectrometer. *Science* 305, 829-832.
- Gellert, R., Rieder, R., Brückner, J., Clark, B.C., Dreibus, G., Klingelhöfer, G., Lugmair, G., Ming, D.W., Wänke, H., Yen, A., Zipfel, J., and Squyres, S.W. (2006) Alpha Particle X-Ray Spectrometer (APXS): Results from Gusev crater and calibration report. *J. Geophys. Res.* 111, E02S05, doi: 10.1029/2005JE002555.
- Gilmore, M. S., Castaño, R., Mann, T., Anderson, R.C., Mjolsness, E.D., Manduchi, R., and Saunders, R.S. (2000) Strategies for autonomous rovers at Mars. *J. Geophys. Res.* 105(E12), 29223-29237.
- Glazner, A.F. (1988) Stratigraphy, structure and potassic alteration of Miocene volcanic rocks in the Sleeping Beauty area, central Mojave Desert, California. *Geol. Soc. Am. Bull.* 100, 424-435.
- Godwin, R. (ed.) (2000) Mars: The NASA Mission Reports, *Apogee Books*, ISBN 1-896522-62-9.
- Golombek, M.P. (1997) The Mars Pathfinder Mission. *J. Geophys. Res.* 102(E2), 3953-3965.

Gonzalez, R.C. and Woods, R.E. (2007) *Digital Image Processing*. Third Edition, Prentice Hall.

Gorevan, S., Myrick, T., Batting, C., Mukherjee, S., Bartlett, P., and Wilson, J. (2003a) Strategies for future Mars exploration: An infrastructure for the near and long-term future exploration of the subsurface of Mars. *Sixth International Conference on Mars (2003)*, abstract 3196.

Gorevan, S., Myrick, T., Davis, K., Chau, J.J., Bartlett, P., Mukherjee, S., Anderson, R., Squyres, S.W., Arvidson, R.E., Madsen, M.B., Bertelsen, P., Goetz, W., Binau, C.S., and Richter, L. (2003b) Rock Abrasion Tool: Mars Exploration Rover mission. *J. Geophys. Res.* 108(E12), 8068, doi: 10.1029/2003JE002061.

Greeley, R. and Guest, J.E. (1987) *Geologic Map of the eastern Equatorial Region of Mars*, U. S. Geol. Surv. Misc. Inv. Series Map I-1802-B.

Greenwood, N.N. and Gibb, T.C. (1971) *Mössbauer Spectroscopy*. Chapman and Hall, New York.

Grieve, R.A.F. (1988) The Haughton impact structure: Summary and synthesis of the results of the HISS project. *Meteoritics* 23, 249-254.

Griffiths, A.D., Coates, A.J., Josset, J.-L., Paar, G., Hofmann, B., **Pullan, D.**, Rueffer, P., Sims, M.R., and Pillinger, C.T. (2005) The Beagle 2 stereo camera system. *Planet. Space Sci.* 53, 14-15, 1466-1482.

Grotzinger, J.P. and Rothman, D.H. (1996) An abiotic model for stromatolite morphogenesis. *Nature* 383, 423-425.

Grotzinger, J.P. and Knoll, A.H. (1999) Precambrian stromatolites: Evolutionary milestones or

environmental dipsticks? *Annual Review of Earth and Planetary Sciences* 27, 313-358.

Gulick, V., Morris, R.L., Ruzon, M.A., and Roush, T.L. (2001) Autonomous image analysis during the 1999 Marsokhod rover field test, *J. Geophys. Res.* 106, pp. 7745-7763.

Hajek, Petr (2006) Fuzzy Logic, *The Stanford Encyclopedia of Philosophy (Fall 2006 Edition)*, Edward N. Zalta (ed.), <http://plato.stanford.edu/archives/fall2006/entries/logic-fuzzy/>

Hamilton, V.E. (2006) Spectral evidence for silica in Eos Chasma, Mars. *American Geophysical Union, Fall Meeting 2006*, abstract P22A-07.

Henry, D.J. (1957) Gem trails of California. *Baldwin Park, California*.

Herkenhoff, K.E., Squyres, S.W., Bell III, J.F., Maki, J.N., Arneson, H.M., Bertelsen, P., Brown, D., Collins, S.A., Dingizian, A., Elliot, S.T., Goetz, W., Hagerott, E.C., Hayes, A.G., Johnson, M.J., Kirk, R.L., McLennan, S., Morris, R.V., Scherr, L., Schwochert, M., Shiraishi, L.R., Smith, G.H., Soderblom, L.A., and Wadsworth M. (2003) The Athena Microscopic Imager investigation. *J. Geophys. Res.* 108(E12), 8065, doi: 10.1029/2003JE002076.

Hiscox, J.A. (2001) An Overview of the Origin of Life: The Case for Biological Prospecting on Mars. *Earth, Moon and Planets* 87, 191-212.

Hofmann, A. and Bolhar, R (2007) Carbonaceous cherts in the barberton greenstone belt and their significance for the study of early life in the archean record. *Astrobiology* 7, 355-388.

Hofmann, B.A. and Farmer, J.D. (2000) Filamentous fabrics in low-temperature mineral assemblages: are they fossil biomarkers? Implications for the search for a subsurface fossil record on the early Earth and Mars. *Planet. Space. Sci.* 48, 1077-1086.

- Hofmann, B.A., Gnos, E., and Eggimann, M. (2005) SSMP Excursion to the Ries and Steinheim meteorite impact craters, Germany, 14-15 October 2005. *Schweizerische Mineralogische und Petrographische Mitteilungen* 85, 255-259.
- Hofmann, B.A., Josset, M., and Josset, J.-L. (2002) Imaging of Mars analogue materials using the Beagle 2 camera system. *Proc. of the Second European Workshop on Exo/Astrobiology, Graz, Austria, 2002, ESA SP-518*, 387-390.
- Hofmann, H.J., Grey, K., Hickman, A.H., and Thorpe, R.I. (1999) Origin of 3.45 Ga coniform stromatolites in Warrawoona Group, Western Australia. *Geol. Soc. Am. Bull.* 111, 8, 1256-1262.
- Hofmann, N. (2000) White Mars: a new model for Mars' surface and atmosphere based on CO₂. *Icarus* 146: 326-343.
- Huntsberger, T.L., Rodriguez, G., and Schenker, P.S. (2000), Robotics challenges for robotic and human Mars exploration. In *Proc. ROBOTICS2000, Albuquerque, NM, Mar 2000*, pp. 340-346.
- Huntsberger, T.L., Stroupe, A., Aghazarian, H., Garrett, M., Younse, P., and Powell, M. (2007) TRESSA: Teamed Robots for Exploration and Science on Steep Areas. *J. Field Robotics* 24(11), 1015-1031.
- Israel, E.J., Arvidson, R.E., Wang, A., Pasteris, J.D., and Joliff, B.L. (1997) Laser Raman spectroscopy of varnished basalt and implications for in situ measurements of Martian rocks. *J. Geophys. Res.* 102(E12), 28705-28716.
- Jakosky, B.M. and Shock, E.L. (1998) The biological potential of Mars, early Earth and Europa. *J. Geophys. Res.* 103(E8): 19359-19364.

- Jolliff, B.L. and the Athena Science Team (2005) Composition of Meridiani hematite-rich spherules: A mass-balance mixing model approach. *LPSC XXXVI*, abstract 2269.
- Jorge Villar, S.E., Edwards, H.G.M., Wynn-Williams, D.D., and Worland, M.R. (2003) FT-Raman spectroscopic analysis of an Antarctic endolith. *Int. J. Astrobiology* 1, 349-355.
- Jorge Villar, S.E. and Edwards, H.G.M. (2006) Raman spectroscopy in astrobiology. *Anal. Bioanal. Chem.* 384, 100-113.
- Jorge Villar, S.E., Edwards, H.G.M., and Benning, L.B. (2006) Raman spectroscopic and scanning electron microscopic analysis of a novel biological colonisation of volcanic rocks. *Icarus* 184, 158-169.
- Josset, J-L., Westall, F., Hofmann, B.A., Spray, J.G., Cockell, C., Kempe, S., Griffiths, A.D., Coradini, A., Langevin, Y., Colangeli, L., Koschny, D., and **Pullan, D.** (2006) CLUPI: CLose-UP Imager, Instrument Information Package (IIP) Part A, In *Pasteur Instrument Payload for the ExoMars Mission, ESA Mission Documentation*.
- Kargel, J.S. (2004) Mars: A Warmer, Wetter Planet. *Springer-Praxis books in Astronomy and Space Sciences*. ISBN 1-85233-568-8
- Keller, H.U., Hartwig, H., Kramm, R., Koschny, D., Markiewicz, W.J., Thomas, N., Fernades, M., Smith, P.H., Reynolds, R., Lemmon, M.T., Weinberg, J., Marcialis, R., Tanner, R., Boss, B.J., Oquest, C., Paige D.A. (2001) The MVACS Robotic Arm Camera. *J. Geophys. Res.* 106(E8), 17609-17621.
- Kieffer, H.H., Jakosky, B.M., Snyder, C.W., and Matthews, M.S. (eds.) (1992) Mars. *Univ. Arizona Press, Tucson*.

- Klein, H.P. (1978) The Viking Biological Experiments on Mars. *Icarus* 34, 666-674.
- Klingelhöfer, G., Morris, R.V., Bernhardt, B., Rodionov, D., de Souza Jr., P.A., Squyres, S.W., Foh, J., Kankeleit, E., Bonnes, U., Gellert, R., Schröder, C., Linkin, S., Evlanov, E., Zubkov, B., and Prilutski, O. (2003) Athena MIMOS II Mössbauer spectrometer investigation. *J. Geophys. Res.* 108(E12), 8097.
- Klingelhöfer, G., Morris, R.V., Bernhardt, B., Schröder, C., Rodionov, D., de Souza Jr., P.A., Yen, A., Gellert, R., Evlanov, E., Zubkov, B., Foh, J., Bonnes, U., Kankeleit, E., Gütlich, P., Ming, D.W., Renz, F., Wdowiak, T., Squyres, S.W., and Arvidson, R.E. (2004) Jarosite and Hematite at Meridiani Planum from Opportunity's Mössbauer Spectrometer. *Science* 306, 1740-1745.
- Klingelhöfer, G., Westall, F., Zegers, T., **Pullan, D.**, and the Mars Origins Scientific Team (2008) Mars Origins Mission. *LPSC XXXIX*, abstract 1265.
- Knoll, A.H., Carr, M., Clark, B., Des Marais, D.J., Farmer, J.D., Fischer, W.W., Grotzinger, J.P., McLennan, S.M., Malin, M., Schröder, C., Squyres, S.W., Tosca, N.J., and Wdowiak, T. (2005) An astrobiological perspective on Meridiani Planum, *Earth Planet. Sci. Lett.* 240, 179-189.
- Knudsen, J.M. (1989) Mössbauer Spectroscopy of ^{57}Fe and the Evolution of the Solar System. *Hyperfine Interactions* 47, 3-31.
- Knudsen, J.M., Mørup, S., and Galazkha-Firedman, J. (1990) Mössbauer spectroscopy and the iron on Mars. *Hyperfine Interactions* 57, 2231-2236.
- Knudsen, J.M., Madsen, M.B., Olsen, M., Vistisen, L., Koch, C.B., Mørup, S., Kankeleit, E., Klingelhöfer, G., Evlanov, E.N., Khromov, V.N., Mukhin, L.M., Prilutski, O.F., Zubkov, B., Smirnov, G.V., and Juchniewicz, J. (1992) Mössbauer spectroscopy on the surface of Mars.

Why? *Hyperfine Interactions* 68, 83-94.

Kojima, S., Hanamuro, T., Hayashi, K., Haruna, M., and Ohmoto, H. (1998) Sulphide minerals in Early Archaean chemical sedimentary rocks of the eastern Pilbara district, Western Australia. *Mineralogy and Petrology* 64(1-4), 219-235, doi: 10.1007/BF01226570.

Leverington, D.W. (2006) Volcanic processes as alternative mechanisms of landform development at a candidate crater-lake site near Tyrrhena Patera, Mars. *J. Geophys. Res.* 111, E11002, doi: 10.1029/2004JE002382.

Leverington, D.W. and Ghent R.R. (2004) Differential subsidence and rebound in response to changes in water loading on Mars: Possible effects on the geometry of ancient shorelines. *J. Geophys. Res.* 109, E01005, doi: 10.1029/2003JE002141.

Lindgren, P., Parnell, J., Bowden, S.A., Taylor, C., Osinski, G.R., and Lee, P. (2006) Preservation of biological signature within impact melt breccias, Haughton impact structure. *LPSC XXXVII*.

Lognonné, P., Spohn, T., Mimoun, D., Ulmanec, S., Biele, J., the MP2SP team, and the Aurora Environmental team (2006) GEP-ExoMars: a Geophysics and Environmental observatory on Mars. *LPSC XXXVII*, abstract 1982.

Longhi, J., Knittle, E., Holloway, J.R., and Wänke, H. (1992) The bulk composition, mineralogy and internal structure of Mars. In Mars (eds. Kieffer *et al.*), *Univ. Arizona Press, Tucson*, 185-208.

Love S.G., and Brownlee, D.E. (1993) A direct measurement of the terrestrial mass accretion rate of cosmic dust. *Science* 262, 550-553.

- Lowe, D. R. (1980) Stromatolites 3,400-Myr old from the Archaean of western Australia. *Nature*, 284, 441-443.
- Lowe, D.R. (1994) Abiological origin of described stromatolites older than 3.2 Ga, *Geology* 22, 287-390.
- Lowe, D.R. and Braunstein, D. (2003) Microstructure of high-temperature (>73 °C) siliceous sinter deposited around hot springs and geysers, Yellowstone National Park: the role of biological and abiological processes in sedimentation. *Canadian J. Earth Sci.* 40(11), 1611-1642.
- Malin, M.C., Bell, J.F., Cameron, J., Dietrich, W.E., Edgett, K.S., Hallet, B., Herkenhoff, K.E., Lemmon, M.T., Parker, T.J., Sullivan, R.J., Sumner, D.Y., Thomas, P.C., Wohl, E.E., Ravine, M.A., Caplinger, M.A., and Maki, J.N. (2005) The mast cameras and Mars descent imager (MARDI) for the 2009 Mars Science Laboratory. *LPSC XXXVI*, abstract 1214.
- Mancinelli, R.L. (1998) Prospects for the evolution of life on Mars, Viking 20 years later. *Adv. Space Res.* 22, 471-477.
- Margolin, P. (2000) The making of Lunar Explorers. *Geotimes* 45, 18-21.
- Marinangeli, L., Hutchinson, I., Baliva, A., Stevoli, A., Ambrosi, R., Critani, F., Delhez, R., Scandelli, L., Holland, A., Nelms, N., and the MARS-XRD Team (2007) A European XRD/XRF instrument for the ExoMars mission. *LPSC XXVIII*, abstract 1322.
- Martinez-Frías, J., Lunar, R., Rodríguez-Losada, J.A., Delgado, A., and Rull, F. (2004) The volcanism-related multistage hydrothermal system of El Joroso (SE Spain): Implications for the exploration of Mars. *Earth Planets Space* 56, v-viii.

- Maurice, S., Wiens, R., Manhès, G., Cremers, D., Barraclough, B., Bernardin, J., Bouyé, M., Cros, A., Dubois, B., Durand, E., Hahn, S., Kouach, D., Lacour, J.-L., Landis, D., Moore, T., Parès, L., Platzner, J., Saccoccio, M., Sallé, B., and Whitaker, R. (2005) ChemCam Instrument for the Mars Science Laboratory (MSL) Rover. *LPSC XXXIX*, abstract 1735.
- McEwen, A. S., Keszthelyi, L., Spencer, J.R., Schubert, G., Matson, D.L., Lopes-Gautier, R., Klaasen, K.P., Johnson, T.V., Head, J.W., Geissler, P., Fagents, S., Davies, A.G., Carr, M.H., Breneman, H.H., and Belton, M.J.S. (1998) High-temperature silicate volcanism on Jupiter's moon Io. *Science* 281, 87-90.
- McGuire, P.C., Ormö, J., Martinez, E.D., Manfredi, J.A.R., Elvira, J.G., Ritter, H., Oesker, M., and Ontrup, J. (2004) The Cyborg Astrobiologist: first field experience. *Int. J. Astrobiology* 3, 187-207, doi: 10.1017/S147355040500220X
- McKay, D.S., Carter, J.L., Boles, W.W., Allen, C.C., and Allton, J.H. (1994) JSC-1: A New Lunar Soil Simulant. *Engineering, Construction and Operations in Space IV, American Society of Civil Engineers*, pp. 857-866.
- McLoughlin, N., Brasier, M.D., Wacey, D., Green, O.R., and Perry, R.S. (2007) On biogenicity criteria for endolithic microborings on early Earth and beyond. *Astrobiology* 7, 1, 10-26.
- Melchiorre, E.B. and Williams, P.A. (2001) Stable isotopic characterization of the thermal profile and subsurface biological activity during oxidation of the Great Australia Deposit, Cloncurry, Queensland, Australia. *Econ. Geol.* 96, 1685-1693.
- Menzies, O.N., Bland, P.A., Cressey, G., and Berry, F.J. (2003) An X-ray Diffraction study of inclusions in Allende using a focussed X-ray Microsource. *LPSC XXXIV*, abstract 1734.
- MEPAG ND-SAG (2008) Science Priorities for Mars Sample Return. *Unpublished white paper, 73p, posted by the Mars Exploration Program Analysis Group (MEPAG) at*

<http://mepag.jpl.nasa.gov/reports/index.html>.

- Merrison, J.P., Jensen, J., Kinch, K.M., and Nørnberg, P. (2004) The Electrical Properties of Mars Analogue Dust. *Planet. Space. Sci.* 52, 279-290.
- Moore, H.J., Hutton, R.M., Clow, G.D., and Spitzer, C.R. (1987) Physical properties of the surface materials at the Viking landing sites on Mars, *USGS Prof. Paper 1389*.
- Mormile, M.R. and Storrie-Lombardi, M.C. (2005) The use of ultraviolet excitation of native fluorescence for identifying biomarkers in halite crystals. In *Astrobiology and Planetary Missions*, edited by Hoover, R.B., Levin, G.V., and Rozanov, A. Y., *Proc. SPIE* 5906, 246-253.
- Morris, R.V., Klingelhöfer, G., Bernhardt, B., Schröder, C., Rodionov, D., de Souza Jr., P.A., Yen, A., Gellert, R., Evlanov, E., Foh, J., Kankeleit, E., Gütlich, P., Ming, D.W., Renz, F., Wdowiak, T., Squyres, S.W., and Arvidson, R.E. (2004) Mineralogy at Gusev Crater from the Mössbauer Spectrometer on the Spirit Rover. *Science* 305, 833-836.
- Morris, R.V., Klingelhöfer, G., Schröder, C., Rodionov, D.S., Yen, A., Ming, D.W., de Souza Jr., P.A., Fleischer, I., Wdowiak, T., Gellert, R., Bernhardt, B., Evlanov, E.N., Zubkov, B., Foh, J., Bonnes, U., Kankeleit, E., Gütlich, P., Renz, F., Squyres, S.W., and Arvidson, R.E. (2006) Mössbauer mineralogy of rock, soil, and dust at Gusev crater, Mars: Spirit's journey through weakly altered basalt on the plains and pervasively altered basalt in the Columbia Hills. *J. Geophys. Res.* 111, E02S13, doi: 10.1029/2005JE002584.
- Moseley, H. G. J. (1913) The high frequency spectra of the elements. *Philosophical Magazine*, 26, 1024-1034.
- Murchie, S., McEwan, A., Christensen, P., Mustard, J., Bibring J.-P., and the CRISM, HiRISE, THEMIS and OMEGA Teams (2008) Discovery of diverse martian aqueous deposits from

orbital remote sensing. *Ground Truth from Mars: Science Payoff from a Sample Return Mission, April 21-23, Albuquerque, New Mexico*, abstract 4035.

Musselwhite, D.S., Swindle, T.D., and Lunine, J. (2001) Liquid CO breakout and the formation of recent small gullies on Mars. *Geophys. Res. Lett.* 28: 1283-1285.

Mutch, T.A., Binder, A.B., Huck, F.O., Levinthal, E.C., Morris, E.C., Sagan, C., and Young, A.T. (1972) Imaging experiment: The Viking Lander, *Icarus* 16, 92-110.

Näränen, J., Parviainen, H., Muinonen, K., Carpenter, J., Nygård, K., and Peura, M. (2008) Laboratory studies into the effect of regolith on planetary X-ray fluorescence spectroscopy. *Icarus* 198, 408-419.

Navarro-González, R., Rainey, F.A., Molina, P., Bagaley, D.R., Hollen, B.J., de la Rosa, J., Small, A.M., Quinn, R.C., Grunthaler, F.J., Cáceres, L., Gomez-Silva, B., and McKay, C.P. (2003) Mars-like soils in the Atacama Desert, Chile, and the Dry Limit of Microbial Life. *Science* 302, pp. 1018-1021, doi: 10.1126/science.1089143.

Nealson, K. and Berelson, W. (2003) Layered Microbial Communities and the Search for Life in the Universe. *Geomicrobiol. J.* 20, 451-462.

Neukum, G., Jaumann, R., Hoffmann, H., Hauber, E., Head, J.W., Basilevsky, A.T., Ivanov, B.A., Werner, S.C., van Gasselt, S., Murray, J.B., McCord, T., and the HRSC Co-Investigator Team (2004) Recent and episodic volcanic and glacial activity on Mars revealed by the High resolution Stereo Camera. *Nature* 432, 971-979.

Nijman, W., de Bruijne, K.H., and Valkering, M. (1998) Growth fault control of Early Archaean cherts, barite mounds and chert-barite veins, North Pole Dome, Eastern Pilbara, Western Australia. *Precambrian Res.* 95, 247-274.

- Orberger, B., Rouchon, V., Westall, F., de Vries, S.T, Pinti, D.L., Wagner, Ch., Wirth, R., and Hashizume, K. (2006) Micro-facies and origin of some Archaean Cherts (Pilbara, Australia). In *Processes on the Early Earth*, edited by Reinold, U. and Gibson, R., *Geol. Soc. Amer. Special Paper*, 133-156.
- Osinski, G.R. and Spray, J.G. (2003) Evidence for the shock melting of sulfates from the Haughton impact crater, Arctic Canada. *Earth Planet. Sci. Lett.* 215, 357-370.
- Owens, A., Bavdaz, M., Beckhoff, B., Fraser, G.W., Kolbe, M., Krumrey, M., Mantero, A., Mantler, M., Peacock, A., Pia, M.G., **Pullan, D.**, and Ulm, G. (2008) Measuring and interpreting X-ray fluorescence from planetary surfaces. *Analytical Chemistry*, doi: 101021_ac8009627 available online.
- Oze, C. and Sharma, M. (2005) Have Olivine, Will Gas: Serpentinization and the Abiogenic Production of Methane on Mars. *Geophysical Research Letters* 32, L10203-L10206.
- Pache, M., Reitner, J., and Arp, G. (2001) Geochemical evidence for the formation of a large Miocene "Travertine" mound at a sublacustrine spring in a soda lake (Wallerstein Castle Rock, Nordlinger Ries, Germany). *Facies* 45, 211-230.
- Parizot, M., Eriksson, P.G., Aifa, T., Sarkar, S., Banerjee, S., Catuneanu, O., Altermann, W., Bumby, A.J., Bordy, E.M., van Rooy, J., and Boshoff, A.J. (2005) Suspected microbial mat-related crack-like sedimentary structures in the Palaeoproterozoic Magaliesberg Formation sandstones, South Africa. *Precambrian Res.* 138, 274-296.
- Parnell, J., Lee, P., Cockell, C.S., and Osinski, G.R. (2004) Microbial colonization in impact-generated hydrothermal sulphate deposits, Haughton impact structure, and implications for sulphates on Mars. *Int. J. Astrobiology* 3, 265-271.
- Pedersen, L. (2000) Robotic Rock Classification and Autonomous Exploration. Doctoral

Dissertation, Tech. Report CMU-RI-TR-01-14, Robotics Institute, Carnegie Mellon University, November 2000.

Pedersen, L., Kortenkamp, D., Wettergreen, D., and Nourbakshk, I. (2003) A Survey of Space Robotics, in *The 7th International Symposium on Artificial Intelligence, Robotics and Automation in Space (i-SAIRAS-03)*.

Pohl, J., Eckstaller, A., and Robertson, P.B. (1988) Gravity and magnetic investigations in the Haughton impact structure, Devon Island, Canada. *Meteoritics* 23, 235-238.

Pohl, J., Stöffler, D., Gall, H., and Ernstson, K. (1977) The Ries Impact Crater. In *Impact and Explosion Cratering*, edited by Roddy, D.J. *et al.*, Pergamon Press., pp343-404.

Potts, P.J. (1987) A handbook of Silicate Rock Analysis. *Blackie & Son Limited, London*.

Potts, P.J., Tindle, A.G., and Webb, P.C. (1992) Geochemical Reference Material Compositions: Rocks, Minerals, Sediments, Soils, Carbonates, Refractories and Ores used in Research and Industry. *Whittles Publishing (UK) and CRC Press Inc. (USA)*. ISBN: 1-870325-40-0.

Potts, P.J., Webb, P.C., Williams-Thorpe, O., and Kilworth, R. (1995) Analysis of Silicate Rocks Using Field-portable X-ray Fluorescence Instrumentation Incorporating a Mercury(II) Iodide Detector: A Preliminary Assessment of Analytical Performance. *Analyst* 120, 1273-1278.

Poulet, F., Bibring, J.-P., Mustard, J.F., Gendrin, A., Mangold, N., Langevin, Y., Ardivison, R.E., Gondet, B., and Gomez, C. (2005) Phyllosilicates on Mars and implications for early martian climate. *Nature* 438, 623-627.

Price, G.J., Fraser, G.W., Pearson, J.F., Nussey, J.P., Hutchinson, I.B., Holland, A.D., Turner, K., and **Pullan, D.** (2004). Prototype imaging x-ray fluorescence spectrometer based on

microchannel plate optics, *Rev. Sci. Instrum.* 75, 2314.

Pullan, D. (2007) The Planetary Analogue Field Studies Network (PAFS-net). *Second International Workshop, Exploring Mars and its Earth Analogues, Trento, Italy, 19-26 June 2007.*

Pullan, D., Sims, M. R., Wright, I. P., Pillinger, C. T., and Trautner, R. (2004) Beagle 2: the Exobiological Lander of Mars Express. In *Mars Express: The Scientific Payload*, edited by Wilson, A., *ESA Special Publication SP-1240.*

Pullan, D., Westall, F., Hofmann, B.A., Parnell, J., Cockell, C.S., Edwards, H.G.M, Jorge Villar, S.E., Schröder, C., Cressey, G., Marinangeli, L., Richter, L., and Klingelhöfer, G. (2008) Identification of Morphological Biosignatures in Martian Analogue Field Specimens using In Situ Planetary Instrumentation, *Astrobiology* 8, 119-156.

Ramsey, M.H., Potts, P.J., Webb, P.C., Watkins, P., Watson, J.S., and Coles, B.J. (1995) An objective assessment of analytical method precision: comparison of ICP-AES and XRF for the analysis of silicate rocks. *Chemical Geology* 124, 1-19.

Richter, L., Coste, P., Gromov, V.V., Kochan, H., Nadalini, R., Ng, T.C., Pinna, S., Richter, H.-E., and Yung, K.L. (2002) Development and testing of subsurface sampling devices for the Beagle 2 lander. *Planet. Space. Sci.* 50, 903-913.

Rieder, R., Economou, T., Wänke, H., Turkevich, A., Crisp, J., Brückner, J., Dreibus, G., and McSween Jr., H.Y. (1997) The chemical composition of martian soil and rocks returned by the mobile alpha proton X-ray spectrometer: Preliminary results from the X-ray mode. *Science* 278, 1771-1774.

Rieder, R., Gellert, R., Anderson, R.C., Brückner, J., Clark, B.C., Dreibus, G., Economou, T., Klingelhöfer, G., Lugmair, G.W., Ming, D.W., Squyres, S.W., d'Uston, C., Wänke, H., Yen,

- A., and Zipfel, J. (2004) Chemistry of Rocks and Soils at Meridiani Planum from the Alpha Particle X-ray Spectrometer. *Science* 306, 1746-1749.
- Rieder, R., Gellert, R., Brückner, J., Klingelhöfer, G., Dreibus, G., Yen, A., and Squyres, S.W. (2003) The new Athena alpha particle X-ray spectrometer for the Mars Exploration Rovers. *J. Geophys. Res.* 108(E12), 8006, doi: 10.1029/2003JE002150.
- Rose, E.C., McLoughlin, N., and Brasier, M.D. (2006) Ground truth: the epistemology of searching for the earliest life on earth. In *Cellular Origins of Life and Its Evolution, Vol. 10: Life as We Know It*, edited by J. Seckbach, Springer-Verlag, New York, pp. 259-285.
- Rothschild, L.J. and Mancinelli, R.L. (2001) Life in extreme environments. *Nature* 409, 1092-1101.
- Ruiz, J.M.G, Carnerup, A., Christy, A.G., Welham, N.J, and Hyde, S.T. (2002) Morphology: An ambiguous indicator of biogenicity. *Astrobiology* 2, 335-351.
- Rull, F. and Martinez-Frias, J. (2006) Raman Spectroscopy goes to Mars. *Spectroscopy Europe* 18, 18-21.
- Sangameshwar, S.R. and Barnes, H.L. (1983) Supergene processes in zinc-lead-silver sulphide ores in carbonates. *Econ. Geol.* 78, 7, 1379-1397.
- Schenker, P.S., Huntsberger, T.L., Pirjanian, P., Baumgartner, E.T., and Tunstel, E. (2003) Planetary rover developments supporting Mars exploration, sample return and future human-robotic colonization. *Autonomous Robots* 14, 2-3, 103-126.
- Schieber, J., Zawar, Y., and Glamoclija, M. (2008) Experiments on silicification of iron microbes – a preliminary report. *LPSC XXXIX*, abstract 2132.

- Schlotz, R. and Uhlig, S. (2006) Introduction to X-ray Fluorescence. *Bruker AXS GmbH, Karlsruhe, Germany*.
- Schröder, C., Klingelhöfer, G., and Tremel, W. (2004) Weathering of Fe-bearing minerals under Martian conditions, investigated by Mössbauer spectroscopy. *Planet. Space. Sci.* 52, 997-1010.
- Schröder, C., Klingelhöfer, G., Bailey, B., and Staudigel, H. (2005) Mössbauer spectroscopy as a tool in astrobiology. *Hyperfine Interactions* 166, 567-571.
- Schulze-Makuch, D., Dohm, J.M., Fan, C., Fairén, A.G., Rodriguez, J.A.P, Baker, V.R., and Fink, W. (2007) Exploration of hydrothermal targets on Mars. *Icarus* 189, 308-324.
- Scott, D. and Hajnal, Z. (1988) Seismic signature of the Haughton structure. *Meteoritics* 23, 239-247.
- Sharma, S.K., Lucey, P.G., Ghosh, M., Hubble, H.W., and Horton, K.A. (2003) Stand-off Raman spectroscopic detection of minerals on planetary surfaces. *Spectrochim. Acta, Part A: Mol. Biomol. Spectrosc.* 59, 2391-2407.
- Shaw, A., Woods, M., Honary, E., Rendell, P., **Pullan, D.**, Barnes, D. Pugh, S., and Long, D. (2007) CREST Robotic Scientist, *Proc. Towards Autonomous Robotic Systems (TAROS)*, 3rd - 5th September 2007, University of Aberystwyth.
- Sherlock, S.C., Kelley, S.P., Parnell, J., Green, P., Lee, P., Osinski, G.R., and Cockell, C.S. (2005) Re-evaluating the age of the Haughton impact crater. *Meteor. Planet. Sci.* 40, 12, 1777-1787.

Shotwell, R. (2005) Phoenix – The First Mars Scout Mission. *Acta Astronautica* 57, 121-134.

Siebert, J, Hirsch, P., Hoffmann, B., Gliesche, C.G., Peissl, K., and M. Jendrach, M. (1996) Cryptoendolithic microorganisms from Antarctic sandstone of Linnaeus Terrace (Asgard Range): diversity, properties and interactions, *Biodiversity and Conservation*, 5, 11, 1337-1363.

Sims, M.R. (ed.) (2004) Beagle 2 Mars: Mission Report. *University of Leicester, UK*. ISBN 1-898489-35-1.

Sims, M.R., Cullen, D.C., Bannister, N.P., Grant, W.D., Henry, O., Jones, R., McKnight, D., Thompson, D.P., and Wilson, P.K. (2005) The specific molecular identification of life experiment (SMILE). *Planet. Space. Sci.* 53, 781-791.

Sims, M. R., **Pullan, D.**, Pillinger, C.T., and Wright, I.P. (2002) An evaluation of in-situ analysis and sample return in the exploration of Mars, *Planet. Space Sci.* 50, 657-668.

Smith, H.D. and McKay, C.P. (2005) Drilling in ancient permafrost on Mars for evidence of a second genesis of life. *Planet. Space. Sci.* 53, 1302-1308.

Smith, T., Thompson, D.R., Weinstein, D., and Wettergreen, D. (2006) Autonomous rover detection and response applied to the search for life via chlorophyll fluorescence in the Atacama Desert. *LPSC XXXVII*.

Smith, P. H., Tomasko, M.G., Britt, D., Crowe, D.G., Reid, R., Keller, H.U., Thomas, N., Gliem, F., Rueffer, P., Sullivan, R., Greeley, R., Knudsen, J.M., Madsen, M.B., Gunlaugssen, H.P., Hviid, S.F., Goetz, W., Soderblom, L.A., Gaddis, L., and Kirk, R. (1997) The imager for Mars Pathfinder experiment, *J. Geophys. Res.* 102(E2), 4003–4025.

- Squyres, S.W., Arvidson, R.E., Baumgartner, E.T., Bell III, J.F., Christensen, P.R., Gorevan, S., Herkenhoff, K.E., Klingelhöfer, G., Madsen, M.B., Morris, R.V., Rieder, R., and Romero, R.A. (2003) Athena Mars rover science investigation. *J. Geophys. Res.* 108(E12), 8062, doi: 10.1029/2003JE002121.
- Squyres, S.W., Arvidson, R.E., Ruff, S., Gellert, R., Morris, R.V., Ming, D.W., Crumpler, L., Farmer, J.D., Des Marais, D.J., Yen, A., McLennan, S.M., Calvin, W., Bell III, J.F., Clark, B.C., Wang, A., McKoy, T.J., Schmidt, M.E., and de Souza Jr., P.A. (2008) Detection of Silica-Rich Deposits on Mars. *Science* 320, 1063-1067.
- Squyres, S.W. and Knoll, A.H. (2005) Sedimentary rocks at Meridiani Planum: Origin, diagenesis, and implications for life on Mars. *Earth Planet. Sci. Lett.* 240, 1-10.
- Steele, A., Beaty, D.W., Amend, J., Anderson, R., Beegle, L., Benning, L., Bhattacharya, J., Blake, D., Brinckerhoff, W., Biddle, J., Cady, S., Conrad, P., Lindsay, J., Mancinelli, R., Mungas, G., Mustard, J., Oxnevad, K., Toporski, J., and Waite, H. (2006) The Astrobiology Field Laboratory. *Unpublished white paper (v3), 72p, posted by the Mars Exploration Program Analysis Group (MEPAG) at <http://mepag.jpl.nasa.gov/reports/index.html>.*
- Steele, A., Fries, M.D., Amundsen, H.E.F., Mysen, B.O., Fogel, M.L., Schweizer, M., and Bockor, N.Z. (2007) Comprehensive imaging and Raman spectroscopy of carbonate globules from Martian meteorite ALH 84001 and a terrestrial analogue from Svalbard. *Meteoritics Planet. Sci.* 42, 1549-1566.
- Storrie-Lombardi, M.C. (2005) Post-Bayesian strategies to optimize astrobiology instrument suites: lessons from Antarctica and the Pilbara. In *Astrobiology and Planetary Missions*, edited by Hoover, R.B., Levin, G.V., and Rozanov, A. Y., *Proc. SPIE* 5906, 288-301.
- Strom, R.G. and Sprague, A.L. (2003) *Exploring Mercury: The Iron Planet*. Springer-Verlag London Ltd, ISBN-13: 978-1852337315.

- Sumner, D.Y. (2004) Poor preservation potential of organics in Meridiani Planum Unit P2 sedimentary rocks. *Mars Astrobiology Science and Technology Workshop, Washington, DC.*
- Sun, H.J. and Friedmann, E.I. (1999) Growth on geological time scales in the Antarctic cryptoendolithic microbial community. *Geomicrobiol. J.* 16:193-202.
- Talboys, D.L. (2006) The Beagle 2 X-ray spectrometer for Mars. PhD thesis, University of Leicester, UK.
- Tarcea, N., Popp, J., Schmitt, M., Kiefer, W., Hochleitner, R., Simon, G., Hilchenbach, M., Hofer, S., and Stuffer, T. (2002) Raman spectroscopy as a suitable tool for biological and mineralogical *in situ* planetary studies. *Proc. of the Second European Workshop on Exo/Astrobiology, Graz, Austria, 2002*, ESA SP-518, 399-402.
- Taylor, R.L., Ashley, J.M., Locke III, W.W., Hamilton, W.L., and Erickson, J.B. (1989) Geological Map of Yellowstone National Park. *Montana State University, Bozeman.*
- Thomas, N., Lüthi, B.S., Hviid, S.F., Keller, H.U., Markiewicz, W.J., Blümchen, T., Basilevsky, A.T., Smith, P.H., Tanner, R., Oquest, C., Reynolds, R., Josset, J.-L., Beauvivre, S., Hofmann, B., Rüffer, P., and Pillinger, C.T. (2004) The microscope for Beagle 2. *Planet. Space Sci.* 52, 853-866.
- Thompson, A. and Vaughan, D. (eds.) (2001) X-Ray Data Booklet (Second Edition). *Center for X-Ray Optics and Advanced Light Sources, Lawrence Berkeley National Laboratory, University of California.*
- Thompson, D. and Castano, R. (2007) Performance Comparison of Rock Detection Algorithms for Autonomous Planetary Geology, In *Proceedings of 2007 IEEE Aerospace Conference, Big Sky Montana, USA.*

- Thompson, D.R., Niekum, S., Smith, T., and Wettergreen, D.S. (2005) Automatic Detection and Classification of geological Features of Interest, In *Proc. IEEE Aerospace Conf.*, March 2005
- Thompson, D.R., Smith, T., and Wettergreen, D. (2006) Autonomous detection of novel biologic and geologic features in Atacama Desert rover imagery, *LPSC XXXVII*.
- Thompson, M. (2004) The amazing Horwitz function. *Royal Society of Chemistry, AMC Technical Brief Number 17*.
- Tice, M. and Lowe, D.R. (2004) Photosynthetic microbial mats in the 3,416-Myr-old ocean. *Nature* 431, 549–552.
- Toporski, J.K.W., Steele, A., Westall, F., Thomas-Keprta, K.L., and McKay, D.S (2002) The simulated silicification of bacteria - new clues to the modes and timing of bacterial preservation and implications for the search for extraterrestrial microfossils. *Astrobiology* 2, 1-26.
- Towner, M.C., Patel, M.R., Ringrose, T.J., Zarnecki, J.C., **Pullan, D.**, Sims, M.R., Haapanala, S., Harri, A.-M., Polkko, J., Wilson, C.F., Zent, A.P., Quinn, R.C., Grunthaner, F.J., Hecht, M.H., and Garry, J.R.C. (2004) The Beagle 2 environmental sensors: science goals and instrument description. *Planet. Space Sci.* 52, pp. 1141-1152.
- Tunstel, E. and Howard, A. (2003) Approximate reasoning for safety and survivability of planetary rovers. *Fuzzy Sets and Systems* 134, 27-46.
- Upfold, R.L. (1984) Tufted microbial (cyanobacterial) mats from the Proterzoic Stoer Group, Scotland. *Geological Magazine* 121, 351-355.

- Vago, J.L., Gardini, B., and Kminek, G. (2003) ESA's new mission to search for signs of life on Mars: ExoMars and its Pasteur scientific payload. EGS-AGU-EUG joint assembly, Nice, France, 6-11 April 2003, *Geophys. Res. Abstracts, Eur. Geophys. Soc.* 5, 02504.
- Vaughan, D.J. and Craig, J. (1978) Mineral chemistry of metal sulfides. *Cambridge Univ. Press, England.*
- Viking Science Team (1977) Scientific results of the Viking project, *J. Geophys. Res.* 82, 3959-4667.
- Walker, J.J., Spear, J.R., and Pace, N.R. (2005) Geobiology of a microbial endolithic community in the Yellowstone geothermal environment. *Nature* 434, 1011-1014.
- Walsh, M.M. (1992) Microfossils and possible microfossils from the Early Archean Onverwacht Group, Barberton Mountain Land, South Africa. *Precambrian Res.* 54, 271-293.
- Walsh, M.M. (2004) Evaluation of early Archean volcanoclastic and volcanic flow rocks as possible sites for carbonaceous fossil microbes. *Astrobiology* 4, 429-437.
- Walter, M.R. (1976) *Stromatolites*. Springer Verlag, Berlin.
- Walter, M.R. (1978) Recognition and significance of Archaean stromatolites, In *Archaean cherty metasediments: Their sedimentology, micropalaeontology, biogeochemistry, and significance to mineralization*, edited by J.E. Glover and D.I. Groves, pp. 1-10, University of Western Australia, Perth, WA
- Walter, M.R., Buick, R., and Dunlop, J.S.R. (1980) Stromatolites 3400-3500 Myr old from the North Pole area, Western Australia. *Nature* 284, 443-445.

- Walter, M.R. and Des Marais, D.J. (1993) Preservation of biological information in thermal spring deposits: Developing a strategy for the search for a fossil record on Mars. *Icarus* 101, p. 129–143.
- Walker, J.J., Spear, J.R., and Pace, N.R. (2005) Geobiology of a microbial endolithic community in the Yellowstone geothermal environment. *Nature* 434, 1011-1014, doi: 10.1038/nature03447.
- Wang, A., Haskin, L.A., Lane, A.L., Wdowiak, T.J., Squyres, S.W., Wilson, R.J., Hovland, L.E., Manatt, K.S., Raouf, N., and Smith, C.D. (2003) Development of the Mars microbeam Raman spectrometer (MMRS). *J. Geophys. Res.* 108(E1), 5005, doi: 10.1029/2002JE001902.
- Watson, J.S. (1996) Fast, Simple Method of Powder Pellet Preparation for X-ray Fluorescence Analysis, *X-Ray Spectroscopy* 25, 173-174.
- Weisbin, C.R., Rodriguez, G., Schenker, P.S., Das, H., Hayati, S.A., Baumgartner, E.T., Maimone, M., Nesnas, I.A., and Volpe, R.A. (1999) Autonomous rover technology for Mars sample return. *Proc. 5th International Symposium on Artificial Intelligence, Robotics and Automation in Space (i-SAIRAS), Noordwijk, Netherlands, 1999.*
- Westall, F. (2004) Early life on Earth: The ancient fossil record. In *Astrobiology: Future perspectives*, edited by Ehrenfreund *et al.*, Kluwer (Dordrecht, Netherlands), pp 287-316.
- Westall, F. (2005a) Life on the early Earth: A sedimentary view. *Science* 308, 366-367.
- Westall, F. (2005b) Early Life on Earth and Analogies to Mars, In *Water on Mars and Life*, edited by Tokano, T., *Adv. Astrobiol. Biogeophys*, Springer, Berlin Heidelberg, pp 45-64.
- Westall, F., de Ronde, C.E.J., Southam, G., Grassineau, N., Colas, M., Cockell, C., and Lammer,

- H. (2006a) Implications of a 3.472–3.333 Gyr-old subaerial microbial mat from the Barberton greenstone belt, South Africa for the UV environmental conditions on the early Earth. *Phil. Trans. R. Soc. B.* 361, 1857-1875.
- Westall, F., de Vries, S.T., Nijman, W., Rouchon, V., Orberger, B. Pearson, V., Watson, J., Verchovsky, A., Wright, I., Rouzaud, J.-N., Marchesini, D., and Anne, S. (2006b) The 3.466 Ga Kitty's Gap Chert, an Early Archaean microbial ecosystem. In *Processes on the Early Earth*, edited by Reimold, W.U., Gibson, R., *Geol. Soc. Amer. Spec. paper* 405, 105-131.
- Westall, F., de Wit, M.J, Dann, J., van der Gaast, S., de Ronde, C.E.J, and Gerneke, D (2001) Early Archaean fossil bacteria and biofilms in hydrothermally-influenced sediments from the Barberton greenstone belt, South Africa. *Precambrian Res.* 106, 93-116.
- Westall, F. and Folk, R.L. (2003) Exogeneous carbonaceous microstructures in Early Archaean cherts and BIFs from the Isua Greenstone Belt: implications for the search for life in ancient rocks. *Precambrian Res.* 126(3-4), 313-330.
- Westall, F., Hofmann, B.A., and Brack, A. (2004) Searching for fossil microbial biofilms on Mars: A case study using a 3.46 billion-year old example from the Pilbara in Australia. *Proc. of the third European Workshop on Exo/Astrobiology. Mars: The search for life, Madrid, Spain, 2003*, ESA SP-545, 37-40.
- Westall, F. and Klingelhöfer, G. (2007) Mars Origins Mission. ESA Cosmic Vision proposal.
- Westall, F. and Southam, G. (2006) Early life on Earth. In *Archean Geodynamics and Environments*, edited by Benn, K., *et al.*, *AGU Geophys. Monogr.*, 164, 283-304.
- Westall, F. and Walsh, M.M. (2006) Early Life on Earth: 3.5-3.3 Ga microbial remains from South Africa. *Geophys. Res. Abs* 8, 11079.

- Wettergreen, D., Cabrol, N., Baskaran, V., Calderon, F., Heys, S., Jonak, D., Luders, R.A., Pane, D., Smith, T., Teza, J., Tompkins, P., Villa, D., Williams, C., and Wagner, M.D. (2005) Second Experiments in the Robotic Investigation of Life in the Atacama Desert of Chile. *8th International Symposium on Artificial Intelligence, Robotics and Automation in Space, September, 2005*.
- Wiens, R., Maurice, S., Bridges, N., Clark, B., Cremers, D., Herkenhoff, K., Kirkland, L., Mangold, N., Manhés, G., Mauchien, P., McKay, C., Newsom, H., Poitrasson, F., Sautter, V., d'Uston, C., Vaniman, D., and Shipp, S. (2005) ChemCam science objectives for the Mars Science Laboratory (MSL) Rover . *LPSC XXXVI*, abstract 1580.
- Wierzchos, J., Ascaso, C., Sancho, L.G., and Green, A. (2003) Iron-rich diagenetic minerals are biomarkers of microbial activity in Antarctic rocks. *Geomicrobiology Journal* 20, 15-24.
- Wilson, A. (ed.) (1999) Exobiology in the Solar System and the Search for Life on Mars. European Space Agency, SP-1231, October 1999.
- Wilson, A. (ed.) (2004) Mars Express: The Scientific Payload. *ESA Special Publication SP-1240*.
- Woods, M., Shaw, A., Barnes, D., Price, D., Long, D., and **Pullan, D.** (2009) Autonomous Science for an ExoMars Rover like Mission, *Journal of Field Robotics* 26, Issue 4, 358-390, doi: 10.1002/rob.20289.
- Woods, M., Shaw, A., Evans, M., Ward, R., Barnes, D., Summers, P., Paar, G., Bauer, A., and **Pullan, D.** (2008a) Image Based Localisation and Autonomous Image assessment for a Martian Aerobot. *In Proc. 9th Int. Symp. on AI in Robotic Automation and Space, 24th February 2008, Los Angeles, USA*.
- Woods, M., Shaw, A., Rendell, P., Barnes, D., Pugh, S., Price, D., **Pullan, D.**, and Long, D. (2008b) CREST Autonomous Robotic Scientist: Developing a Closed-Loop Science

Exploration Capability for European Mars Missions. *In Proc. 9th Int. Symp. on AI in Robotic Automation and Space, 24th February 2008, Los Angeles, USA.*

Wynn-Williams, D.D. and Edwards, H.G.M. (2000) Proximal analysis of regolith habitats and protective biomolecules in situ by laser raman spectroscopy: Overview of terrestrial Antarctic habitats and Mars analogs. *Icarus* 144, 486-503.

Wynn-Williams, D.D., Edwards, H.G.M., Newton, E.M., and Holder, J.M. (2002) Pigmentation as a survival strategy for ancient and modern photosynthetic microbes under high ultraviolet stress on planetary surfaces. *Int. J. Astrobiology* 1, 39-49.

Yen, A.P., Morris, R.V., Clark, B.C., Gellert, R., Knudsen, A.T., Squyres, S.W., Mittlefehldt, D.W., Ming, D.W., Arvidson, R., McCoy, T.J., Schmidt, M., Hurowitz, J., Li, R., and Johnson, J.R. (2008) Hydrothermal processes at Gusev Crater: An evaluation of Paso Robles class soils. *J. Geophys. Res.* 113, E06S10, doi: 10.1029/2007JE002978.

Yen, A.S., Kim, S.S., Hecht, M.H., Frant, M.S., and Murray, B. (2000) Evidence That the Reactivity of the Martian Soil Is Due to Superoxide Ions. *Science* 289, 1909-1912.